Control of electron injection and acceleration in Laser-Wakefield Accelerators

Emilien Guillaume

▶ **To cite this version:**

Emilien Guillaume. Control of electron injection and acceleration in Laser-Wakefield Accelerators. Plasma Physics [physics.plasm-ph]. École Polytechnique, 2015. English. NNT : . tel-01249964v2

Control of electron injection and acceleration in Laser-Wakefield Accelerators

THÈSE

présentée et soutenue publiquement le 11 Décembre 2015

pour l'obtention du

Doctorat de l'École Polytechnique

par

Emilien GUILLAUME

Composition du jury

Rapporteurs :	Fabien DORCHIES	CELIA, Bordeaux
	Guy BONNAUD	CEA, Saclay
Examinateurs :	Manuel JOFFRE	LOB, Palaiseau
	Jean-Raphaël MARQUÈS	LULI, Palaiseau
	Olle LUNDH	LLC, Lund
Membre invité :	Cédric THAURY	LOA, Palaiseau
Directeur de thèse :	Victor MALKA	LOA, Palaiseau

« The spectre showed a spectre's ordinary caprice: it gave no sign of being. »

Emily Brontë, *Wuthering Heights*, Chap. III, 1847

« Le spectre a témoigné de l'ordinaire caprice des spectres : il n'a donné aucun signe d'existence. »

Emily Brontë, *Les Hauts de Hurlevent*, Chap. III, 1847

Remerciements

Le travail réalisé au cours de ces trois années de thèse n'aurait en aucun cas été possible sans la contribution et le soutien de nombreuses personnes que j'aimerais remercier vivement.

Je remercie en premier lieu mon directeur de thèse, Victor Malka. Grâce à son exceptionnelle disponibilité et ses nombreux conseils avisés, il a su guider mes travaux tout en me laissant une grande autonomie. Je lui suis extrêmement reconnaissant pour tout ce qu'il a pu m'apporter, que ce soit scientifiquement ou humainement, ainsi que pour sa bonne humeur contagieuse responsable de l'excellente ambiance de travail qui a régné tout au long de mon séjour dans son groupe de recherche. J'ai également eu l'opportunité de beaucoup voyager pour aller présenter mes travaux ou réaliser des expériences, ce dont je lui suis très reconnaissant.

Je souhaite ensuite remercier particulièrement Cédric Thaury, mon encadrant de thèse, qui m'a accompagné jour à jour dans mon aventure doctorale. En plus de m'initier au travail d'expérimentateur avec une patience à toute épreuve et une pédagogie incroyable, il a toujours été d'un soutien sans faille au cours de mes trois années passées à travailler en sa compagnie. J'ai eu la chance de profiter de sa forte expertise physique et expérimentale sur l'accélération d'électrons au cours d'innombrables discussions. Je lui suis infiniment reconnaissant pour son dynamisme et son enthousiasme permanent. Son côté railleur a énormément participé à l'excellente ambiance qui régnait en Salle Jaune, bien que j'en ai été parfois (souvent ;)) la cible.

Je suis également très reconnaissant envers les différentes personnes avec qui j'ai pu réaliser les expériences en Salle Jaune : Kim Ta Phuoc, Andreas Döpp et Julien Gautier particulièrement. Toutes les expériences réalisées en leur compagnie se sont toujours déroulées dans une ambiance de travail excellente. La génération de chocs en écoutant des musiques de Noël en plein mois de juin n'aurait pas été aussi agréable sans eux. Je souhaite remercier vivement Agustin Lifschitz, pour sa disponibilité et sa bonne humeur, ainsi que pour toutes les simulations qu'il a pu réaliser pour que l'on puisse comprendre ce que subissaient nos électrons. Un grand merci également à Jean-Philippe Goddet et Amar Tafzi, les laséristes de la Salle Jaune, pour leur gentillesse, leur forte implication dans les campagnes expérimentales et leur patience quand il s'agissait, pour la n-ième fois, de changer le Phi 3 sur le Dazzler.

Je souhaite exprimer toute ma gratitude à Antoine Rousse de m'avoir accueilli au LOA, laboratoire dans lequel règne un environnement de travail des plus agréables et particulièrement stimulant. Plus généralement, je tiens à remercier tous les membres (anciens et actuels) des groupes SPL et FLEX avec qui j'ai eu la chance d'interagir, et qui ont participé fortement à l'excellente ambiance que j'ai tant apprécié pendant ma thèse : merci à Sébastien Corde, Jérôme Faure, Alessandro Flacco, Julien Gautier, Jean-Philippe Goddet, Guillaume Lambert, Agustin Lifschitz, Victor Malka, Kim Ta Phuoc, Stéphane Sebban, Amar Tafzi, Cédric Thaury, Fabien Tissandier et Boris Vodungbo. Merci aussi à tous les stagiaires, thésards et post-docs avec qui j'ai pu partager à la fois mon bureau et de nombreuses discussions (scientifiques ou pas) dans la meilleure ambiance qui soit : Adrien Depresseux, Andreas Döpp, Rémi Lehe, Rachel Bruch, Florian Mollica, Gabrielle Grittani, Loann Pommarel, Antoine Doch, Benoît Beaurepaire, Benjamin Vauzour, Benoît Mahieu, Evgeny Chelnokov et Igor Andriyash. Merci pour tous ces moments passés, que ce soit en jouant au ping-pong, en écoutant des hymnes régionaux ou en mangeant des Papa Burger. Un merci tout particulier à Adrien, mon co-thésard, avec qui j'ai passé la majeure partie de mon temps en Salle Jaune. Merci également à Andreas, avec qui j'ai travaillé des heures durant la tête plongée dans ROSA. Nous avons trimé tous les trois ensemble

Contents

Contents

Introduction

Context

Acceleration of electrons to high energies is of major importance for several fields in the scientific community. High energy electrons can for instance be used for studying collisions with positrons or for generating intense x-ray beams. In these cases, electrons are generally accelerated to high energies using conventional radio-frequency (RF) accelerators. Whereas the electron beam has a very good quality (low energy spread, low emittance, high charge), these costly devices are constrained by the maximum amplitude of the oscillating electric fields in RF cavities (a few dozens of MeV.m^{-1}), thus requiring several kilometers of acceleration distance to achieve very high energies. For instance, in the Stanford Linear Accelerator (SLAC, the longest linear accelerator in the world), electrons are accelerated over 3.2 km to reach the 50 GeV range.

Alternatively, Laser Wakefield Acceleration (LWFA) is a process allowing for the acceleration of electrons in laser-driven relativistic plasma waves in which electric fields are 10^3 - 10^4 times larger than in RF accelerators. This induces a considerable reduction of the accelerator length (and hence the cost) to produce high energy electron beams. The concept, first introduced by Tajima and Dawson [1979], relies on the generation of an accelerating structure by focusing an ultra-intense femtosecond laser pulse in a gas target, in which electrons can be trapped and accelerated.

Since the first experimental demonstration of quasi-monoenergetic electron beam in the bubble regime in 2004 [Faure et al., 2004; Geddes et al., 2004; Mangles et al., 2004], several major steps in LWFA development were achieved. The 1 GeV barrier was broken down two years later [Leemans et al., 2006]. The highest electron energy from LWFA to date is around 4.2 GeV [Leemans et al., 2014], with several other experimental demonstration of multi-GeV beams [Kim et al., 2013a; Wang et al., 2013] made possible thanks to the development of Petawatt laser systems. LWFA experiments suffer from a lack of stability due notably to a non perfect control of electron injection in the accelerating cavity. A lot of work has been dedicated over the past few years towards controlling this injection and thus improving the quality and stability of electron beams, specifically in terms of energy spread and charge. Several methods for controlling injection were developed, either by shaping the plasma density profile [Geddes et al., 2008; Faure et al., 2010a; Schmid et al., 2010; Buck et al., 2013], by using additional laser pulses [Umstadter et al., 1996; Esarey et al., 1997; Faure et al., 2006a; Davoine et al., 2009; Lehe et al., 2013] or by using different gas compositions [Pak et al., 2010; McGuffey et al., 2010; Pollock et al., 2011a]. The improvement of these injection techniques to obtain an electron beam with the better quality and stability is one of the major axis developed in this thesis.

Many potential applications of LWFA electron beams require low energy spread, low divergence and high charge electron beams with a good stability. For instance, LWFA based

Free-Electron Lasers (FELs) [Maier et al., 2012; Couprie et al., 2014] require further improvement of the beam quality to achieve efficient lasing. Other applications such as high-resolution gamma radiography [Glinec et al., 2005] or radiobiology experiments [Malka et al., 2010; Lundh et al., 2012] would benefit from a charge increase while conserving a good overall quality.

Objective and outline

In this context, the principal objectives of my thesis were to study different injection techniques and to better understand the physical dynamics of Laser-Wakefield Acceleration in order to improve the electron bunch quality and reproducibility. This work mainly focuses on the experimental comparison of a whole set of different injection techniques to improve important electron beam parameters (charge and energy spread). Furthermore, several experimental demonstrations were performed to have a better control of the beam during the acceleration, notably by monitoring the longitudinal phase-space or the divergence thanks to density-tailored plasmas. These experimental studies are supported by Particle-In-Cell simulations and analytical models to have a better insight of the physics undergoing in these processes. The structure of the manuscript is as follows :

- Chapter 1 presents the theory of laser propagation in an underdense plasma and the main principle of Laser-Wakefield Acceleration. Experimental bunch parameters and injection issue are particularly developed and referred to in the rest of the manuscript.

- Chapter 2 deals with the density transition injection technique. The formation of sharp transitions in shock fronts is particularly studied numerically. These shocks are used in experiment to generate good quality, quite stable electron beams with low charge and tunable energy.

- The ionization injection method is studied in detail in chapter 3. First, experimental acceleration of electrons in pure high Z gases is presented as a way to produce heavily-charged beams. By combining ionization and density transition methods, it is possible to obtain very stable, high-quality tunable electron beams.

- Chapter 4 proposes a new technique to overcome the dephasing limit in laser-wakefield accelerators by using a tailored plasma density profile. A first experimental demonstration presents the technique to manipulate the electron longitudinal phase-space. This method is used in a second experiment to rephase monoenergetic electron beams and enhance their energy.

- Chapter 5 focuses on the origin of the beam angular momentum and its evolution during the acceleration. This important effect has to be taken into account in measurements of the transverse quality of the beam relying on the properties of x-ray emitted by electrons.

- Finally, the beam divergence may be important for various applications. A new method using a second gas jet to reduce the divergence is proposed in chapter 6 : the laser-plasma lens. The experimental demonstration of this technique allows for an important reduction of the beam divergence.

- In addition, Appendice A details the calculations of phase-locking and phase-resetting of electrons presented in chapter 4 and Appendice B lists my publications in peer-reviewed journals.

Chapter 1

Physics of laser-plasma acceleration

This chapter covers the main theoretical foundations behind laser-wakefield acceleration which are needed to understand the experimental results. I first discuss the theoretical description of laser propagation in an underdense plasma. In a second part is detailed the principle of plasma wave generation and electron injection and acceleration in the linear and bubble regimes. The accelerated bunch properties are presented in the third section. Finally, the last section is focused on the experimental facility "Salle Jaune" on which the work presented in this thesis has been performed.

Contents

1.1 Laser pulse propagation in an underdense plasma

1.1.1 Laser formalism

Electromagnetic fields

A laser pulse is an electromagnetic wave confined with a spatio-temporal envelope $\boldsymbol{E_{env}}$ and $\boldsymbol{B_{env}}$ that can be described by the following equations :

$$\boldsymbol{E}(\boldsymbol{x}, t) = \boldsymbol{E_{env}}(\boldsymbol{x}, t) \cos[\omega_0 t - \boldsymbol{kx} + \varphi_0(t)] \tag{1.1}$$

$$\boldsymbol{B}(\boldsymbol{x}, t) = \boldsymbol{B_{env}}(\boldsymbol{x}, t) \cos[\omega_0 t - \boldsymbol{kx} + \varphi_0(t)] \tag{1.2}$$

Here, $\boldsymbol{E}$ and $\boldsymbol{B}$ are the electric and magnetic field respectively, $\boldsymbol{E_{env}}$ and $\boldsymbol{B_{env}}$ define the envelope amplitude and the polarization direction of the laser, ω_0 is the angular frequency, $\boldsymbol{k}$ is the wave vector with $|\boldsymbol{k}| = k_0 = \omega_0/c$ (c the speed of light in vacuum) and $\varphi_0(t)$ is the absolute phase of the pulse. The angular frequency of the field ω_0 is related with the laser wavelength λ_0 as $\omega_0 = 2\pi c/\lambda_0$, considering a monochromatic pulse. The propagation of an electromagnetic wave is described by Maxwell's equations :

$$\boldsymbol{\nabla}.\boldsymbol{E} = \frac{\rho}{\varepsilon_0} \tag{1.3}$$

$$\boldsymbol{\nabla}.\boldsymbol{B} = 0 \tag{1.4}$$

$$\boldsymbol{\nabla} \times \boldsymbol{E} = -\frac{\partial \boldsymbol{B}}{\partial t} \tag{1.5}$$

$$\boldsymbol{\nabla} \times \boldsymbol{B} = \frac{1}{c^2} \frac{\partial \boldsymbol{E}}{\partial t} + \mu_0 \boldsymbol{j} \tag{1.6}$$

where ε_0 and μ_0 are the vacuum permittivity and permeability, ρ is the charge density of the medium and $\boldsymbol{j}$ is the current density of the medium. The electric and magnetic fields fulfill the wave equations defined as :

$$\left(\frac{\partial^2}{\partial t^2} - v^2 \nabla^2 \right) \boldsymbol{X}(\boldsymbol{x}, t) = 0 \text{ with } \boldsymbol{X} = \boldsymbol{E}, \boldsymbol{B} \tag{1.7}$$

where v represents the propagation velocity of the wave in the medium ($v = c$ in vacuum). The energy flux carried by the electromagnetic wave in vacuum is defined by the Poynting vector :

$$\boldsymbol{S} = \varepsilon_0 c^2 (\boldsymbol{E} \times \boldsymbol{B}) \tag{1.8}$$

The intensity I of the laser pulse in vacuum is calculated by averaging the modulus of the Poynting vector (eq. (1.8)) over one oscillation period of the field T. The intensity of the laser is the physically important parameter which is easily measured experimentally.

$$I = \langle |\boldsymbol{S}| \rangle_T = \varepsilon_0 c \langle |\boldsymbol{E}|^2 \rangle_T \tag{1.9}$$

In the frame of ultra-short lasers, a laser pulse is typically defined as an electric field E at a frequency ω_0 with a Gaussian temporal envelope E_{env} as

$$E_{env}(t) = E_0 \, e^{-t^2/\tau_e^2} \tag{1.10}$$

$$E(t) = E_{env}(t) \cos[\omega_0 t + \varphi_0(t)] \tag{1.11}$$

where E_0 is the amplitude of the envelope and τ_e represents the pulse duration as the half width at 1/e of the electric field envelope. It is related to the duration at Full Width at Half Maximum (FWHM) τ_0 of the intensity envelope as $\tau_0 = \sqrt{2\ln(2)}\tau_e$, which is the useful parameter in the experiment. The intensity in vacuum is thus $I = (\varepsilon_0 c/2)|E_{env}|^2$. Figure 1.1 shows the temporal profile of electric field and intensity of a gaussian laser pulse with $\tau_0 = 28$ fs.
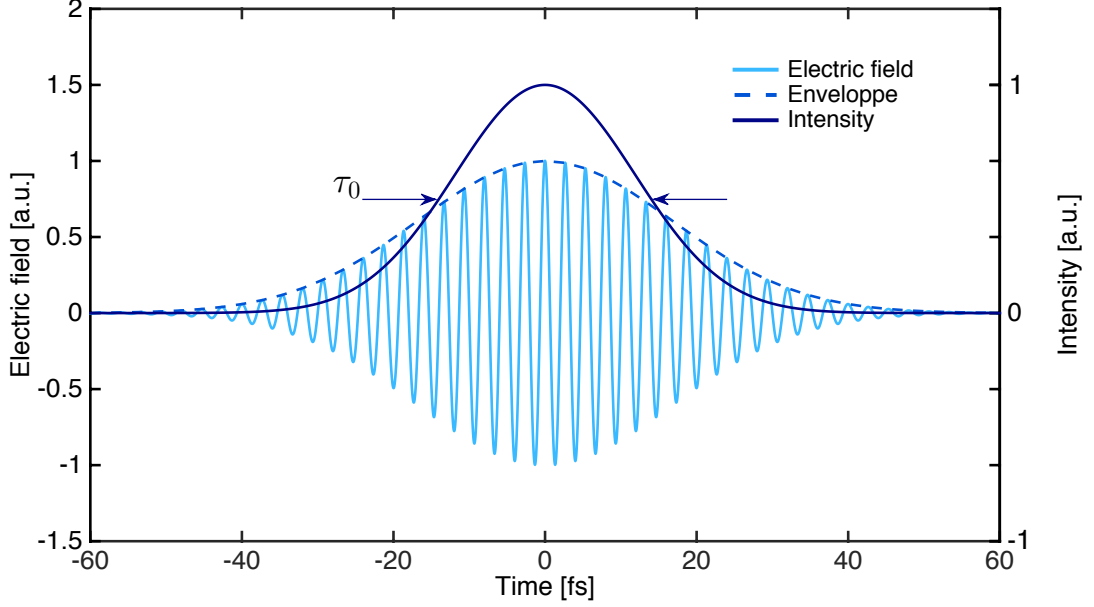
Figure 1.1: Electric field E, gaussian envelope E_{env} and intensity profile I of a laser pulse with a wavelength $\lambda_0 = 800$ nm, a zero absolute phase and a duration $\tau_0 = 28$ fs FWHM.

The electric and magnetic fields $\boldsymbol{E}$ and $\boldsymbol{B}$ can also be represented by a vector potential $\boldsymbol{A}$ and a scalar potential Φ :

$$\boldsymbol{E} = -\frac{\partial}{\partial t}\boldsymbol{A} - \boldsymbol{\nabla}\Phi \tag{1.12}$$

$$\boldsymbol{B} = \boldsymbol{\nabla} \times \boldsymbol{A}. \tag{1.13}$$

These potentials are not defined in a unique way, as it is possible to find other solutions to Maxwell's equations with a gauge transformation. In the Lorenz gauge, the potentials solve the wave equation

$$\boldsymbol{\nabla}.\boldsymbol{A} + \varepsilon_0\frac{\partial}{\partial t}\Phi = 0. \tag{1.14}$$

A solution of this equation in vacuum ($\rho = 0$, $\boldsymbol{j} = \boldsymbol{0}$) is

$$\boldsymbol{A}(\boldsymbol{x}, t) = -\boldsymbol{A_{env}}(\boldsymbol{x}, t)\sin[\omega_0 t - \boldsymbol{k}\boldsymbol{x} + \varphi_0(t)] \tag{1.15}$$

$$\Phi(\boldsymbol{x}, t) = 0 \tag{1.16}$$

with $A_0 = E_0/\omega_0$ the amplitude of $\boldsymbol{A_{env}}(\boldsymbol{x}, t)$ (considering a monochromatic laser pulse).

Gaussian beams

In order to easily describe the propagation of a laser pulse, it is convenient to approximate it by a 3D gaussian beam profile (which is valid only close to the focal point of the beam). For such

a monochromatic beam with a FWHM duration τ_0 and a transverse spot size w propagating in the z direction, the amplitude is denoted as

$$\boldsymbol{A}(r,z,t) = A_{env}(r,z,t)Re[e^{i(k_0z-\omega_0t)}e^{i\varphi_z}\boldsymbol{e_{pol}}] \tag{1.17}$$

$$= A_0 e^{-\frac{r^2}{w(z)^2}} e^{-2\ln(2)\frac{(z-ct)^2}{c^2\tau_0^2}} Re[e^{i(k_0z-\omega_0t)}e^{i\varphi_z}\boldsymbol{e_{pol}}]$$

where $\boldsymbol{e_{pol}}$ is the unit vector describing the laser polarization in the (x,y) plane. For a linear polarization in the y direction, $\boldsymbol{e_{pol}} = \boldsymbol{e_y}$, and for a circular polarization, $\boldsymbol{e_{pol}} = 1/\sqrt{2}(\boldsymbol{e_x} \pm i\boldsymbol{e_y})$. The waist w_0 of a gaussian beam propagating in free space is defined as the minimum transverse radius of the beam at $1/e$ where the spot size is the smallest (as seen in fig. 1.2), located in the focal plane $z = 0$. Note that the waist of the beam w_0 and the FWHM spot diameter at focus $\Phi_{spot,FWHM}$ are related through $\Phi_{spot,FWHM} = \sqrt{2\ln(2)}w_0$. The Rayleigh length is defined as the distance from the focal plane after which the intensity is divided by two and is given by

$$Z_R = \frac{\pi w_0^2}{\lambda}. \tag{1.18}$$

The depth of focus of the beam can be defined as twice the Rayleigh length. The transverse radius of the beam evolves along the propagation as

$$w(z) = w_0\sqrt{1 + \left(\frac{z}{Z_R}\right)^2}. \tag{1.19}$$

The transverse size $w(z)$ increases linearly with z for $z \gg z_R$. Far from the focal plane (when $z \gg Z_R$), one can define the total divergence of the beam (see fig. 1.2) as

$$\theta = \frac{2\lambda_0}{\pi w_0} \tag{1.20}$$
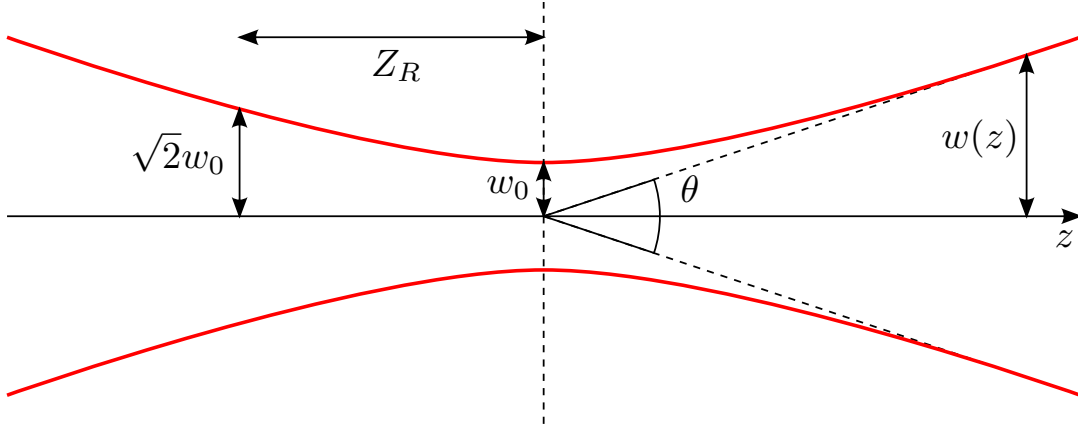
Figure 1.2: Diagram of a gaussian beam showing the waist w_0, the Rayleigh length Z_R and the divergence θ.

From these parameters, one can define the peak intensity of the laser pulse in the focal plane $z = 0$ as

$$I_0 = \frac{2\sqrt{\ln(2)}}{\sqrt{\pi}\tau_0}\frac{2U_0}{\pi w_0^2} \approx \frac{2U_0}{\tau_0.\pi w_0^2} \quad [W.cm^{-2}] \tag{1.21}$$

with U_0 the energy contained within the pulse.

1.1.2 Basic interaction with a single electron

The relativistic motion of an electron (charge $q_e = -e$, mass m_e) in an electromagnetic field $(\boldsymbol{E}, \boldsymbol{B})$ is described by the Lorentz force :

$$\frac{d}{dt}(m_e \gamma \boldsymbol{v_e}) = -e(\boldsymbol{E} + \boldsymbol{v_e} \times \boldsymbol{B}) \tag{1.22}$$

where γ is the relativistic factor defined as $\gamma = 1/\sqrt{1 - \beta^2}$ with $\beta = v_e/c$. In the non-relativistic case ($v_e \ll c$, $\gamma \approx 1$), $B = E/c \ll E$ then the equation reduces to $d(m_e \boldsymbol{v_e})/dt = -e\boldsymbol{E}$. Considering an electric field as defined in eq. (1.1), one can integrate the equation and obtain

$$\boldsymbol{v_e}(\boldsymbol{x}, t) = -\frac{e}{m_e} \int \boldsymbol{E_{env}}(\boldsymbol{x}, t) \cos[\omega_0 t - \boldsymbol{k}\boldsymbol{x} + \varphi_0(t)] + \boldsymbol{v_0}. \tag{1.23}$$

Considering a zero initial velocity for the electron and an amplitude E_0 for the envelope, one can derive the maximum velocity an electron can reach in a light field as

$$v_{e\ max} = \frac{e\,|\boldsymbol{E_0}|}{m_e \omega_0}. \tag{1.24}$$

When this maximum velocity approaches c, the electron reaches relativistic energy and the magnetic component of the Lorentz force cannot be neglected anymore. A normalized laser vector potential a_0 can be defined as a limit between the classic and relativistic regimes :

$$a_0 = \frac{e\,|\boldsymbol{E_0}|}{m_e c \omega_0} = \frac{e\,|\boldsymbol{A_0}|}{m_e c} = 0.854\sqrt{I_0[\times 10^{18}\ W.cm^{-2}]}\ \lambda_0[\mu m]. \tag{1.25}$$

$a_0 = 1$ defines the relativistic threshold : for $a_0 < 1$, the electron has a classical behavior within the electric field of the laser, whereas $a_0 > 1$ corresponds to relativistic regime. An electron interacting with a typical Ti:Sa laser system ($\lambda_0 = 800$ nm) reaches this regime for a laser intensity of $I_0 \approx 2 \times 10^{18}$ W.cm^{-2}.

The maximum kinetic energy of a non-relativistic electron can reach in the electric field of a laser pulse is defined as $E_{e\ laser} = m_e\,|v_e|^2/2$ (from eq. (1.24)). By averaging over one optical period T, one can derive the so-called ponderomotive potential

$$U_p = \langle E_{e\ laser} \rangle_T = \frac{e^2}{4m_e \omega_0^2}\,|E_0|^2 \propto I_0 \lambda^2 \tag{1.26}$$

which is proportional to the laser intensity, and then larger at the center of the pulse than on the sides. Non-relativistic electron experience the ponderomotive force defined as the spatial derivative of the ponderomotive potential :

$$\boldsymbol{F}_p = -\boldsymbol{\nabla}U_p = -\frac{e^2}{4m_e \omega_0^2}\boldsymbol{\nabla}E_0^2. \tag{1.27}$$

Electrons are pushed away from the regions of strong laser intensity because of this force. The ponderomotive force is proportional to the intensity gradient. Note that this simple expression is valid only for non-relativistic electrons and allow for understanding the physics of the ponderomotive process. In the relativistic case, by separating the electron motion into a fast oscillating component (following the vector potential $\boldsymbol{A}$) and a slow component, the relativistic

ponderomotive force can be derived under some assumptions (a detailed derivation can be found in [Mora and Antonsen, 1997]) :

$$\boldsymbol{F}_{p,\ relat} = -\frac{e^2 m_e}{2 <\gamma>} \boldsymbol{\nabla} < A_0^2 > .$$ (1.28)

While the electron motion is only transverse for small laser intensities, the magnetic term of the Lorentz force plays an important role for larger laser intensities, leading to a more complex electron motion and allowing for a longitudinal motion of particles. It is predominant in the generation mechanism of very large amplitude wakefields in the LWFA frame.

1.1.3 Ionization mechanism

High intensity laser pulses have the ability to ionize the matter, forming a partially or even fully ionized plasma. Indeed, the electric potential of a high-power laser pulse is similar to the binding potential of electrons to the nucleus of their atom. Two ionization regimes can be observed depending on the laser pulse intensity, and the limit between these regimes is determined by the Keldysh parameter γ_k [Keldysh, 1965] defined as

$$\gamma_k = \omega_0 \sqrt{\frac{m_e c \varepsilon_0}{e^2}} \sqrt{\frac{E_{ion}}{I_0}}.$$ (1.29)

It is calculated from the laser electric field which is required to equal the binding electric field E_{ion} of a hydrogen atom.
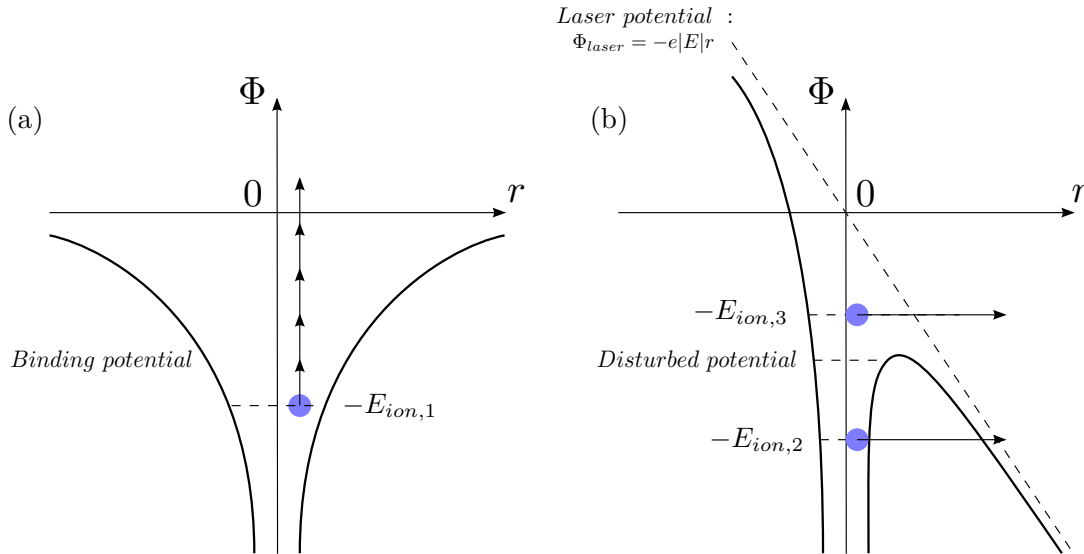
Figure 1.3: Two ionization mechanisms : (a) Multi-photon ionization of the electron at $E_{ion,\ 1}$ for $\gamma_k > 1$. (b) Tunnel ionization at $E_{ion,\ 2}$ and barrier-suppression ionization at $E_{ion,\ 3}$ for $\gamma_k < 1$.

For small laser intensities, $\gamma_k > 1$ the ionization mechanism is dominated by multi-photon ionization [Mainfray and Manus, 1991]. In this case, the binding potential of the electron is weakly disturbed by the laser field and the energy of one photon is not sufficient for direct photo-ionization ($E_{photon@800nm} = \hbar\omega_0 = 1.5$ eV $< E_{ion,\ 1} = 13.6$ eV). However, the total energy

brought by $N = E_{ion,1}/E_{photon@800\ nm}$ simultaneously absorbed incident photons can trigger the multi-photoionization of the atom (as seen in fig. 1.3(a)).

For $\gamma_k < 1$, the laser electric field strongly disturbs the potential well that binds the electron to the nucleus, and the dominant ionization mechanism is tunnel ionization. Electrons in the state $-E_{ion,2}$ can tunnel through the potential barrier, all the more so as the barrier width is smaller (as seen in fig. 1.3(b)). If the electric field is strong enough, the mechanism of barrier suppression ionization can happen : the electron in state $-E_{ion,3}$ is freed spontaneously under the laser potential. The threshold laser intensity for this mechanism to happen can be estimated by considering the disturbed potential equal to the ionization potential [Gibbon, 2005] :

$$I_{ionizaton}\ [\text{W.cm}^2] = 4 \times 10^9 \frac{(E_{ion}[eV])^4}{Z^2} \tag{1.30}$$

where Z is the atomic number and E_{ion} the ionization energy of the considered electron. In the following table are computed the intensity threshold to reach different ionization states with typical species used in laser-plasma experiments :

Ionization state	E_{ion} [eV]	$I_{ionizaton}$ [W.cm^2]
He$^+$	24.59	1.4×10^{15}
He^{2+}	54.42	8.8×10^{15}
N^{5+}	97.89	7.5×10^{15}
N^{6+}	552.1	7.6×10^{18}
N^{7+}	667.1	1.6×10^{19}
Ar^{8+}	143.5	5.2×10^{15}
Ar^{9+}	422.5	3.9×10^{17}
Ar^{18+}	4426	4.7×10^{21}

For focused laser intensities greater than 10^{18} W.cm^{-2}, helium atoms are completely ionized through barrier-suppression ionization almost two order of magnitude below the peak intensity : the plasma is formed by the leading edge of the laser pulse. Hence, the laser pulse is assumed to interact with a fully ionized plasma. For heavier atoms as nitrogen or argon, the plasma is not fully ionized, which is a very important aspect for a particular injection technique discussed in chapter 3.

1.1.4 Propagation in an underdense plasma

Plasma parameters

A plasma is a state of matter formed with a mixture of free electrons and partially or fully ionized ions. In all the following study, we consider a globally neutral, cold (initial electron velocity is neglected) non-collisional plasma. Considering a non-relativistic electron in the plasma shifted away by a small distance from its equilibrium position (then generating an electrostatic field $\boldsymbol{E}$), the restoring force $\boldsymbol{F} = -e\boldsymbol{E}$ pulls it back. Due to the kinetic energy gain, the electron exceeds its initial position and starts an harmonic oscillation with a characteristic pulsation often referred as the plasma frequency :

$$\omega_p = \sqrt{\frac{n_e e^2}{\varepsilon_0 m_e}} \tag{1.31}$$

where n_e is the initial electron density of the plasma. On the time scale corresponding of the electron motion, the ions are considered as a stationary motionless background due to their

larger mass. The plasma wavelength is defined as $\lambda_p = 2\pi c/\omega_p$, and depends only on the electron density n_e. It can be easily estimated with

$$\lambda_p \ [\mu\text{m}] = \frac{3.34 \times 10^{10}}{\sqrt{n_e \ [\text{cm}^{-3}]}}. \tag{1.32}$$

To understand the propagation of a laser pulse in a plasma, the plasma frequency ω_p has to be compared with the laser frequency ω_0. If $\omega_p < \omega_0$, the characteristic response time of the plasma is longer than the optical period of the incoming laser pulse, which can propagate : the plasma is called *underdense*. Conversely, if $\omega_p > \omega_0$, the density is too high for the laser to propagate (the electrons can move quickly enough to adapt to the incident laser oscillations and reflecting it) : the plasma is *overdense*. The limit between these two domains (when $\omega_p = \omega_0$) is defined by the critical plasma density $n_c \ [\text{cm}^{-3}] = \omega_0^2 m_e \varepsilon_0 / e^2 \approx 1.1 \times 10^{21} / \lambda_0^2 \ [\mu m]$. The experimental electron densities presented in this thesis range between 10^{18}cm^{-3} and 10^{20}cm^{-3}, corresponding to an underdense plasma for $\lambda_0 = 800$ nm.

Dispersion relation in a plasma

By combining Faraday's (1.5) and Maxwell's (1.6) laws, the usual wave equation is found :

$$\left(c^2 k^2 - \omega_0^2\right) \boldsymbol{E} = -\frac{n_e e^2}{\varepsilon_0 m_e} \boldsymbol{E} \tag{1.33}$$

where we recognize the plasma frequency in the right-hand-side. The dispersion equation for an electromagnetic wave in a cold plasma is

$$\omega_0^2 = \omega_p^2 + c^2 k^2. \tag{1.34}$$

In an underdense plasma, $\omega_p < \omega_0$ then the laser pulse can propagate. One can define the phase and group velocity v_{ph} and v_g for the laser in the plasma thanks to η the index of refraction

$$v_{ph} = \frac{\omega_0}{k} = \frac{c}{\eta}$$
$$v_g = \frac{d\omega_0}{dk} = \eta c \tag{1.35}$$
$$\eta = \sqrt{1 - \frac{\omega_p^2}{\omega_0^2}} = \sqrt{1 - \frac{n_e}{n_c}} < 1.$$

The refraction index of a plasma is always smaller than one, so the group velocity (resp. the phase velocity) of the laser is smaller (resp. larger) than the speed of light in vacuum c. One can also define the relativistic factor associated with the group velocity of the laser as $\gamma_g = \omega_0/\omega_p$. In laser wakefield experiments, the final velocity of electrons is related to the group velocity of the driving laser pulse : to get large electron energies, the pulse must propagate as quick as possible, η must be close to unity, then the electron density be as low as possible.

Self-focusing and guiding

A high intensity ($a_0 > 1$) laser pulse propagating in an underdense plasma experiences self-focusing. This effect, as well as the self-compression of the pulse, increases the laser intensity along the propagation and allows for the generation of large amplitude wakefields up to a regime where a cavity free of electrons is created in the laser wake. Non-linear mechanism can also guide

the pulse over longer distances than the Rayleigh length and increase the acceleration length to get higher electron energies.

The ponderomotive force of the laser expels electrons from the high intensity regions, generating a density gradient with low electron density, thus high refractive index, on the optical axis. This creates a transverse density and refractive index profile, with high η on axis and lower η off-axis, acting as a lens for the pulse. As the laser self-focuses, intensity on axis increases, enhancing the ponderomotive force effect and lowering the electron density, thus raising the focusing power. The laser self-focusing counter-interacts the diffraction, enabling the laser to self-guide beyond the Rayleigh length.

The refraction index (1.35) of a plasma with local density variations $\bar{n}_e(r, z)$ can be rewritten as [Esarey et al., 1996]

$$\eta(r, z) = \sqrt{1 - \left(\frac{\omega_p}{\omega_0}\right)^2 \frac{\bar{n}_e(r, z)}{\gamma_0 n_e(r, z)}} \approx 1 - \frac{1}{2}\left(\frac{\omega_p}{\omega_0}\right)^2 \left(1 + \frac{\delta n_e(r, z)}{n_e} - \frac{a_0^2(r, z)}{4}\right) \qquad (1.36)$$

where $\delta n_e(r, z) = \bar{n}_e(r, z) - n_e$ is the density variation due to ponderomotive force of the laser. The relativistic self-focusing term $a_0^2(r, z)/4$ is predominant to the ponderomotive self-focusing term $\delta n_e/n_e$ [Hafizi et al., 2000]. This correction term is due to the mass increase of electrons at relativistic energies. Note however that these two effects happen roughly at the same time. For relativistic self-focusing to happen, the laser power must be larger than a critical power P_c that when reached, the diffraction of the laser is balanced by self-focusing.

The critical power for self-focusing (concerning only the relativistic term a_0^2) is [Sun et al., 1987]:

$$P_c[\text{GW}] = 17\frac{\omega_0^2}{\omega_p^2}. \qquad (1.37)$$

If $P < P_c$, diffraction dominates and the laser pulse cannot be self-guided. For $P > P_c$, the laser is focused until other non-linear processes (as ionization induced diffraction in the case of a partially-ionized plasma) balance self-focusing. The focal spot size evolves during the self-focusing process as [Esarey et al., 2009] (note that this description is very simplistic and only allows for the understanding of main physical processes)

$$\frac{w(z)}{w_0} = 1 + \left(1 - \frac{P}{P_c}\right)\frac{z^2}{Z_R^2}. \qquad (1.38)$$

Typical experimental parameters presented in this thesis ($n_e = 10^{19}$ cm^{-3}, $\lambda_0 = 800$ nm) lead to an estimation of the critical power $P_c \approx 3$ TW, which is easily accessible with the "Salle Jaune" laser system used in all presented experiments.

For high intensity ultrashort laser pulses with $\tau_0 c < \lambda_p$, the ponderomotive self-focusing term $\delta n_e/n_e$ can become important. Indeed, the ponderomotive force at the front of the laser pulse pushes the electrons forward and generates a large density region, thus a low refractive index zone [Ting et al., 1990; Sprangle et al., 1990]. The leading front of the laser diffracts and compensates relativistic self-focusing : the pulse is not guided. However, if the power is high enough ($P > P_c$), the diffracting leading edge of the pulse transfers its energy to accelerated electrons [Decker et al., 1996a]. If the pulse front depletes more quickly than it diffracts, the extracted energy is coupled to the plasma wave, generating an electron-free cavity behind which can guide the rear of the pulse [Bulanov et al., 1992a; Decker and Mori, 1994; Decker et al., 1996b]. Moreover, the ponderomotive term $\delta n_e/n_e$ is also responsible for temporal self-compression of the pulse during

propagation. Indeed, the local density variation induces a group velocity modulation in the pulse : the back of the pulse finds itself in an upward density gradient and goes faster than the front of the pulse, resulting in a temporal shortening as well as self-phase modulation creating new frequencies in the pulse and front pulse steepening [Ren et al., 2001; Malka et al., 2002; Faure et al., 2005; Gordon et al., 2003; Schreiber et al., 2010]. This is a useful phenomenon if the laser pulse duration is too long to resonantly excite a wakefield at a given density. Note that it is also possible to externally form a specific plasma density profile to guide the pulse over longer distances with various techniques such as preionized plasma columns [Rowlands-Rees et al., 2008] or capillary discharges [Leemans et al., 2006; Karsch et al., 2007a; Leemans et al., 2014].

1.2 Acceleration of electrons

1.2.1 Excitation of plasma waves

When a high intensity laser pulse is focused in an underdense plasma, the ponderomotive force of the pulse expels large amount of plasma electrons and can excite large amplitude plasma waves in the wake of the laser. The plasma wave excitation theory described in the following section rests upon several assumptions : we consider a cold, collisionless underdense fully-ionized plasma in one dimension in which a linearly polarized ultra-intense laser pulse propagates with a group velocity $v_g < c$. Recombination of electrons with ions are neglected on the considered time scale. The ions are considered motionless in the plasma. Normalized physical quantities are used for easier understanding : normalized laser amplitude $a = eA/mc$, normalized scalar potential of the plasma $\varphi = e\Phi/mc^2$ and normalized electron velocity $u = \gamma v_e/c$. The derivation of the one-dimensional wakefield excitation done in the following pararagraphs are more detailed in [Kruer, 2003] and [Gibbon, 2005].

The relativistic equation of motion of an electron described in eq. (1.22) can be written as

$$\frac{1}{c}\frac{d\boldsymbol{u}}{dt} = \frac{1}{c}\frac{\partial \boldsymbol{a}}{\partial t} + \frac{1}{c}\boldsymbol{\nabla}\varphi - \frac{1}{\gamma}\boldsymbol{u} \times \boldsymbol{\nabla} \times \boldsymbol{a}. \tag{1.39}$$

From this equation, one can derive the γ factor of the electrons of the plasma wave (with z the wave direction of propagation) :

$$\gamma = \frac{\sqrt{1+a^2}}{\sqrt{1-\beta_z^2}} = \sqrt{1+a^2+u_z^2} \tag{1.40}$$

with u_z the wave normalized velocity along the propagation direction. From the continuity equation of electrons is found the equation describing the electron density distribution :

$$\frac{\partial \delta n_e}{\partial t} + n_{e0}\frac{c}{\gamma}\boldsymbol{\nabla}.\boldsymbol{u} = 0 \tag{1.41}$$

where $\delta n_e = n_e/n_{e0}$ is the density perturbation and n_{e0} the background electron density. The plasma scalar potential is formed by the charge separation in the plasma and therefore can be describes with Poisson's equation

$$\boldsymbol{\nabla}^2\varphi = \frac{\omega_p^2}{c^2}\frac{\delta n_e}{n_{e0}}. \tag{1.42}$$

Equations (1.39), (1.41) and (1.42) form a closed set of equations describing the coupled system electromagnetic pulse and plasma wave. The equations are solved using the co-moving coordinates $(t, \xi = z - v_g t)$ propagating at the laser group velocity v_g. Furthermore, the laser pulse and plasma wave propagate at a velocity close to c, and can be considered stationary during the time a plasma electron needs to go through the pulse (quasi-static approximation), then $\partial/\partial t \ll v_g \partial/\partial \xi$. From these approximations, one can derive the equation describing the excitation of a plasma wave with a short laser pulse [Osterhoff, 2009]:

$$\frac{\partial^2 \varphi}{\partial \xi^2} = \frac{k_p^2}{2} \left(\frac{1 + a^2}{(1 + \varphi)^2} - 1 \right). \tag{1.43}$$

The wakefield described by this equation strongly depends on the intensity of the laser pulse $\sim a^2$: two different regimes can be highlighted.

1.2.2 Linear regime

In the case with $a_0^2 \ll 1$, the plasma density is weakly perturbed and then the wave is not efficiently excited : it is referred as the linear regime. By developing eq. (1.43) with $a \ll 1$ (thus developing $(1 + \varphi)^2$ considering φ close to zero), one can derive the linear equation for the plasma wave

$$\left(\frac{\partial^2}{\partial \xi^2} + k_p^2 \right) \varphi = \frac{k_p^2}{4} a^2. \tag{1.44}$$

In this regime, the two-dimensional solution in the co-moving coordinate system $(t, r, \xi = z - v_g t)$ can be calculated, with r the transverse coordinate perpendicular to the propagation direction z. The solution for which the potential is null before the laser pulse is written as

$$\varphi(r, \xi) = -\frac{k_p}{4} \int_{\xi}^{+\infty} a^2(r, \xi') \sin(k_p(\xi - \xi')) d\xi'. \tag{1.45}$$

We now consider a short laser pulse with a gaussian envelope (longitudinally and transversally) as defined in eq. (1.17), the plasma potential is calculated as (note that the transverse dependance in r only concerns the laser potential a_0) :

$$\varphi(r, \xi) = -\sqrt{\pi} a_0^2 \frac{k_p l_0}{4} e^{-k_p^2 l_0^2/4} e^{-2r^2/w_0^2} \sin(k_p \xi) \text{ with } l_0 = \frac{c\tau_0}{2\sqrt{\ln(2)}}. \tag{1.46}$$

The wave is a simple sinusoidal oscillation of the plasma electron density behind the laser pulse : this is the plasma wakefield. The expressions for the longitudinal and transverse electric fields E_z and E_r can be written :

$$E_z = -\frac{\partial \varphi}{\partial \xi} = E_0 \sqrt{\pi} a_0^2 \frac{k_p l_0}{4} e^{-k_p^2 l_0^2/4} e^{-2r^2/w_0^2} \cos(k_p \xi) \text{ with } E_0 = \frac{m_e c \omega_p}{e} \tag{1.47}$$

$$E_r = -\frac{\partial \varphi}{\partial r} = -E_0 \sqrt{\pi} a_0^2 \frac{r l_0}{w_0^2} e^{-k_p^2 l_0^2/4} e^{-2r^2/w_0^2} \sin(k_p \xi). \tag{1.48}$$

The expression of the density perturbation in the plasma is

$$\frac{\delta n_e}{n_{e0}} = \frac{1}{k_p^2} \frac{\partial^2 \varphi}{\partial \xi^2} = -E_0 \sqrt{\pi} a_0^2 \frac{l_0}{4} e^{-k_p^2 l_0^2/4} e^{-2r^2/w_0^2} \sin(k_p \xi). \tag{1.49}$$

Note that E_0 corresponds to the maximal electric field in the linear regime, when the density perturbation is total. This critical field can be calculated with the simple formula

$$E_0[\text{GV.m}^{-1}] = 96\sqrt{n_{e0}[10^{18} \text{ cm}^{-3}]}. \tag{1.50}$$

The linear wakefield is driven more efficiently (the maximal wakefield amplitude φ_{max} is obtained) when the laser pulse length is shorter than half the plasma wavelength. More precisely, the optimal pulse FWHM length to achieve the resonant condition is $l_{res} = c\tau_{0,res} \approx 0.26\lambda_p$. For a typical laser pulse duration of $\tau_0 \sim 30$ fs as delivered by Ti:Sa lasers, this requires to use a plasma density of about $n_{e0} = 10^{18}$ cm^{-3} to optimally drive the wakefield.

Figure 1.4: Linear wakefield quantities for $a_0 = 0.2$: (a) Normalized laser amplitude a, plasma potential φ, longitudinal electric field E_z/E_0 and density perturbation $\delta n_e/n_{e0}$ on axis in the co-moving coordinate system. Colormaps of the two-dimension plasma density perturbation $\delta n_e(r,\xi)/n_{e0}$ (b), longitudinal electric field $E_z(r,\xi)/E_0$ (c) and radial electric field $E_r(r,\xi)/E_0$ (d).

According to the previous expressions, it is possible to represent the different normalized quantities. Figure 1.4(a) shows the normalized laser amplitude a, plasma potential φ, longitudinal electric field E_z/E_0 and density perturbation $\delta n_e/n_{e0}$ on axis for $a_0 = 0.2$. The two-dimension plasma quantities can also be depicted considering a 3D gaussian laser pulse. Figure 1.4(b) shows the colormap of the plasma density perturbation driven by the laser pulse, and Fig. 1.4(c-d) show the normalized radial and longitudinal electric fields in the wakefield. Note that for the longitudinal electric field, the red regions are accelerating (negative field) and the blue regions are decelerating (positive field) for an electron. In the same way, for the radial electric field, the red regions are defocusing and the blue regions are focusing for an electron. It is then possible to separate a linear plasma period in four successive regions : decelerating-defocusing, accelerating-defocusing, accelerating-focusing and decelerating-focusing. Efficient acceleration of electrons in a linear wakefield can take place only in the accelerating-focusing part (over a quarter plasma wavelength). However, as the laser intensity a_0^2 increases, the plasma

potential rapidly increases. As soon as a_0 gets close to 1, the linear approximation is not valid anymore and the wakefield regime is modified.

1.2.3 Non-linear regime and wave-breaking

For laser intensities such as $a_0^2 > 1$, the linear approximation is not valid anymore : the plasma wave is described in the non-linear regime. In this regime, eq. (1.43) can easily be solved analytically in one dimension, and numerically in two or three dimensions. The expressions for the plasma potential, longitudinal electric field and plasma density on axis can be calculated by integrating this equation. Figure 1.5 shows the non-linear plasma wave quantities for a laser amplitude $a_0 = 3$. Note that the non-linear plasma wave is not sinusoidal anymore and presents a sawtooth longitudinal electric field with a non-linear plasma wavelength $\lambda_{p,NL}$ increasing with the laser amplitude. Over a large part of one plasma period, the longitudinal electric field is quasi-linear and the density is almost constant. If an electron is injected around the rear part of one period with a velocity exceeding the wakefield phase velocity v_p (i.e. at $\xi \approx -32$ μm in Fig. 1.5), it can be efficiently accelerated up to relativistic energies over half a plasma wavelength, assuming transverse fields are focusing over this length. Because their velocity exceeds the wakefield phase velocity, injected electrons catch up the plasma wave and eventually reach the point when the sign of the electric field changes (i.e. at $\xi \approx -25\mu$m in Fig. 1.5) where they start to be decelerated

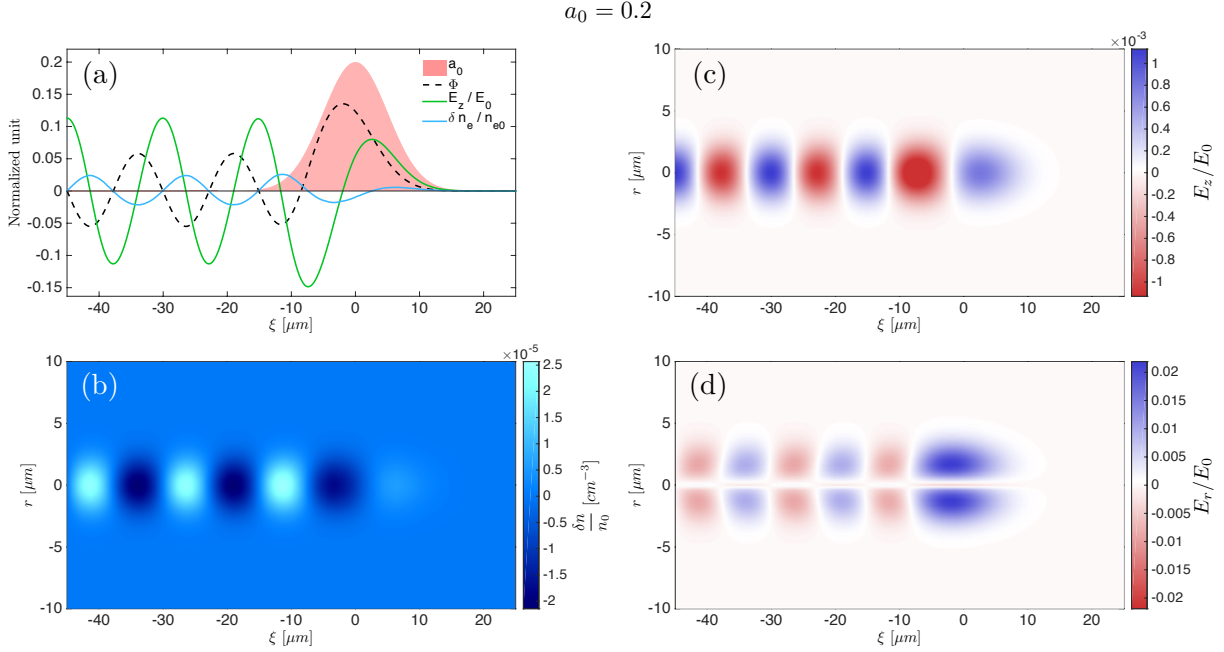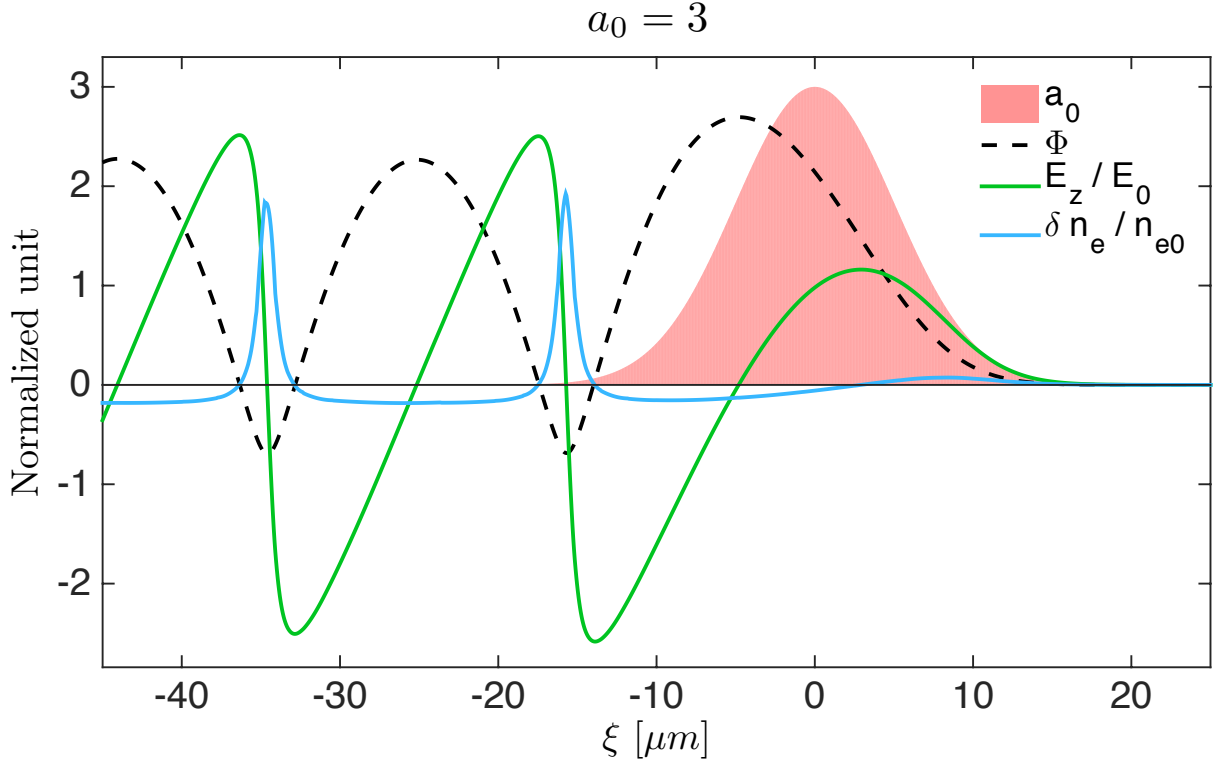Figure 1.5: Non-linear wakefield quantities for $a_0 = 3$: Normalized laser amplitude a, plasma potential φ, longitudinal electric field E_z/E_0 and density perturbation $\delta n_e/n_{e0}$ on axis in the co-moving coordinate system.

The plasma potential slope changes abruptly, which is associated to a maximum slope of the

electric field and electron density peaks formation due to the accumulation of plasma electrons with a velocity close to the phase velocity of the plasma wave v_p. If the wakefield is excited with a very large amplitude, accelerated electrons can go faster than v_p : in this case, the electron density presents a singularity and electron trajectories start to cross each other (this is the validity limit of the fluid model for plasma electrons). This process is called longitudinal wave breaking. The maximum electric field supported by the plasma wave before wavebreaking is, for a cold collisionless plasma, $E_w = \sqrt{2(\gamma_p - 1)}E_0$ [Teychenné et al., 1993; Schroeder et al., 2005], where $\gamma_p = 1/\sqrt{1 - (v_g/c)^2}$ is the relativistic factor of the plasma wave. This value is lower for a plasma in which thermal effects are being considered [Esarey et al., 2007].

The dynamics of an electron trapped and accelerated in the wakefield is now presented. The longitudinal dynamics of an electron is described by combining eq. (1.39) and eq. (1.43). One can write the normalized Hamiltonian describing the total energy of a single electron in the wakefield as [Esirkepov et al., 2006]

$$H(\xi, u_z) = \gamma - \beta_p\sqrt{\gamma^2 - 1} - \varphi(\xi) = \sqrt{1 + a^2(\xi)/2 + u_z^2} - \beta_p u_z - \varphi(\xi) = H_0 \qquad (1.51)$$

with $\gamma = \sqrt{1 + a^2/2 + u_z^2}$, $\beta_p = v_p/c = v_g/c$ and u_z the longitudinal velocity of the electron. The hamiltonian H_0 is constant over the particle acceleration. By solving the Hamiltonian for u_z, one can derive the electron trajectories in phase space :

$$u_z(\xi) = \beta_p \gamma_p^2 (H_0 + \varphi(\xi)) \pm \gamma_p \sqrt{\gamma_p^2 (H_0 + \varphi(\xi))^2 - (1 + a^2(\xi)/2)}. \qquad (1.52)$$

If the laser amplitude $a(\xi)$, the plasma potential $\varphi(\xi)$ and the total energy of the electron H_0 are known, all the initial conditions are defined and thus the trajectory of the electron in the phase space $u_z(\xi)$ can be calculated. Figure 1.6 shows the phase space in the co-moving frame (ξ, u_z) deduced from this Hamiltonian. The contour lines represent possible electron trajectories $(\xi(t), u_z(t))$ of constant total energy.

Looking at the figure, different notable trajectories can be distinguished. The fluid orbit (black line, trajectory A in Fig. 1.6) corresponds to a electrons initially at rest in front of the laser and constituting the plasma wave. Despite being pushed forward by the laser ponderomotive force, they are not fast enough compare to the laser and are caught up by the pulse after a while, pushed backward again by the ponderomotive force and start to oscillate to generate the plasma wave. This trajectory is denoted :

$$u_{fluid} = \beta_p \gamma_p^2 (1 + \varphi(\xi)) \pm \gamma_p \sqrt{\gamma_p^2 (1 + \varphi(\xi))^2 - (1 + a^2(\xi)/2)}. \qquad (1.53)$$

The separatrix (red line in Fig. 1.6) defines the boundary between the electrons circulating in the plasma wave and the electrons able to gain enough energy to be trapped in a wakefield period and accelerated [Teychenné et al., 1994; Esarey and Pilloff, 1995]. An electron following this orbit can gain the maximum energy in the wakefield. Note that in the period just behind the laser pulse, the electromagnetic field of the laser modifies the plasma potential and thus the electron trajectories. The closed trajectories in each plasma period (dashed blue lines in Fig. 1.6) correspond to trapped orbits of electrons that can be accelerated or decelerated in the wakefield. By moving clockwise in the phase-space (trajectory B), a trapped electron with initial kinetic energy is accelerated up to the point where the accelerating field turns positive, and is then decelerated.

In this one-dimensional analytical study, transverse effects and laser evolution are neglected. However, they play a very important role during the interaction. The multi-dimensional non-linear study of wakefield excitation cannot be done analytically anymore, and need a numerical
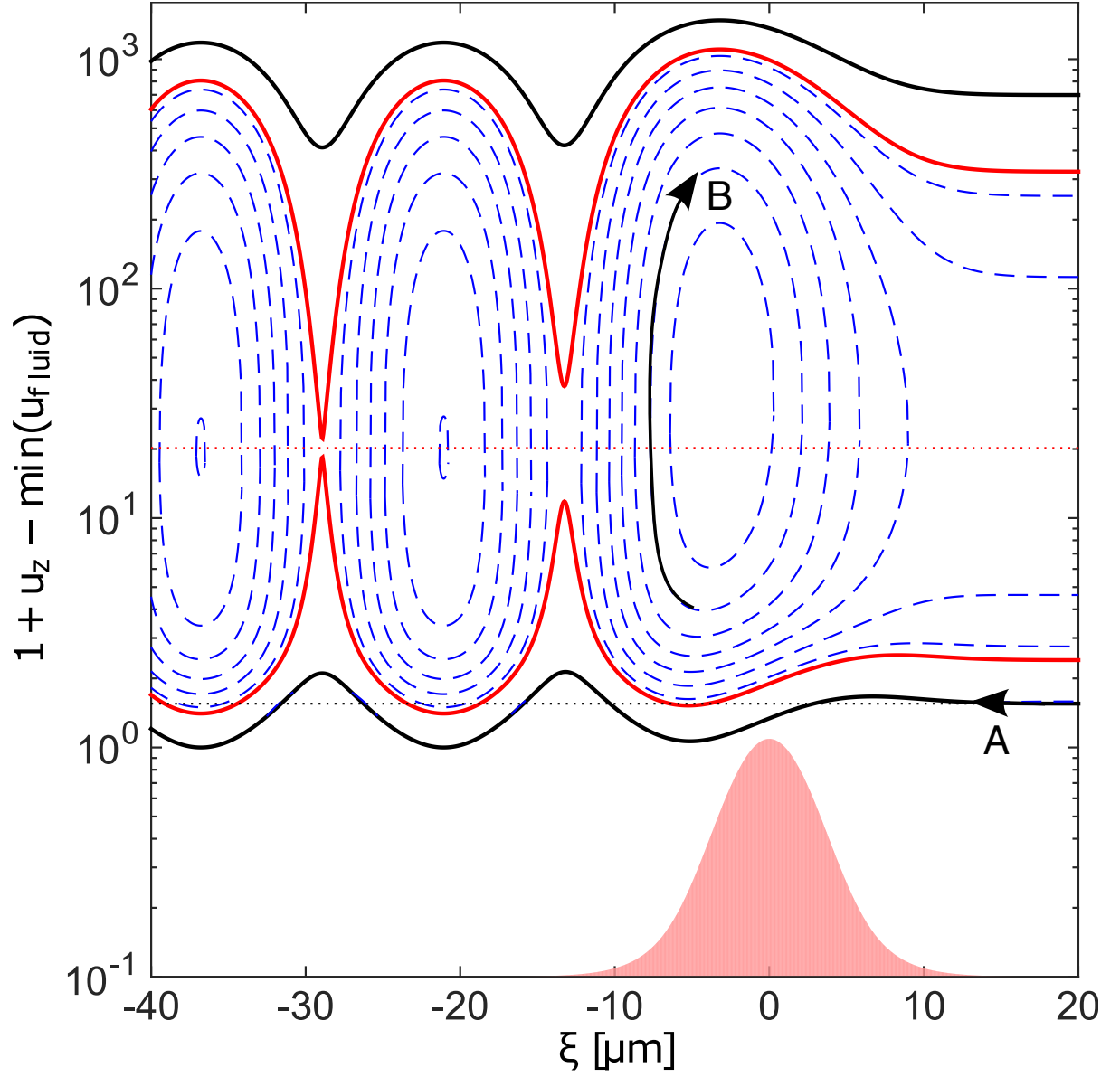
Figure 1.6: Phase space of a plasma wave in the co-moving coordinates driven by a laser pulse with $a_0 = 3$, $\tau_0 = 30$ fs in a plasma with a background electron density $n_e = 5 \times 10^{18}$ cm^{-3}. The laser pulse is plotted without vertical scale just to indicate its location. Trapped orbits (dashed blue lines), separatrix (red line) and fluid orbit (black line) are represented.

study. This study can be done using Particle-In-Cell codes (based on kinetic plasma theory) which allow to describe the full dynamics of non-linear, multi-dimensional wakefields.

1.2.4   Bubble regime

For $a_0^2 \gg 1$ and the laser pulse transverse and longitudinal dimensions resonant with the plasma period ($k_p w_0 \approx \sqrt{2} a_0$ and $c\tau_{0,res} \approx 0.26\lambda_p$ [Lu et al., 2007]), multi-dimensional effects are predominant and the ponderomotive force of the laser pulse tends to expel all the electrons from its wake. This is the so-called bubble (or blow-out) regime [Pukhov and Meyer-ter Vehn, 2002; Lu et al., 2006; Xie et al., 2007; Lu et al., 2007], represented in fig. 1.7. Plasma electrons are pushed in front and on the sides of the pulse, creating an ion cavity just behind the pulse. The expelled electrons form a thin sheath around the cavity. They are then pulled towards the axis because of the transverse force produced by the ion cavity. Electron trajectories cross behind the cavity and close it. The ion bubble is a three-dimension accelerating and focusing structure in which trapped electrons are able to reach high energies.
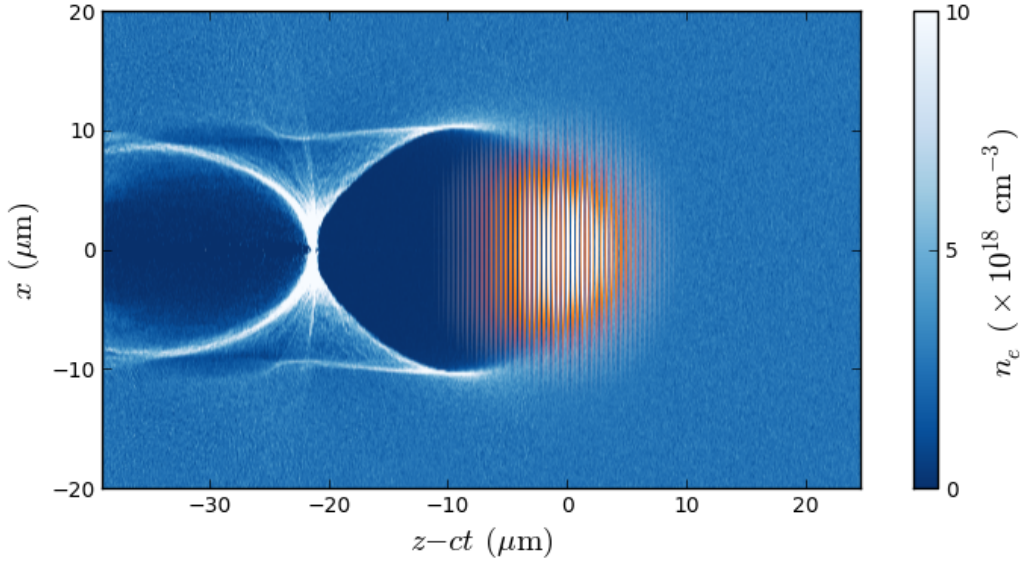
Figure 1.7: Representation of the bubble regime in the co-moving frame : the laser pulse (in red) propagates from left to right in the plasma (electron density in blue).

The blow-out regime provides a self-guided accelerating and focusing structure for electrons, forming a cavity with a radius $r_b = 2\sqrt{a_0}/k_p$ [Lu et al., 2007]. Considering a perfectly spherical bubble in the quasi-static approximation, one can derive the expression for the normalized potential and the longitudinal and transverse electric fields as well as their associated forces in the cavity using the cylindrical coordinates (r, θ, z) [Lu et al., 2006; Xie et al., 2007]

$$\varphi = -\frac{k_p^2}{8}(\xi^2 + r^2) \tag{1.54}$$

$$\frac{E_z}{E_0} = \frac{k_p}{2}\xi \quad \text{and} \quad \boldsymbol{F_z} = -\frac{m_e \omega_p^2}{2}\xi \; \boldsymbol{e_z} \tag{1.55}$$

$$\frac{E_r}{E_0} = \frac{k_p}{4}r \quad \text{and} \quad \boldsymbol{F_r} = -\frac{m_e \omega_p^2}{2}r \; \boldsymbol{e_r} \tag{1.56}$$

with the center of the bubble at $(r = 0, \xi = 0)$ and E_0 the cold wavebreaking maximum field. The expression of the longitudinal force experienced by an electron in the cavity (eq. (1.55)) shows that the first half of the bubble ($\xi < 0$) is accelerating with a linear force in ξ independent from r, and the second part ($\xi > 0$) is decelerating. An electron bunch can be efficiently accelerated as soon as it does not overtake the center of the bubble. The order of magnitude of the longitudinal accelerating field can be evaluated by considering the typical length of the bubble [Lu et al., 2007] as $4\sqrt{a_0}/k_p$, thus $E_z[\text{GV.m}^{-1}] \approx 96\sqrt{a_0}\sqrt{n_{e0}[10^{18} \text{ cm}^{-3}]}$. On the other hand, the transverse force is linear in r and independent of ξ (eq. (1.56)), and always focusing : the electron bunch is transversally confined in the bubble during the acceleration.

1.2.5 Laser-Wakefield Acceleration

Injection of electrons and beamloading

For an electron to be accelerated in the bubble regime, it must have sufficient initial kinetic energy along the longitudinal direction once it finds itself in the rear part of the bubble (accelerating and focusing region). Thus, an injection process is necessary for an electron to stay a long enough time in the bubble, be trapped and accelerated up to high energy. During injection, a fraction of plasma electrons enter the cavity with sufficient initial speed so they can remain in it and gain energy.

Considering a stationary wakefield, electrons are unable to be injected in the bubble as they are expelled by the ponderomotive force of the laser and simply go around the cavity. Injection must then be triggered by another physical phenomenon. A common way for electrons to be injected is caused by the sudden expansion of the bubble size [Kalmykov et al., 2009a; Kostyukov et al., 2010a]. Indeed, due to self-focusing of the laser pulse (as described in section 1.1.4) during the propagation, the waist is not stationary and tends to shrink, increasing the laser intensity and thus the ponderomotive force. Electrons are pushed further away, resulting in a larger cavity. Because of this expansion, electrons at the back of the bubble can remain longer in the accelerating region, reaching a sufficient velocity to be trapped in the cavity. This mechanism is often reffered as *self-injection*. Nevertheless, self-injection is not a stable injection technique and several methods exist to inject electrons in the wakefield in a controllable and more stable way, which will be explained in more details in section 1.2.6.

When the injected charge is very high, the electron bunch distorts the electric fields of the wakefield : this is the *beamloading* phenomenon (represented in Fig. 1.8). Indeed, the charge forces of the bunch repel the plasma electrons away by creating its own wakefield, altering the bubble shape and thus the longitudinal accelerating field, which flattens (and can even inverse) due to beamloading. Eventually, the longitudinal field becomes so weak that electrons do not gain enough energy to be trapped : the injection process stops.

Electron acceleration and betatron oscillations

Once they are injected, electrons start to be accelerated in the wakefield. As seen in Fig. 1.8, electrons are accelerated up to the middle of the bubble (red gradient) where the longitudinal field is negative. The acceleration stops as soon as they reach the decelerating region, when the field switches sign. Furthermore, electrons can be injected with a non-zero transverse momentum. They oscillate in the transverse focusing fields : these are the so-called *betatron oscillations* (as seen in Fig. 1.9). Assuming a perfectly spherical bubble with radius r_B, one can write the
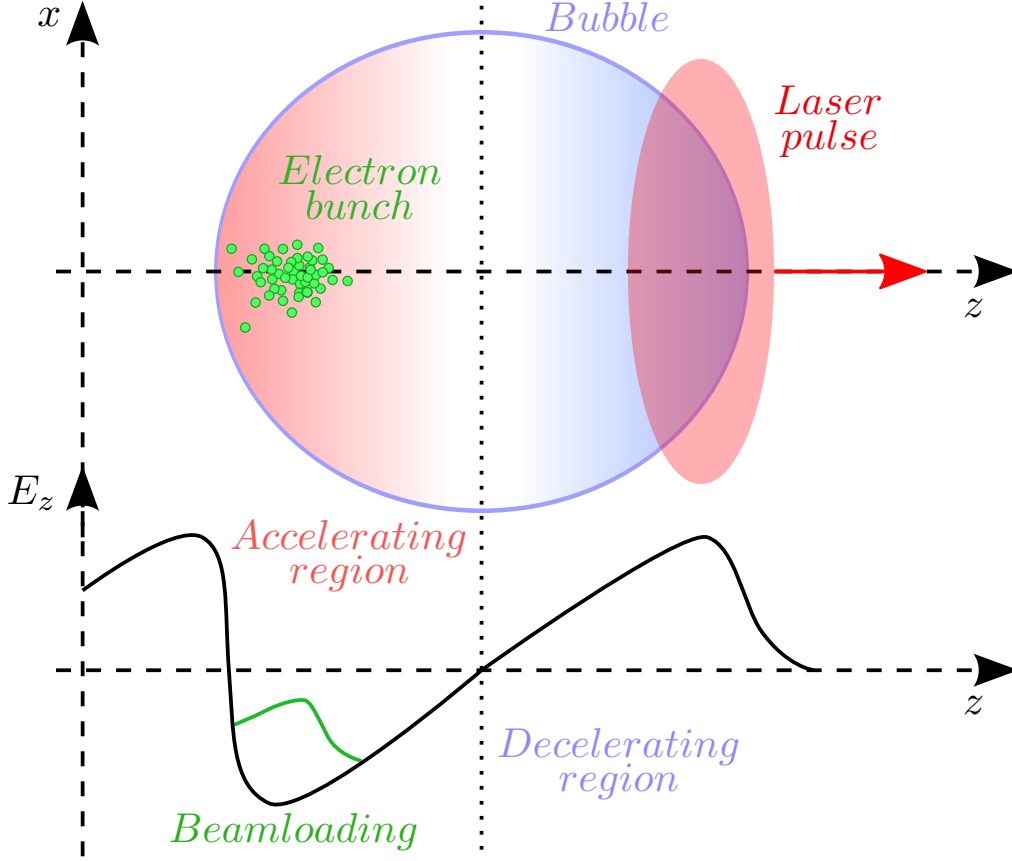
Figure 1.8: Representation of the wakefield in the bubble regime and illustration of the beam-loading effect. The laser pulse propagating in the z-direction drives a bubble with accelerating field (red gradient) for $z < 0$ and decelerating field (blue gradient) for $z > 0$. Injected electrons (green dots) distort the electric field in the bubble (in green).

transverse force seen by an electron [Corde et al., 2013a] :

$$F_x = -\frac{1}{2}m_e\omega_p^2 x \quad \text{for} \quad x < r_B. \tag{1.57}$$

Neglecting the initial transverse momentum of trapped electrons, the equation of motion for betatron oscillations can be written as

$$\frac{d^2x}{dt^2} = -\frac{1}{2\gamma}\omega_p^2 x \tag{1.58}$$

which is the equation of a harmonic oscillation whose characteristic frequency is the betatron frequency [Esarey et al., 2002]

$$\omega_\beta = \omega_p\sqrt{\frac{1}{2\gamma}}. \tag{1.59}$$

For adiabatic acceleration, eq. (1.58) can be integrated, leading to the expression of the transverse oscillation

$$x(t) = x_0\left(\frac{\gamma_i}{\gamma(t)}\right)^{\frac{1}{4}}\cos\left[\int_0^t \omega_\beta(t')dt' + \varphi_x'\right] \quad \text{with} \quad \omega_\beta(t) = \omega_p\sqrt{\frac{1}{2\gamma(t)}} \tag{1.60}$$

with x_0 the electron initial position and γ_i the value of γ at injection. During the acceleration, $\gamma(t)$ increases, then the betatron frequency and the amplitude of oscillations $x_\beta = x_0\gamma_i^{\frac{1}{4}}\gamma^{-\frac{1}{4}}$ decrease. Note that this amplitude is stronger for electrons injected far from the axis (large x_0), and that electrons can also be injected on axis with a large transverse injection velocity. One can deduce the angle of the electron trajectory with respect to z-axis during the acceleration

$$\theta_x(t) = \frac{1}{c}\frac{dx}{dt} = -\frac{k_p}{\sqrt{2\gamma_i}}x_0\left(\frac{\gamma_i}{\gamma(t)}\right)^{\frac{3}{4}}\sin\left[\int_0^t\omega_\beta(t')dt' + \varphi_x'\right] \quad \text{with} \quad \omega_\beta(t) = \omega_p\sqrt{\frac{1}{2\gamma(t)}}. \quad (1.61)$$

The divergence of the electron beam scales as $\theta \propto \gamma^{-\frac{3}{4}}$.

An inevitable consequence of electron betatron oscillations is the emission of betatron radiation. A relativistic electron oscillating transversally in the bubble emits synchrotron radiation collimated along the trajectory with a critical frequency $\omega_{\beta rad} \approx 2\gamma^2\omega_\beta$ (as seen in Fig. 1.9). It produces a synchrotron-like broad spectrum emission in the range of a few keV. The characteristic critical energy of betatron radiation estimated for usual experimental parameters ($n_{e0} = 10^{19}$ cm^{-3}, 250 MeV electrons) yields $E_{\beta rad} = \hbar\omega_{\beta rad} \sim 2$ keV, in the X-ray range. The characteristic divergence of betatron radiation from an electron is $\theta_{bet} = 1/\gamma$.
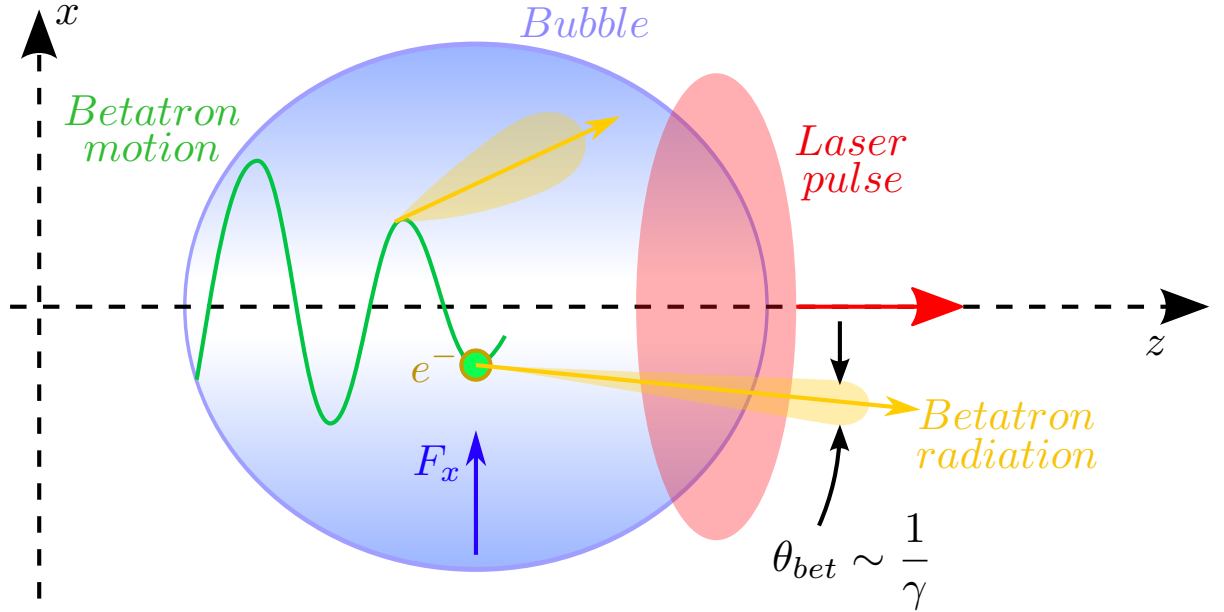
Figure 1.9: Representation of the focusing transverse fields (blue gradient) in the bubble regime and illustration of betatron motion (green trajectory) and radiation (in orange) of electrons during the acceleration.

1.2.6 Injection of electrons in the wakefield

From previous section, it is clear that laser-produced wakefields constitute an efficient accelerator for electron bunches. Nevertheless, the process of injection of electrons into the accelerating phase of the plasma wake is one of the most important aspect in LWFA. Indeed, the bunch has to be injected into a small accelerating structure ($\sim \lambda_p \approx 10 - 50$ μm) with an adapted initial

velocity and a length smaller than the plasma wavelength, which is far from being trivial. If the initial electron velocity is too small, electrons cannot be trapped in the wake. They follow the fluid orbit (as seen in section 1.2.3) and slip through successive accelerating and decelerating regions of the plasma wake. Furthermore, the injection process determines not only the charge of the electron beam, but also its duration, energy spread and emittance properties. A crucial challenge in the LWFA community is to find new and efficient injection techniques to improve the quality of laser-accelerated electron beams.

External injection

The first experimental demonstrations of laser-plasma acceleration were performed by injecting an external electron beam from a conventional accelerator [Clayton et al., 1993; Nakajima et al., 1995; Amiranoff et al., 1998]. In these experiments, a few MeV electron beam is injected into plasma waves. Due to the fact that the accelerating structure was much smaller than the injected bunch length ($\lambda_p \approx 100~\mu m \ll l_{bunch} \approx 3$ cm), the beam quality was not satisfactory (especially the energy spread, close to 100 %). Electrons are indifferently injected in accelerating and decelerating phases of the plasma wake, leading to a large energy dispersion.

In order to get good quality electron beams with small energy spread, one has to externally produce beams with a duration much lower than $\lambda_p/c \approx 100$ fs. Such electron beams are difficult to obtain with conventional accelerators at the moment, because of space charge problems potentially important at these low energies. Using an external beam injected in front of the laser pulse [Khachatryan, 2002; Lifschitz et al., 2005] is a promising way to achieve low duration, low energy spread electron beams. However, the synchronization between the injected bunch and the laser remains a challenging issue.

Transverse self-injection

An easier way to inject electrons in the wakefield is to directly use the electrons from the plasma itself by delivering them the necessary initial velocity to be trapped in the accelerating structure. The so-called *self-injection* scheme is based on this technique.

When the maximum velocity of the plasma electrons is larger than the phase velocity of the plasma wake, some electrons move faster than the wave itself and can be injected and further accelerated. This wavebreaking of the plasma wave [Katsouleas and Mori, 1988; Bulanov et al., 1997] happens when the separatrix and the fluid orbit overlap (see Fig. 1.6). This phenomenon occurs only at ultra-high intensity when highly non-linear waves are excited. First experimental demonstrations of self-injection [Modena et al., 1995; Gordon et al., 1998] were performed with long laser pulses (few hundreds of femtoseconds) and relatively high density ($n_e > 10^{19}$ cm^{-3}). The plasma waves were excited through self-modulation, with a non-localized wave-breaking, leading to Maxwellian electron spectra. With the rise of Ti:Sa laser systems (with pulse durations around 30 - 40 fs), it became possible to reach a regime where the laser pulse can be guided through self-focusing in the plasma, enabling to accelerate electrons at higher energies [Malka et al., 2002]. Finally, by reducing the plasma density, it was possible to generate the first quasi-monoenergetic electron spectra in the bubble regime by self-injection [Mangles et al., 2004; Faure et al., 2004; Geddes et al., 2004].

As seen in section 1.2.4, an ultra-intense laser pulse propagating through an underdense plasma pushes the electrons out of its path via ponderomotive force. The blown-away electrons are then attracted back to the axis due to the positively charged cavity behind the driving pulse. The trajectories of these electrons cross the laser propagation axis after approximately
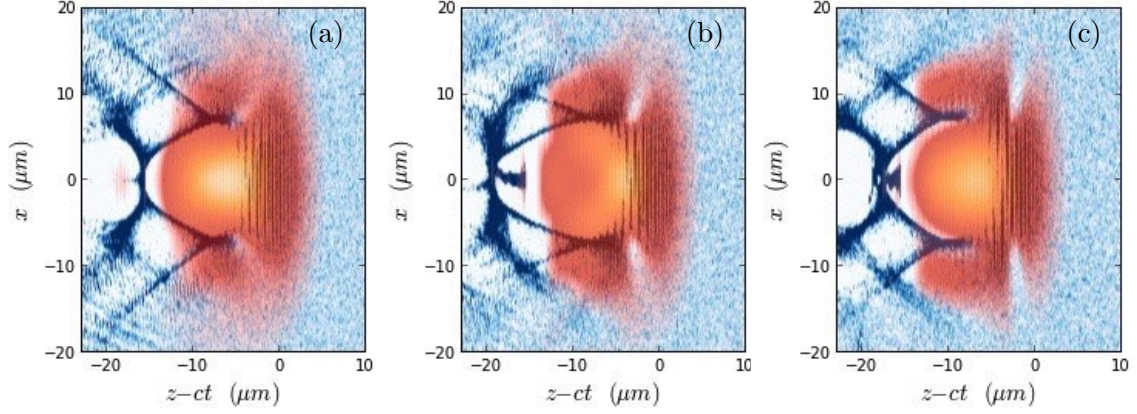
Figure 1.10: Transverse self-injection in the bubble regime : while the laser pulse is self-focusing (a), the non-linear process trigger fluctuations in the spot size leading to a sudden expansion of the bubble (b). Electrons are then trapped in the cavity and accelerated further as the pulse propagates in the plasma (c). The blue colorscale represents the plasma electron density. *Courtesy of R. Lehe*

one plasma period, enclosing an ion bubble. This bubble is thus surrounded by this dense layer of electrons flowing backwards, with a radius r_b. According to [Lu et al., 2007], a bubble radius as low as $r_b \sim 0.64\lambda_p$ leads to a high enough longitudinal velocity for some electrons at the back of the cavity to be trapped. Transverse self-injection of an electron depends on its initial distance r_0 from the laser propagation axis [Kostyukov et al., 2010a]. Electrons close to the center ($r_0 < r_b$) see a strong ponderomotive force and are pushed too far away by the laser to be part of the bubble layer, while electrons with $r_0 > r_b$ cannot be injected into the back of the bubble because of an insufficient velocity. For $r_0 \approx r_b$, the electrons can flow down to the back of the cavity and feel the strong fields pulling them towards the center of the bubble. They enter the bubble but are usually not trapped because their velocity is lower than the phase velocity of the cavity.

A way to facilitate injection is by a sudden expansion of the bubble cavity [Kalmykov et al., 2009b; Kostyukov et al., 2010b]. In this case, electrons that are already inside the accelerating phase of the bubble can remain for a longer time and reach a sufficient velocity to be trapped (as shown in Fig. 1.10). The sudden expansion of the bubble spontaneously occurs because of the strong self-focusing of the laser : as the laser pulse evolves to reach the matched spot size, the laser intensity increases and the bubble widens accordingly (as its length scales as $4k_p^{-1}\sqrt{a_0}$ according to [Lu et al., 2007]). While transverse self-injection is easily achieved with current setups, the method lacks stability (as it is triggered by the self-focusing of the pulse, which is highly non-linear) and inject electrons far from the axis (leading to strong betatron oscillations, thus a large beam divergence). Moreover, it is not temporally limited and can happen during the whole acceleration process, leading to electron beams with large energy spread.

Longitudinal self-injection

Self-injection can also be obtained from longitudinal wave-breaking. In this case, the electrons initially close to the laser propagation axis ($r_0 < r_b$) can be trapped due to the wakefield elongation. Longitudinal wave-breaking occurs if the maximum electron longitudinal velocity is larger
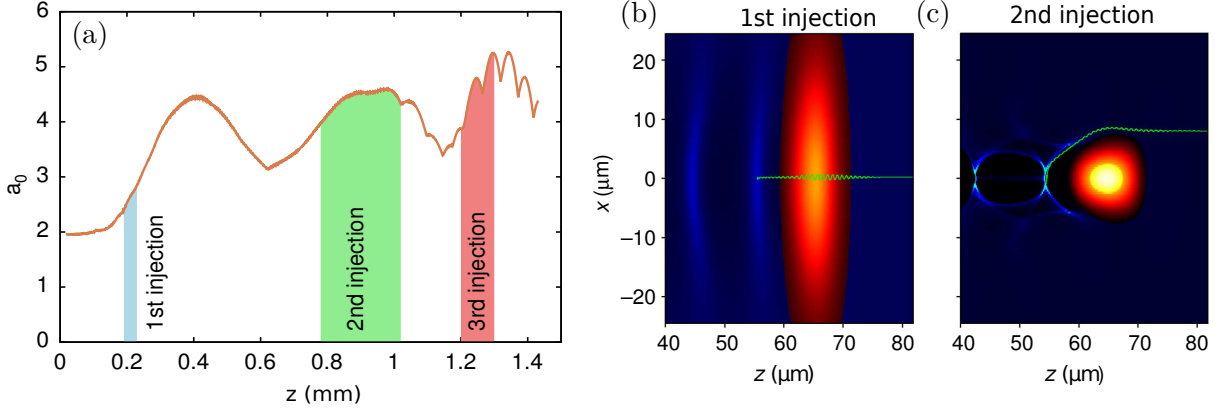
Figure 1.11: PIC simulation results of transverse self-injection. (a) Evolution of a_0 along the laser propagation in the plasma. Several self-injection process occur each time a_0 increases as it self-focuses. The first process is longitudinal self-injection (b), followed by transverse self-injection for larger laser amplitude (c). The green plots show the typical trajectory of an injected electron in each case. *Figure from [Corde et al., 2013b]*

than the wakefield phase velocity. Electrons can then be injected without a substantial transverse motion if the laser waist is large enough so that electrons stay close to the axis (as seen in Fig. 1.11). Longitudinal injection was experimentally demonstrated by [Corde et al., 2013b], producing electron beams with a relatively low divergence (as betatron oscillations are much weaker than in transverse injection), low charge (a few pC only) and a good shot-to-shot stability (as longitudinal injection happens at the beginning of the self-focusing process, which is less fluctuating than the intensity oscillations during the propagation and less sensitive to radial inhomogeneities due do transverse filtering). In principle, it is more difficult to longitudinally inject an electron than transversally, because an electron initially on-axis experience a decelerating longitudinal field before entering the accelerating phase of the wakefield. Longitudinal self-injection is then possible when the bubble expands suddenly (the plasma wavelength increases, thus the wake phase velocity suddenly drops). This is the case when the pulse strongly self-focuses at the beginning of the propagation : a_0 steeply increases, the cavity expands and electrons close to the axis are trapped. Usually, longitudinal self-injection is favored with low electron plasma density, as transverse self-injection is predominant at high density. The pulse self-focuses at the beginning of the low-density plasma, triggering longitudinal self-injection, then diffracts without being self-focused again if the density is too low, preventing the transverse self-injection to occur. The density threshold between transverse and longitudinal self-injection allows to easily choose the desired regime.The existence of this transverse wave-breaking threshold is of great interest to obtain high quality beams through a controlled injection method without being disturbed by self-injection.

Although longitudinal self-injection produces more stable electron beams than transverse injection, the charge is very low and the energy spread quite high. In order to improve the electron bunch quality, more control over the injection process is desirable. In the following, several controlled injection methods are presented.

Density transition injection

As explained in the previous section, a sudden expansion of the bubble tends to trigger injection of plasma electrons. One way to control this expansion is by forming a downward density transition in the gas jet [Bulanov et al., 1998]. The length of the bubble scales as $4k_p^{-1}\sqrt{a_0} \propto n_e^{-1/2}$, thus the cavity expands as the pulse propagates in the longitudinally decreasing plasma density.

If the density downramp length is long compared to the plasma wavelength λ_p, the local phase velocity of the plasma wave is slowed down until it equals the fluid velocity of plasma electrons, which can then get trapped in the wakefield. The local phase velocity is expressed as [Esarey et al., 2009]

$$v_{p,\varphi} = c\left(1 - \frac{\xi}{2n_e}\frac{dn_e}{d\xi}\right) \tag{1.62}$$

with ξ the longitudinal coordinate in the co-moving frame ($\xi = 0$ at the peak of the laser pulse, $\xi < 0$ behind the pulse). For a density downramp, $dn_e/d\xi < 0$, thus the phase velocity of the back of the bubble is lower than the one of the bubble front, leading to the expansion of the bubble during the propagation. This method was demonstrated experimentally using the natural downward gradient at the end of a gas jet to produce a low energy electron beam [Geddes et al., 2008; Gonsalves et al., 2011], or using a plasma density depletion created by a second beam transversely focused in the plasma, few nanoseconds before the main beam [Faure et al., 2010b; Brijesh et al., 2012]. While a long downramp can trap many electrons in the wakefield, it presents some issues. Firstly, the continuous trapping along the density gradient can lead to large energy spread. Moreover, as the bubble expands and the electron bunch accelerates, it quickly reaches the center of the bubble where the longitudinal field switches sign. The electron bunch dephases and cannot reach high energies.

If the density transition is sharper, with a scale length smaller than the plasma wavelength, the injection mechanism is slightly different. At the density transition, λ_p increases steeply, which causes a large amount of electrons just behind the bubble to be instantly loaded in the accelerating phase of the wakefield. The phase velocity of the plasma wave is essentially frozen during the sharp transition, thus the injection is caused by the sudden plasma wavelength increase rather than the reduced phase velocity in this case. This scheme has been extensively studied numerically [Suk et al., 2001; Kim et al., 2004a; Brantov et al., 2008]. Up to now, the density transition was formed with a second laser pulse propagating transversely to the main interaction pulse, locally depleting the electron density but also strongly changing the density ahead of the pulse, thus generating broad energy spectra [Chien et al., 2005; Faure et al., 2010a]. More recently, experimental injection in a sharp density transition formed by a shock in a supersonic gas flow (either with a razor blade [Schmid et al., 2010; Buck et al., 2013] or a wire [Burza et al., 2013]) has been demonstrated, producing high quality electron beams. By correctly tailoring the density transition, the injection process is stabilized and leads to tunable, high-quality electron beams. An extensive study of this injection technique is presented in chapter 2 of this manuscript.

Ionization injection

Ionization injection is a recent technique based on the fact that some electrons can be stripped from their atom later than others. A small percentage of a high-Z gas (for instance argon or nitrogen) is mixed with the usual low-Z gas (hydrogen or helium) used in the gas jet. Electrons from the low-Z atoms, as well as the electrons from the outer shells of the high-Z atoms, are

released far ahead from the pulse peak intensity and preform the plasma. However, the electrons from the inner shell of the high-Z atoms have a much higher ionization potential and are ionized near the peak of the pulse, directly in the bubble. When this happens, electrons can be in the accelerating phase of the wakefield and be accelerated [McGuffey et al., 2010; Pak et al., 2010; Pollock et al., 2011a]. An other way is to accelerate electrons in a pure high-Z gas [Singh and Sajal, 2009; Mori et al., 2009; Kotaki et al., 2011; Mo et al., 2012; Guillaume et al., 2015a], leading to highly-charged electron beams. This technique is extensively discussed in 3.

Although ionization injection is easily implemented, it suffers from the fact that electrons are continuously injected during the laser propagation, thus leading to electron beams with high charge but also large energy spread (because the electrons ionized at the beginning of the propagation are accelerated for a longer time than those ionized at the end of the jet). One way to overcome this issue is the use of two stages accelerators, with a first injection stage based on ionization injection followed by an accelerator stage with a low-Z gas [Pollock et al., 2011a; Bourgeois et al., 2013].

Optical injection

Another way to trigger electron injection in the wakefield below the transverse wave-breaking threshold is the use of a second laser pulse in order to uncouple injection from the acceleration. In optical injection, the interaction between the two laser pulses creates a beat wave confined in space and time where electrons can be injected in the wakefield. The first configuration to be studied, with two perpendicular pulses, gave mitigated results [Umstadter et al., 1996; Zhang et al., 2003]. A scheme with counter-propagating pulses was then implemented, providing a very good control over the injected charge and energy gain [Faure et al., 2006b].

With this method, a beat wave with half the wavelength of the driving laser is formed where the two pulses cross each other [Esarey et al., 1997]. The large ponderomotive force accelerates locally some electrons which are able to catch up with the wakefield and be accelerated. By varying the delay between the two pulses, the overlap position can be longitudinally shifted in the gas jet, thus the acceleration distance changes and the electrons final energy can be easily tuned. The bunch charge and energy spread are determined by the intensity and polarization of the injection pulse [Rechatin et al., 2009]. Usually, the injection pulse has a much lower intensity than the main pulse and is unable to drive its own large amplitude wakefield. For easier experimental implementation, the interaction and injection laser beams do not have to be perfectly counter-propagating at 180 degrees, but instead at 135 degrees for instance [Kotaki et al., 2004; Fubiani et al., 2004].

Another colliding laser pulse scheme was recently proposed with a similar experimental geometry, the so-called *cold optical injection* [Davoine et al., 2009, 2010; Lehe et al., 2013]. In this scheme, the longitudinal motion of electrons is frozen by the injection pulse and the electrons dephase up to be trapped in the wakefield with no net velocity gain. This method has been numerically studied and is potentially interesting to produce lower energy spread electron beams but has not been experimentally demonstrated so far.

Although this method can generate high quality, stable electron beams, the main drawback of optical injection is the scheme experimental complexity. A second laser pulse has to be perfectly overlapped (both spatially and temporally) with the main pulse for optical injection to happen.

1.2.7 Limitations

Acceleration of electrons can stop due to several processes limiting the maximum attainable energy. These effects are described in the following paragraphs.

Laser diffraction : The laser focused at the entrance of the gas target progressively defocuses along the propagation, and its intensity becomes too weak to efficiently drive an accelerating wakefield. The diffraction length L_{diff} is governed by the Rayleigh length Z_R : $L_{diff} = 2Z_R$. For a focal spot size matching the plasma wavelength ($w_0 \approx \lambda_p$), then :

$$L_{diff} = 2\pi \frac{\omega_0}{\omega_p} \lambda_p. \tag{1.63}$$

Outside this range, the laser spot size grows quickly, reducing the intensity. This effect is mitigated by self-focusing, yet it typically extends the acceleration length over a few Rayleigh lengths only. An external guiding is thus mandatory to maintain the acceleration over a distance which is not limited by laser diffraction, for example by using a preformed plasma column or a capillary waveguide [Leemans et al., 2006; Karsch et al., 2007b; Leemans et al., 2014].

Laser energy depletion : Another important limitation for the maximum energy gain is the energy depletion of the laser pulse. Once the laser has lost a substantial amount of energy, the plasma wave amplitude decreases and thus the acceleration terminates. The pump depletion length L_{depl} [Bulanov et al., 1992b; Shadwick et al., 2009] can be estimated by comparing the energy contained in the laser pulse with the energy transferred to the wakefield. For linearly polarized laser pulses, the depletion length can be estimated as [Esarey et al., 2004b] :

$$L_{depl} = \left(\frac{\omega_0}{\omega_p}\right)^2 \lambda_p \times \begin{cases} \frac{2}{a_0^2} & \text{for} \quad a_0 \leq 1. \\ 1 & \text{for} \quad a_0 \gg 1. \end{cases} \tag{1.64}$$

Pump depletion is bound to happen, but its limiting effects can be avoided by increasing the initial energy contained in the driver pulse and decreasing the plasma density.

Electron dephasing : Although relativistic electrons can reach velocities extremely close to the speed of light in vacuum, the plasma wave is bound to the group velocity of the laser pulse $v_{l,g}$. As electrons are faster than the plasma wave, they can reach the point where the accelerating field is zero, enter the decelerating part of the wave and start to lose energy. The dephasing length L_{deph} can be estimated by calculating the acceleration distance (in the laboratory frame) it takes for electrons to travel quarter a plasma wavelength

$$(c - v_{l,g}) \frac{L_{deph}}{c} = \frac{\lambda_p}{4} \tag{1.65}$$

$$L_{deph} = \frac{\lambda_p^3}{4\lambda_0^2} \propto n_e^{-\frac{3}{2}}. \tag{1.66}$$

This simple calculation is valid only if $a_0 \approx 1$: for $a_0 \gg 1$, the effective plasma wavelength increases and the point where electrons start to dephase depends on the laser intensity. Esarey et al. [2004a] derive a more detailed analysis considering linear and non-linear regimes :

$$L_{deph} = \left(\frac{\omega_0}{\omega_p}\right)^2 \lambda_p \times \begin{cases} 1 & \text{for} \quad a_0 \leq 1. \\ \frac{4}{3}\sqrt{a_0} & \text{for} \quad a_0 \gg 1. \end{cases} \tag{1.67}$$

The dephasing length increases when background electron density gets lower whatever the laser intensity. Although electrons dephasing cannot be avoided, relatively low electron densities can be used to overcome dephasing and reach higher electron energies.

1.3 Electron bunch properties in a Laser-Plasma Accelerator

Electron beams generated from Laser-Wakefield Accelerators are promising candidates for various applications such as Free-Electron Lasers (FEL) [Nakajima, 2008; Schlenvoigt et al., 2008] or compact high-energy colliders [Schroeder et al., 2010] which require high-quality electron bunches. Currently, many researchers investigate new ways to further improve the beam properties, for example by using different plasma sources (capillary waveguide [Leemans et al., 2014], tailored density profiles [Gonsalves et al., 2011]). To date, electron beams from LWFA suffer from quite large energy spread (in the order of a few percents [Wiggins et al., 2010; Pollock et al., 2011b], in comparison with conventional accelerators reaching 10^{-4} percent energy spread) and divergence (down to almost 1 mrad [Plateau et al., 2012]). The best way to quantify the beam transverse quality is its emittance, which is defined in section 1.3.1. The beam charge is another important property, as many applications require a large number of electrons (as radiobiology or radiotherapy). Electron bunches from LWFA are intrinsically short, leading to high peak currents when coupled with a relatively high charge. Finally, the energy distribution of electrons in the beam is of major importance : to reach capabilities of conventional accelerators, the peak energy must be increased and the energy spread strongly reduced.

1.3.1 Transverse quality of an electron bunch

A single electron has a well-defined mass, charge, position and energy, but the situation is more complex for electron beams. At any time t, each electron is represented by a single point in the six-dimensional phase space $(\boldsymbol{x}, \boldsymbol{y}, \boldsymbol{z}, \boldsymbol{p_x}, \boldsymbol{p_y}, \boldsymbol{p_z})$ of the beam. The phase space can represent the beam distribution as a continuous particle density with a well-defined volume V or an ensemble of discrete particles. An ensemble of particles is considered as a "beam" if the longitudinal mean momentum p_z is much larger than the transverse momenta p_x, p_y. As electrons move in time, the orientation and shape of the phase space changes. According to Liouville's theorem [Goldstein, 1980], the phase space volume V remains constant for a conservative system. The emittance of the beam, denoted ε, is a measure of the phase-space volume, directly related to the beam quality. It combines the bunch length and energy spread as well as its transverse size and divergence. The emittance is conserved under propagation of the bunch in vacuum or through linear focusing systems.

The six-dimensional phase space is usually decomposed in three phase space areas by projecting the volume V onto the orthogonal planes $(\boldsymbol{x}, \boldsymbol{p_x})$, $(\boldsymbol{y}, \boldsymbol{p_y})$ and $(\boldsymbol{z}, \boldsymbol{p_z})$, where $\boldsymbol{x}$ and $\boldsymbol{y}$ are the transverse coordinates and $\boldsymbol{z}$ is the propagation direction. In fact, the term "emittance" is frequently used to refer to transverse emittance alone (ε_x, ε_y). Furthermore, it is more convenient to use the trace space quantities $x' = p_x/p_z$ and $y' = p_y/p_z$ as a measure of angular deviation from straight motion along the propagation axis, thus relating to the beam divergence directly (in the paraxial approximation $p_x, p_y \ll p_z$, true for relativistic bunches). For simplicity, we limit the discussion to the x-dimension, however, similar relations will hold for y-dimension.

It is convenient to describe the beam distribution in trace space as an ellipse (as shown in Fig. 1.12) with equation

$$\gamma x^2 + 2\alpha x x' + \beta x'^2 = \varepsilon \tag{1.68}$$
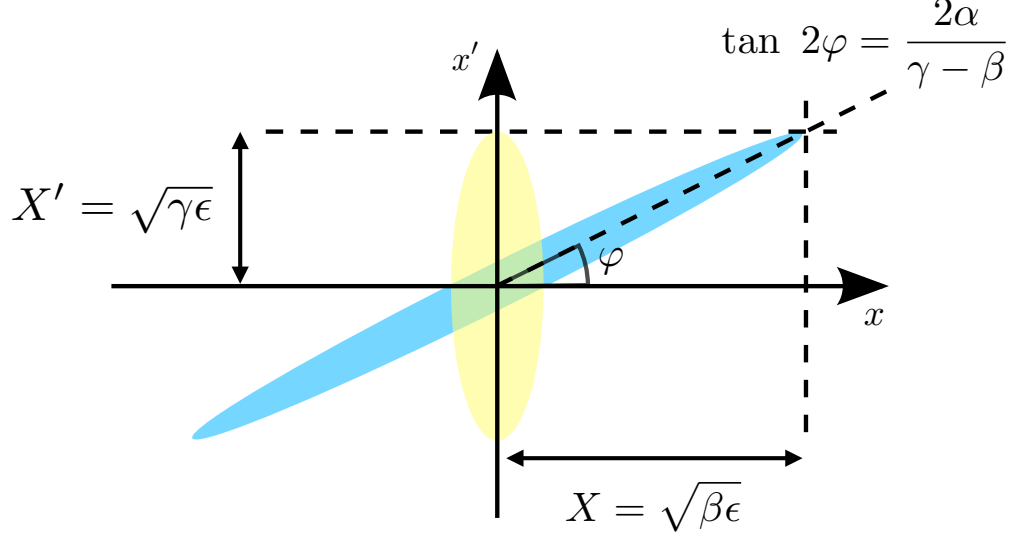
Figure 1.12: Trace space ellipse representing the distribution of electrons in (x, x') space. The ellipse area is the emittance ε multiplied by π. The yellow ellipse represents a bunch at waist while the blue ellipse represents a bunch drifting in free space, diverging from the waist.

where α, β and γ are the Twiss parameters and ε the emittance of the beam. These parameters are related through $\beta\gamma - \alpha^2 = 1$. β and γ quantify the projected bunch size and divergence respectively while α is a measure of whether the bunch is converging towards the waist ($\alpha > 0$) or diverging away from it ($\alpha < 0$, as exemplified by the blue ellipse in Fig. 1.12). As the beam propagates, the Twiss parameters vary accordingly, and the trace space ellipse changes in size and orientation as well. The projected bunch size is $X = \sqrt{\beta\varepsilon}$ (β has the dimension of a length), and the beam divergence is $X' = \sqrt{\gamma\varepsilon}$ (γ has the inverse dimension of a length). The angle φ (see Fig. 1.12) depends only on the Twiss parameters and fully defines the bunch evolution during a drift in free space (rotation of the ellipse in the trace space, as seen in Fig. 1.12). The emittance is calculated from the area occupied by the ellipse in the trace space :

$$\varepsilon = \frac{1}{\pi} \int_{ellipse} dx dx' \tag{1.69}$$

This defines the geometrical emittance of the beam. Real electron beams have complex shapes : one has to find the best fitting area of the particle distribution and deduce the emittance value.

During the propagation of the beam in a free space of length L, the ellipse evolves (keeping a constant area, as emittance is conserved during the drift) and the Twiss parameters change according to the following

$$\begin{pmatrix} \alpha' \\ \beta' \\ \gamma' \end{pmatrix} = \begin{pmatrix} 1 & 0 & -L \\ -2L & 1 & L^2 \\ 0 & 0 & 1 \end{pmatrix} \begin{pmatrix} \alpha \\ \beta \\ \gamma \end{pmatrix} \tag{1.70a}$$

Primed Twiss parameters are those after the drift space. Figure 1.13 shows the evolution of the trace space ellipse diverging away from the beam waist (at z_0, with a bunch size x_0 and a divergence x'_0). After a given propagation length $L = z_2 - z_0$, the divergence $x'_2 = \sqrt{\gamma'\varepsilon} =$
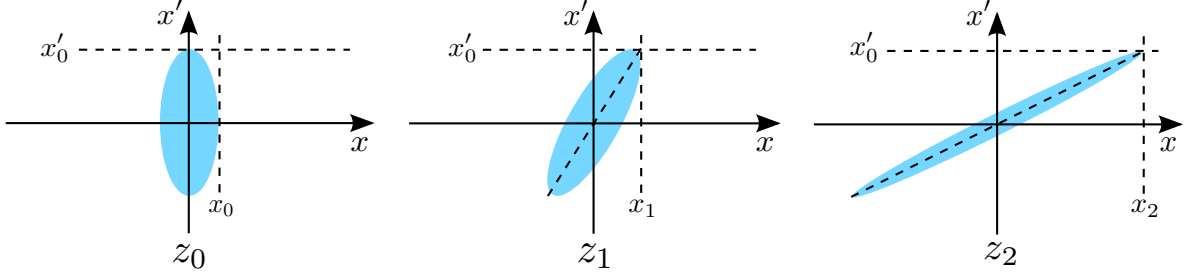
Figure 1.13: Transverse trace space evolution of an electron beam propagating in a drift space. The beam waist is at z_0.

$\sqrt{\gamma \varepsilon} = x_0'$ stays the same, and the bunch size evolves as

$$x_2 = \sqrt{\beta' \varepsilon} = \left(1 + \sqrt{\frac{L}{\beta}(\gamma L - 2\alpha)} \right) x_0. \tag{1.71}$$

In practice, electron beams do not have a well-defined shape, it is then difficult to fit the phase space distribution with an ellipse. Emittance can also be defined using the root mean square (rms) values for the first and second momenta of the distribution. The first momenta $\langle x \rangle$ and $\langle x' \rangle$ represent the mean size and divergence of the electron distribution, while the second moments $\langle x^2 \rangle$ and $\langle x'^2 \rangle$ are the standard deviation from the mean. The rms emittance is defined as

$$\varepsilon_{rms} = \sqrt{\langle x^2 \rangle \langle x'^2 \rangle - \langle xx' \rangle^2} \tag{1.72}$$

where the term $\langle xx' \rangle^2$ expresses the correlation between the bunch size x and divergence x' (close to zero at the beam waist). This definition of emittance is not limited by geometrical boundaries and defines the statistical transverse quality of the beam. Usually, $\varepsilon_{rms} > \varepsilon$. In laser-wakefield accelerators, the longitudinal momentum of electrons increases while the transverse momenta stay roughly the same, resulting in a divergence reduction and therefore a rms emittance decrease. A useful quantity in such a system is the normalized rms emittance which is invariant during acceleration :

$$\varepsilon_n = \gamma_0 \varepsilon_{rms} \tag{1.73}$$

with γ_0 the mean relativistic Lorentz factor of the bunch. The main advantage of representing an electron bunch by its normalized rms emittance is the concatenation of all transverse properties in a single quantity invariant during acceleration in the wakefield and during drifting in free space.

So far, the smallest transverse normalized rms emittance directly measured in a laser-wakefield accelerator is about 0.2 π.mm.mrad for a 250 MeV electron beam [Weingartner et al., 2012] (similar than in conventional accelerators). Small emittance implies high focusability and the potential of generating high quality radiation sources. Moreover, emittance is a conserved quantity in linear systems, thus it is a useful figure to describe the quality of the electron beam throughout a full system (accelerator, beam transport line and synchrotron for example). However, in reality, electron beams experience nonlinear forces that can increase the emittance, such as chromatic aberration of the focusing magnetic optics or transport line misalignment.

1.3.2 Bunch properties : duration, charge and peak current

The longitudinal length of the electron bunch is related to the time scale over which electrons are trapped in the wakefield. The characteristic length of the accelerating cavity is the plasma wavelength λ_p. In order to be in the accelerating part of the bubble, the electron bunch maximum duration is limited to $\lambda_p/2$. The temporal structure of an electron bunch is often assumed to be Gaussian with a FWHM pulse duration τ_{bunch}. Experimental measurements of laser-accelerated electron bunches revealed typical durations of only a few femtoseconds [Lundh et al., 2011, 2013; Bajlekov et al., 2013].

As more and more plasma electrons are trapped at the back of the ion bubble, the total charge of the bunch Q_{bunch} increases. As the cavity is loaded, the longitudinal field E_z is screened and eventually electron trapping ceases (beamloading effect, see section 1.2.5). One can define a peak current for the electron bunch as

$$I_{peak} = \frac{Q_{bunch}}{\tau_{bunch}} \tag{1.74}$$

Typical laser accelerated electron bunches have a total charge of 50 pC and a FWHM duration of 5 fs, leading to typical peak current values of 10 kA.

Some injection techniques (as ionization injection) are favorable for generating heavily-charged electron beams up to a few hundreds of picocoulombs (see chapter 3), but it usually goes along with worse transverse properties because of space-charge effects.

1.3.3 Energy distribution of electrons

Figure 1.14: Typical experimental spectrum of a laser-accelerated quasi mono-energetic electron beam at LOA
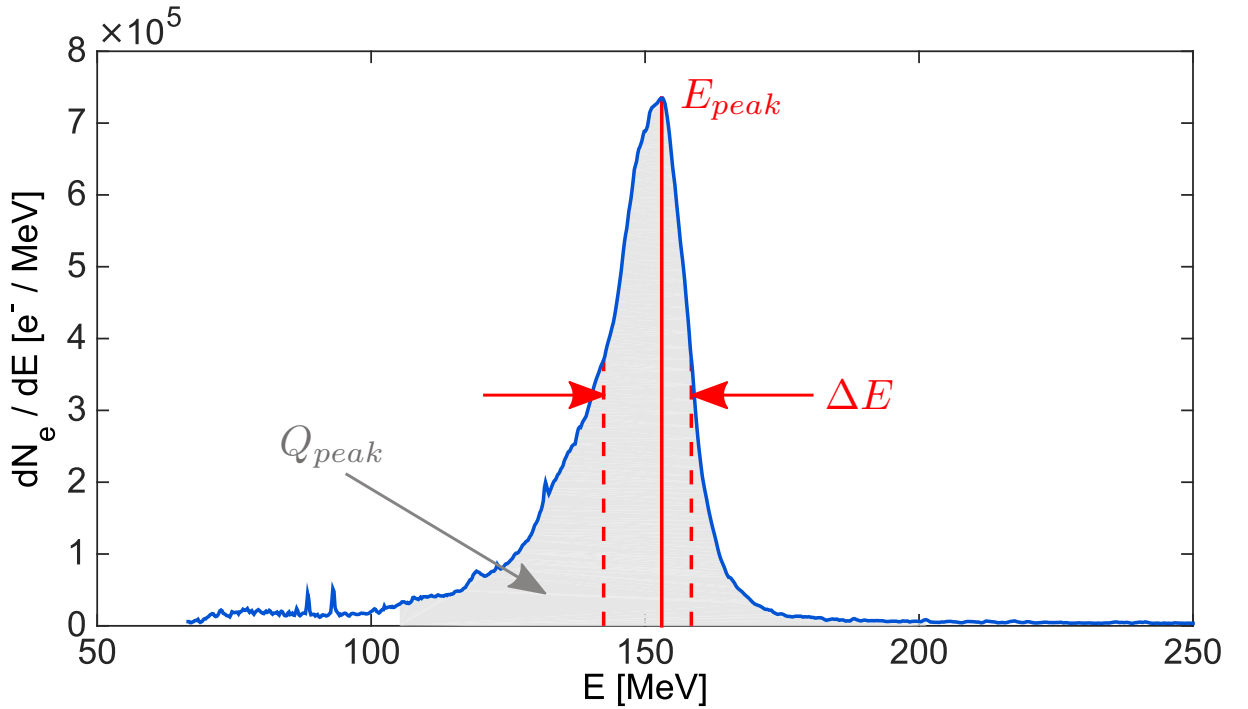
Electron energy distribution in the beam is a major property to study when defining the beam quality. Although it is still a long way for laser-plasma accelerated beams to be as mono-energetic as beams from conventional accelerators, recent breakthroughs made this goal foreseeable (see section 1.4 for details on the experimental setup). A typical experimental spectrum of a quasi mono-energetic electron beam is shown in Fig. 1.14. In all the manuscript, the quantities are specified as the following, unless stated otherwise. The peak energy of the beam E_{peak} is defined as the energy where the charge per MeV is maximum. The energy spread of the bunch ΔE is the FWHM of the peak, not necessarily centered on E_{peak}. The charge of the peak Q_{peak} is defined as the charge contained between $E_{peak} - 3\Delta E$ and $E_{peak} + 3\Delta E$, and may be slightly different from the total charge of the beam Q_{tot} (for instance if there is a large low energy tail in the spectrum).

1.4 Experimental study of Laser-Wakefield acceleration

1.4.1 "Salle Jaune" laser system

The experiments reported in this manuscript were performed with the "Salle Jaune" laser system at Laboratoire d'Optique Appliquée. The system is a 5-stages Ti:Sa laser producing 28 fs pulses with peak powers up to 60 TW at a carrier wavelength of 810 nm and 1 Hz repetition rate. Such ultrashort pulses can be produced thanks to *Chirped Pulse Amplification* technique [Strickland and Mourou, 1985], consisting in stretching the pulse temporally before amplification and compressing it down once it is amplified. This method allows to avoid the damaging of transmission optics occurring at high laser intensities. A layout of the laser system is shown in Fig. 1.15.

The commercial front end starts with a Ti:Sa oscillator producing 9 fs pulses at the nJ-level at a repetition rate of 88 MHz. The spectrum is broad with a full width at half-maximum of 150 nm and centered around 800 nm (as shown in Fig. 1.16(a)). Those pulses are then stretched out temporally up to a duration of 20 ps and amplified up to 2 mJ at a rate of 10 Hz. A diffractive prism based compressor is then used to reduce the duration down to 20 fs. The femtosecond pulses go through a XPW (Cross-Polarized Wave) filter in order to enhance the temporal contrast (which is the ratio between the main pulse peak power and the pedestal), reaching up to 10^{10} at 100 ps and 10^7 at 10 ps at the end of the laser chain. The efficiency of this contrast-enhancement technique is about 15 %, reducing the energy of the pulse down to 35 μJ. The energy loss is compensated in the following amplification stages.

The laser pulses are stretched up to 500 ps by a second stretcher and enter an acousto-optic modulator, or Dazzler, to precisely control the spectral phase of the laser [Verluise et al., 2000]. The spectral phase control is very important as it allows to pre-compensate the spectral shortening due to the amplifiers' gain. Furthermore, the spectral phase properties of the laser have a substantial influence on the pulse propagation in the plasma. The pulses are then amplified by a series of five Ti:Sa multi-pass amplifier stages pumped with frequency-doubled (532 nm) Nd:YAG commercial lasers, as seen in Fig. 1.15. The first and second amplifiers increase the pulses energy up to 1 mJ and 20 mJ. The pulses are then spatially filtered by traveling through an afocal system and a few tens of microns holes to clean out the focal spot. They are finally amplified by the third, fourth and fifth amplifiers up to 600 mJ, 3 J and finally 6 J. After each amplification stage, the beam size is increased with an afocal system to keep the fluence below the Ti:Sa crystals damage threshold of around 1 J.cm^{-2}. The repetition rate of the full system is limited to 1 Hz because of thermal disturbances which can be induced at higher repetition (thermal lens in amplifier crystals for example).

At the output of the fifth amplifier, the beam is separated into three beams : P1 and P2

« Salle Jaune » laser room
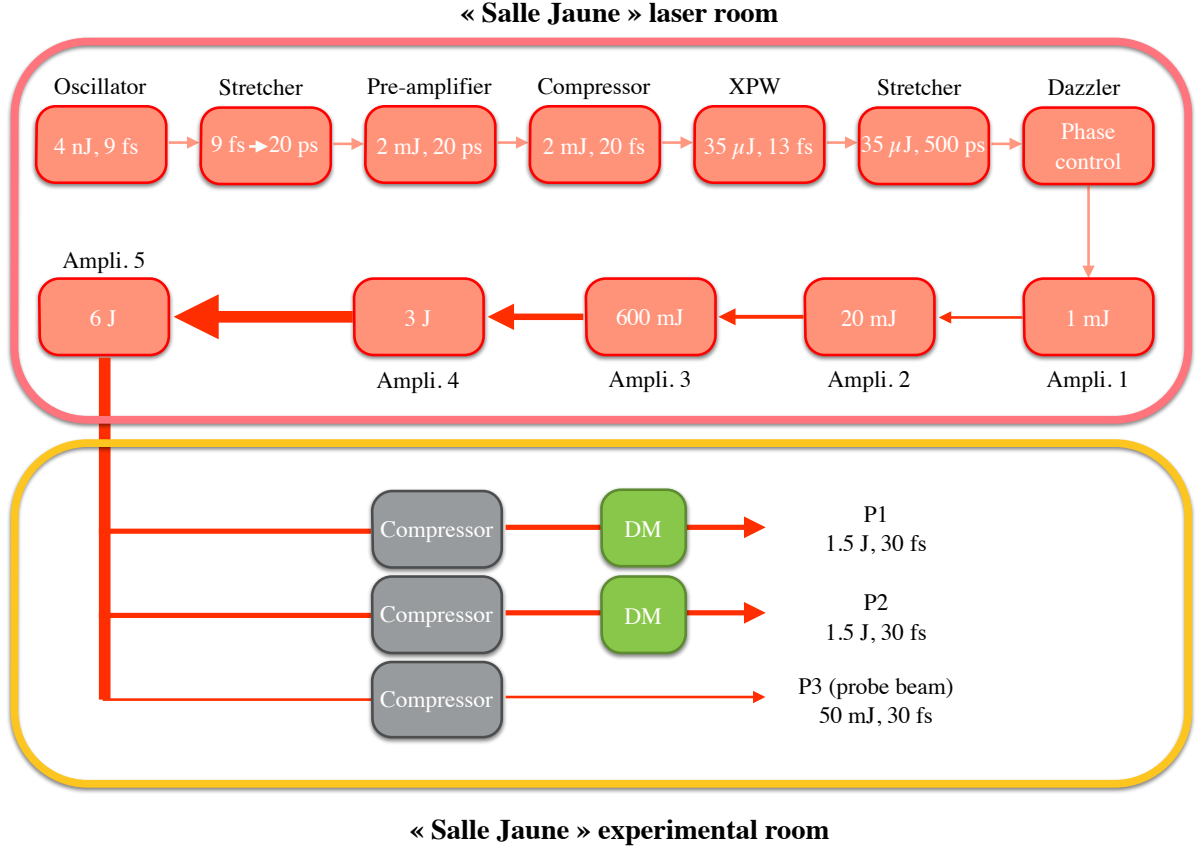
Figure 1.15: Layout of the "Salle Jaune" laser system from the oscillator to the experimental vacuum chambers.

are the main interaction beams while P3 which has much less energy is used as a probe beam in most of the experiments. The laser spectrum after amplification is slightly red-shifted, with the laser central wavelength at full-power measured around 810 nm. The laser beam exits the amplification stages with an almost "top-hat" spatial profile (as seen in Fig. 1.16(c)) and a linear polarization along the p-polarization in the horizontal direction.

The three beams are transported to the compressor chamber by afocal systems of lenses in oder to adapt the transverse beam size to the gratings damage threshold and dimensions. The beam diameters are almost 60 mm FWHM for P1 and P2 (as seen in the transverse cut of the beam profile in Fig. 1.16(d)) and 30 mm FWHM for P3. The three beams are then compressed independently with three systems of double gratings down to 30 fs. The resulting temporal shape of the pulse is shown in Fig. 1.16(b), with a duration of 28 fs FWHM. After compression, two deformable mirrors (DM) are used to improve the wavefront spatial quality of the two main interaction beams P1 and P2. The latter is measured by imaging the deformable mirror surface onto a HASO device (a Shack-Hartmann type wavefront sensor). It measures the phase aberrations of the beam and reconstruct the wavefront by decomposing it over the orthogonal base of Zernike polynomials. Each of these polynomials correspond to a well-defined optical aberration which can be compensated by using the deformable mirror, leading to an improvement of the laser focal spot quality. After correction, typical focal spots have 50/60 % of the energy contained in the first Airy disk. Figure 1.17 shows two pictures of the laser system and the chamber containing the deformable mirrors.
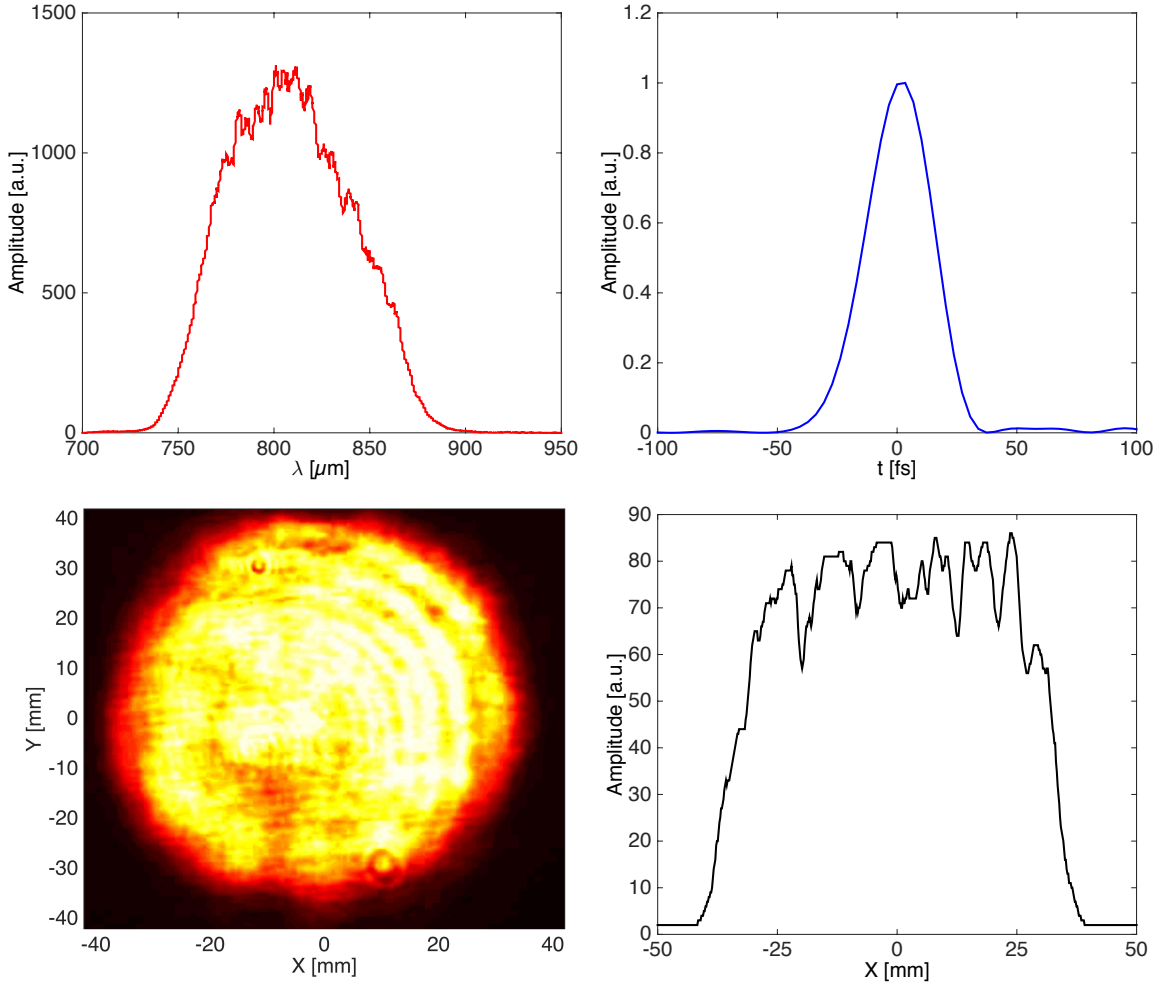
Figure 1.16: Output parameters of the "Salle Jaune" laser system. (a) Laser spectrum at the output of the oscillator. (b) Temporal shape of the main interaction beam P1 after compression measured with a FROG system. (c) Beam spatial profile at the output of the amplification stages. (d) Transverse cut of the beam spatial profile at Y = 0 mm. The "top-hat" shape allows for a homogeneous distribution of energy on optics, reducing hot spots appearance and material damaging.

1.4.2 Basic experimental setup

The electron acceleration experiments presented in this manuscript were performed in a dedicated experimental chamber in the "Salle Jaune" experimental room at LOA. The basic setup in general is evolved from the one presented above, with various configurations of off-axis parabolas, gas targets and diagnostics. A photograph of the inside of the experimental chamber can be seen in Fig. 1.18, and a general schematic drawing of the setup is shown in Fig. 1.19.

The main interaction beam P1 is focused with an Off-Axis Parabola (OAP) onto the target medium. OAP with different focal lengths and off-axis angles were used for different experimental campaigns : they are specified in the different chapters of the manuscript. A typical focal spot size obtained with a 780 mm focal length OAP has a diameter (FWHM) of 12 μm, leading to a peak intensity of $I_0 \approx 9 \times 10^{18}$ - 1×10^{19} W.cm^{-2} depending on the pulse energy. The focal
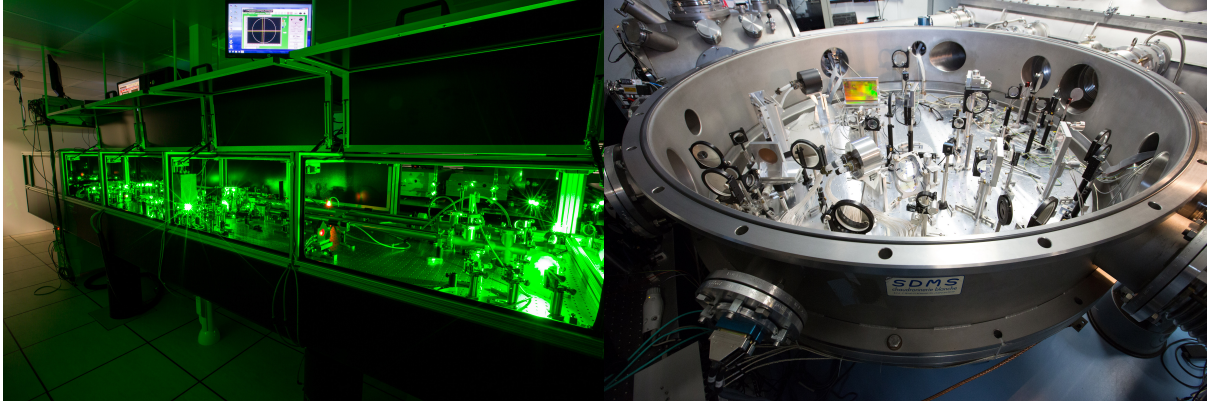
Figure 1.17: Pictures of the "Salle Jaune" laser system (left) and the vacuum chamber containing the two deformable mirrors for P1 and P2 and the compressor for P3 (right).
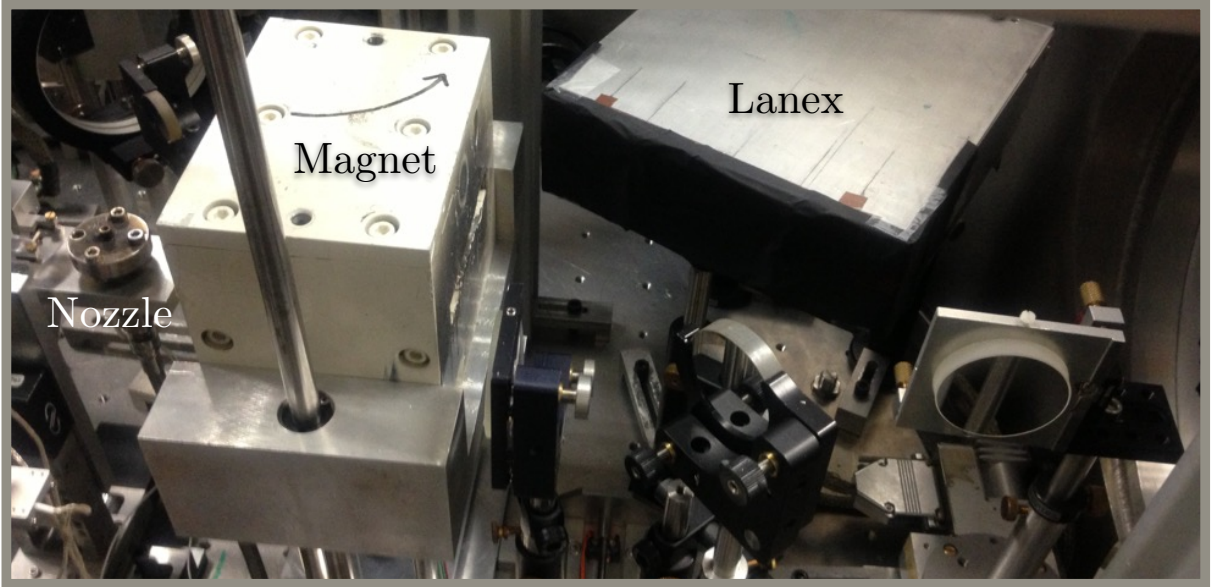
Figure 1.18: Photograph of the basic experimental setup for electron acceleration in the "Salle Jaune", presenting the gas nozzle, the magnet and the Lanex screen composing the electron spectrometer.

spot was characterized for each experiment using a microscope objective and a CCD camera (as shown in Fig. 1.19). Its quality was manually optimized by setting the adaptive mirror to correct for the residual aberrations. The laser polarization is horizontal (parallel to the chamber floor).

The gas target used in the presented experiments is provided by a pulsed gas jet. Nozzles with different kinds (subsonic or supersonic) and sizes were used depending on the desired plasma density profile. The density was measured *in situ* for each shot using the probe beam P3 going through the plasma and a Nomarski interferometer (see section 1.4.3). The plasma emission (essentially Thomson scattering) was imaged through a top-view imaging line by a 16 bit CCD.

The electron energy distribution was measured by an electron spectrometer composed of a permanent magnet and a scintillating screen (Kodak Lanex) imaged with a CCD camera.
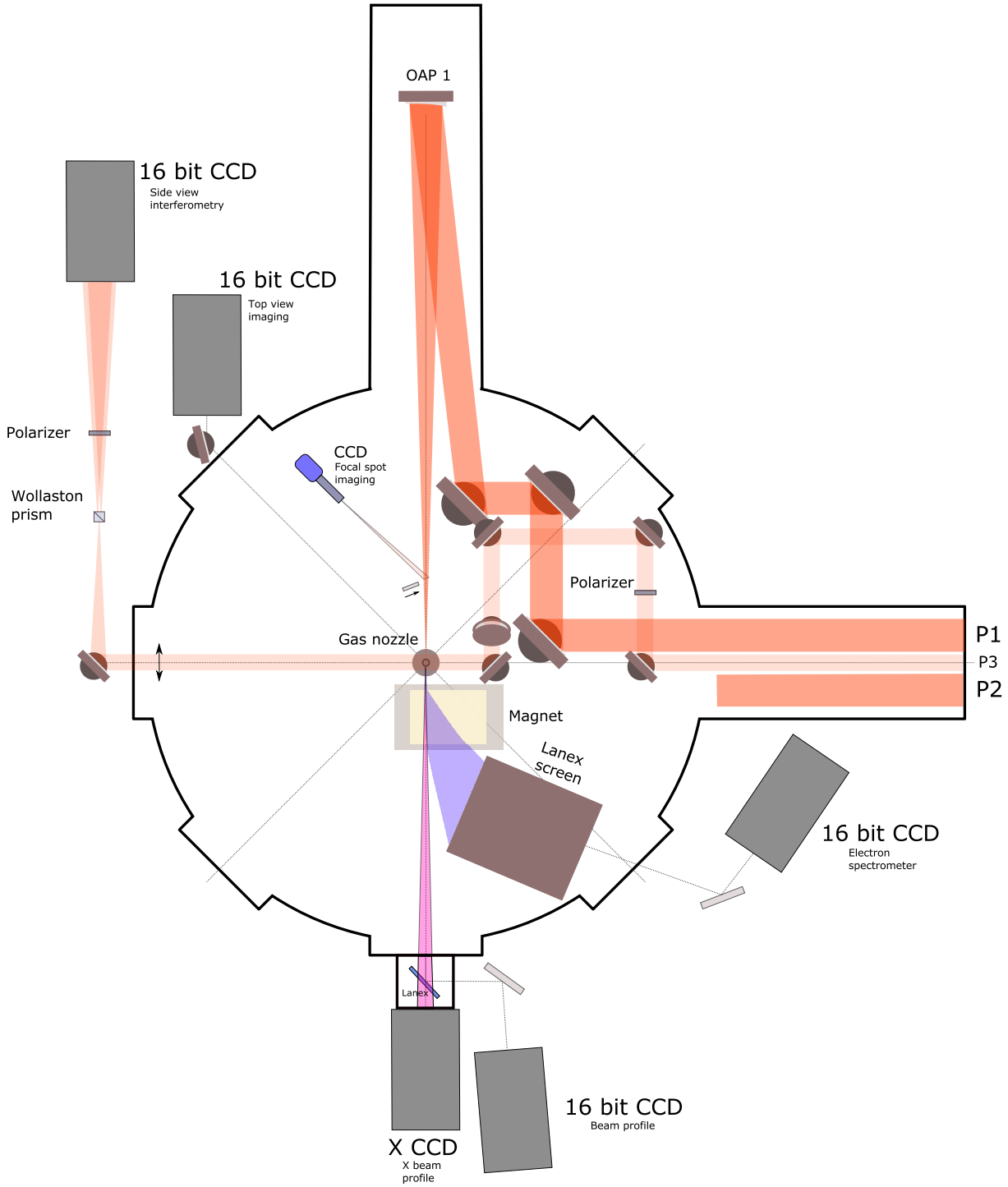
Figure 1.19: Basic experimental setup drawing for electron acceleration : the main interaction beam P1 is focused onto a gas nozzle with an Off-Axis Parabola (OAP1), coupled with a camera for focal spot optimization. The electron spectrum is measured with a spectrometer (magnet + Lanex + CCD) and the divergence with a second Lanex screen. The plasma density is characterized with the probe beam P3 going into a Nomarski interferometer. Top view imaging enables for side scattering analysis. The second beam P2 can have different role depending on the experiment (for instance colliding injection).

More details about the spectrometer are given in section 1.4.3. The electron beam profile and divergence were measured with another scintillating screen placed at the end of the chamber by pulling the magnet out of the electron beam path. This additional Lanex screen was also useful to detect X-ray beams emitted during electron acceleration (betatron radiation). For more precise measurements of the X-ray beam profile and spectrum, a X-sensitive CCD camera was used, placed at the end of the chamber with the second Lanex flipped out.

1.4.3 Diagnostics

The laser-accelerated electrons are significantly fluctuating shot-to-shot, thus single-shot diagnostics are crucial to get a good insight into electron and plasma characteristics. The different basic diagnostics used for the experiments presented in this thesis are detailed in the following section. The most specific diagnostics will be presented in the corresponding chapters.

Electron Spectrometer

A major diagnostic in LWFA experiment is the electron spectrometer, allowing to measure the energy distribution of electrons in the beam. It has to be able to measure a large parameter range both in energy (a few MeV to hundreds of MeV) and charge (from a few hundreds of fC to a few nC). The electron spectrometer (ESM) is the combination of a permanent dipole, a scintillating screen and an imaging system.
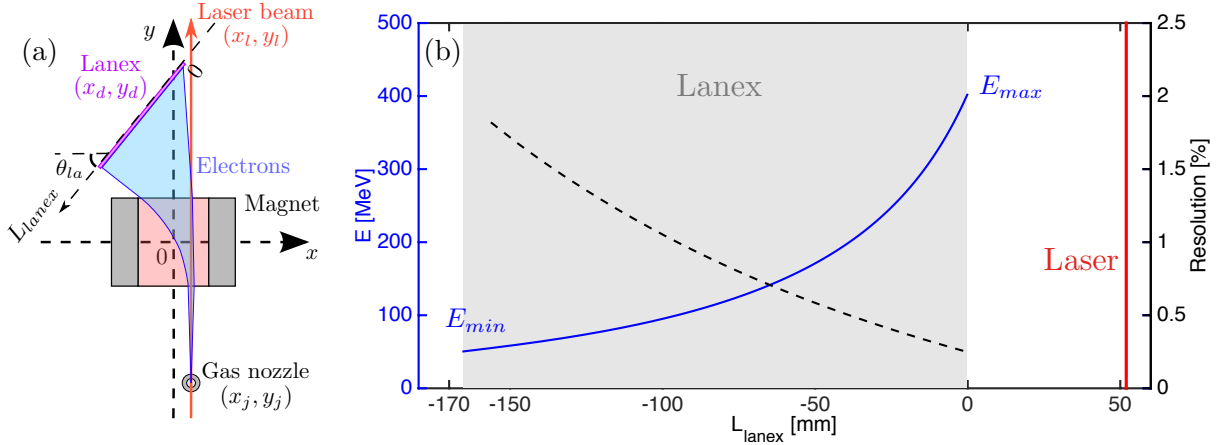
Figure 1.20: (a) Sketch of the electron spectrometer used in the experiments. The electrons are deflected energy dependently by the permanent magnet and detected onto a Lanex screen imaged with a CCD camera. The calibration of the spectrometer is calculated from the position of the electron source (x_j, y_j), the position of the Lanex (x_d, y_d, θ_{la}) and the position of the laser beam (x_l, y_l) corresponding to the non-deflected electron trajectory. All positions are considered in an orthonormal coordinate system with the origin 0 in the center of the magnet. (b) Dispersion curve (in blue) and resolution (dotted black) of the spectrometer function of the position of the electron hitting the Lanex. The grey area represents the Lanex screen, and the red line corresponds to the position of the laser (trajectory of an electron with an infinite energy).

In most of the experiments, a 10-cm long, 1.1 Tesla permanent magnet was used to disperse the electrons depending on their energy (the one seen in Fig. 1.18). Such a magnet was suitable to disperse electrons with energies in the range 30 - 500 MeV. To analyze less energetic electrons, a smaller magnet (2-cm long, 0.76 T) was employed. The magnetic map on the center

plane for both magnets were measured in order to compute the electron trajectories when going throughGlinec et al. [2006a].

Electrons are then dispersed onto a 35-mm large, 170-mm long scintillating screen (Kodak Lanex fine) placed behind the magnet. The screen is covered with a black aluminum foil to prevent stray light from the laser to disturb the measurements. It is imaged on a 16 bit CCD camera (Andor) with a telephoto lens and an interference filter (centered on the emission main wavelength of the Lanex).

A drawing of the electron spectrometer is presented in Fig. 1.20(a). The energy calibration of the ESM is computed considering its geometry defined in the orthonormal coordinate system $(0, x, y)$ with 0 at the center of the magnet. The electron source is considered to be at the center of the nozzle (x_j, y_j). Electrons dispersed by the magnet hit the Lanex at a position L_{lanex} depending on their energy. The Lanex position is defined by its side (x_d, y_d) closer to the laser beam (this point also corresponds to the position $L_{lanex} = 0$, defining the maximum electron energy measurable with the screen) and its angle θ_{la} measured from the x-axis. The position where the laser beam crosses the Lanex plane $(x_l = x_j, y_l)$ is the point where an electron with infinite energy would hit this plane. It serves as reference to set the dispersion curve of the spectrometer (electron energy function of the position on the screen). The dispersion curve of the ESM calculated for a typical configuration is shown in Fig. 1.20(b). The resolution of the spectrometer is estimated considering a mean beam divergence of 3 mrad over the whole spectrum. This configuration allows for the detection of electrons between 50 and 400 MeV, with an energy resolution better than 2% in this range. In the transverse direction, the beam divergence is measured (with a resolution of about 0.5 mrad in this configuration). In order to get a more precise value of the electron beam divergence, an additional Lanex screen placed directly in the beam path is used (by removing the magnet from the beam path). The absence of magnetic dipole plus the increased propagation length allows for more precise divergence measurements (with a resolution below 0.1 mrad).

In order to obtain absolute charge values, we use the calibration of the Kodak Lanex screen done a few years ago by Glinec et al. [2006a]. The global transmission factor (chamber window, interference filter and camera window) as well as the total collection angle are considered to deduce the charge per pixel count on the CCD.

Side view interferometry

Pulsed gas nozzles (Parker Hannifin) opened during a few milliseconds are used as gas targets for LWFA experiments presented in this thesis. The gas density at the nozzle output is modified by varying the backing pressure. The shape of the nozzle (the evolution of the diameter from the entrance hole to the exit) determines the radial gas profile at the nozzle output. Cylindrically shaped nozzles presenting a subsonic gas flow produce Gaussian-like density distributions, whereas supersonic nozzles (accelerating the gas above the speed of sound) create profiles with sharp gradients. In order to characterize the plasma density profile created by the laser propagating in the gas flow, a single-shot interferometry diagnostic is used. The plasma has to be placed in one of the arms of the interferometer. A 30-femtoseconds probe beam (in the presented experiments, the low energy beam P3 is used, as seen in Fig. 1.19) penetrates the plasma and experience different refractive indexes depending on the crossed electron density (the plasma refractive index evolves as $\eta = \sqrt{1 - \frac{n_e}{n_c}}$, as seen in eq. (1.36)). When the probe interferes with a reference beam, the accumulated phase shift leads to a modified fringe spacing depending on the refractive index. A two-dimensional phase map of the plasma is measured, and the corresponding map of the electron plasma density can be obtained using the Abel inversion technique
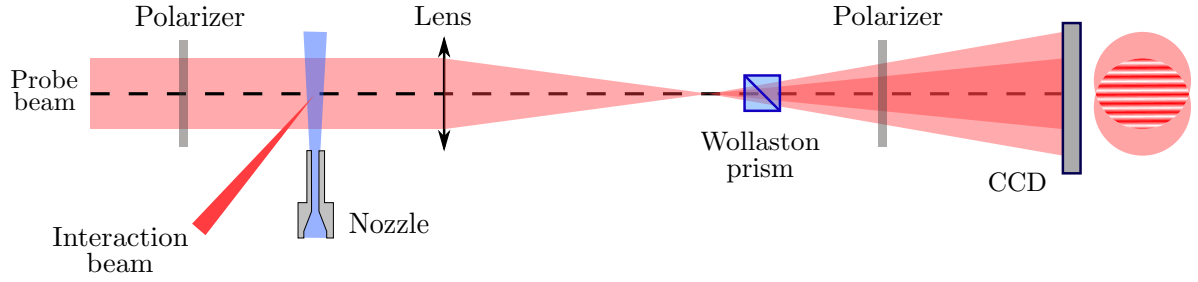
Figure 1.21: Basic scheme of a Nomarski interferometer

with the hypothesis of a cylindrically symmetric plasma column [Kalal and Nugent, 1988].

Although it is common to use a Michelson or a Mach-Zehnder interferometer, we use a No-marski interferometer in our experiments. The Nomarski interferometer employs a Wollaston prism as a beam splitter, the main advantages being the relative simplicity and the absence of alignment problems. The principle scheme of the Nomarski interferometer is shown in Fig. 1.21. The probe beam is polarized at 45 degrees from the vertical with a first polarizer and propagates through the plasma. A converging lens is used after the plasma to image the plasma plane onto the detector with a sufficient magnification to correctly resolve the potentially interesting structures in the density profile (density transitions for instance). The laser goes through a Wollaston prism, splitting it into two beams (respectively with vertical and horizontal polarizations) with an angular separation of a few degrees. A second polarizer, oriented parallel to the first one, is placed after the prism so that the two polarizations are projected onto a 45 degrees axis and can interfere. The two beams interfere in the CCD plane, conjugated with the plasma plane by the lens. Note that the Wollaston prism can be placed before the lens to reduce aberrations on the final image.

The Nomarski interferometer creates two partially overlapped images of the region of interest, thus two images of the object are visible in the CCD plane. The key idea is to place the plasma column on a side of the probe beam, so that a non-perturbed part of the first beam coming out of the Wollaston (the reference) can interfere with the part of the second beam which went through the plasma. The fringe separation in the detector plane is given by $\delta = \lambda_0 D/\alpha d$, with D the distance between the prism and the CCD, α half the separation angle induced by the Wollaston prism and d the distance between the prism and the lens. It can be easily adjusted by moving the Wollaston prism. From the measured interference pattern (an example si shown in Fig. 1.22(a)), the Abel inversion technique allows for the calculation of the two-dimensional plasma density map (presented in Fig. 1.22(b)). Usually the Abel inversion technique can be used only for a perfectly cylindric plasma column, which is not necessary the case. By considering that the plasma is created by the laser, which is axisymmetric by neglecting the optical aberrations, the cylindrical symmetry can be reasonably assumed. Note that the imperfect cylindrical symmetry of the plasma is partly responsible for the non perfect reconstruction of the plasma density.

Specific diagnostics and PIC simulations

The previous diagnostics are common to all LWFA experiments presented. However, some experiments require more advanced diagnostics. For instance, X-ray beams created by laser-
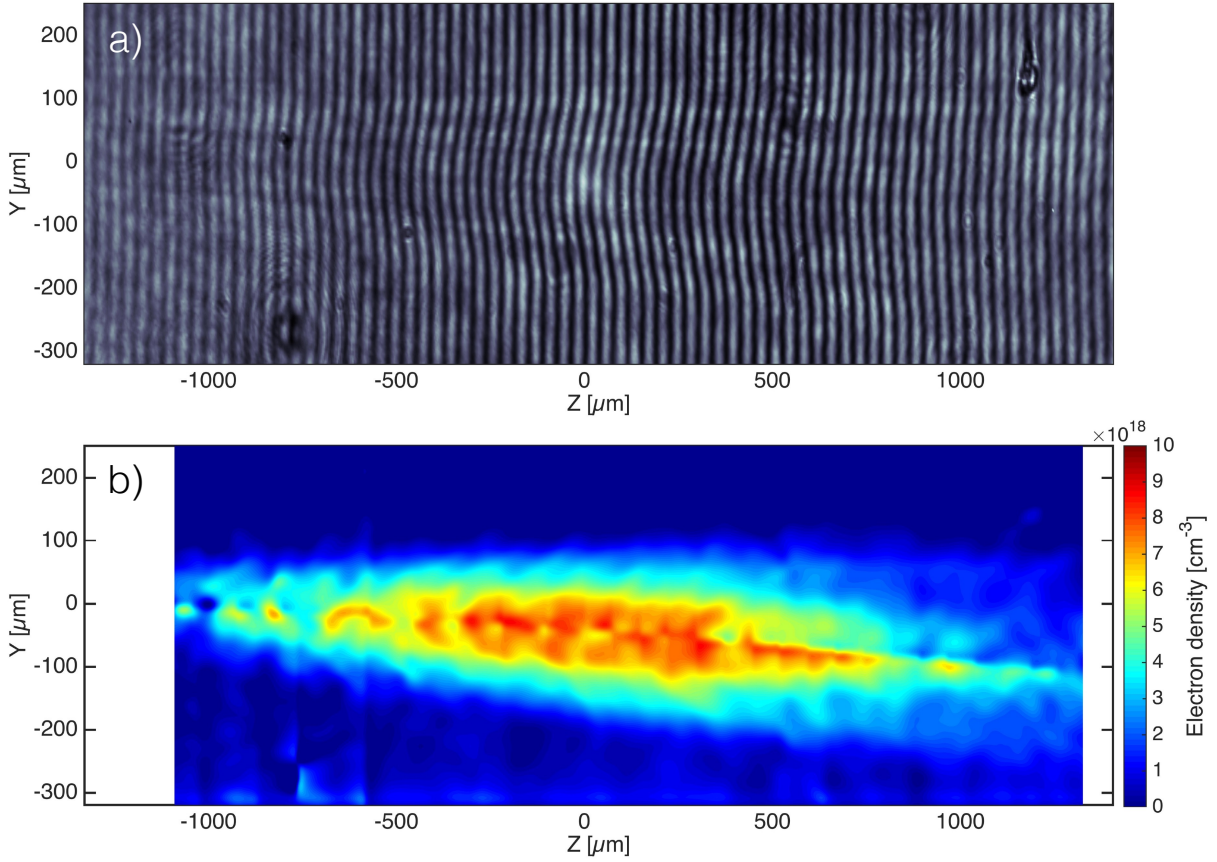
Figure 1.22: (a) Example of a recorded interferogram of a plasma column with a Nomarski interferometer. (b) Corresponding electron density map reconstructed with the Abel inversion technique.

accelerated electrons (via betatron radiation, Thomson scattering or Compton radiation) have to be measured (transversally and spectrally) to characterize the quality of the considered radiation source. Moreover, the precise characterization of transverse quality of the beam (divergence for instance) require more specific diagnostics. These diagnostics are presented in the specific sections when used in an experiment.

In this manuscript, every experimental result is supported with PIC simulations to have more insight in the physical process at stake. Most of these simulations were performed by A. Lifschitz using the quasi-cylindrical 3D PIC code CALDER-CIRC [Lifschitz et al., 2009], which solves Maxwell equations using Fourier decomposition along the poloidal direction with respect to the laser propagation axis. Only the lower modes of the Fourier expansion are calculated, thus strongly reducing the computational time while being sufficient to simulate laser interaction with low density plasma as the physics stays quasi-axisymmetric. The simulation parameters are given in each chapter depending of the performed calculation.

Chapter 2

Controlled injection in sharp density transitions

This chapter presents a detailed study of controlled electron injection in sharp density transitions. In a first part, the principle of electron trapping in a density transition is presented. The second part is focused on the generation of hydrodynamic shocks in a supersonic gas jet: theoretical elements are reminded, followed by a numerical study of shock formation. Finally, the third part shows the experimental study of shock injection of electrons, presenting the influence of the shock position (transverse and vertical) with respect to the nozzle.

Contents

2.1   Injection in a density transition

Figure 2.1: Schematic representation of downramp electron injection in a long (a) and sharp (b) density transition.

Injection of electrons in a density transition is based on the idea to control the bubble expansion. Indeed, the bubble size scales as $4k_p^{-1}\sqrt{a_0} \propto n_e^{-1/2}$, thus the cavity expands as the laser travels through a longitudinally decreasing plasma density.

As explained in section 1.2.6, for a long density downramp, the phase velocity of the back of the bubble is lower than the one of the bubble front, leading to the expansion of the bubble during the propagation, as seen in Fig. 2.1(a). The bubble half-size before downramp is denoted as λ_{p1}. In this region, the wake phase velocity is too large for electrons inside the cavity to be trapped : they slip across the bubble without being injected. Once it enters the downramp, the back of the bubble experiences a larger plasma density than the front, and is thus locally decelerated, leading to an increase of the bubble size during the propagation ($\lambda_{p2} > \lambda_{p1}$). Electrons inside the cavity are then able to stay a longer time in the accelerating gradients, gaining more energy up to the point where they are eventually trapped in the wake.

Long downramp injection of electrons present some drawbacks. Firstly, electrons may enter the bubble and be trapped continuously in the density gradient, leading to rather high charges but also large energy spread. Furthermore, the cavity slows down during the electron bunch acceleration, and the bunch quickly reaches the center of the cavity where the accelerating field switches sign. The energy gain of the electron bunch is then quickly limited by dephasing.

With a sharper density transition, the injection mechanism is slightly different, as seen in Fig. 2.1(b). When crossing the downramp, the cavity half-size λ_p increases steeply, causing electrons just behind the bubble to be instantly loaded in the accelerating phase of the wakefield. The phase velocity of the bubble is frozen in the sharp transition, thus the injection is caused by the sudden plasma wavelength increase rather than the reduced phase velocity in this case. Electron injection in a sharp density transition formed by a shock in a supersonic gas flow (either with a razor blade [Schmid et al., 2010; Buck et al., 2013] or a wire [Burza et al., 2013]) has been experimentally demonstrated in the past few years, producing high quality electron beams. In the following section, a complete study of sharp density transition generation and experimental injection of electrons in such a transition are presented. The topic of the shock position is notably discussed in details.

2.2 Hydrodynamic shock generation in a supersonic gas jet

In order to achieve good experimental conditions for laser-wakefield acceleration (LWFA), a spatially confined gas target is needed so that interaction happens only at the laser focal spot. A gas jet positioned close to the focus of the laser is a common method for producing an underdense plasma for LWFA experiments. Supersonic gas jets are employed to produce reproducible flat-top density profiles with steep upward and downward gradients. Tailoring the gas density profile flowing out of a supersonic nozzle can be very useful to control electron injection and acceleration. The formation of a hydrodynamic shock into a supersonic gas jet in order to create a sharp density transition to assist electron injection is explained in the following section.

2.2.1 Theoretical elements of compressible fluid flow

The thermodynamic properties of an isotropic and homogeneous medium are fully defined by three state variables : temperature T (K), pressure P (Pa) and density ρ (kg.m^{-3}). They depend on each other, and are linked by the equation of state of the medium. For a perfect gas, the well-known equation of state is

$$P = \rho R T \tag{2.1}$$

where R [J.kg^{-1}.K^{-1}] is the specific gas constant. The medium is also defined by its specific heats c_v for constant volume and c_p for constant pressure. The ratio between the specific heats is called the Poisson constant $\kappa = c_p/c_v$, which is 5/3 for perfect monoatomic gases.

A flow of a perfect monoatomic gas is considered in the following. Such a medium is assumed to be ruled by an isentropic transformation of state when flowing through a nozzle. State variables in an isentropic transformation between state 1 and state 2 are linked by :

$$\frac{\rho_2}{\rho_1} = \left(\frac{T_2}{T_1}\right)^{\frac{1}{\kappa-1}} \tag{2.2}$$

$$\frac{P_2}{P_1} = \left(\frac{T_2}{T_1}\right)^{\frac{\kappa}{\kappa-1}} \tag{2.3}$$

$$\frac{P_2}{P_1} = \left(\frac{\rho_2}{\rho_1}\right)^{\kappa}. \tag{2.4}$$

The following equations describe the evolution of state between two spatial positions (1) and (2) of a flowing compressible medium in steady state. It is determined by two thermodynamic state variables and an additional variable which is the flow velocity v.

$$\rho_1 v_1 = \rho_2 v_2 \qquad \text{Mass conservation} \tag{2.5}$$

$$P_1 + \rho_1 v_1^2 = P_2 + \rho_2 v_2^2 \qquad \text{Momentum conservation} \tag{2.6}$$

$$\frac{v_1^2}{2} + E_1 + \frac{P_1}{\rho_1} = \frac{v_2^2}{2} + E_2 + \frac{P_2}{\rho_2} \qquad \text{Energy conservation} \tag{2.7}$$

with E the internal energy of the system, depending only on the temperature T for a perfect gas. From eq. (2.1) and eqs. (2.5) to (2.7), one can derive an implicit relation between P and ρ describing a general evolution of state :

$$\frac{P_2 - P_1}{\rho_2 - \rho_1} = \kappa \frac{P_2 + P_1}{\rho_2 + \rho_1}. \tag{2.8}$$

Evolution of states where large pressure ratios P_2/P_1 are at stake can be described by the previous relation, which is the Rankine-Hugoniot relation, plotted in light blue in Fig. 2.2. For very large pressure ratios, the density ratio tends asymptotically towards $(\kappa+1)/(\kappa-1)$, which is 4 for a perfect monoatomic gas. This means that the density ratio between two positions along a stream line of a gas flow cannot be larger than 4 whatever the pressure ratio and whatever the distance between the two points. The Rankine-Hugoniot equation can be used to describe supersonic compression shocks, such as the one happening in a supersonic nozzle when the gas flow encounters the walls.
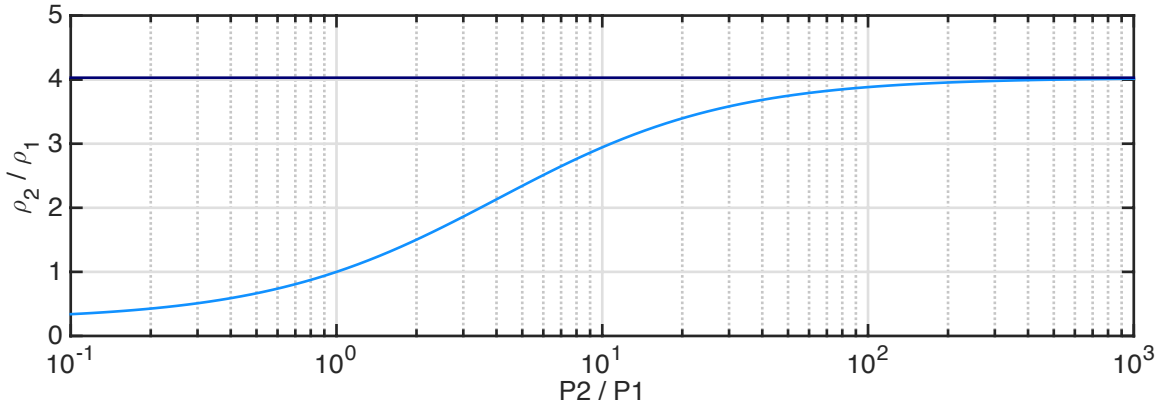
Figure 2.2: Rankine-Hugoniot curve (light blue) for a perfect gas with constant specific heat. It tends asymptotically towards $(\kappa+1)/(\kappa-1)$ (dark blue).

The sound velocity in a compressible perfect gas is defined as :

$$c = \sqrt{\kappa R T} = \sqrt{c_p(\kappa-1)T}. \tag{2.9}$$

The Mach number of a gas flow is defined as the ratio between the flow velocity and the sound velocity :

$$M = \frac{v}{c}. \tag{2.10}$$

For a subsonic gas flow ($M < 1$) encountering an obstacle in its path, the flow can smoothly adapt well ahead of the position of the obstacle because the shock information (going at the speed of sound) is able to travel faster than the flow velocity. This leads to a smooth transition between the unperturbed upstream flow and the adapted downstream flow. For a supersonic gas flow however ($M \geq 1$), only strong perturbations can travel fast enough upstream, eventually forming a steady-state shock front. From eqs. (2.5) to (2.7), one can derive the relations for an evolution of state in a shock front for a perfect gas, with the state (1) before the shock and the
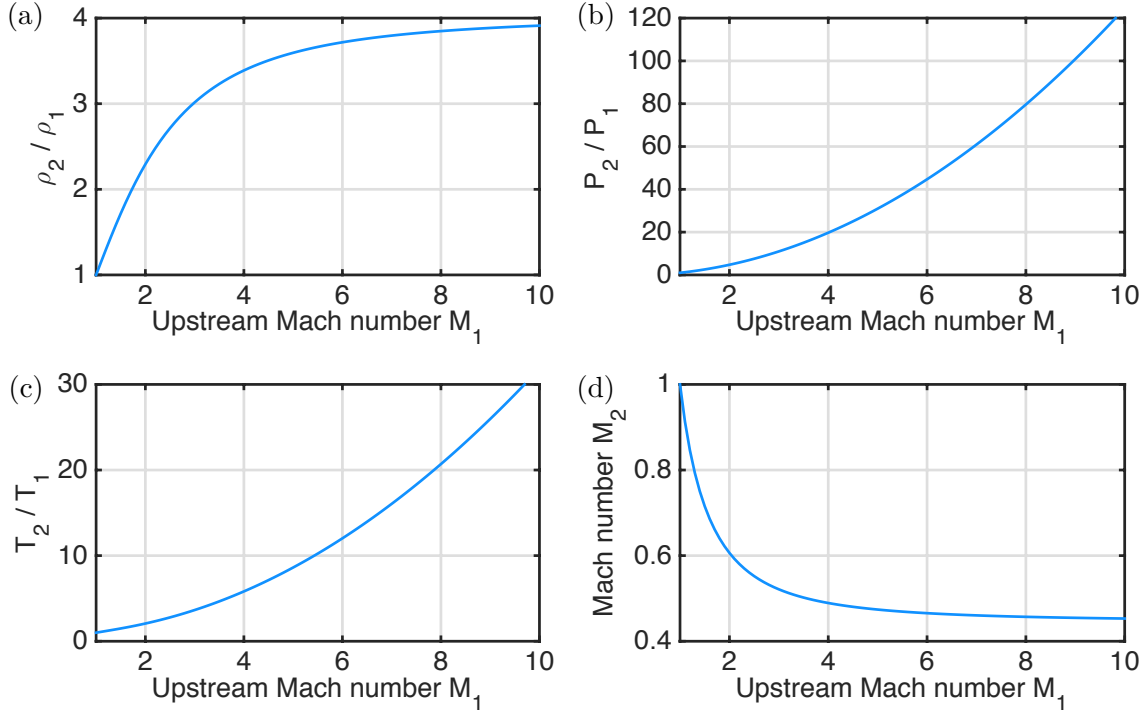
Figure 2.3: Change of variables ρ (a), P (b), T (c) and M (d) in a normal shock in a perfect gas (Helium) as a function of the initial Mach number of the flow M_1.

state (2) after [Von Mises et al., 2004]:

$$\frac{\rho_2}{\rho_1} = \frac{v_1}{v_2} = \frac{1}{1 - \frac{2}{\kappa+1}\left(1 - \frac{1}{M_1^2}\right)} \tag{2.11}$$

$$\frac{P_2}{P_1} = 1 + \frac{2\kappa}{\kappa+1}(M_1^2 - 1) \tag{2.12}$$

$$\frac{T_2}{T_1} = \frac{1}{M_1^2}\left(1 + \frac{2\kappa}{\kappa+1}(M_1^2 - 1)\right)\left(1 + \frac{\kappa-1}{\kappa+1}(M_1^2 - 1)\right) \tag{2.13}$$

$$M_2 = \sqrt{\frac{1 + \frac{\kappa-1}{\kappa+1}(M_1^2 - 1)}{1 + \frac{2\kappa}{\kappa+1}(M_1^2 - 1)}}. \tag{2.14}$$

As can be seen, all the variables changes in a shock depend only on the initial Mach number M_1 of the flow before the shock, and are only valid for supersonic flows ($M_1 \geq 1$). These relations are plotted in Fig. 2.3 for Helium. It shows that the density ratio (Fig. 2.3(a)) converges towards an asymptotic value of 4 (maximum value reachable for a Rankine-Hugoniot transformation for a monoatomic gas) while the pressure (Fig. 2.3(b)) and temperature (Fig. 2.3(c)) ratios grow consistently. Fig. 2.3(d) shows that the gas flow is always subsonic after the shock, with M_2 decreasing as M_1 increase. In summary, for high initial Mach number, the flow is compressed, heated up and decelerated.

In order to form a nice density transition, the gas flow Mach number must be high enough at the output of a nozzle without any obstacle. In the following is studied how to form such a flow with a supersonic nozzle by considering a continuous gas flow with no discontinuous shock occuring. The subsequent analysis of the gas flow is quasi-1D along the flow direction, as the
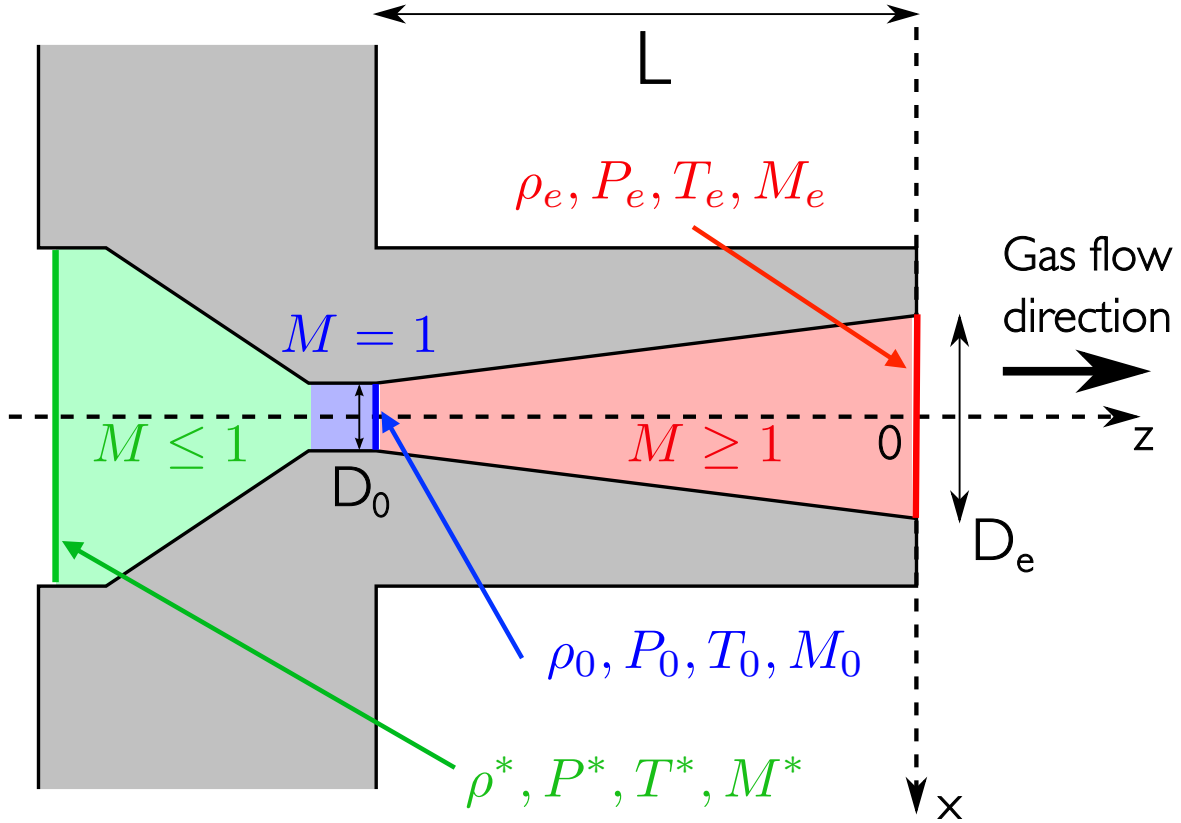
Figure 2.4: Schematic of a converging - diverging supersonic nozzle.

nozzle walls bound the gas flow. A schematic of a simple nozzle is drawn in Fig. 2.4, with D_0 the throat diameter, D_e the exit diameter and L the distance between throat and exit.

The governing equations of the gas flow can be derived by considering the cross section of the nozzle S normal to the flow propagation axis z. In 1D, all the describing variables (ρ, P, T, M) are constant over each vertical section S. From eqs. (2.2) to (2.4), one obtain the following differential equations for a continuous, isentropic flow in a nozzle :

$$\frac{d\rho}{\rho} + \frac{dv}{v} + \frac{dS}{S} = 0 \qquad \text{Mass continuity equation} \qquad (2.15)$$

$$-SdP = (S\rho v)dv \qquad \text{Momentum continuity} \qquad (2.16)$$

$$\frac{dP}{d\rho} = c^2 \qquad \text{Isentropic transformation} \qquad (2.17)$$

$$\frac{dT}{T} = -(\kappa - 1)M^2 \frac{dv}{v} \qquad \text{Energy conservation.} \qquad (2.18)$$

From eqs. (2.16) and (2.17), one can derive the relation :

$$\frac{d\rho}{\rho} = -M^2 \frac{dv}{v}. \qquad (2.19)$$

Thus, for Mach numbers smaller than one, the relative variation of density is smaller than the relative variation of velocity. A flow with a very low Mach number is then almost incompressible. For high Mach number (hypersonic flow), the maximum velocity is almost constant (with

the density) and density, pressure, and temperature vary strongly. By combining eqs. (2.15) and (2.19), the relation between Mach number variation and the flow cross section variation is given by :

$$\frac{dS}{S} = (M^2 - 1)\frac{dM}{M}. \tag{2.20}$$

The flow kinetic in the nozzle is ruled by this equation. For a subsonic flow ($M < 1$), the flow velocity increases with shrinking cross section and for supersonic flows it increases with growing cross section. This effect is exploited in converging-diverging nozzles (as depicted in Fig. 2.4) in order to obtain millimeter scale supersonic gas flows.

First, in the converging section (in green in Fig. 2.4), the gas flow leaves the reservoir with the parameters (ρ^*, P^*, T^*, M^*) and accelerates up to M close to 1, which is reached in the throat (in blue). When the flow cross section reaches a minimum, the flow changes from subsonic to supersonic : it is the so-called *critical plane*, for which the flow parameters are ($\rho_0, P_0, T_0, M_0 \sim 1$). Then, the flow can expand further in the diverging section of the nozzle (in red in Fig. 2.4) and thereby acquires supersonic velocity $M > 1$. The length L over which the gas flow accelerates is directly linked to the surface ratio S/S_0. The final Mach number M of the flow accelerated up to the surface S from the critical surface S_0 is given by :

$$\frac{S}{S_0} = \frac{1}{M}\left(\frac{2 + (\kappa - 1)M^2}{\kappa + 1}\right)^{\frac{\kappa+1}{2(\kappa-1)}}. \tag{2.21}$$

The Mach number at the exit of a supersonic gas nozzle thus depend only on the surface ratio between the exit surface $S_e = \pi D_e^2/4$ and the throat surface $S_0 = \pi D_0^2/4$. Figure 2.5 shows the evolution of M_{exit} function of the surface ratio for a converging - diverging nozzle. Note that typical supersonic nozzles can easily have surface ratios up to $S_e/S_0 = 25$, leading to high Mach numbers, up to $M_{exit} = 7$.
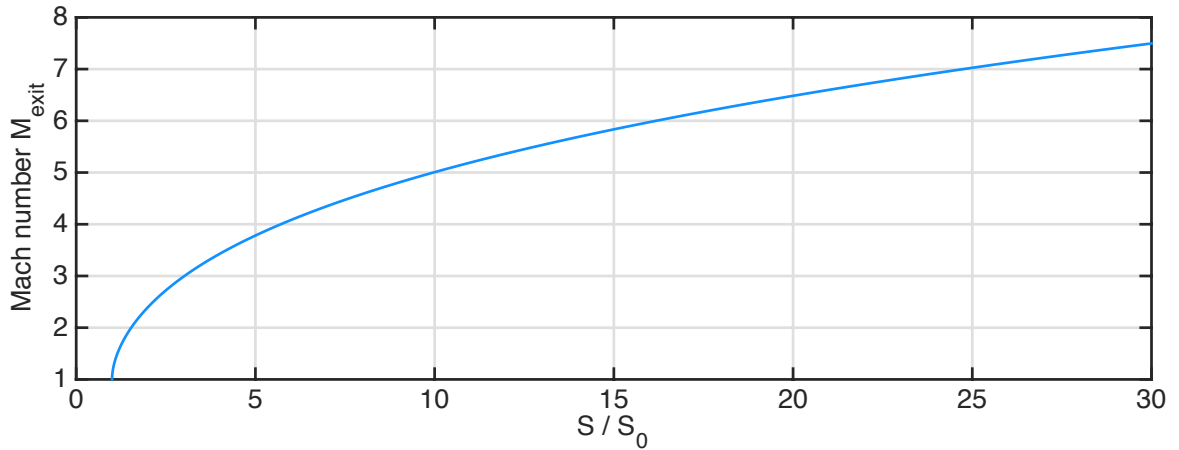
Figure 2.5: Mach number at the exit of a supersonic converging-diverging nozzle function of the surface ratio S/S_0, with κ of a monoatomic perfect gas.

The density and pressure of the gas at the nozzle exit depends on the gas parameters (ρ^*, P^*, T^*, M^*) in the reservoir and on the exit Mach number as :

$$\rho = \rho^* \left(1 + \frac{(\kappa - 1)M^2}{2} \right)^{\frac{-1}{\kappa - 1}} \tag{2.22}$$

$$P = P^* \left(1 + \frac{(\kappa - 1)M^2}{2} \right)^{\frac{-\kappa}{\kappa - 1}} . \tag{2.23}$$

These quantities are shown in Fig. 2.6 as a function of the surface ratio S/S_0, with S the surface in the diverging region of the nozzle where the density is calculated. The larger the surface ratio, the more supersonic the gas flow, and the lower the density and pressure. The pressure at the nozzle exit for a surface ratio $S/S_0 = 20$ (corresponding to an exit Mach number $M_{exit} = 6.5$) drops by almost three orders of magnitude (Fig. 2.6(b)) compare to the throat pressure.
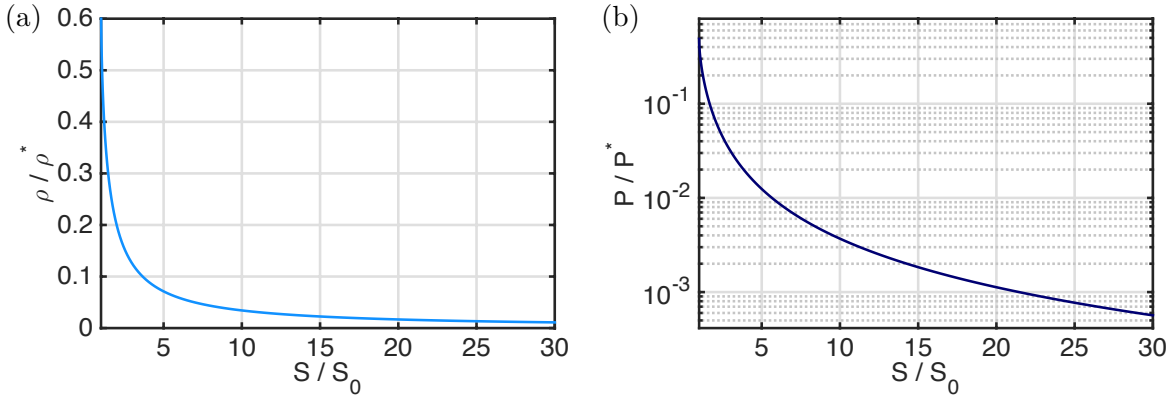
Figure 2.6: Mach number at the exit of a supersonic converging-diverging nozzle function of the surface ratio S/S_0.

The nozzle geometry (through the surface ratio S_{exit}/S_0) directly fixes the Mach number of the gas flowing out of the nozzle. The relation between the pressure and density in the reservoir and the output pressure and density depends only on this geometry. Thus, by tuning the backing pressure in the reservoir, one can change the output gas density with a well-known factor linking the two quantities, depending only on the nozzle geometry. Using a strongly supersonic nozzle allows for the generation of high velocity gas flow with sharp gradients (as the gas is highly collimated in the flow direction) but needs a strong backing pressure (a few dozens of bar) to reach typical pressure we need in LWFA experiments (a few hundreds of mbar, corresponding to a gas neutral density in the range $10^{18} - 10^{19}$ cm^{-3}).

To conclude, in order to generate strong shocks to get sharp density gradients, the gas flow Mach number must be high enough to get maximum compression of the gas, thus the use of highly supersonic gas nozzle (with a large surface ratio S_{exit}/S_0) is desirable.

2.2.2 Computational Fluid Dynamics of a supersonic gas flow

In order to correctly design a working setup to generate a sharp density transition in a supersonic gas jet, the flow formation was studied by resolving the Navier-Stokes equations. To this end, I used the commercial code ANSYS FLUENT to numerically predict the gas flow parameters.
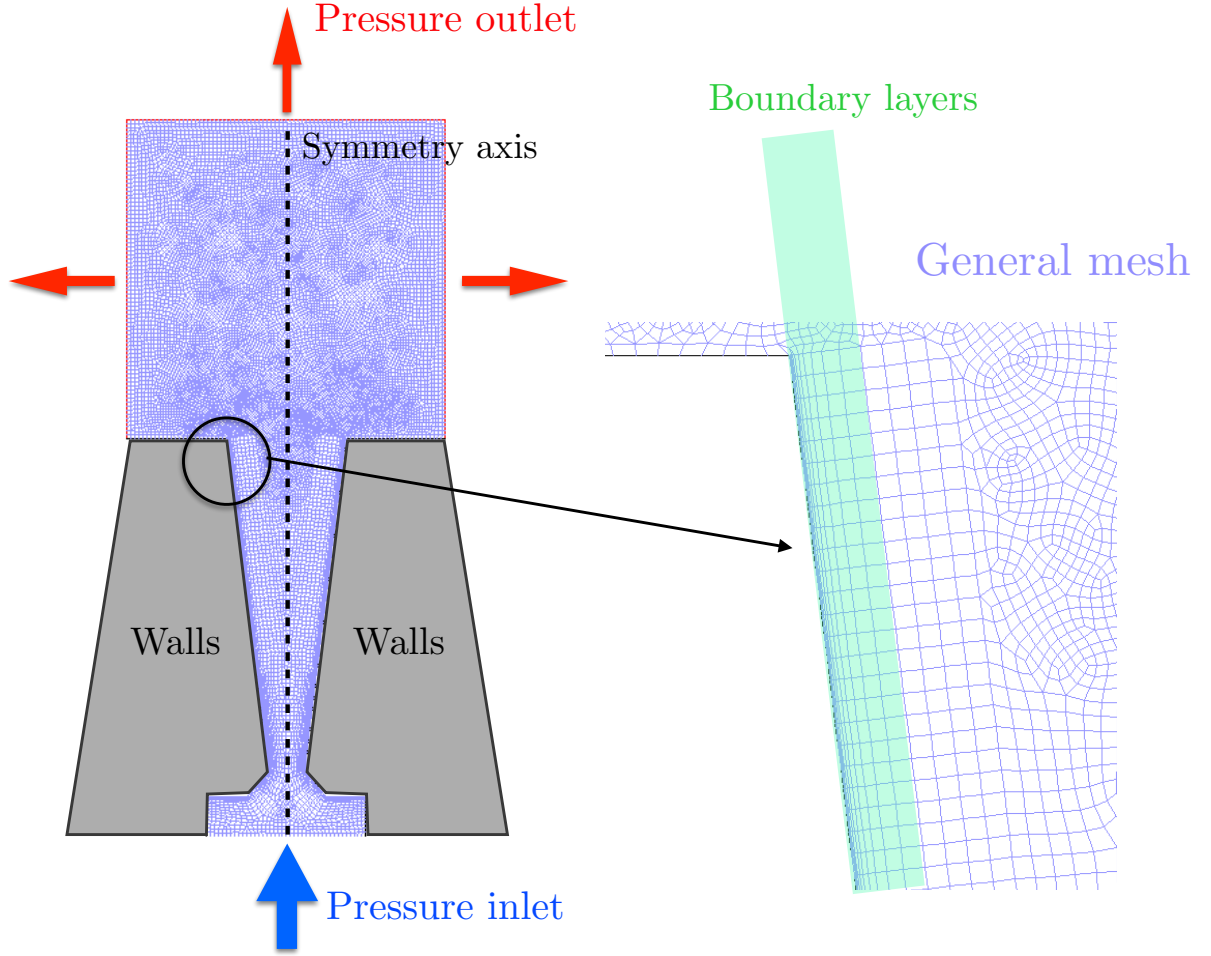
Figure 2.7: (Left) Typical mesh used in the 2D-planar simulations. The gas enters the pressure inlet (blue), propagates in the nozzle (dark grey, defined as walls in the simulation) along the axis and extends in vacuum through the pressure outlets (red). (Right) Magnified portion of the mesh along the walls. The radial mesh resolution is increased towards the wall by adding twenty boundary layers (light green).

In the following section, the computed fluid is helium (which is assumed to be a perfect gas) in a converging - diverging nozzle (as schemed in Fig. 2.4) with the following geometrical parameters : $D_0 = 0.5$ mm, $D_e = 1.5$ mm and $L = 4$ mm. From the previous section, the corresponding exit Mach number should be analytically $M_e = 4.8$, and the factor linking the reservoir density to the output density is 0.4.

The numerical problem is set up in 2D-planar geometry, as shown in Fig. 2.7. The mesh is generated with the built-in generator and is refined up to a point where the solution is not mesh-dependent anymore. Full 3D simulations and 2D-axisymmetric simulations are also performed and it is verified that the axisymmetric or 2D-planar hypothesis give identical results in this case. The near-wall meshing is of major significance for the quality of Computational Fluid Dynamics (CFD) numerical solutions, because the walls are the main source of flow turbulence. Thus, the boundary layers must be sufficiently resolved for the simulation turbulence models to correctly compute the flow behavior close to the walls. The boundary layers can be seen in the

(a)

(b)
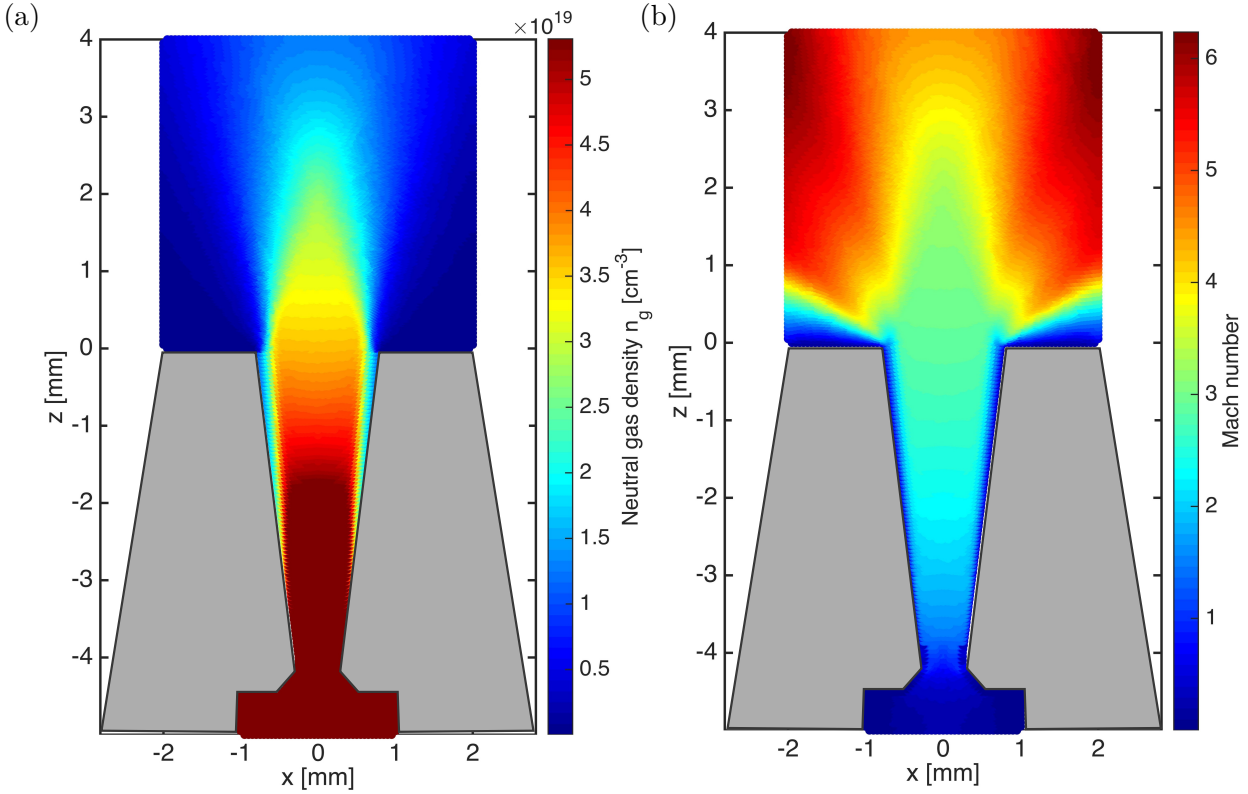
Figure 2.8: 2D gas density (a) and Mach number (b) maps of the simulated gas flow.

zoomed mesh presented in Fig. 2.7.

The boundary conditions are defined as the following : a pressure inlet on the reservoir side ($P^* = 11$ bar) and a pressure outlet outside the nozzle exit ($P_{vacuum} \sim 0$ bar). It is also considered that the gas does not exchange any energy with the walls. After the gas flow exits the supersonic nozzle, it emanates into an extremely low pressure medium (as perfect vacuum cannot be correctly simulated) and leaves the simulation box through the pressure outlets. The simulation is run up to it converges on a steady-state with a high enough stability. In order to achieve fast and stable convergence, the simulation is initialized with the hybrid initialization function of FLUENT, which defines an initial state which approaches the final solution, though with extremely poor accuracy.

Figure 2.8 shows the 2D maps of the neutral gas density n_g (a) and the Mach number (b) of the simulated gas flow. The gas expands in the diverging part of the nozzle, with the flow being guided by the walls into the forward direction. The gas flow is well confined with a rather large kinetic energy in the forward direction when exiting the nozzle. Thus, the transverse acceleration of the gas is much smaller than the forward velocity when leaving the nozzle, leading to low divergence gas jet with rather sharp density gradients. Far away from the exit (a few millimeters), the divergence is approximately the same. Indeed, due to the low pressure at the nozzle exit, the gas flow is essentially collisionless and the particles follow almost ballistic trajectories, roughly maintaining the divergence of the jet. The faster particles are those at the edge of the jet forming the density gradients, since they can expand freely in vacuum without being perturbed by the gas flow pressure (as seen in Fig. 2.8(b)). Indeed, in the center of the flow, the pressure experienced by a fluid element is the same whatever the direction, so the

velocity is constant. On the flow edges however, the pressure is weaker on the sides and the fluid is accelerated away from the center, leading to the formation of density gradients (which are larger when getting away from the nozzle as the transverse velocity becomes larger).
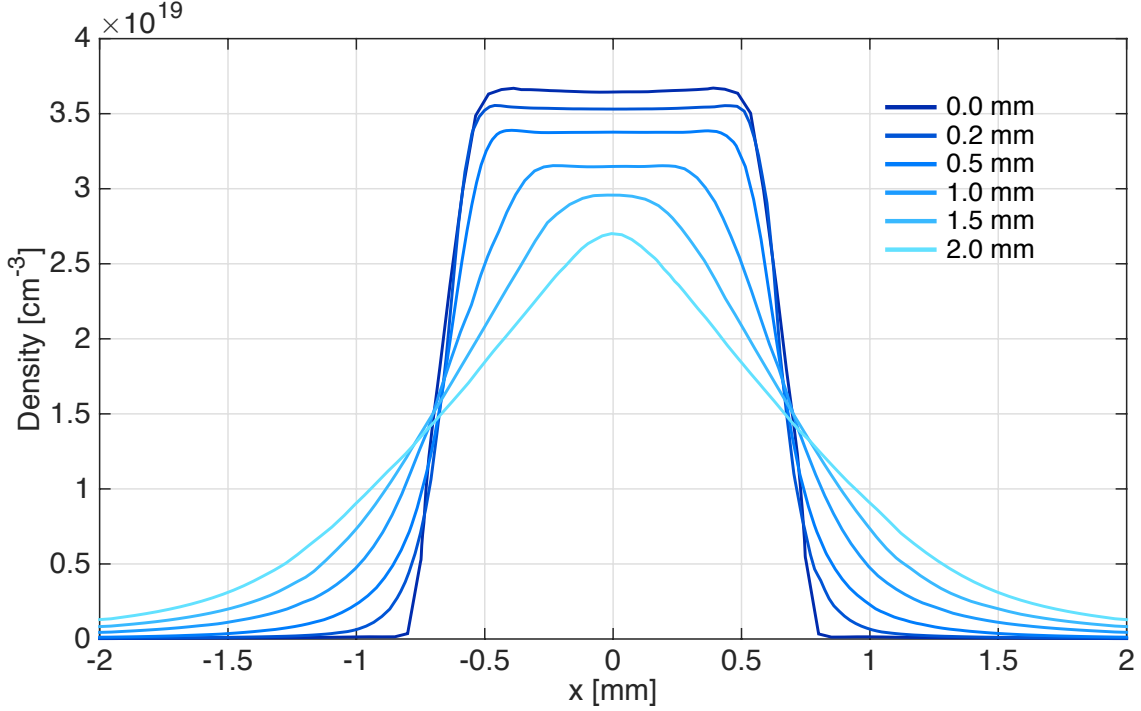
Figure 2.9: Transverse density profiles for different heights z from the nozzle exit.

The transverse density profiles depend on the height after the nozzle exit, as shown in Fig. 2.9. Directly at the nozzle exit ($z = 0$ mm, darker blue), the density profile consists in a 1 mm long plateau at $n_g = 3.6 \times 10^{19}$ cm^{-3} with 250 μm long gradients. It keeps roughly the same shape up to $z = 0.5$ mm. Higher than that, the plateau shape starts to transform into a more parabolic shape with smoother gradients and a lower peak density. At $z = 1.5$ mm, the peak density decreases down to $n_g = 3 \times 10^{19}$ cm^{-3} with 2 mm long gradients. Note that these long gradients consist of particles with much higher velocity than the center of the gas jet (as seen in Fig. 2.8(b)) : maximum Mach number is found on the gradients. The peak density evolves slowly with the height, as well as the FWHM diameter of the flow (which is observed to be roughly equal to 1.5 mm from $z = 0$ mm up to $z = 2$ mm).

Figure 2.10 shows the Mach number profiles for the same heights. As explained, the gas flow velocity is much higher on the sides than in the center of the jet once the gas has expanded. Close to the exit, the jet is still very collimated and cannot expand yet, thus the velocity is maximum at the center. Higher from the nozzle output however, the gas flow is able to expand freely in vacuum and can accelerate further, especially on its sides where no gas pressure restrain it. At $z = 2$ mm, the particles in the jet gradients can reach Mach numbers up to 6, forming a very supersonic flow in these regions. Neutral density and Mach number line-outs at this height are shown in Fig. 2.11(a), while Fig. 2.11(b) represents pressure and temperature line-outs. The peak pressure of the gas flow (0.24 bar) is much lower than the backing pressure in the reservoir (11 bar). Indeed, the gas expanded both in the diverging section of the nozzle and in vacuum. The fast expansion of the gas also lead to a strong cooling down to roughly 60 K.
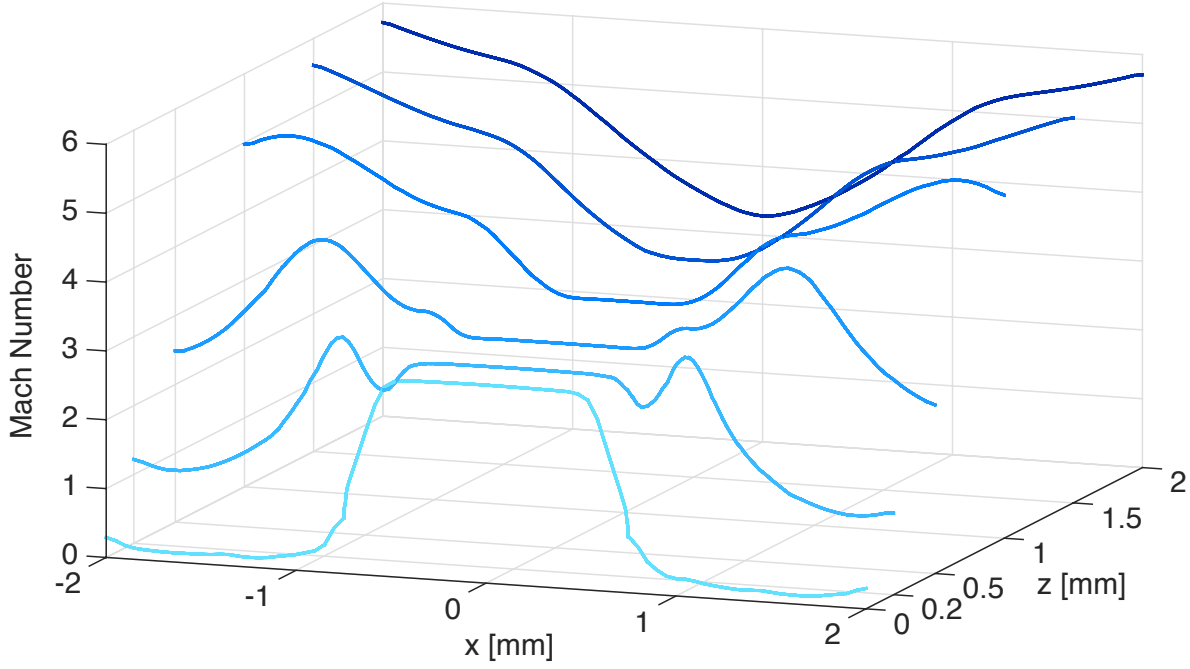
Figure 2.10: Mach number transverse profiles for different heights z from the nozzle exit.
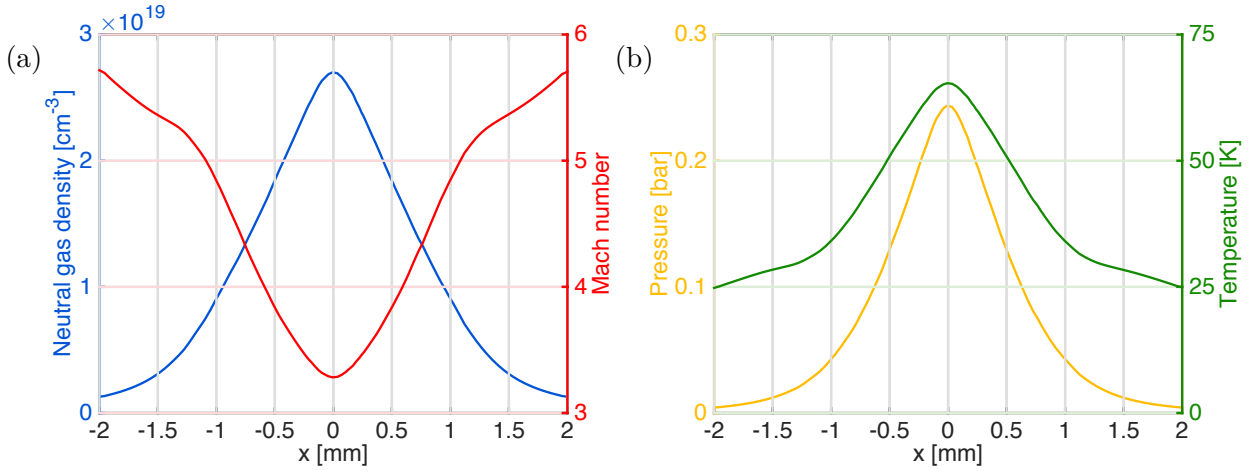
Figure 2.11: (a) Density and Mach number transverse line-outs of the gas flow at $z = 2$ mm. (b) Pressure and temperature transverse line-outs of the gas flow at $z = 2$ mm.

In order to understand the evolution of the gas flow parameters from the reservoir to the vacuum chamber, Fig. 2.12 represents the neutral gas density and Mach number (a), the pressure and temperature (b) along the flow propagation axis z (for $x = 0$ mm, in the center of the jet). In the converging region of the nozzle (in green), $M < 1$ and the jet is subsonic, with the pressure and temperature dropping quickly. In the diverging section (in red), the jet becomes more and more supersonic while the density and pressure decrease slows down. In the exit plane, Mach number is around 3, forming a well-collimated supersonic gas jet. The pressure is much lower than at the nozzle throat (0.3 bar compared to 5 bar, divided by a factor of 15) for a not so different density (which is only divided by 3), as well as the temperature (around 75 K at the
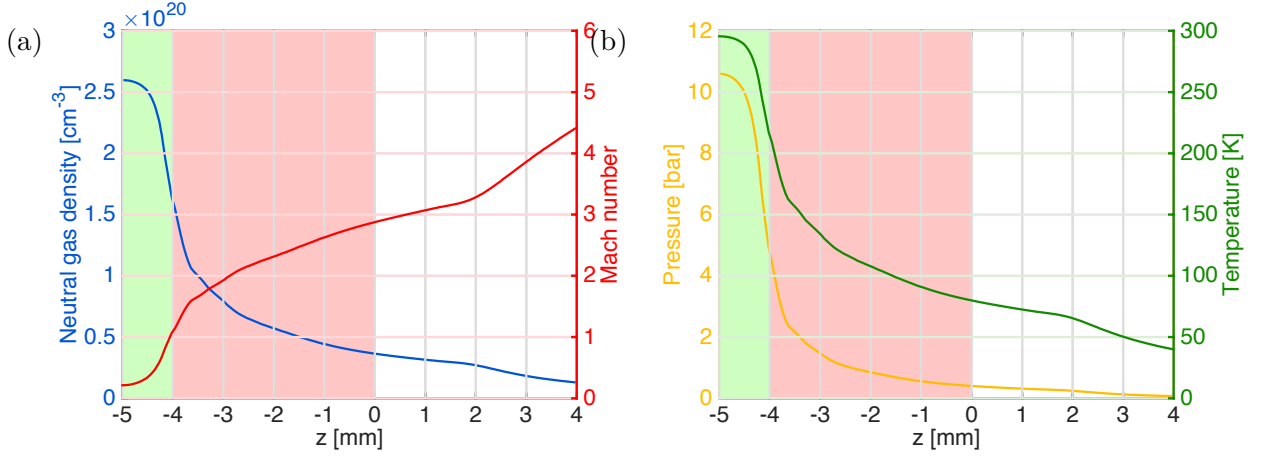
Figure 2.12: (a) Density and Mach number line-outs along the the gas flow direction at $x = 0$ mm. (b) Pressure and temperature line-outs along the the gas flow direction at $x = 0$ mm. The green (resp. red) area represents the converging (resp. diverging) section of the nozzle.

exit compared to 300 K in the reservoir). Since the main cause for gas transversal spread is the pressure, such a supersonic gas jet with low exit pressure allows for the flow to maintain its divergence over a significantly large propagation distance while expanding in vacuum.

2.2.3 Simulations of shock front generation in a supersonic gas jet

Electron injection in a density transition requires the generation of sharp shock fronts. The supersonic properties of the gas flow can be used in order to easily obtain shocks by placing a solid obstacle in the way of the gas jet (up to now, these were the nozzle walls but can also be another object, for instance a sharp edge of a blade). This idea was mainly developed in [Schmid et al., 2010; Buck et al., 2013], and is studied in details in the current section. It has been explained in section 2.2.1 how shock fronts are generated in supersonic gas flows when encountering a solid obstacle. It was determined that the relation of gas parameters before and after the shock front only depend on the Mach number of the unperturbed gas flow (as seen in Fig. 2.3).

The same nozzle presented in section 2.2.2 is considered in 2D-planar geometry, with a perfectly rectangular blade placed in the path of the gas jet. The position of the right-down corner of the blade (x_{blade}, z_{blade}) defines its placement in the jet. The mesh is refined from this point to get a better resolution around the blade where the shock is formed, as shown in Fig. 2.13. The minimum cell size is 1 μm at the vicinity of the blade corner, with the mesh inflating slowly up to 50 μm cell size where the flow resolution is less critical. The boundary conditions and system initialization are the same than in the simulation presented in section 2.2.2.

The blade is first placed at $(x_{blade} = -1$ mm, $z_{blade} = 1.3$ mm). The simulated gas density map is shown in Fig. 2.14(a), with the generated shock front clearly visible when the flow encounters the blade. The sharp density transition can easily be observed, forming an angle with the flow direction of $\theta_{shock} = 15°$. Line-outs of gas density and Mach number at $z = 3$ mm are plotted in Fig. 2.14(b). The density ratio across the density transition is $n_1/n_2 = 1.52$ with n_1 (resp. n_2) the gas density before the shock (resp. after the shock). The zone denoted as "after" the shock corresponds to the unperturbed region of the gas jet, while "before" refers to the gas zone the laser encounters prior to cross the shock front (with the laser propagating
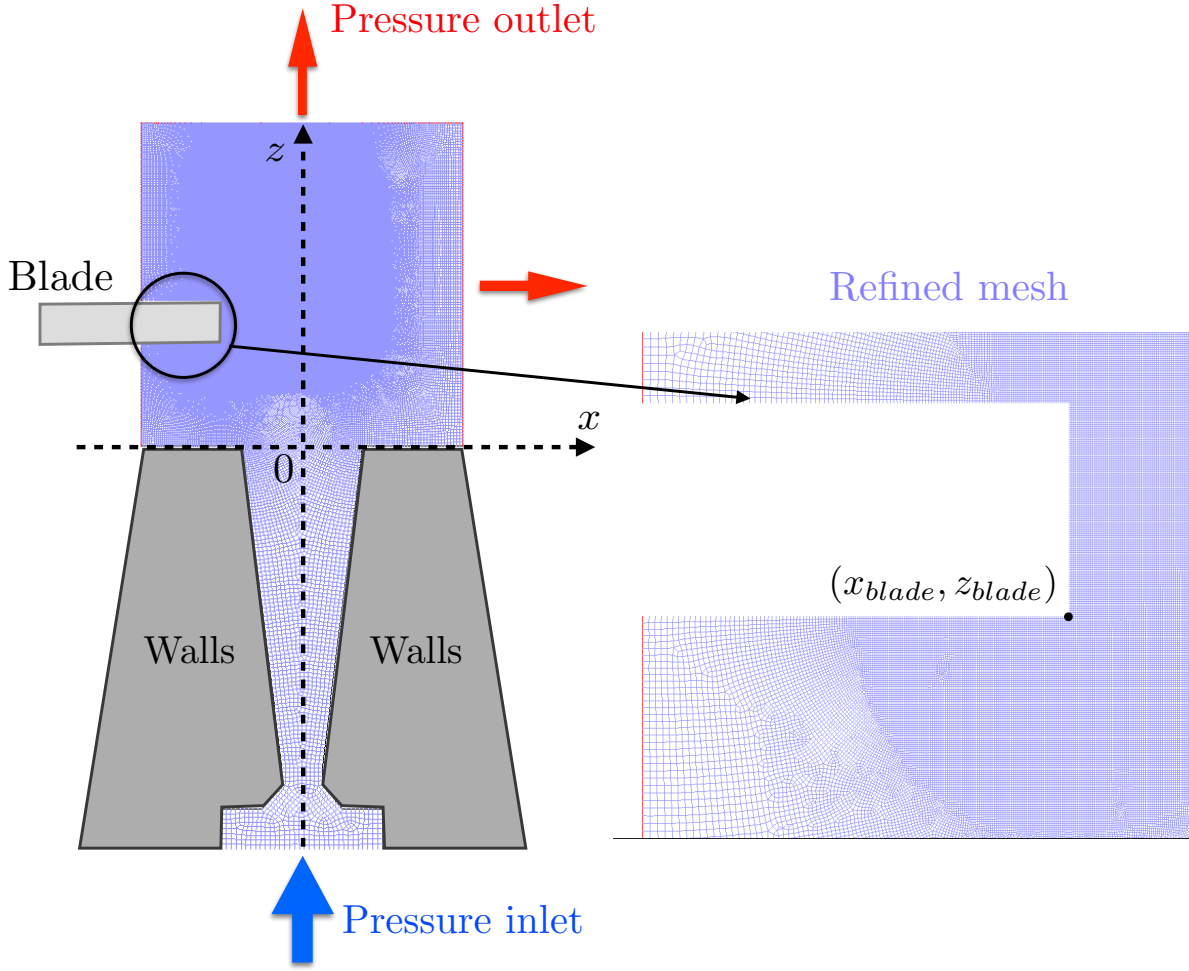
Figure 2.13: (Left) Typical mesh used in the 2D-planar simulations of shock front generation. The position of the blade is referred as (x_{blade}, z_{blade}), the coordinates of the right-down corner. (Right) Refined mesh in the vicinity of the blade. The cell size decreases towards the blade down to 1 μm.

from the left in Fig. 2.14(a)). According to eq. (2.11), and taking into account the shock angle with the jet direction θ_{shock}, one can derive [Schmid et al., 2010] :

$$\frac{n_1}{n_2} = 1 - \frac{2}{\kappa + 1}\left(1 - \frac{1}{(M_1 \sin(\theta_{shock}))^2}\right) \tag{2.24}$$

with M_1 the initial Mach number of the gas flow. From the line-outs, $M_1 = 3$ and $\theta_{shock} = 15°$, then one can derive $n_1/n_2 = 1.50$ which is in good agreement with the computed solution. Figure 2.14(c) shows that the pressure and temperature also drop after the shock front, with $P_1/P_2 = 2.15$ and $T_1/T_2 = 1.41$. From eqs. (2.12) and (2.13), one can compute $P_1/P_2 = 2.19$ and $T_1/T_2 = 1.47$. The simulation gives very similar relations between parameters before and after the shock than predicted by the theory explained in section 2.2.1, validating the theoretical model correctness.

The shock front can be described with two useful parameters for electron injection experiments : the density ratio n_1/n_2 and the transition width e_{shock}. This width is defined between
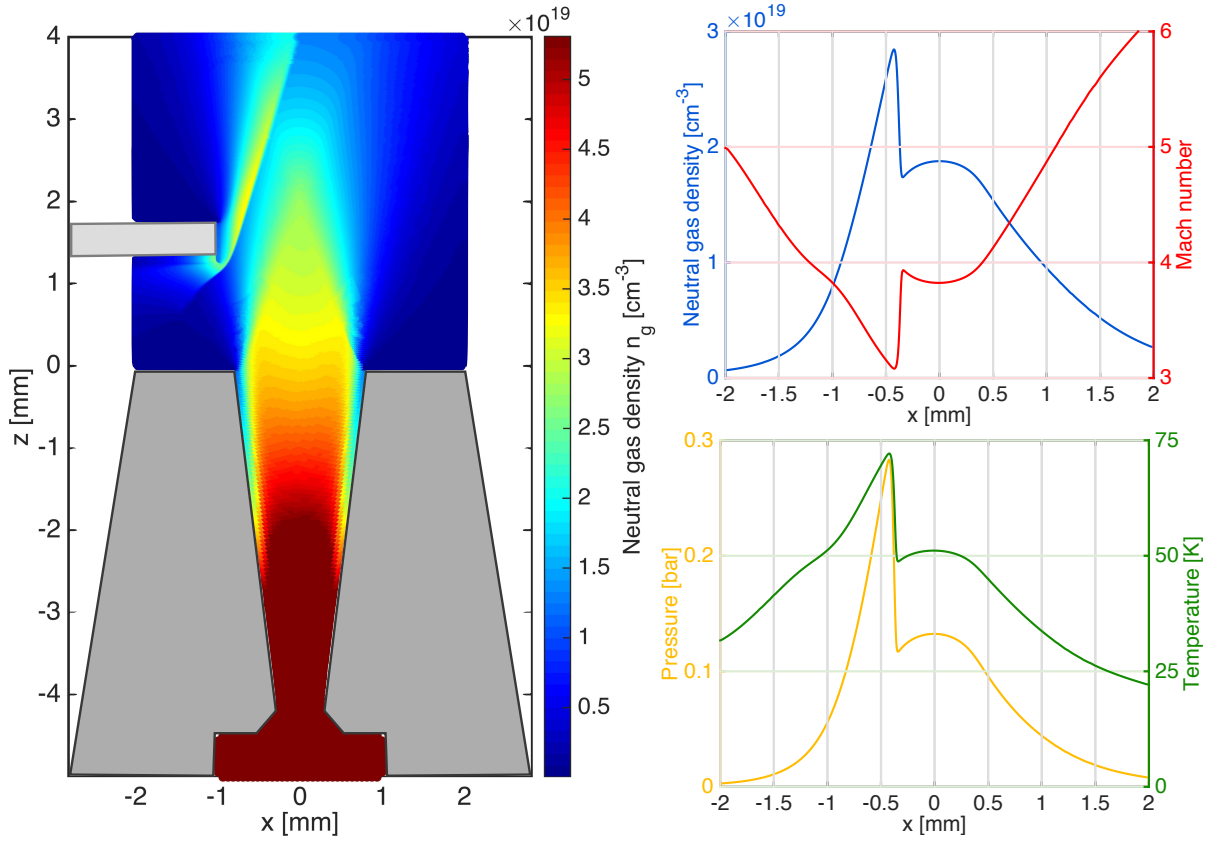
Figure 2.14: (a) 2D gas density map of the simulated shock generation in a supersonic gas flow. (b) Density and Mach number transverse line-outs of the gas flow at $z = 3$ mm. (c) Pressure and temperature transverse line-outs of the gas flow at $z = 3$ mm.
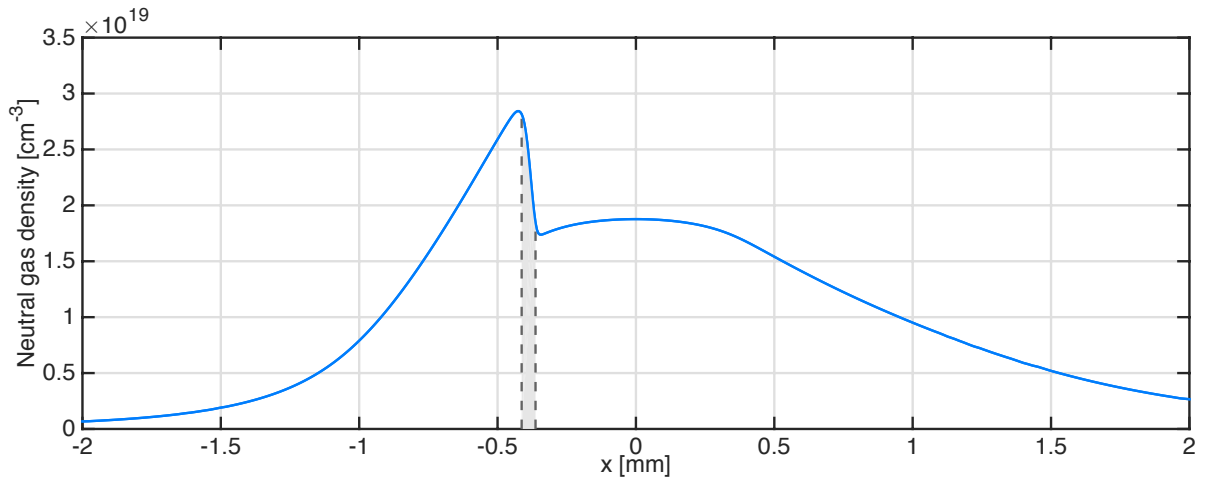
Figure 2.15: Density transverse line-out of the gas flow at $z = 3$ mm. The grey area represents the width of the shock e_{shock} at that height.

$0.95n_1$ and $1.05n_2$. By taking a closer look at the density line-out, these two quantities can be finely estimated (see Fig. 2.15) at $z = 3$ mm, which is a typical height at which the laser was fired in shock injection experiments : $n_1/n_2 = 1.52$ and $e_{shock} = 55$ μm. Note that the shock width rapidly drops down to around 10 μm closer to the blade. However, in the experiments presented in this manuscript, the laser was fired about 1 mm from the blade because of mechanical constraints due to the blade mount. Hence, all the following shock parameters scan are considered at height of 1 mm from the blade to efficiently compare with the experimental results.
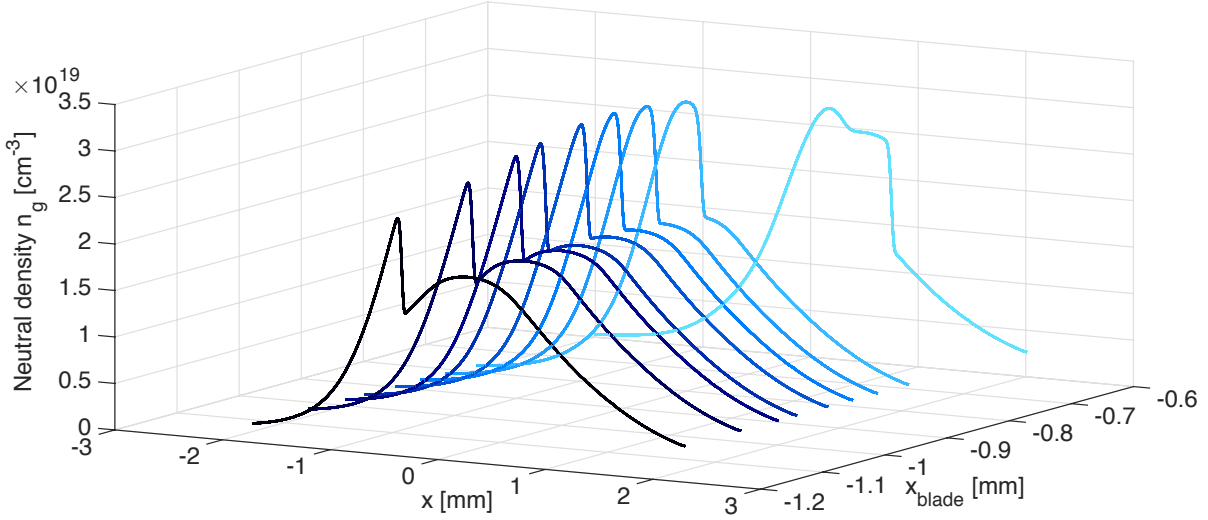
Figure 2.16: Density transverse line-outs at $z = 3$ mm for different transverse positions of the blade x_{blade} measured from the center of the gas jet ($x = 0$ mm).
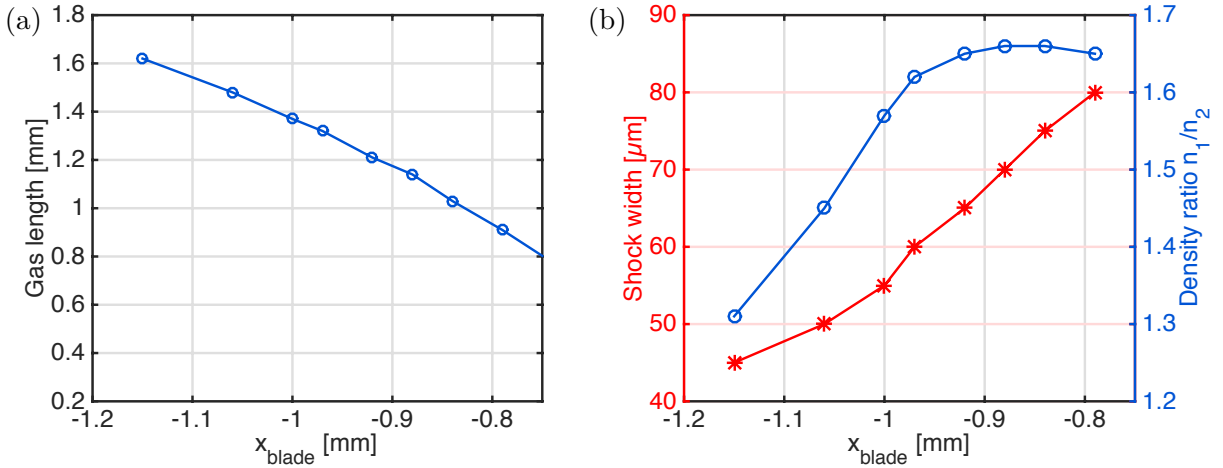
Figure 2.17: (a) Remaining gas length (from the shock front to the half height of the downward gradient) for different transverse positions of the blade x_{blade}. (b) Shock width e_{shock} and density ratio n_1/n_2 for different transverse positions of the blade x_{blade}.

Equations (2.11) to (2.14) determine how the shock parameters are modified as the blade is moved in and out the gas flow. Indeed, the pressure and density ratio (respectiveley P_1/P_2 and n_1/n_2) depend only on the initial local Mach number of the gas, which changes in the transverse direction for a given height (as seen in Fig. 2.10). Figure 2.16 shows density line-outs for different values of x_{blade}, corresponding to different transverse positions of the blade. The shock parameters evolve when the blade enters the flow. As the blade is moved more and more into the gas jet, a larger part of the flow is blocked and it encounters a lower and lower Mach number. The gas being less supersonic, the non-negligible transverse velocity tends to increase the shock width. However, the shock is more efficiently generated and the density ratio tends to increase. The remaining length of gas after the shock obviously decreases when entering the blade. These variations are presented in Fig. 2.17(a-b). By moving the blade out, the density ratio is reduced. However, the encountered Mach number is higher on the flow edges and the shock width decreases. Once the blade does not encounter enough gas flow anymore, the shock strongly decays. For electron injection, the sharpest the transition, the lower the energy spread. Thus, it is better to move the blade as far as possible from the jet center while maintaining a stable and strong enough shock. By doing this, the transition is as sharp as possible while the remaining gas length is maximized, allowing for a better energy gain.
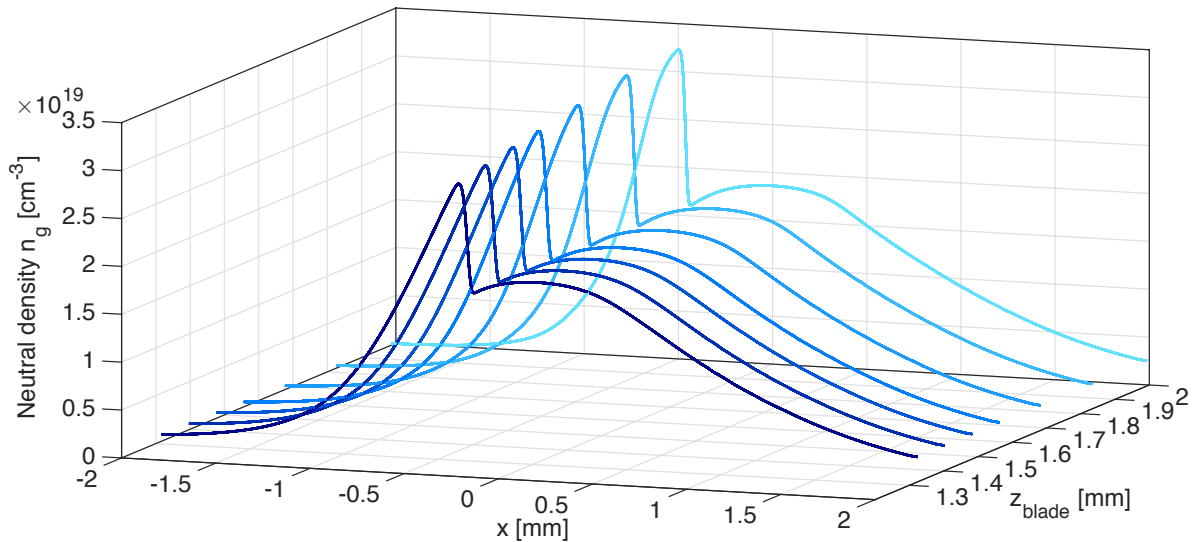
Figure 2.18: Density transverse line-outs at 1 mm height from the blade for different heights of the blade z_{blade} measured from the exit of the gas jet ($z = 0$ mm).

The blade height from the nozzle exit is also an important parameter to be taken into account. Figure 2.18 shows density line-outs at $(z_{blade} + 1)$ mm for different values of z_{blade}, corresponding to different heights of the blade. While the density profile keeps a similar shape whatever the height, the shock parameters are modified. Indeed, for a same transverse position of the blade, the Mach number of the unperturbed gas flow increases with the height (as shown in Fig. 2.10). As explained in the previous paragraph, this leads to the generation of a sharper shock. When moving the blade up, the length of remaining gas after the shock slightly increases due to the wider flow, as seen in Fig. 2.19(a), while the shock width is reduced (Fig. 2.19(b)). The density ratio is however increased, due to the fact that when increasing z_{blade} while maintaining x_{blade} constant, the local density is higher, forming a stronger shock. In order to form a stable and strong shock, it is better to increase the blade height as much as possible (to optimize the shock
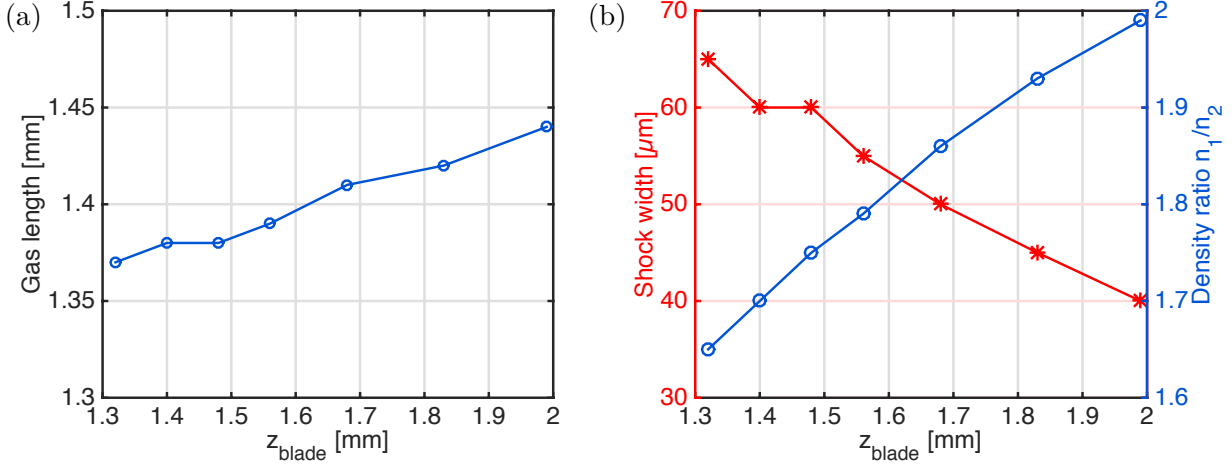
Figure 2.19: (a) Remaining gas length (from the shock front to the half height of the downward gradient) for different heights of the blade z_{blade}. (b) Shock width e_{shock} and density ratio n_1/n_2 for different heights of the blade z_{blade} at $z = 3$ mm.

parameters) while maintaining a high enough density in the plateau to efficiently generate a wakefield in laser-electron acceleration experiments.

In conclusion, the position of the blade edge in the supersonic gas flow is of major importance to optimize the shock front formation for density transition injection. In order to obtain a sharp transition with a maximum density ratio, the blade should be placed far enough from the jet center and from the nozzle exit. This way, the shock width is reduced (which is interesting to instantaneously change the wakefield properties when crossing the transition), the density ratio is increased (to trigger electron injection in the shock while shutting it down after the transition) and the remaining gas length is maximized (to have the maximum energy gain for accelerated electrons).

2.3 Experimental injection of electrons in a sharp density gradient

In order to obtain better quality electron beams than in the self-injection scheme, a sharp density transition is used to inject electrons in the wakefield. Indeed, the self-injection process is highly non-linear and leads to largely fluctuating electron beams. Shock injection allows for more reproducible and stable electrons as it is less dependent on the laser pulse evolution during its propagation. A comprehensive experimental study of shock front injection is presented in this section.

2.3.1 Experimental setup and diagnostics

The main interaction beam P_1 from the "Salle Jaune" laser system (linearly polarized, 28 fs FWHM, 1.8 J) is focused at the entrance of a gas jet using a f/15 Off-Axis Parabola (OAP with a focal length of 1000 mm). The experimental setup is pictured in Fig. 2.20. The $1/e^2$ focal spot diameter is measured to be 26 ± 0.6 μm. An image of the focal spot and its transverse profile can be seen in Fig. 2.21(a). The energy contained in this spot diameter is 53 ± 2 % of
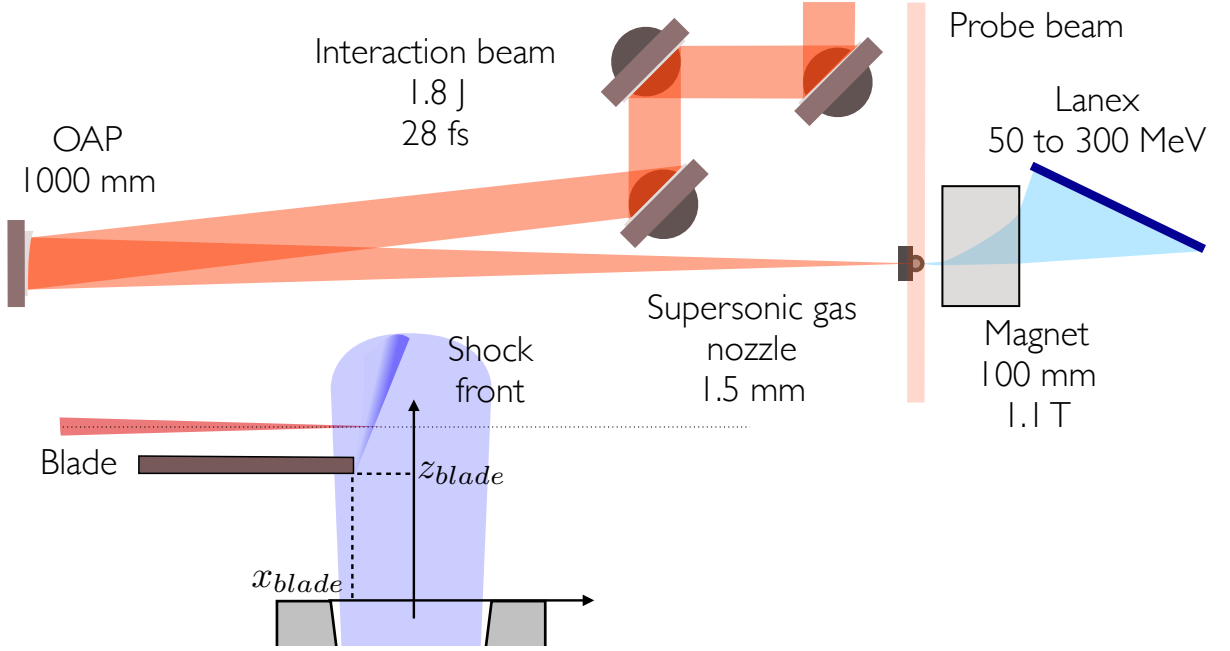
Figure 2.20: Drawing of the experimental setup for electron injection in a density transition.

the total energy. The peak laser intensity and the corresponding normalized vector potential a_0 are $1.45 \pm 0.5 \times 10^{19}$ W.cm^{-2} and 2.60 ± 0.05, respectively.

The helium gas jet is formed with a De Laval supersonic nozzle with an output diameter of 1.5 mm. The laser is fired at a height of 3 mm from the nozzle exit, leading to the formation of a 3.2 mm long plasma. A low energy probe beam is used to measure a shadowgraph of the formed plasma (as seen in Fig. 2.21(b)). The electron density is varied by changing the backing pressure ahead of the nozzle, and its density profile is characterized using a Nomarski interferometer afterwards. If not stated otherwise, the electron plasma density without shock is $n_2 = 7.5 \times 10^{18}$ cm^{-3}.
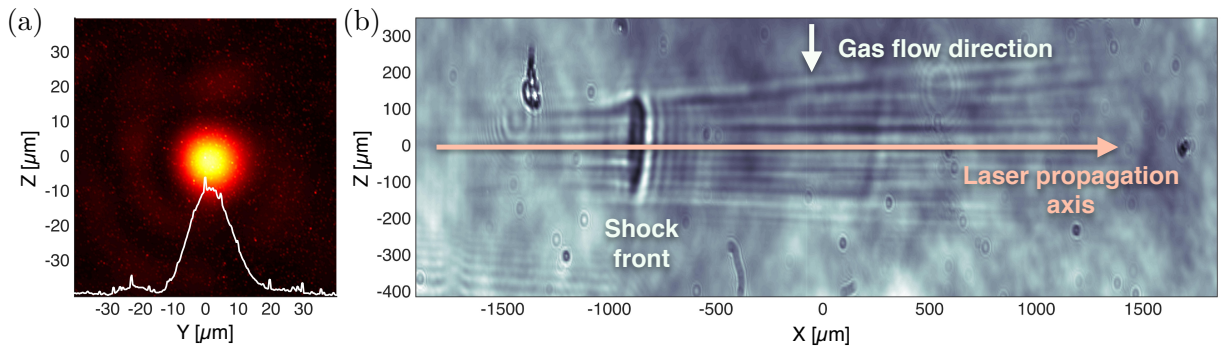
Figure 2.21: (a) Experimental laser focal spot obtained with a 1 m focal length off-axis parabola. (b) Shadowgraph image of the propagation of the laser in a pure helium gas jet. $Z = 0$ μm corresponds to the center of the nozzle. The shock is visible at $Z = -900$ μm.

The shock is produced by introducing a 500 μm thick silicon wafer into the gas flow, forming a sharp density transition as presented in section 2.2. The shock formed in the plasma is clearly

visible in Fig. 2.21(b)). The position of the silicon blade (referred as (x_{blade}, y_{blade})) defines the position and density ratio n_1/n_2 of the transition. The blade is moved into the flow at a height of about 2 mm from the nozzle exit, with the laser fired at about 1 mm above the blade (due to the blade mount obstructing the beam if focused closer). In this scheme, electrons are injected at the shock position and accelerated in the remaining part of the gas jet.

2.3.2 Stable generation of electron beams

Firstly, the electron density is set high enough (around $n_2 \sim 2 \times 10^{19}$ cm^{-3}) in order to be in the self-injection regime with the blade out of the jet, so that the laser focus position can be optimized. Once the electron signal is maximum, the electron density is lowered down to the point where self-injection completely stops (around $n_2 = 7.5 \times 10^{18}$ cm^{-3}). When moving slightly the silicon wafer in the flow and creating the shock front, electron acceleration starts again, with a very bright spot appearing in the top view image at the position of the shock. The light emitted at this position is due to the very large acceleration of injected electrons from null velocity at injection to c, leading to a strong emitted radiation [Thomas et al., 2007], supporting the idea that observed electrons are indeed injected in the bubble at the density transition.
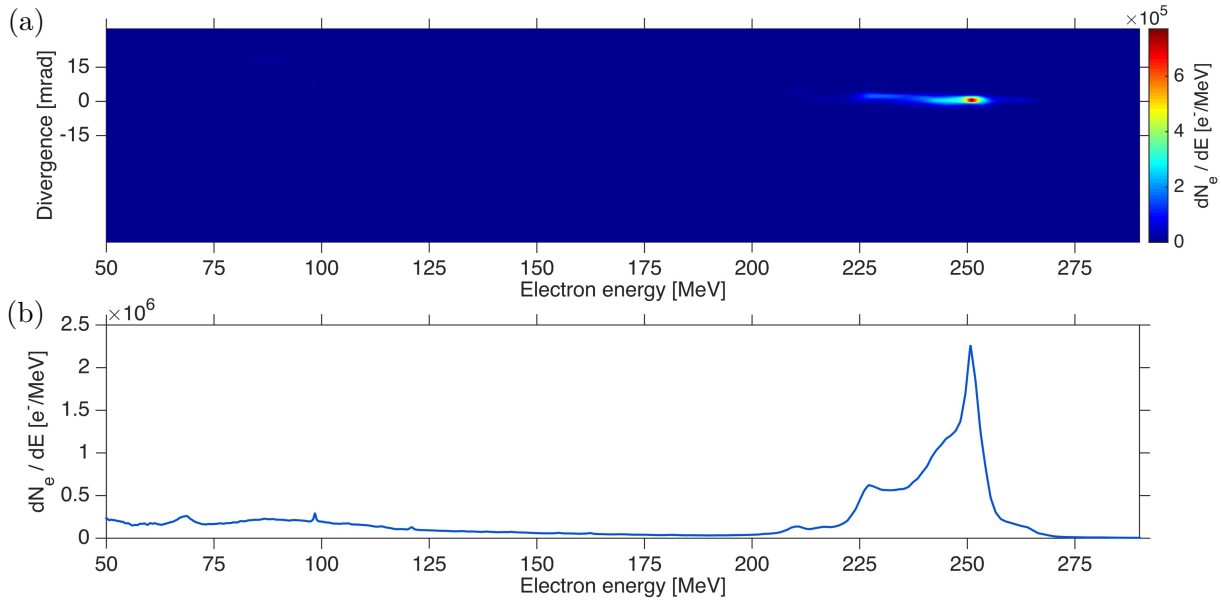
Figure 2.22: (a) Experimental spectrum (corrected from the spectrometer dispersion) of shock injected electrons in a plasma density $n_2 = 7.5 \times 10^{18}$ cm^{-3}. (b) Spectrum integrated over the transverse direction.

A typical experimental electron spectrum for the optimized blade position is visible in Fig. 2.22(a), with the integrated spectrum over the transverse dimension shown in (b). Shock injection allows to generate a mono-energetic electron beam with a peak energy $E_{peak} = 250$ MeV, a FWHM energy spread $\Delta E = 9.5$ MeV (relative energy spread of 3.8 %), a charge in the peak $Q_{peak} = 3.2$ pC and a divergence FWHM of 1.9 mrad. Beams generated from transverse self-injection are more charged (few dozens of picocoulombs) but the energy spread is typically larger (in the range of 10 - 20 %) and much more unstable.

Figure 2.23 shows five consecutive shots for the same density and blade position. The beam parameters are more stable than in the self-injection regime, with an injection probability larger
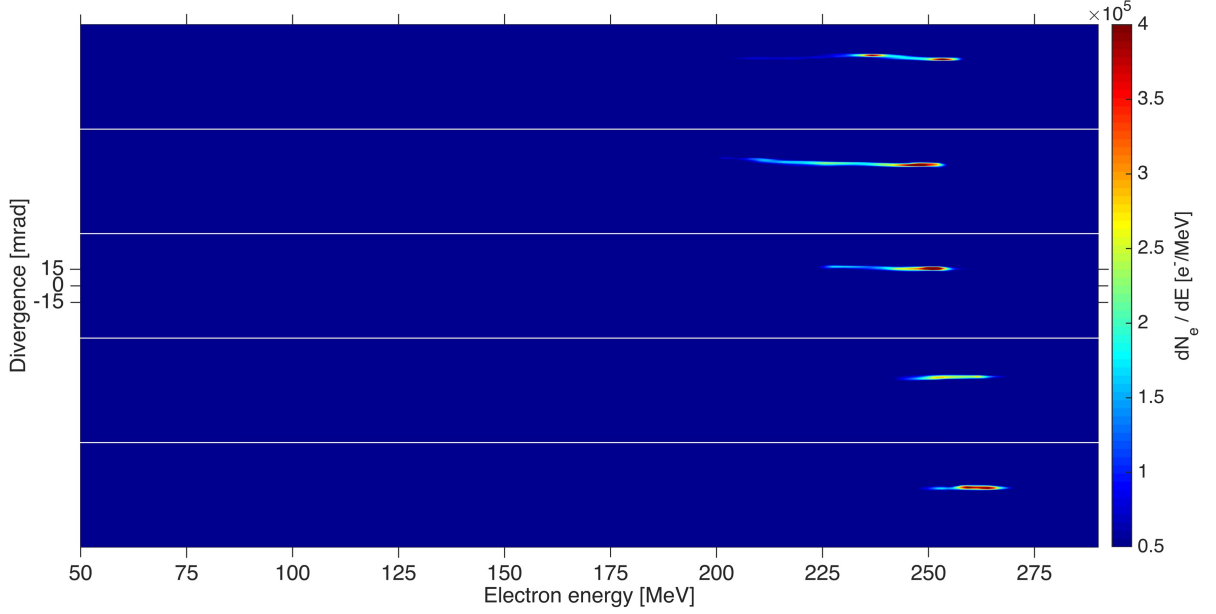
Figure 2.23: Experimental spectra of shock injected electrons for five consecutive shots.

than 90 %. It is due to the fact that shock front injection is less dependent on the nonlinear evolution of the laser pulse (which is responsible for transverse self-injection), with a fixed injection position as soon as the density transition is generated steadily. The standard error of the mean is calculated over five shots for each beam parameters :

$$E_{peak} = 256.5 \pm 4 \text{ MeV}$$
$$\Delta E = 15.5 \pm 2 \text{ MeV}$$
$$\Delta E/E = 6 \pm 1\%$$
$$Q_{peak} = 3.2 \pm 0.4 \text{ pC}$$
$$\text{Divergence} = 2.0 \pm 0.3 \text{ mrad}$$

Density transition injection is an interesting regime to create low divergent mono-energetic electron beams with a quite narrow energy spread at the cost of a reduced charge (only a few pC) compare to transverse self-injection (few dozens of pC). The number of low-energy electrons is however very small, all electrons being trapped at the same time and gaining about the same amount of energy (therefore leading to low energy spread). Almost all of the charge is contained in the mono-energetic peak for all the shots.

2.3.3 Beam parameters scaling

An interesting property of shock front injection is the possibility to change multiple parameters (electron density, blade position) in order to tune the electron parameters. As seen in section 2.2, the density transition parameters can be modified by changing the transverse position of the blade x_{blade} while maintaining the blade height z_{blade}. x_{blade} is varied between -2 mm and -0.5 mm, with 0 mm at the center of the gas jet.

The electron energy is tuned by moving the blade in the jet, as shown in Fig. 2.24(a). When the blade is out of the jet ($x_{blade} < -1.6$ mm), no shock is generated and only very few
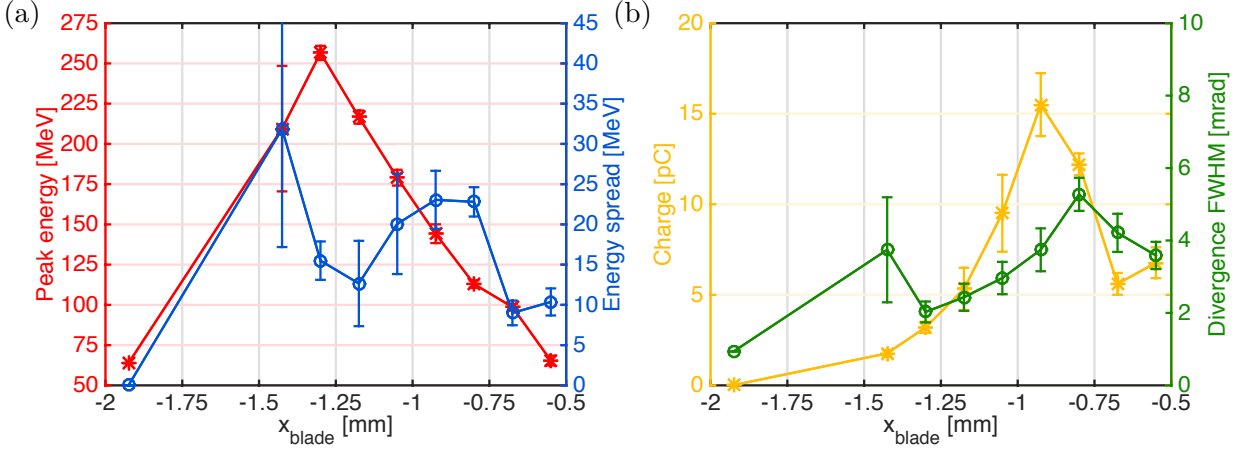
Figure 2.24: (a) Peak energy (in red) and energy spread (in blue) of the electron beam for different transverse positions of the blade x_{blade}. (b) Charge (in yellow) and FWHM divergence of the electron beam for different transverse positions of the blade x_{blade}. $x_{blade} = 0$ mm corresponds to the center of the jet. The error bars represent the standard error of the mean over at least five shots. The laser normalized intensity is $a_0 \sim 2.6$.

electrons (less than 0.1 pC) are self-injected in the wake. When sufficiently in the jet so that it generates a shock ($x_{blade} = -1.3$ mm), electrons are trapped and accelerated. For this position, the remaining accelerating length is maximum after the transition, leading to the maximum electron energy with this nozzle. The more the blade is inserted, the lower the peak energy, due to a reduced accelerating length.

Since the injection is limited in a narrow time window when the bubble crosses the shock front, the absolute energy spread is defined at injection and does not change much for different acceleration lengths (staying between 10 and 20 MeV). The divergence of the electron beam increases significantly from 2 to 5 mrad for lower electron energies (due to the energy dependance of the divergence), as seen in Fig. 2.24(b). The charge of the peak increases when entering the gas jet, up to 15 pC. Indeed, it was simulated in section 2.2.3 that the closer the blade gets to the center, the larger the shock width and the density ratio n_1/n_2. With a wider shock, the injection is not as temporally confined as with a sharp transition, thus the electrons are injected for a longer time (increasing the number of injected electrons). Furthermore, a larger n_1 also tends to increase the number of electrons potentially able to be injected as this position. For $x_{blade} > -0.8$ mm, the blade is too close to the center and the shock is not generated finely (very large width and low density ratio, as seen in Fig. 2.16) and the accelerating length is quite short. The energy peak and charge drop considerably for such blade positions.

The Helium backing pressure of the nozzle was scanned in order to study the influence of the background plasma density n_2 on shock injected accelerated electrons. A two-dimensional scan was performed by recording electron spectra while changing the blade position x_{blade} for different electron densities n_2. The mean peak energy (resp. the charge) of five consecutive shots for different values of (x_{blade},n_2) are shown in Fig. 2.25(a) (resp. (b)). If the electron density is too low (under 3.0×10^{18} cm^{-3}), no electrons are injected in the transition as the wakefield is too weak. The larger the electron density, the larger the peak energy for a constant x_{blade} because of stronger longitudinal electric fields and a longer length over which the bubble is sustained. As n_2 increases, the beam charge is larger when the blade gets out of the gas flow (as seen in the tilted colored region between -0.6 mm and -1.2 mm in Fig. 2.25(b)). Indeed,
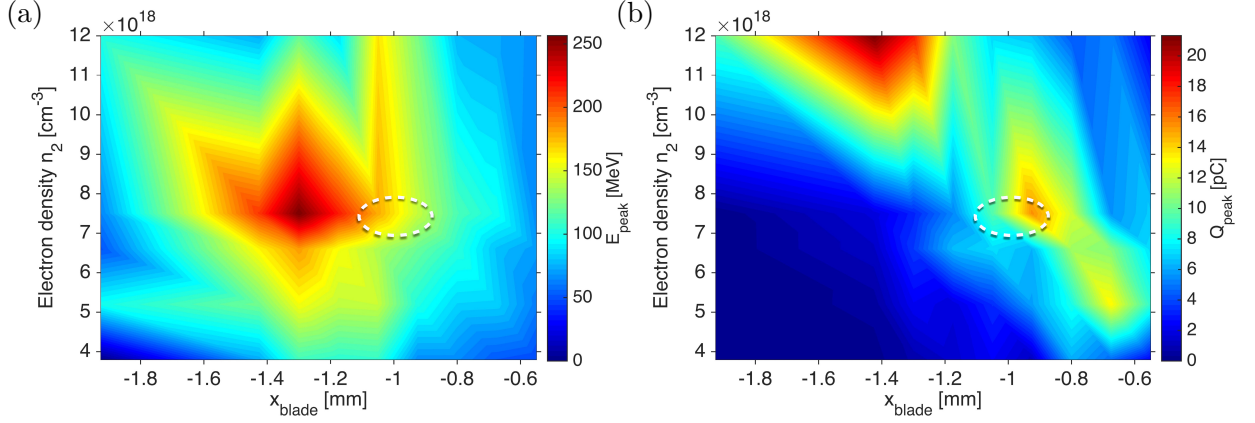
Figure 2.25: (a) Peak energy (a) and charge (b) of the electron beam for different transverse positions of the blade x_{blade} and electron plasma density n_2. The white dotted circles represent the optimum set of parameters to get the highest peak energy and charge.

more electrons are injected in the transition for larger n_1, as more of them accumulated at the back of the bubble before the density transition (as pictured in Fig. 2.1(b)). On the contrary, if n_2 increases too much while the blade is still too close to the center, the local Mach number of the flow strongly decreases and a shock cannot be generated efficiently (the subsonic flow simply goes around the blade), thus no electrons are injected (as observed in the right corner of the 2D maps). If the electron density is too large (1.2×10^{19} cm^{-3}), self-injection is triggered leading to higher charged lower energy electron beams (upper left corner in Fig. 2.25(b)). An optimum set of parameters to get the highest peak energy and charge with $a_0 \sim 2.6$ is ($n_2 = 7.5 \times 10^{18}$ cm^{-3}, $x_{blade} = -1.1$ mm).

Controlled injection in a density transition allows to generate electrons in a very wide and tunable energy range (between 75 and 250 MeV) and low charge (between 3 and 15 pC) with an easy implemented experimental setup. The simple tunability in such a regime is particularly interesting in numerous application experiments.

2.3.4 Tunability with the blade position in the jet

As seen previously, the position of the blade in the jet is of major importance in density transition injection. Another experimental campaign has been performed to study the influence of this position. The same setup presented in Fig. 2.20 is used, with slightly lower laser intensity. The laser pulse contains 1.3 J, with a $1/e^2$ focal spot diameter of 31 ± 0.7 μm. The energy contained in this spot diameter is $55 \pm 2\%$ of the total energy. The peak laser intensity and the corresponding normalized vector potential a_0 are $7.5 \pm 0.5 \times 10^{18}$ W.cm^{-2} and 1.9 ± 0.06, respectively. The background plasma density is set at $n_2 = 7 \times 10^{18}$ cm^{-3}.

By optimizing the blade position, we obtained the experimental angular resolved electron spectrum presented in Fig. 2.26(a), with the integrated spectrum over the transverse dimension shown in (b). The generated mono-energetic electron beam has a peak energy $E_{peak} = 87$ MeV, a FWHM energy spread $\Delta E = 5$ MeV (relative energy spread of 5.7 %), a charge in the peak $Q_{peak} = 2.1$ pC and a divergence FWHM of 2.6 mrad. The beam parameters are overall worse than in the previous experiment (lower charge and peak energy, larger divergence). This is likely due to the lower laser intensity (thus a wakefield excitation not as efficient as before), and by the fact that the laser was fired at 3 mm from the blade (thus leading to wider shock fronts with

(a)

(b)
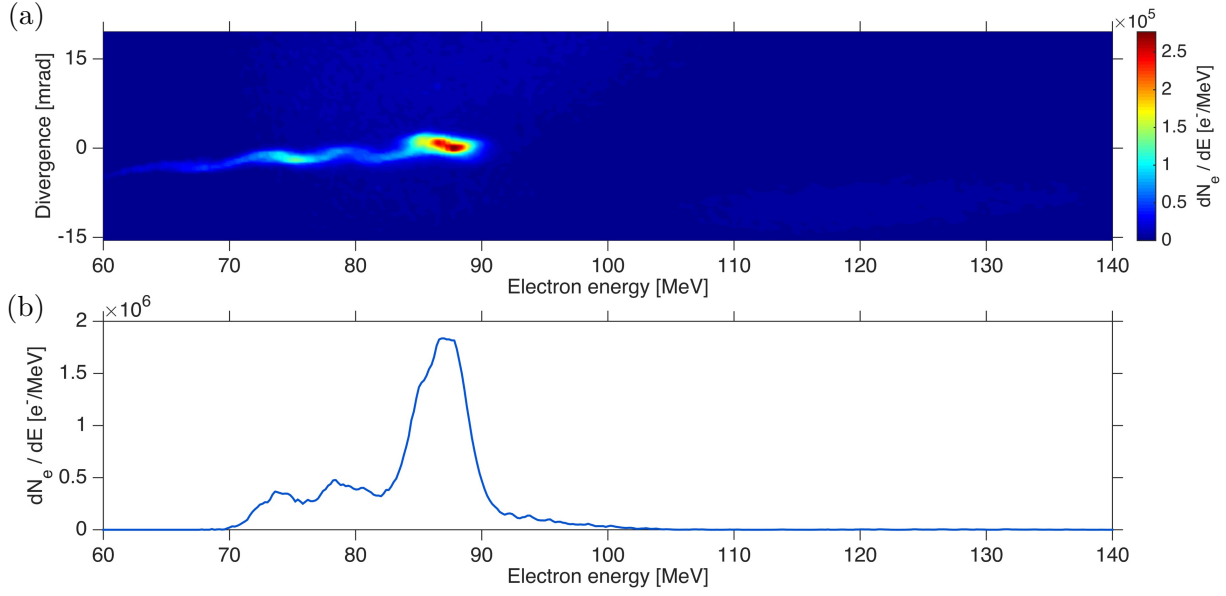
Figure 2.26: (a) Experimental spectrum of shock injected electrons in a plasma density $n_2 = 5 \times 10^{18}$ cm^{-3}. (b) Spectrum integrated over the transverse direction. The laser normalized intensity is $a_0 \sim 1.9$
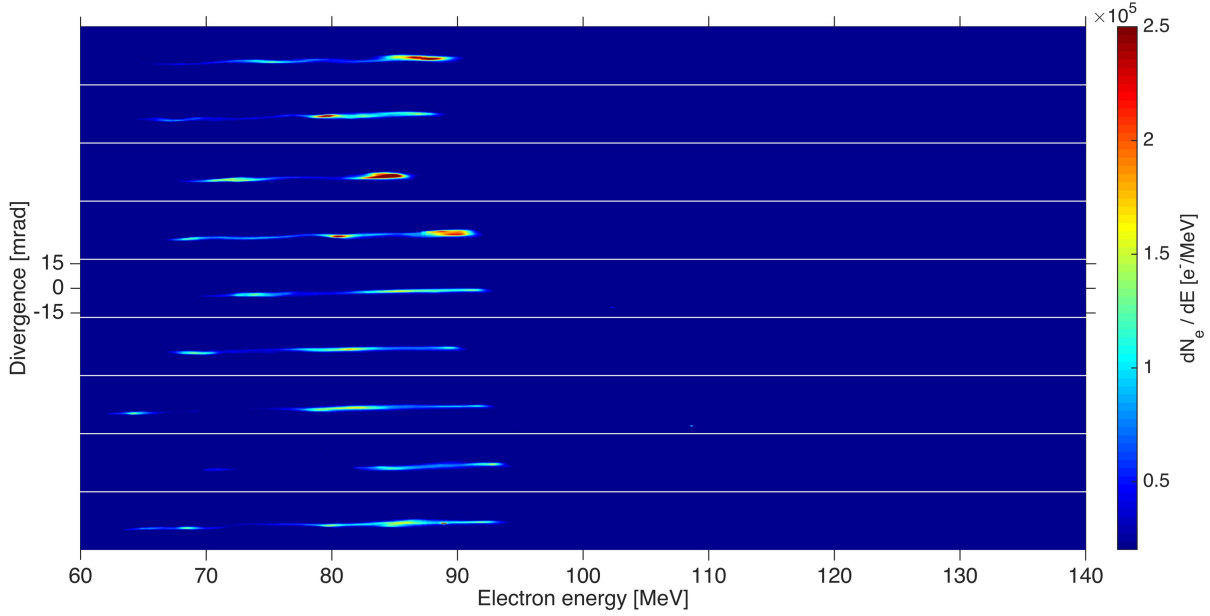

Figure 2.27: Experimental spectra of shock injected electrons for nine consecutive shots. The colorscale represents the charge per energy unit and per angular unit (in e^-/MeV.sr).

a reduced density ratio).

The stability is also poorer than in the previous study, as shown in Fig. 2.27 which represents nine consecutive shots with the same density and blade position. A deficient laser wavefront or inhomogeneities in the laser spot may be the reason for the stability decrease of shock injection in this experiment. The standard error of the mean is calculated over nine shots for each beam
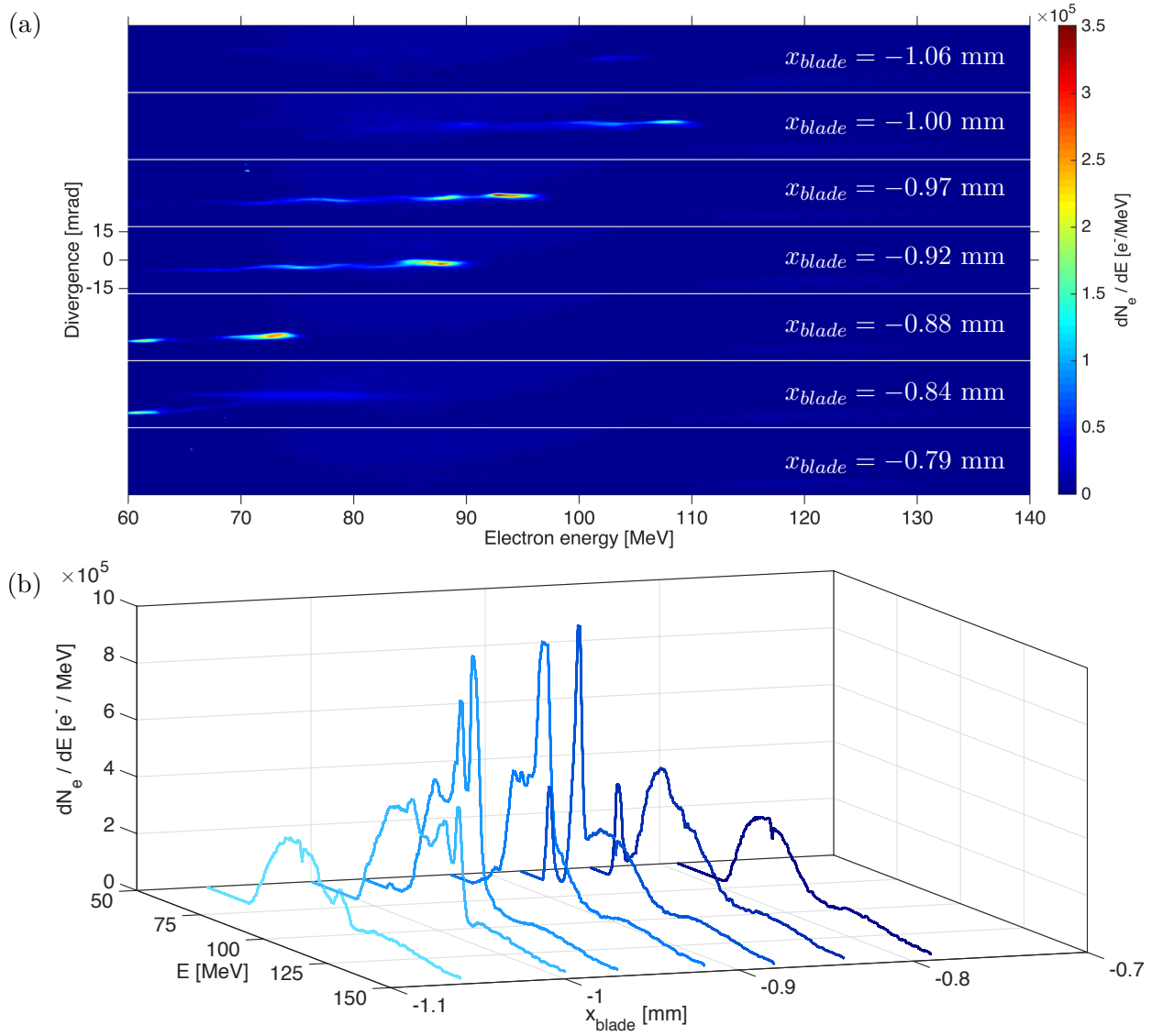
Figure 2.28: Experimental spectra for different transverse positions of the blade x_{blade} (a) and their corresponding integrated electron spectra (b).

parameters :

$$E_{peak} = 84.7 \pm 1.3 \text{ MeV}$$
$$\Delta E = 7.7 \pm 1.7 \text{ MeV}$$
$$\Delta E/E = 9.1 \pm 2\%$$
$$Q_{peak} = 2.9 \pm 0.3 \text{ pC}$$
$$\text{Divergence} = 2.1 \pm 0.3 \text{ mrad}$$

A second peak with a lower energy appeared in this experimental run. This is likely due to the fact that the laser being fired further from the nozzle output and the blade, the shock is wider and electrons can be injected over a larger region (thus with different energy than those directly

65
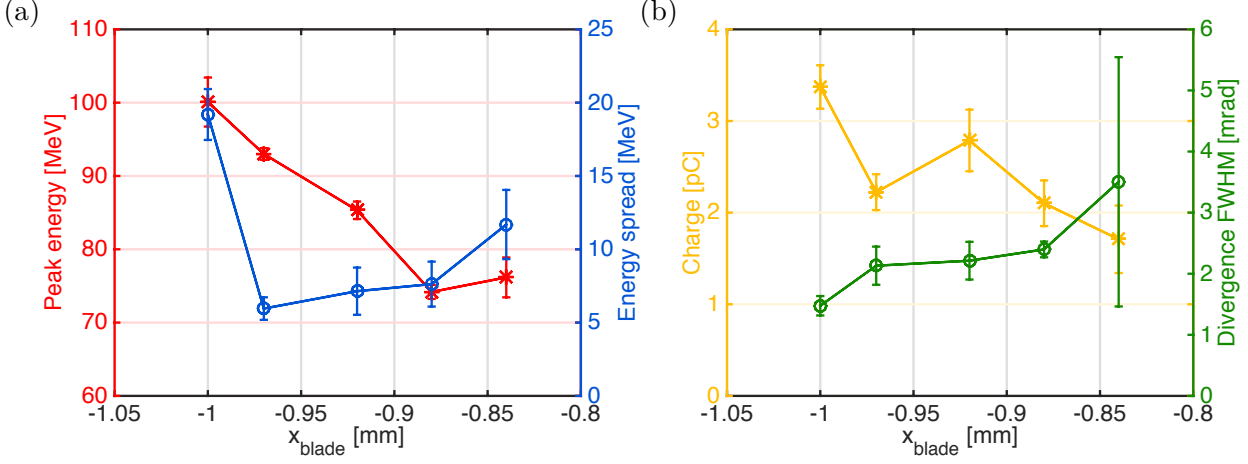
Figure 2.29: (a) Peak energy (in red) and energy spread (in blue) of the electron beam for different transverse positions of the blade x_{blade}. (b) Charge (in yellow) and FWHM divergence of the electron beam for different transverse positions of the blade x_{blade}. The laser normalized intensity is $a_0 \sim 1.9$.

injected at the very beginning of the downward density transition). A complete study of the beam parameters dependance with the blade position is presented in the following paragraph.

Firstly, the blade is moved transversally in and out the gas jet: x_{blade} ranges from -1.06 mm to -0.79 mm, with $x_{blade} = 0$ mm at the center. As seen in Fig. 2.28(a-b), the electron spectra depend strongly on the shock position. When the blade is too far away ($x_{blade} = -1.06$ mm) or too much inside the jet ($x_{blade} = -0.79$ mm), almost no electrons are injected. The range over which shock injection is triggered is much smaller than in the previous experiment, due to the weaker laser intensity. Figure 2.29(a-b) shows the beam parameters evolution with the shock position. The same behavior than observed in the previous study is found again, yet with a reduced tunability range for the peak energy and charge.

The height of the blade z_{blade} is now modified while keeping the same transverse position $x_{blade} = -0.98$ mm. z_{blade} ranges from 1.32 mm to 1.99 mm from the nozzle exit, while the laser is shot at 3 mm above the exit. The effect on electron spectra is shown in Fig. 2.30(a-b). When the blade is moved up (and closer to the laser), the electron energy does not vary much at the beginning, then decreases quickly down to a point when electrons are not injected anymore. The beam parameters are shown in Fig. 2.31(a-b). If the blade is too close from the exit ($z_{blade} = 1.32$ mm), few electrons are accelerated. Indeed, as seen in Fig. 2.12, the Mach number decreases quickly when getting closer to $z = 0$ mm while maintaining a constant x. Thus, the density ratio n_1/n_2 of the shock is smaller for small z_{blade}, as shown in Fig. 2.19. The density is not sufficient enough to trap and accelerate a lot of electrons in this case. Also, the laser is fired too high from the blade, thus encountering quite a wide shock leading to poorer electron parameters. When increasing z_{blade}, the acceleration length increases slowly and the shock width decreases (Fig. 2.19). Experimentally, the beam parameters are not strongly influenced by the blade height between 1.4 mm and 1.8 mm. Over this range, the shock parameters do not have a clear effect on electrons. When the blade is too far from the nozzle output however, the peak energy decreases because of the reduced density n_2, leading to weaker accelerating fields.

(a)

(b)
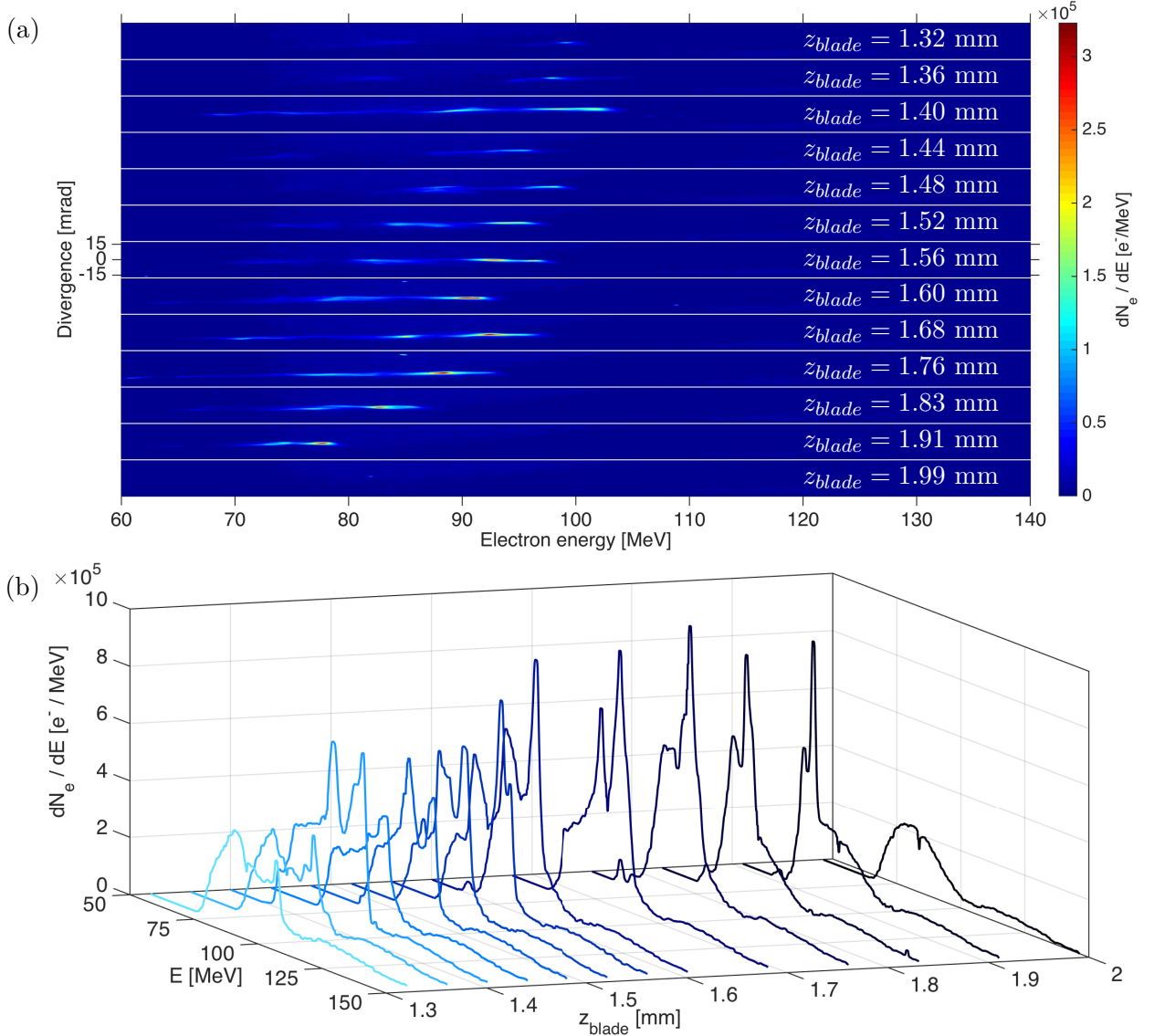
Figure 2.30: Experimental spectra for different heights of the blade z_{blade} (a) and their corresponding integrated electron spectra (b).

2.4 Conclusion

In conclusion, we presented in this section a detailed study of shock generation in supersonic gas jets and controlled electron injection in such sharp density transitions. In this injection mechanism, instabilities of the electron beam parameters are greatly reduced compared to the transverse self-injection regime. Tunable electrons up to 250 MeV were accelerated in a stable and reproducible way with a very good injection probability. The accelerated electrons have a low divergence around 2 mrad and a small energy spread (down to 4 %). The beam charge however is relatively small (around 3 pC), but can be increased (up to 15 pC) when moving the blade in (at the cost of a reduced peak energy due to a reduced acceleration length). Such good quality, lowly charged beams are interesting candidates for multi-staged laser-plasma accelerators [Schroeder et al., 2010; Kim et al., 2013a], where the transport between stages require high quality beams.

Such beams would also be interesting for LWFA-based FEL [Nakajima, 2008] if not the low charge. An important and useful step would be to enhance the charge while maintaining the beam quality in shock injected electron beams.

(a)

(b)
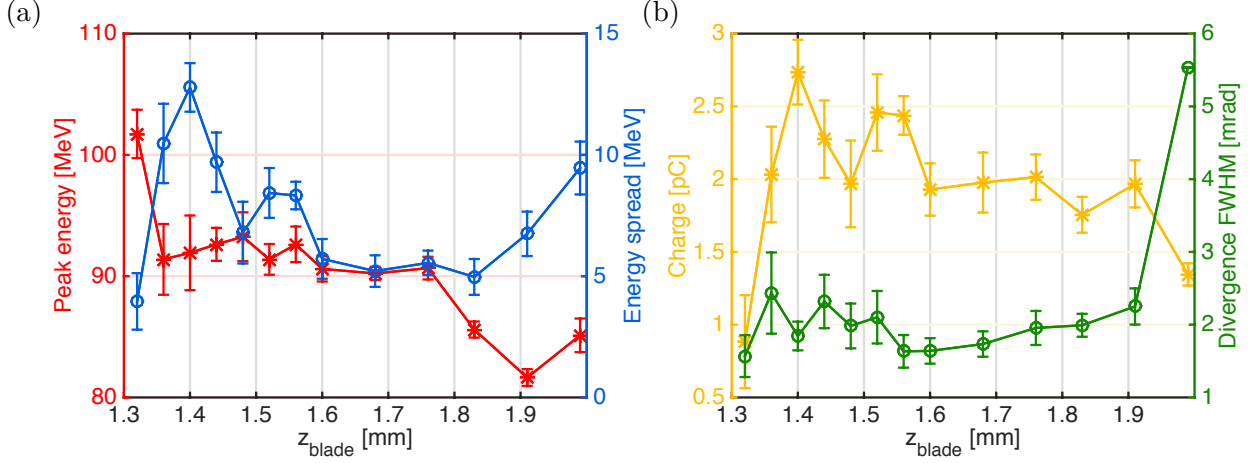
Figure 2.31: (a) Peak energy (in red) and energy spread (in blue) of the electron beam for different heights of the blade z_{blade}. (b) Charge (in yellow) and FWHM divergence of the electron beam for different distances of the blade from the nozzle output z_{blade}.

Chapter 3

Ionization injection in a laser-plasma accelerator

This chapter is focused on the ionization injection mechanism in a high Z gas. In the first part is detailed the injection principle based on tunnel-ionization of inner shell electrons. The experimental and numerical results of electron acceleration in a pure high Z gas are presented in the second part, with a detailed study of the physics of a fully-loaded laser-plasma accelerator. In the third part, the combination of ionization and shock injection mechanisms is introduced, allowing for the acceleration of stable, high quality electron beams in a gas mixture with a density transition.

Contents

3.1 The mechanism of ionization injection

Injection in a density transition presented in chapter 2 allows for the generation of good quality electron beams, however with a very low charge of a few pC. In this chapter, we are looking for an injection technique allowing for increasing the charge while maintaining good bunch properties. Moreover, a desirable injection technique would lead to electron injection at every shots while driving such an electron beam while conserving the previous parameters. Ionization induced injection which is presented below may be a suitable way to match these requirements.

3.1.1 Tunnel ionization of electrons into a LWFA

For large laser intensities, the Keldysh parameter γ_k is smaller than 1, and the electric field is strong enough to perturb the binding potential between an electron and the nucleus in an atom (as presented in section 1.1.3). Therefore, for typical laser intensities used in LWFA, the dominant ionization mechanism is tunnel ionization. Tunnel ionization not only creates the plasma, but can also be the mechanism which injects electrons in the wakefield.

Whereas a number of analytical tunneling ionization models exist, the following discussion uses the Ammosov-Delone-Krainov, or so called ADK, model [Ammosov et al., 1986]. The ADK model was shown to be in good agreement with Schrödinger's equation to model the effect of an external electric field onto the binding potential of a hydrogen atom as long as the electric field remains smaller than the critical value

$$E_{crit}[\text{GV.m}^{-1}] = 514(\sqrt{2} - 1)\left(\frac{\zeta_i}{27.2}\right)^{3/2} \tag{3.1}$$

where ζ_i is the undisturbed ionization potential of the considered electron in eV [Bruhwiler et al., 2003]. This critical value comes from the fact that the ionization probability increases exponentially with the electric field : when it becomes too strong, the approximation is not valid anymore. The ADK model allows for a good prediction of the ionization rate for atoms with multiple ionization states while remaining below this critical value. In the following, tunnel ionization of nitrogen electrons is particularly studied. Thus, the ADK model accurately describes the ionization mechanism if the maximum electric field used to ionize K-shell electrons of nitrogen is lower than E_{crit} for these electrons. The ionization potential of N^{7+} is 667 eV, therefore $E_{crit} = 2.6 \times 10^4$ GV.m^{-1}.

The laser electric field is related to the normalized vector potential through

$$E_{max,laser}[\text{GV.m}^{-1}] = 10^{-9}\frac{m_e c}{e}\omega_0 a_0 \tag{3.2}$$

For typical value of laser intensity before self-focusing (when the plasma is formed) used in the experiment ($a_0 \sim 2.3$), we get $E_{max,laser} = 9.2 \times 10^3$, which is below the critical value. This indicates the ADK model is suitable to predict the ionization rates for the plasma formation in the range of parameters we studied. After self-focusing of the pulse however, this is not true anymore and the model allows only for understanding the main physics undergoing.

The ADK ionization probability rate for an electron depends on the amplitude of the laser electric field and the ionization potential of the considered state :

$$W[\text{s}^{-1}] \approx 1.52 \times 10^{15}\frac{4^{n^*}\zeta_i[\text{eV}]}{n^*\Gamma(2n^*)}\left(20.5\frac{\zeta_i^{3/2}[\text{eV}]}{E[\text{GV.m}^{-1}]}\right)^{2n^*-1}\exp\left(-6.83\frac{\zeta_i^{3/2}[\text{eV}]}{E[\text{GV.m}^{-1}]}\right) \tag{3.3}$$

with $n^* \approx 3.69Z/\sqrt{\zeta_i}$ the effective principal quantum number of the electron, Z being the ionization state level, and Γ the standard Gamma function. The fraction of species which is ionized during a time Δt is given by $W\Delta t$.

With the ADK ionization probability rate, one can determine the ionization dynamics of nitrogen when an ultra-intense laser pulse propagates through nitrogen gas, thus the fraction of each ionization state level as a function of time. Considering a Gaussian laser pulse with parameters close to what we used in the experiments ($\lambda_0 = 800$ nm, $\tau_0 = 28$ fs FWHM, peak normalized amplitude $a_0 = 2.3$ in vacuum), propagating in a neutral nitrogen gas with a density $n_0 = 10^{19}$ cm^{-3}, the ionization process (neglecting self-focusing of the pulse) can be modelled. The results are shown in the co-moving frame in Fig. 3.1.
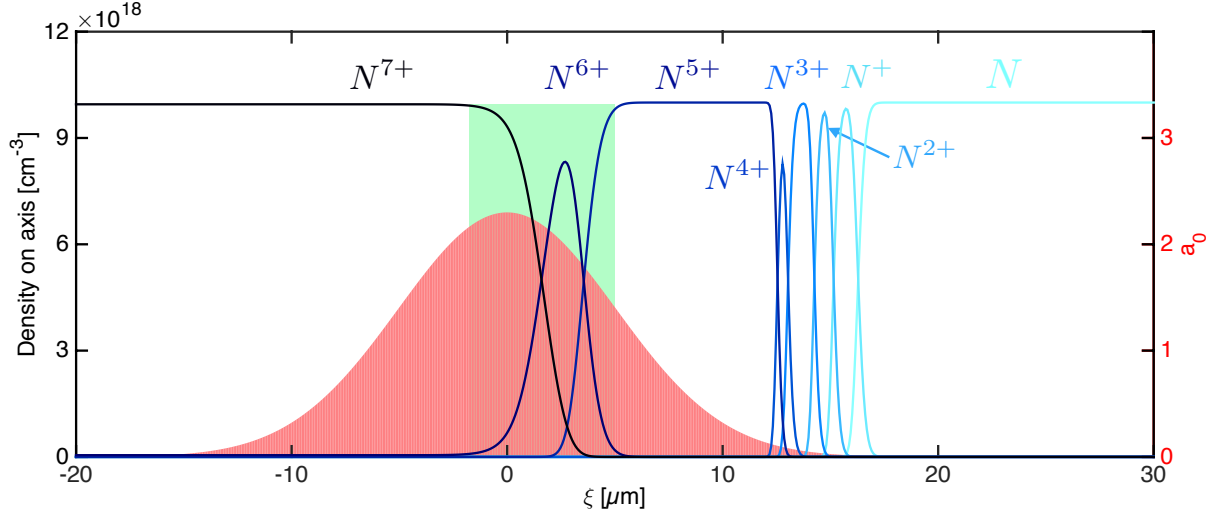
Figure 3.1: Density of the different ionized states of nitrogen (different shades of blue) function of the position in the co-moving frame. The envelope of the laser pulse is shown in red. The green area indicates the position where electrons from N^{6+} and N^{7+} are ionized.

Ionization of neutral nitrogen starts at the very beginning of the pulse, while a_0 is still very low. All nitrogen atoms are quickly ionized up to the N^{5+} state when a_0 reaches 0.1. Then, a large step in ionization potentials between N^{5+} and N^{6+} leads to a large step in ξ between these two ionized states. Electrons from N^{6+} and N^{7+} are created near the peak of the laser pulse (in the green region in Fig. 3.1). Thus, the intensity of the pulse, as well as its duration, can be used to control the relative position within the laser pulse at which K-shell electrons are ionized. This feature is taken advantage of to inject electrons directly in the wakefield.

3.1.2 Trapping of electrons from ionization in the bubble regime

Tunneling ionization allows for the use of atoms with multiple ionization states to control the injection in the wake. Indeed, the ionization level of the considered species (in our case, nitrogen) increases as the electric field of the laser interacts with the ionized gas. As shown in Fig. 3.2(a), the ionization state of nitrogen atoms on axis rapidly increases up to 5 when the very beginning of the laser pulse interacts with the neutral gas (note that the laser normalized amplitude is depicted in logarithmic scale). Indeed, the rising edge of the laser pulse is intense enough to fully ionize the five electrons from the L-shell of nitrogen (in the case of Helium, the total ionization state is reached even faster). The ponderomotive force of the laser pushes away these electrons,

(a)

(b)

(c)
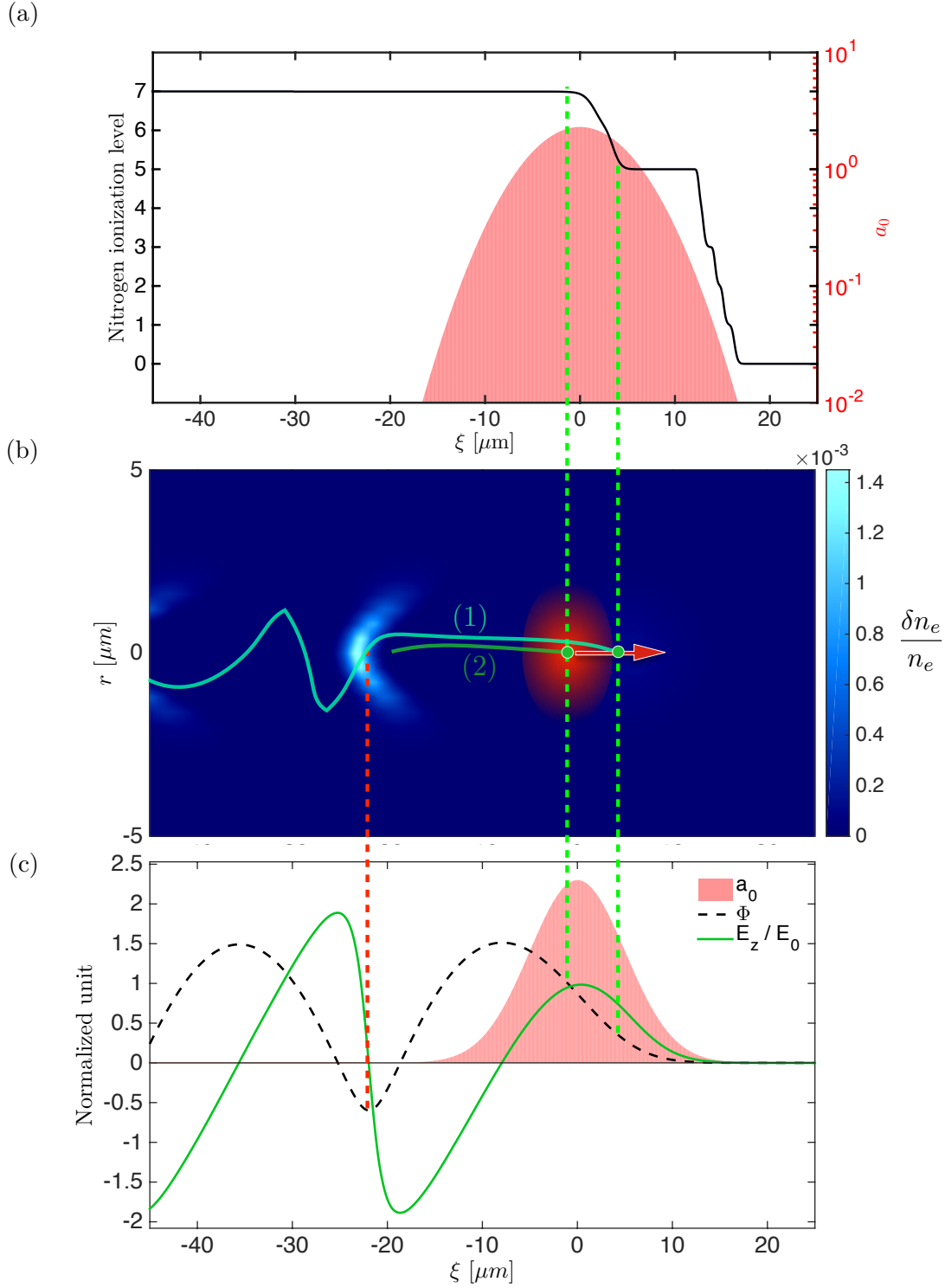
Figure 3.2: Trapping of tunnel-ionized electrons in the wakefield. The laser pulse propagates to the right, ionizes pure nitrogen and drives a wake. a) Envelope of the laser normalized amplitude (in red) in logarithmic scale and ionization state of the nitrogen atoms (black line) on axis. b) Density map of the wake (simulated with the WAKE code [Mora and Antonsen, 1997]), with two electron trajectories coming from electrons ionized the K-shell (in green). Electron (1) is freed too early and is not trapped while electron (2) is trapped. c) Normalized laser amplitude a_0, wake potential Φ and longitudinal electric field E_z on axis.

forming a wake in the bubble regime. The large difference between the ionization potentials of the nitrogen 5th electron (98 eV) and the two K-shell electrons (552 eV and 667 eV) leads to a significant delay before reaching a high enough laser intensity to produce N^{6+} and N^{7+}. This step can be matched to the laser intensity profile so that the 6th and 7th electrons of nitrogen are tunnel ionized close to the peak of the laser pulse, where the wake is already fully formed (as seen in Fig. 3.2(b)). These ionized electrons appear at rest directly into the bubble, and slip backwards from the laser pulse and the wake. If they can gain enough energy during their stay in the accelerating region of the bubble such that they reach the phase velocity of the wake, they are trapped and will gain more energy while moving forward with the wakefield.

An electron which is ionized too early in the laser pulse (case (1) in Fig. 3.2(b)) travels through a large region of decelerating phase before entering the accelerating half part of the bubble, thus it will not gain enough energy to be trapped in the wake. It slips backwards and leaves the first period of the wakefield without being injected. If the electron is ionized closer to the peak of the pulse (case (2) in Fig. 3.2(b)), it experiences a shorter decelerating length before entering the accelerating phase (as seen in Fig. 3.2(c)), gain enough energy to catch up the wake and is trapped to be further accelerated.

From Fig. 3.2(c), it can be seen that the normalized wake potential difference (between the potential where the electron is injected, pointed out by the green dashed line, and the minimum potential at the very back of the bubble, indicated by the red dashed line) varies depending on the ionization position of the electron. Indeed, electron (1) is ionized before electron (2), thus the potential difference is smaller. In order to be trapped, this potential difference must be larger than the minimum potential for trapping. Electrons which are the most likely to be trapped are those created at the very center of the bubble, where the potential difference is the maximum. Electrons created at the center only experience the accelerating phase of the bubble, maximizing their energy gain during the first backwards slippage. If these electrons are not trapped in the wakefield, no electron ionized at rest can be.

In order to get more insight of the dynamics of an electron tunnel ionized at rest in the wake, one can calculate its phase space trajectories. We saw in section 1.2.3 that these trajectories write as the following :

$$u_z(\xi) = \beta_p \gamma_p^2 (H_0 + \varphi(\xi)) \pm \gamma_p \sqrt{\gamma_p^2 (H_0 + \varphi(\xi))^2 - (1 + a^2(\xi)/2)} \tag{3.4}$$

with φ the normalized wake potential, a the normalized amplitude of the laser pulse, u_z the longitudinal velocity of the electron and H_0 the normalized Hamiltonian describing the total energy of the electron in the wakefield. The right initial conditions for the Hamiltonian have to be considered to describe a ionized electron in the wakefield. The electron is assumed to be ionized at phase ξ_{ion} at rest, close to the peak of the laser field, thus :

$$u_z(\xi_{ion}) = 0 \tag{3.5}$$

$$u_\perp(\xi_{ion}) = 0. \tag{3.6}$$

The Hamiltonian of the electron, which is constant over the acceleration, writes as

$$H_0 = \sqrt{1 + u_\perp^2(\xi_{ion}) + u_z^2(\xi_{ion})} - \beta_p u_z(\xi_{ion}) - \varphi(\xi_{ion}) = 1 - \varphi(\xi_{ion}). \tag{3.7}$$

By solving the Hamiltonian for u_z, one can derive the electron trajectories in phase space. Figure 3.3(a) shows the phase space in the co-moving frame (ξ, u_z) for a maximum normalized laser amplitude $a_0 = 2.3$ and a plasma electron density $n_e = 5 \times 10^{18}$ cm^{-3}. An electron is trapped in the wakefield by ionization injection if, and only if, it is ionized ($a(\xi_{ion}) >$
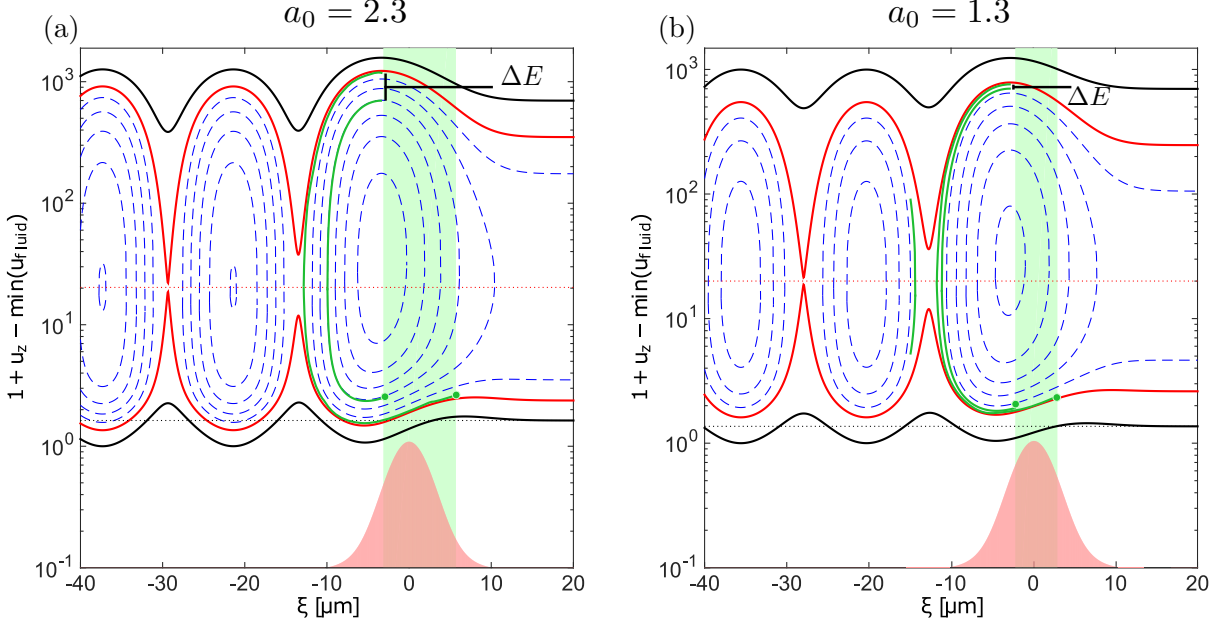
Figure 3.3: Phase-spaces of a plasma wave in the co-moving frame for $a_0 = 2.3$ (a) and $a_0 = 1.3$ (b) describing the ionization injection mechanism. The green region points out the ionization zone of K-shell electrons of nitrogen (as seen in Fig. 3.1). An ionized electron (green point) at rest gains energy in the wake (following the phase-space trajectory depicted in green). The final energy spread ΔE depends on a_0.

$a_{ionization\ threshold}$) and its Hamiltonian H_0 is smaller than the separatrix one (as seen in section 1.2.3). This defines a trapping region in phase space, represented in green in Fig. 3.3(a). The width of the trapping region is directly related to the energy spread of the trapped electron bunch at injection : the wider the trapping region, the larger the energy spread. This is a very interesting feature of ionization injection, since reducing the size of the trapping region would lead to a smaller energy spread. A way to achieve this is to reduce the laser pulse intensity. Figure 3.3(b) shows the phase space of an electron ionized by a laser pulse with $a_0 = 1.3$. The trapping region width is effectively reduced (high ionization state electrons are created around the center of the pulse), thus the bunch energy spread is much better. Simply by reducing the pulse energy, one can potentially control the energy spread of an electron bunch trapped thanks to the ionization injection mechanism. The counterpart of this effect is a reduced charge in the bunch and a lower electron energy due to smaller laser energy.

3.1.3   General bunch properties in ionization-induced injection

The ionization injection technique is mostly used by adding small concentrations of high Z dopant gas in the Helium gas typically used in LWFA experiments. The dopant gas is chosen in a range of noble gases, along with nitrogen and oxygen. Typically, the high Z gas consists of 0.1 % to 5 % of the gas mixture. The effect of the additive gas was found to strongly depend on the gas type for a certain laser energy [McGuffey et al., 2010]. In this study, certain gas mixtures were found to significantly increase the bunch charge as well as the injection probability compare to pure Helium at the same density. Indeed, for a laser pulse of a few dozens of terawatts, the optical field ionization threshold is not reached for the different species. While K-shell electrons

of nitrogen are ionized near the peak of the laser pulse with an intensity close to 10^{19} W.cm^{-2}, K-shell electrons of xenon or krypton have an ionization threshold about ten times higher. Such gas additives cannot be used for ionization injection with a limited laser pulse power. Even more, these heavy species have a large number of outer shells electrons that may cause ionization defocusing of the pulse and prevent efficient acceleration. The choice of gas additive is thus of major importance for a given laser system. In the case of the "Salle Jaune" laser system, with typical intensities on target of 10^{19} W.cm^{-2}, nitrogen is a suitable gas additive.

As long as the laser amplitude is high enough to tunnel-ionize K-shell electrons of the high Z gas additive, ionization injection happens, thus leading to highly charged beams but also to very large energy spread. This effect can be reduced by precisely controlling the laser intensity in order to limit the distance over which the pulse is intense enough to ionize K-shell electrons into the wake. If a significant acceleration length remains after the ionization injection stopped, this can generate electron spectra without a low energy tail [Pak et al., 2010]. The existence of a sharp intensity threshold in laser intensity to trigger ionization injection for a given gas composition allows for a good monitoring of the characteristics of the injected bunch, notably its charge and energy spread.

This effect is the main idea behind the two-stage laser-plasma accelerator presented in Pollock et al. [2011a]. A first injection stage filled with a mixture of Helium and nitrogen is followed by a longer stage containing pure Helium. Ionization injection generates a stable electron bunch with moderate charge, which is further accelerated in the second stage. This methods allows for the generation of quasi-monoenergetic beams moderately charged (about 30 pC) with a good energy spread (about 5 %).

Another idea based on ionization injection is to use a pure high Z gas. This technique was found to be suitable to generate low-charge, high energy electron beams in pure argon [Mori et al., 2009] or nitrogen [Kotaki et al., 2011; Mo et al., 2012]. While ionization induced defocusing of the laser actively competes with relativistic self-focusing [Fedosejevs et al., 1997], this effect can be mitigated with a low enough plasma density. For higher plasma densities, this process can be capitalized on in order to reduce the effective acceleration length so that the final energy of the bunch is limited to a few dozens of MeV. In these previous studies however, the beam charge was limited to a few dozens of picocoulombs with peak energies around 200 MeV.

3.2 Electron acceleration in a pure high Z gas

Several applications for laser-accelerated electron bunches require highly charged beams in the few MeV range. This is particularly the case in radiobiology [Rigaud et al., 2010], femtosecond chemistry [Malka et al., 2010] or industrial radiography [Ben-Ismaïl et al., 2011]. In industrial radiography for example, electrons with low energy can be used to produce bremsstrahlung X-rays with energy not exceeding few MeV. This prevents the use of expansive radiation shielding, not suitable in an industrial environment. In the following part, we point out that electron acceleration in a pure high Z gas coming out of a 700 μm diameter nozzle is a promising way to produce heavily-charged electron beams with relatively low energy. We present the experiment we did at LOA to study this acceleration regime [Guillaume et al., 2015a].

3.2.1 Experimental setup and diagnostics

The main interaction beam of the "Salle Jaune" laser system (28 fs FWHM, 2.1 J) is focused at the entrance of a gas jet using a f/10 off-axis parabola (focal length of 700 mm). The experimental setup is shown in Fig. 3.4. The focal spot FWHM diameter is measured to be 26
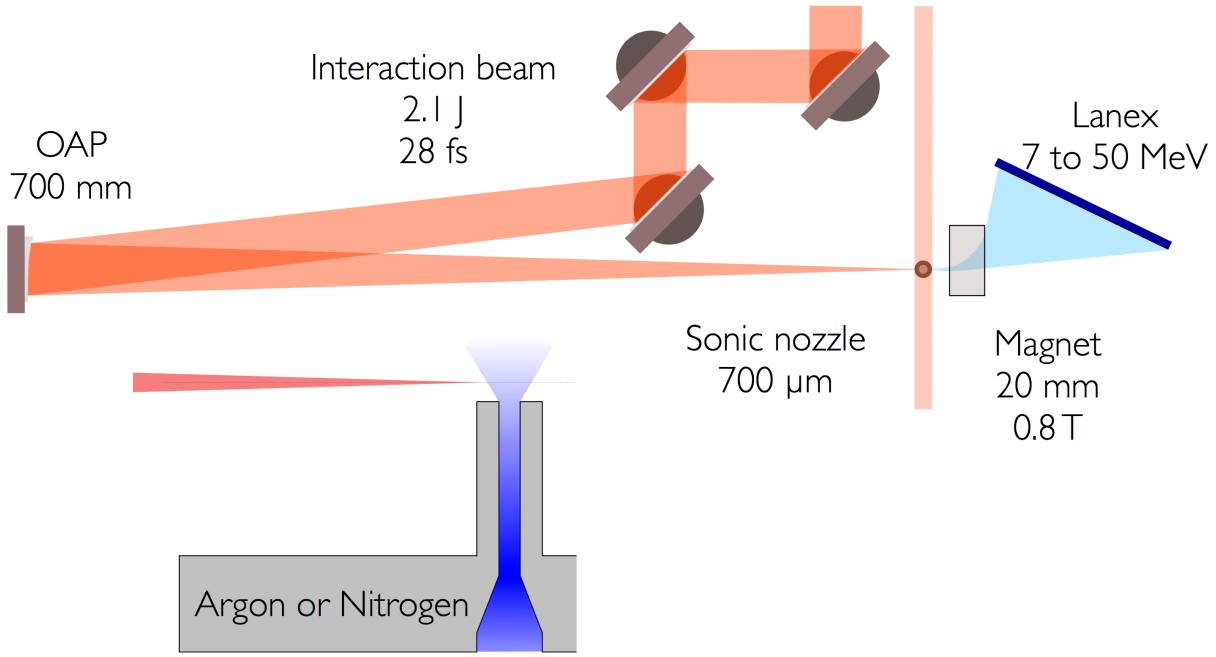
Figure 3.4: Drawing of the experimental setup for electron acceleration in a pure high Z gas.

μm. An image of the focal spot and its transverse profile can be seen in Fig. 3.5(a). The energy contained in this spot diameter is $52 \pm 2\%$ of the total energy. The peak laser intensity and the corresponding normalized vector potential a_0 are $5.1 \pm 0.4 \times 10^{18}$ W.cm^{-2} and 1.60 ± 0.04, respectively.

The gas jet is formed with a 700-μm-diameter sonic gas nozzle (in order to obtain low electron energies) and its density profile is characterized using a Nomarski interferometer afterwards. The laser is fired at a height of 1 mm from the nozzle exit, leading to the formation of a 1.5 mm long plasma. The low energy probe beam is used to measure a shadowgraph of the formed plasma column (as seen in Fig. 3.5(b)). The electron density is varied by varying the backing pressure ahead of the nozzle. Both argon and nitrogen were tested during this experimental campaign. The electron density is estimated considering the electric field ionization threshold for argon and
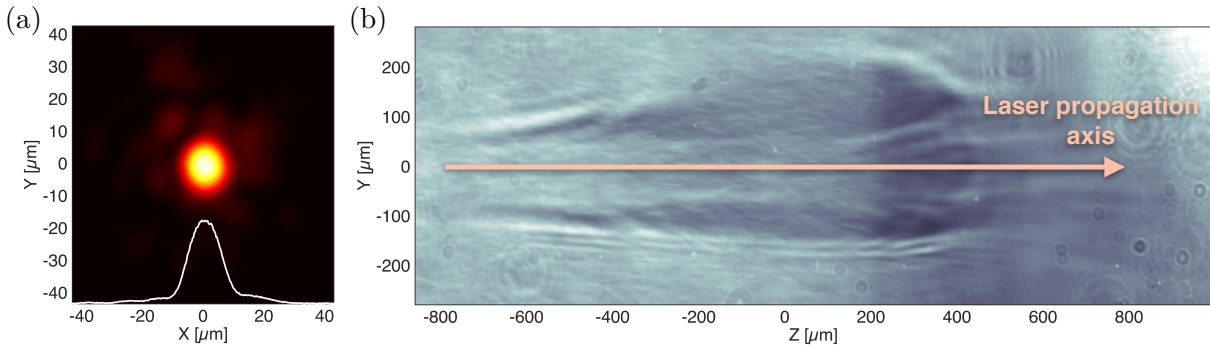
Figure 3.5: (a) Experimental laser focal spot obtained with a 700 mm focal length off-axis parabola. (b) Shadowgraph image of the propagation of the laser in a pure nitrogen gas jet. $Z = 0$ mm corresponds to the center of the nozzle.

nitrogen [Augst et al., 1989]. As explained in section 3.1.1, the ionization threshold for L-shell (and M-shell in the case of argon) electrons is below 10^{17} W.cm^{-2}, meaning that the gas can be considered pre-ionized by the leading edge of the laser pulse up to the ionization states Ar^{8+} or N^{5+}.

Electron spectra are measured with a spectrometer consisting of a permanent magnet (760 mT over 20 mm) combined with a Lanex placed 322 mm after the nozzle output. This is a different electron spectrometer than the one presented in section 1.4.3 as we want to observe lower electron energies. The Lanex is imaged on a 16 bit CCD camera. In the chosen configuration, the minimum (resp. maximum) cut-off energy of the electron spectrometer is 7 MeV (resp. 50 MeV). The transverse acceptance angle of the Lanex for this geometry is 110 mrad.

In order to get more insight of the underlying physics of injection and acceleration in this regime, simulations are performed using the PIC code CalderCirc [Lifschitz et al., 2009]. This fully electromagnetic 3D code uses cylindrical coordinates (r, z) and Fourier decomposition of electromagnetic fields in the poloidal direction. The two first Fourier modes of the decomposition $(m = 0, 1)$ are considered, allowing for the description of the linearly polarized laser pulse and the quasi-cylindrical fields of the plasma wave.

3.2.2 Experimental results

We first use a gas target composed of pure argon with a plasma electron density of $n_e = 1.9 \times 10^{19}$ cm^{-3} (considering a plasma of Ar^{8+}). Figure 3.6 shows the electron spectra measured with the Lanex for five consecutive shots. We observe a very good shot-to-shot stability, at the same time in pointing, spectrum shape and total charge. Due to the large acceptance angle of the electron spectrometer, we are able to collect completely the charge of the electron beam between 7 and 50 MeV. The total integrated charge above 7 MeV is 910 pC, which is a rather large value for a laser-accelerated electron beam with these laser and plasma conditions.
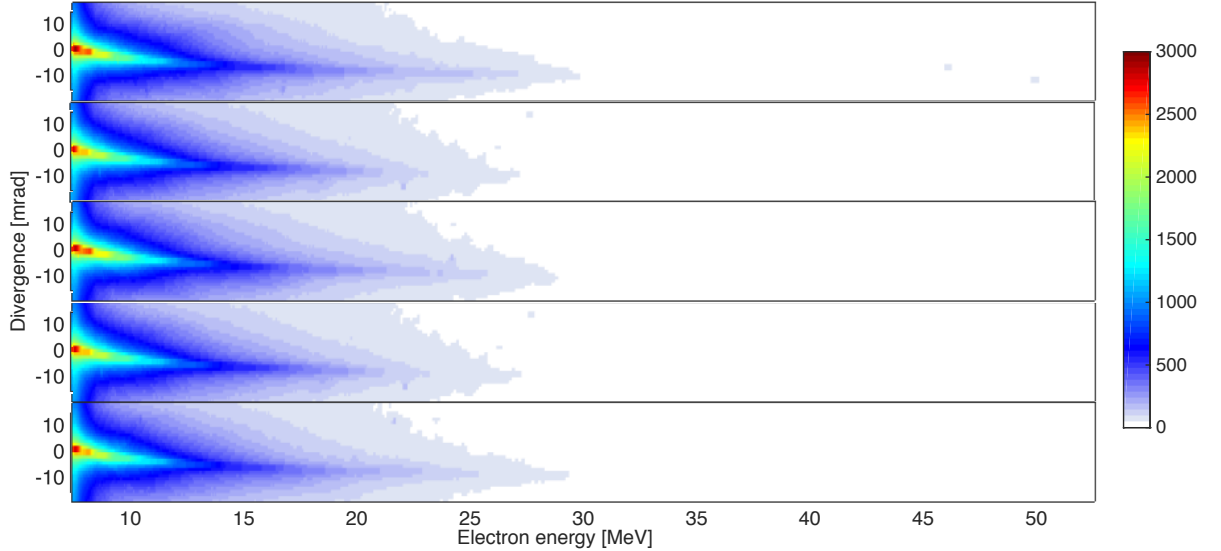
Figure 3.6: Raw electron spectra for five consecutive shots for an argon plasma with $n_e = 1.9 \times 10^{19}$ cm^{-3}.

The mean integrated spectrum over the transverse direction is shown in Fig. 3.7(a). Note that the spectrum is represented in logarithmic scale, thus the charge per MeV is divided by
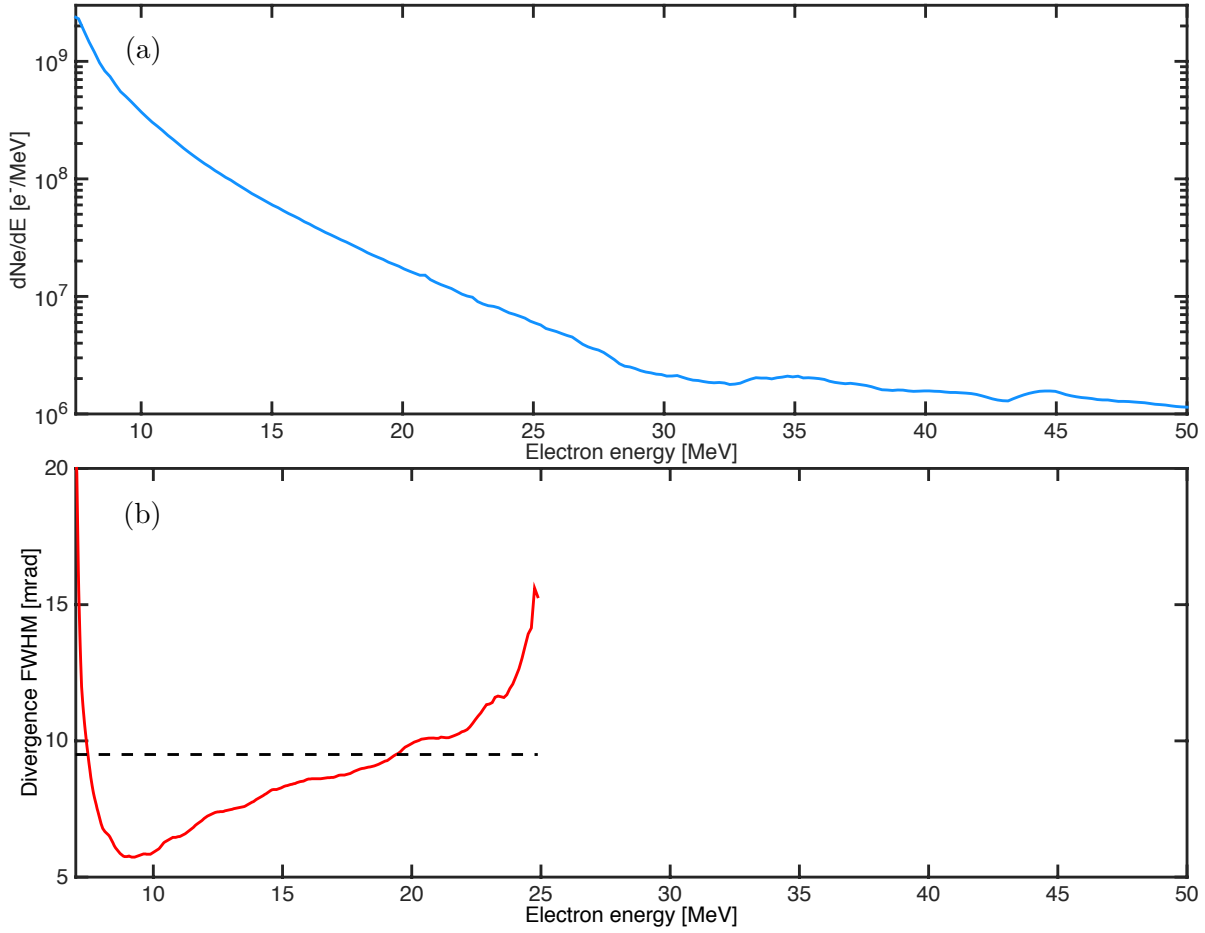
Figure 3.7: (a) Experimental electron spectrum obtained in an argon plasma with a plasma density of $n_e = 1.9 \times 10^{19}$ cm^{-3}. (b) FWHM divergence of the beam function of electron energy. The signal is too low above 25 MeV to calculate the divergence.

almost a factor 100 between 7 MeV and 20 MeV. The energy distribution has a quasi-Maxwellian shape, underlining continuous injection of electrons during the acceleration. Indeed, the peak laser normalized amplitude a_0 is likely high enough during the whole propagation to tunnel-ionize Ar^{9+} (ionization potential of 422 eV, corresponding to a $a_{0,threshold} = 0.9$ for the laser amplitude) and beyond, leading to ionization induced injection over the propagation in the plasma. Figure. 3.7(b) shows the FWHM divergence of the beam as a function of electron energy, as measured on the Lanex. Note that above 25 MeV, the charge is too weak to effectively calculate a divergence. The divergence quickly drops from 20 mrad to 6 mrad between 7 and 8 MeV, and increases again up to 15 mrad at 25 MeV. Ionization injected electrons are supposedly created close to the propagation axis, producing low divergence electron beams. Indeed, 10 mrad at 8 MeV is a rather low divergence for such a low energy (typically a few dozens of milliradians in the self-injection regime).

Laser filamentation can be an issue for laser propagation in a high Z gas. Such a phenomenon is observed in Fig. 3.5(b), where filamentation induced by ionization defocusing appears mainly on the sides of the plasma (lower electron density region). In this case, laser filamentation occurs after around 600 μm after the beginning of the plasma for a plasma density of $n_e =$
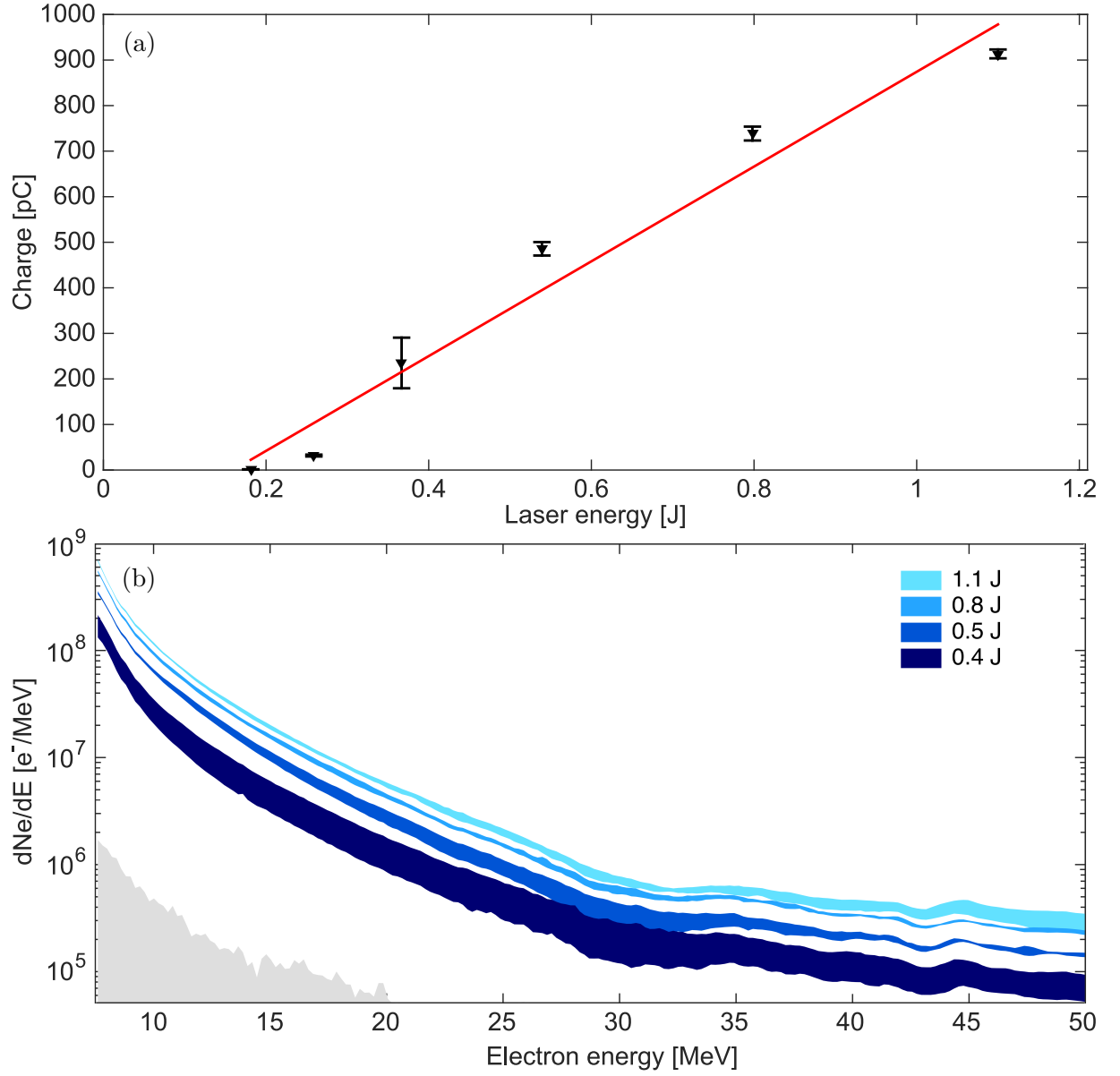
Figure 3.8: (a) Variation of the charge above 7 MeV with the laser energy. The black triangles represent the mean charge over five consecutive shots, with the error bars showing the standard deviation. The red line is a linear fit of the charge evolution. (b) Experimental electron spectra for four different laser energies. The width of the colored area indicates the standard deviation over five consecutive shots. The grey area represents the detection threshold of the spectrometer.

1.9×10^{19} cm^{-3}. However, as the depletion length of the laser is about 600 μm, the injection and acceleration are almost finished when the laser starts to defocus and filament. The filamentation process does not affect the electrons during the acceleration but mainly in the downward density gradient of the gas jet, where the laser does not play an important role on the physics of the electron beam anymore.

Electron acceleration in pure argon allows for the generation of highly-charged electron beams (up to almost 1 nC) with relatively low energies (most of accelerated electrons are below 12 MeV). Very similar results were obtained in a pure nitrogen plasma. These beam parameters are interesting, as the energy distribution look very stable shot-to-shot.

3.2.3 Energy laser influence : beamloading effect

The laser energy in the focal spot is varied between 1.1 J and 0.2 J (corresponding to a peak intensity on target of 5.1×10^{18} W.cm^{-2} and 9.7×10^{17} W.cm^{-2}) by rotating a half-wave plate followed by a polarizer in the path of the laser beam before compression. Figure 3.8(a) shows the evolution of the total integrated charge above 7 MeV (lower limit of the electron spectrometer) obtained in an argon plasma with an electron plasma density of 1.9×10^{19} cm^{-3} as function of the laser energy. There is almost no electrons below 0.4 J : the laser energy is not sufficient for the pulse to self-focus in the plasma, so the intensity is too low to trigger ionization injection of inner-shell electrons of argon. Above this energy threshold, the total charge linearly increases by 110 pC per 100 mJ, up to 910 pC for the maximum laser energy (1.1 J on target). Very similar results were obtained with a nitrogen gas jet. The charge is very stable shot-to-shot (standard deviation is 23 % for the worst case at 0.36 J, down to 1 % at 1.1 J).
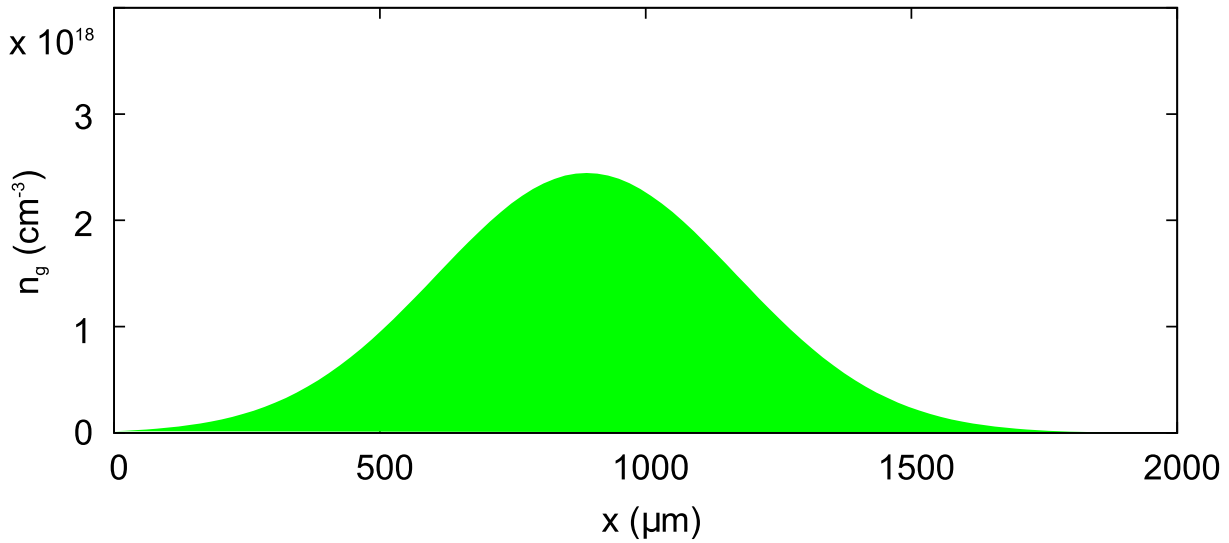
Figure 3.9: Neutral density profile used in the simulations of electron acceleration in pure nitrogen.

Figure 3.8(b) shows the dependency of the electron spectra shape for four different laser energies, from 0.4 J to 1.1 J (darker to lighter blue). The width of each curve represents the standard deviation of the spectrum over five consecutive shots. The spectra have a very good shot-to-shot stability in this laser energy range. For lower laser energy, ionization injection is not triggered and the measured signal is below the detection threshold (represented in grey in Fig. 3.8(b)). Note that the vertical axis is shown in logarithmic scale, underlining the stability of
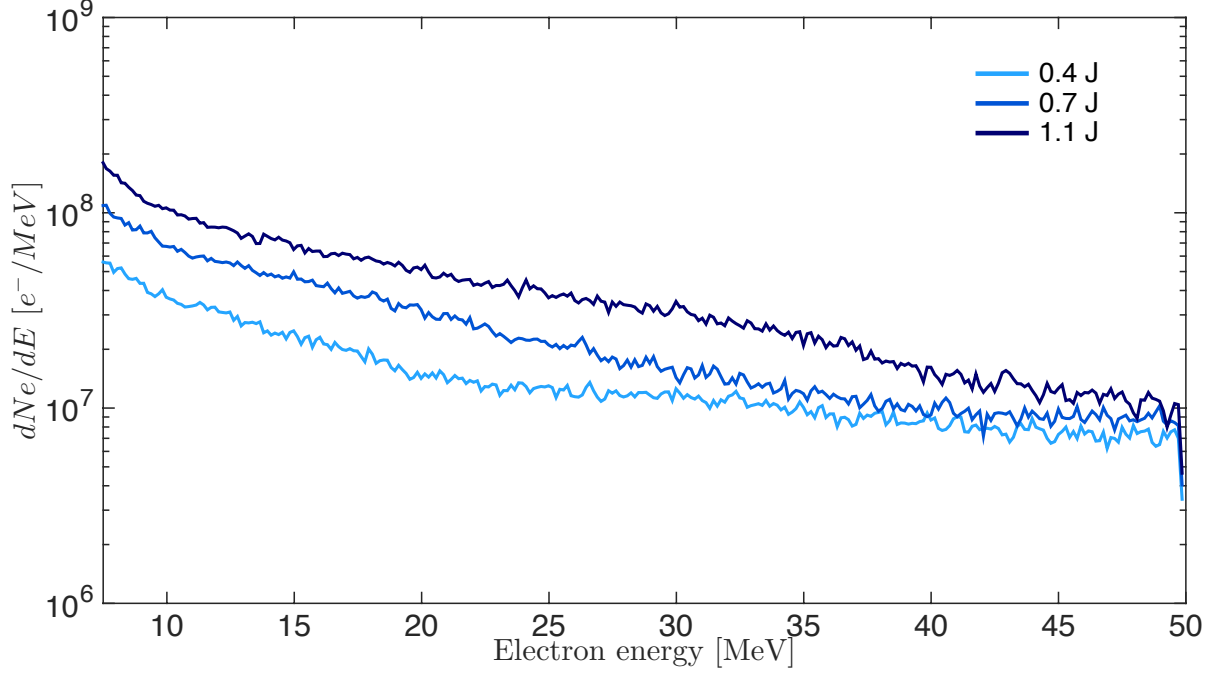
Figure 3.10: Simulated electron spectra (plasma density of $n_e = 1.9 \times 10^{19}$ cm^{-3}) for three different laser energies.

these spectra. Whereas the total charge varies linearly with the laser energy, the general shape of the electron spectrum stays roughly the same (the ratio of high energy electrons compare to low energy electrons is almost the same whatever the laser energy). This is an unexpected feature, because usually the wakefield amplitude, and thus the amplitude of the accelerating field, strongly depends on the laser intensity. There should be more high energy electrons when the laser intensity increases. The straightforward charge tunability of this source with the laser energy and the constant shape of the spectrum are very convenient to study the charge influence on the electron beam acceleration and propagation.

To get more insight on this striking effect, simulations are performed using a mesh with $\Delta x = 0.2 \ k_0^{-1}$, $\Delta r = 1.5 \ k_0^{-1}$ (with $k_0 = 1/\lambda_0$). The neutral gas density profile defined from the experimental characterization can be seen in Fig. 3.9. The peak density is at 900 μm. Simulations begin with pure neutral nitrogen, which is ionized via tunnel ionization, resulting in a peak electron density of $n_e = 1.9 \times 10^{19}$ cm^{-3}. The number of macro-particles per cell before ionization is 100, which corresponds to 500 macro-electrons per cell in the region of full ionization of the L-shell of nitrogen. The other parameters are considered from the experiment.

Figure 3.10 depicts the simulated electron spectra for three different laser energies (0.4, 0.7 and 1.1 J). The very weak dependency of the spectra shape with the laser energy is retrieved. Indeed, while the integrated charge in the considered energy range is reduced by lowering the laser energy, the energy distribution remains roughly the same. The ratio of low energy electrons compare to high energy electrons keeps roughly the same value for energies higher than 0.7 J,
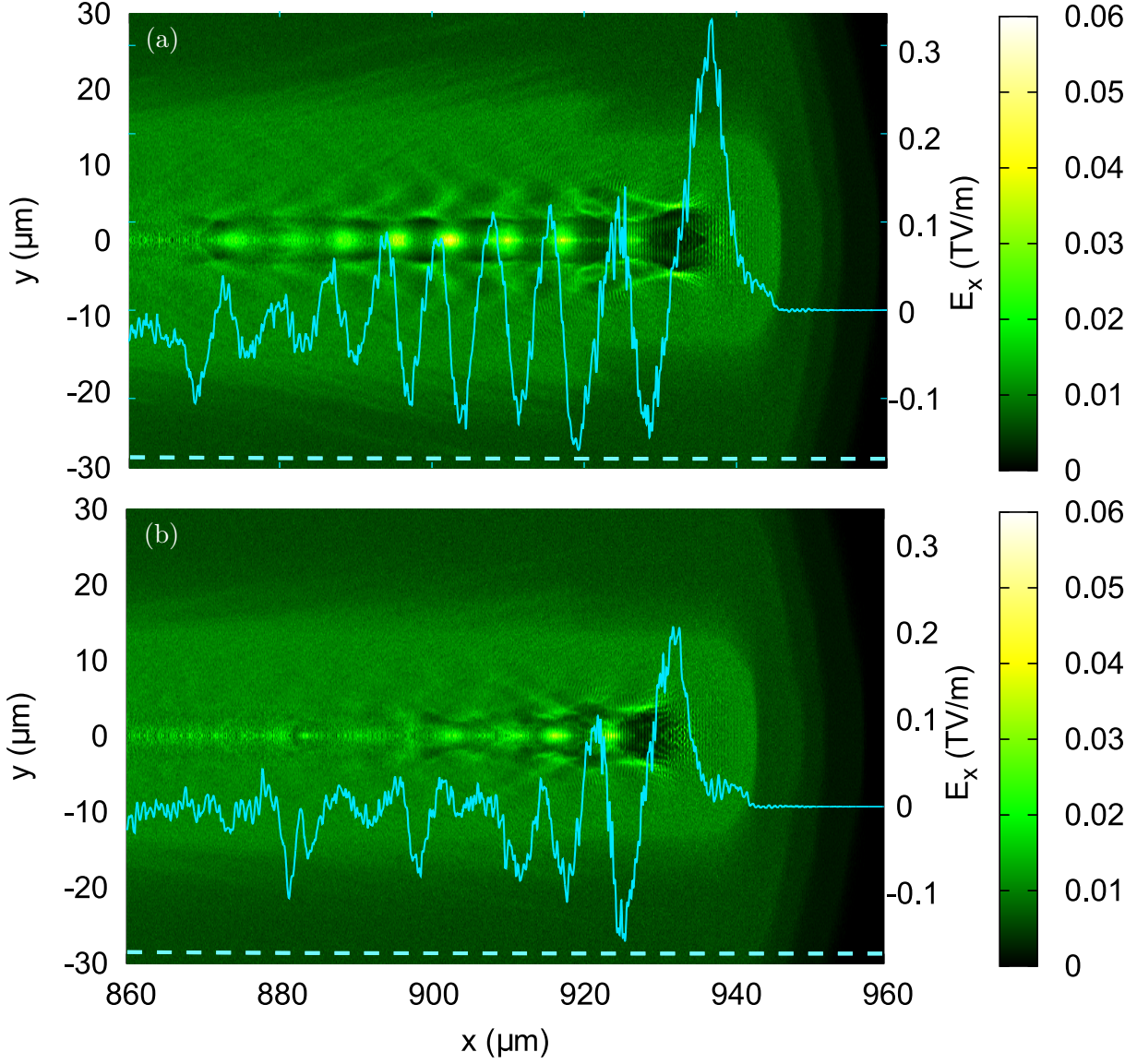
Figure 3.11: Spatial distribution of electron density for laser energies of 1.1 J (a) and 0.4 J (b) around the middle of the gas jet (background electron density $n_e = 1.9 \times 10^{19}$ cm^{-3}). The superimposed plots show the longitudinal electric field on the axis (light blue). The dashed light blue line represents the theoretical injection threshold for an electron created around the middle of the gas jet ($E_{sat} = 0.47E_0$).

and is even slightly lower for the smallest laser energy :

$$\frac{dN_e/dE_{10MeV}}{dN_e/dE_{40MeV}} = \begin{cases} 5.5, & \text{for } E_{laser} = 1.1 \ J \\ 5.3, & \text{for } E_{laser} = 0.7 \ J \\ 3.2, & \text{for } E_{laser} = 0.4 \ J \end{cases} \tag{3.8}$$

The number of macro-particles over 30 MeV is likely quite low for 0.4 J (the simulation noise is substantial in Fig. 3.10), thus the different ratio for this laser energy may originate from that. The electron energy distribution coming out of the laser-plasma accelerator is related to the longitudinal electric field the electrons experienced during the acceleration. To understand the dependency upon the laser energy, we show in Fig. 3.11 the accelerating field and the spatial distribution of electron density around the middle of the gas jet for two different laser energies from the PIC simulations.

For the high energy pulse (1.1 J, Fig. 3.11 (a)), the laser strongly excites the wakefield, generating up to seven buckets with similar amplitude, each loaded with electrons. The total charge of the beam is around 1 nC, very close from the experimentally measured charge (910 pC). Note that electrons with energies under 7 MeV are considered in the simulations. The accelerating field in each of these plasma periods is almost the same, close to -0.17 TV.m^{-1}.

In contrast, only two periods of the wakefield are loaded behind the low energy pulse (0.4J, Fig. 3.11 (b)). Behind the third plasma period, the wakefield is completely blurred out and no electrons are trapped. The charge injected in these two buckets is roughly five times lower than in the previous case (around 200 pC in the beam). However, the maximum accelerating field inside the buckets is similar for both cases ($E_x = -0.17$ TV.m^{-1}).

Figure. 3.11 (a) shows that six periods are fully loaded and the seventh period is partially loaded with 1.1 J. In contrast, only the first period is fully-loaded and the second is partially loaded with 0.4 J (Fig. 3.11 (b)). Therefore one can estimate that the increase of the charge due to the number of loaded periods is about 4.2, whereas the total charge is multiplied by a factor of 5. The lengthening of the bubble when laser energy is increased can explain the missing factor in the total charge increase. Indeed, as laser energy is increased, the bubble radius evolves as the square root of the normalized vector potential as $r_b \sim 2k^{-1}\sqrt{a_0}$ [Lu et al., 2007]. The size of the first bubble is estimated to increase by a factor around 1.3 from the density map in Fig. 3.11. Although the main effect of the charge increase is the trapping of electrons into multiple wave periods, the bubble size increase also plays a role. Furthermore, the higher the laser energy, the more evacuated the bubble is, allowing to trap more electrons and increasing the charge.

Figure. 3.11 shows that the charge increase goes along more and more loaded buckets, but does not explain the reason of the spectrum shape. Simulations provide additional explanations to understand the effect of laser energy onto the electron spectra shape and total charge. As electrons are ionized at rest in ionization injection [Pak et al., 2010], they must acquire sufficient energy to be injected in the wakefield. The most favorable ionization position to get injection corresponds to the point of the bubble where the accelerating field vanishes, towards the center of the bubble. Electrons resulting from ionization at that position experience the longer accelerating length. In other terms, as ionization injection is the dominant process of injection, if these electrons are not trapped, no other electron will be trapped (as explained in section 3.1.2).

Simulation shows that electrons ionized in the upward density gradient cannot be trapped in the first plasma bucket because the phase velocity of the rear of the plasma cavity is very
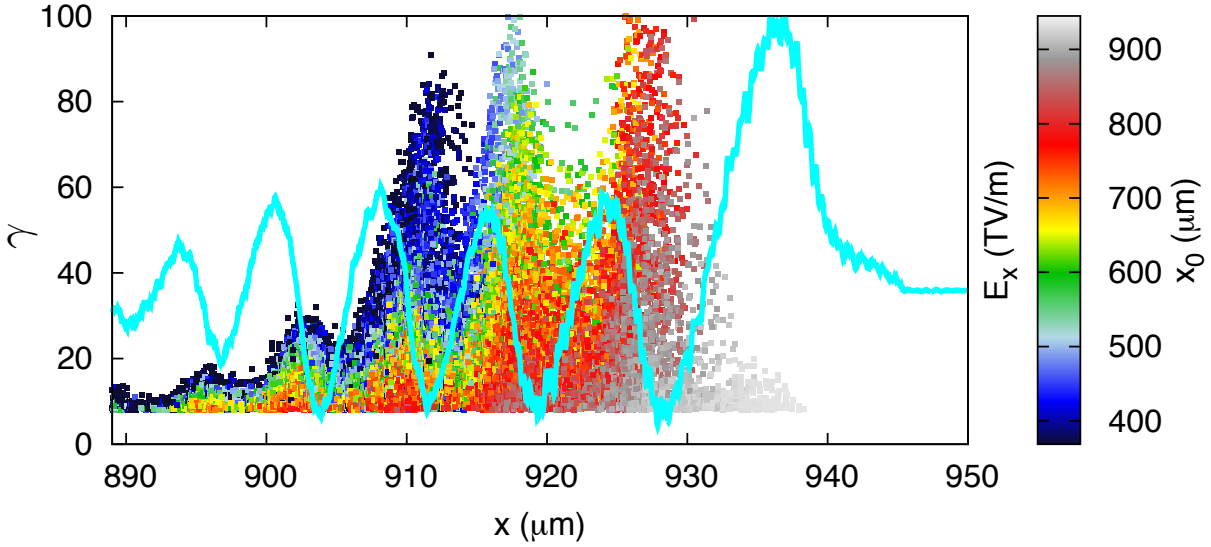
Figure 3.12: Phase space distribution (x,γ) of electrons coming from ionization of N^{5+} at a position around the middle of the gas jet. The color scale x_0 represents the position of ionization of each colored macro-particle in the plasma. The superimposed plot shows the longitudinal electric field on the axis (light blue) at that position.

high in the upward gradient, possibly even larger than *c*. As the laser approches the peak of the plasma density profile, the bubble slows down and electrons can start to be injected. They slipped across several buckets while the laser is crossing the upward density gradient, thus they can be in a bucket which is several periods after the laser when their velocity exceeds the wake phase velocity (i.e when they are trapped).

To get insight into this dynamics, one can observe the energy gained by electrons depending on their ionization position, noted x_0. The phase space distribution (x, γ) of electrons coming from ionization of N^{5+} is shown in Fig. 3.12, at a position around the middle of the gas jet. Each simulated macro-particle is colored depending on its ionization position x_0. Electrons ionized at the beginning of the upward density gradient are depicted in dark blue, while electrons ionized almost at the center of the jet are shown in red/grey (as seen in the colorbar). Electrons ionized in the upward density ramp (between $x_0 \sim 400$ μm and $x_0 \sim 600$ μm, corresponding to the purple/blue dots) are accelerated in the first bubble to relativistic energies, but they are not trapped because in this density region the wakefield transiently is superlumineous (meaning that the rear of the cavity shrinks with a local velocity higher than the local group velocity of the laser pulse). These electrons dephase in the first plasma periods, passing from one bucket to another. They are eventually trapped in a bucket far from the laser, when the pulse approaches the density peak (the wakefield velocity around this position is smaller than in the upward ramp, allowing for electrons to be injected). At this position, tunnel ionization continues in the first bubble, ionizing electrons depicted in pink in the first bucket. The result is that electrons ionized early during the propagation are trapped in a wave period far from the laser, and electrons ionized in the density peak are trapped preferentially in the first bubble (corresponding to red/grey dots in Fig. 3.12). All these electrons are trapped roughly at the same time.

Due to the beamloading of each plasma period, the accelerating field decreases as more and more electrons are injected. The longitudinal field decreases down to a point when injection stops because electrons cannot gain enough energy from the wake to be trapped. The longitudinal
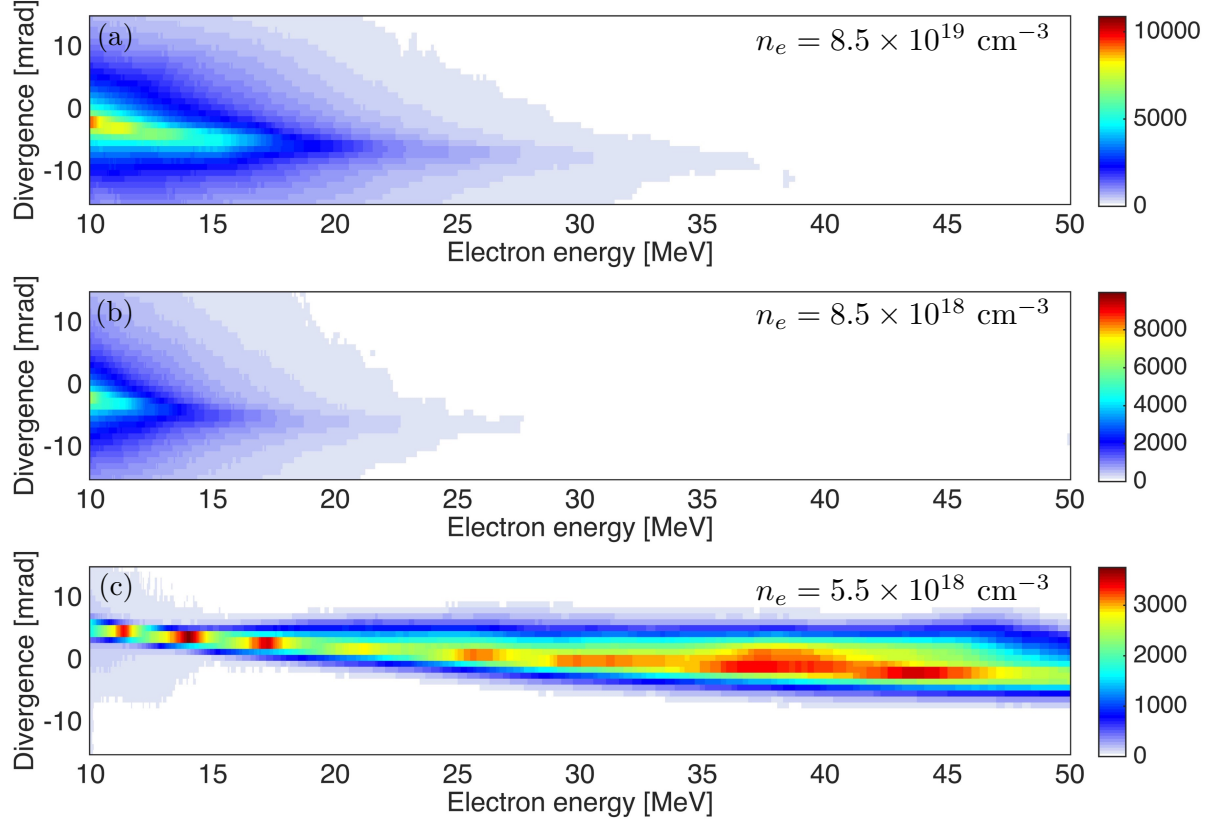
Figure 3.13: Raw experimental electron spectra for three different electron plasma densities : (a) $n_e = 8.5 \times 10^{19}$ cm^{-3}, (b) $n_e = 8.5 \times 10^{18}$ cm^{-3} and (c) $n_e = 5.5 \times 10^{18}$ cm^{-3}.

field is depicted in light blue in Fig. 3.12. It reaches almost the same saturation level whatever the considered plasma period. As seen in Fig. 3.11, this saturation level is also independent from the laser energy, and is reached in a bucket once it is fully loaded.

The saturation field can be estimated in the frame of the 1D non-linear plasma wave model [Esarey and Pilloff, 1995]. The minimum field for injection of an electron initially at rest at the center of the bubble is $E_{sat} = -0.47E_0$, where E_0 is the critical field in the linear regime defined in eq. (1.50). For the peak density of the gas jet ($n_e = 1.9 \times 10^{19}$ cm^{-3}), the calculation gives $E_{sat} = -0.18$ TV.m^{-1}, which is in good agreement with the maximum accelerating field found in the simulations $E_x = -0.17$ TV.m^{-1}. As soon as the field is lower than E_{sat} in a bucket, injection stops because the velocity of electrons never exceeds the wake phase velocity (as the accelerating field is too low). Electrons go onto the following bucket, and so on.

3.2.4 Electron density influence : spectrum flattening

As presented in the previous section, the laser energy hardly impacts the electron spectral distribution because the longitudinal field saturates in a plasma period as soon as it is fully loaded with electrons. Nonetheless, the electron plasma density is found to have a strong influence on the energy distribution.

The plasma density is varied from 8.5×10^{19} cm^{-3} to 5.5×10^{18} cm^{-3} by reducing the nitrogen backing pressure at the sonic nozzle input. Figure 3.13 shows the electron spectra measured for three electron densities for maximum laser energy (intensity on target of 8.9×10^{18}
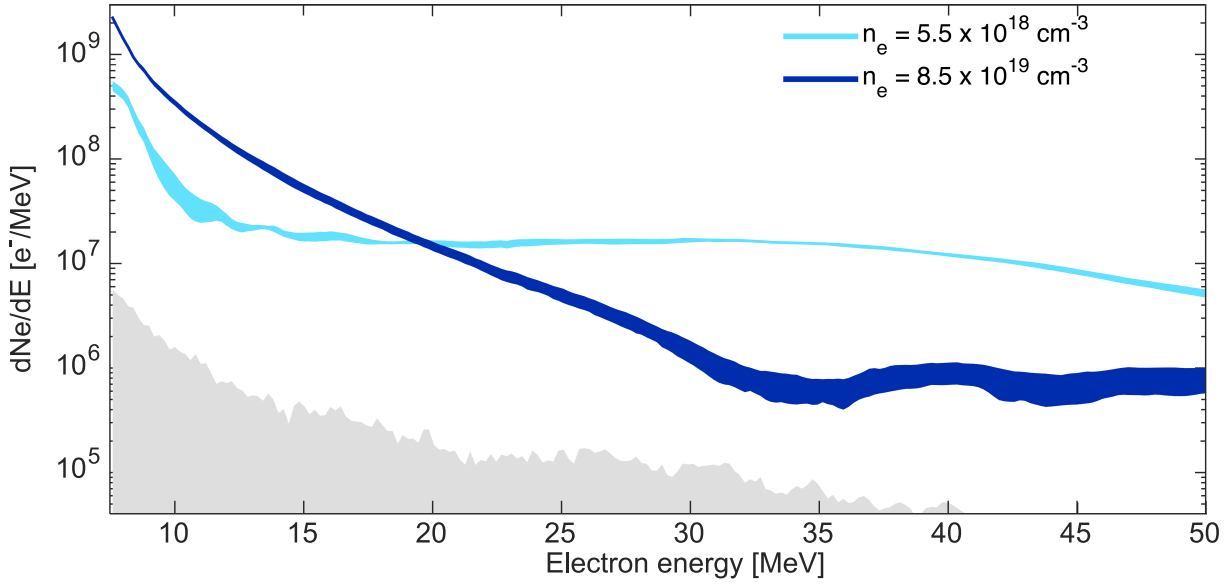
Figure 3.14: Influence of the electron density on the experimental energy distribution of electrons for a nitrogen plasma at two electron densities, $n_e = 8.5 \times 10^{19}$ cm^{-3} and $n_e = 5.5 \times 10^{18}$ cm^{-3}. The colored area indicates the standard deviation over five consecutive shots. The grey shaded area indicates the detection threshold of the spectrometer.

W.cm^{-2}). The spectrum shape does not vary while the density is decreased by a decade (as seen in Fig. 3.13(a-b)), and then changes abruptly for 5.5×10^{18} cm^{-3} (Fig. 3.13(c)). In the following, a plasma density of 8.5×10^{19} cm^{-3} is referred to as the high density case while a plasma density of 5.5×10^{18} cm^{-3} is referred to as the low density case. The electron spectrum in Fig. 3.13(a) for the high density case has been presented in the previous section. When the plasma density is reduced, the electron spectrum shape drastically changes, turning into a much flatter energy distribution from 10 to 50 MeV, as seen in Fig. 3.13(c). The total charge of the beam is also reduced from 250 pC to 50 pC. Note that the Root-Mean-Square divergence of the beam drops from 7 mrad to 2 mrad at 20 MeV when the plasma density is reduced. Such a low divergence at that low electron energy is a very good feature. The divergence does not depend much on the electron energy in the low density case and stays roughly the same up to 50 MeV. Note that oscillations can be seen in the electron spectrum presented in Fig. 3.13(c) : they may originate from the multi-bunch structure of the electron beam in several buckets, each micro-bunch having a different mean energy.

Figure 3.14 shows the average electron spectra integrated over the transverse direction for five consecutive shots each, at $n_e = 5.5 \times 10^{18}$ cm^{-3} (lighter blue) and $n_e = 8.5 \times 10^{19}$ cm^{-3} (darker blue). Note that the oscillations in the spectrum are not visible anymore due to the mean). The width of the lines corresponds to the standard deviation of the spectra. For the high density case, the number of electrons per MeV decreases by roughly four orders of magnitude from 7 MeV to 35 MeV, with the spectrum shape close to a thermal one. The quasi-Maxwellian shape of the spectrum is due to the continuous injection of electrons in multiple buckets along the acceleration, as explained in the previous section. However, as the electron density is lowered, the electrons undergo a different regime during the acceleration in which the charge per MeV drops quickly below 12 MeV, but then is much flatter and keeps roughly the same order of magnitude up to the spectrometer cut-off over 50 MeV.
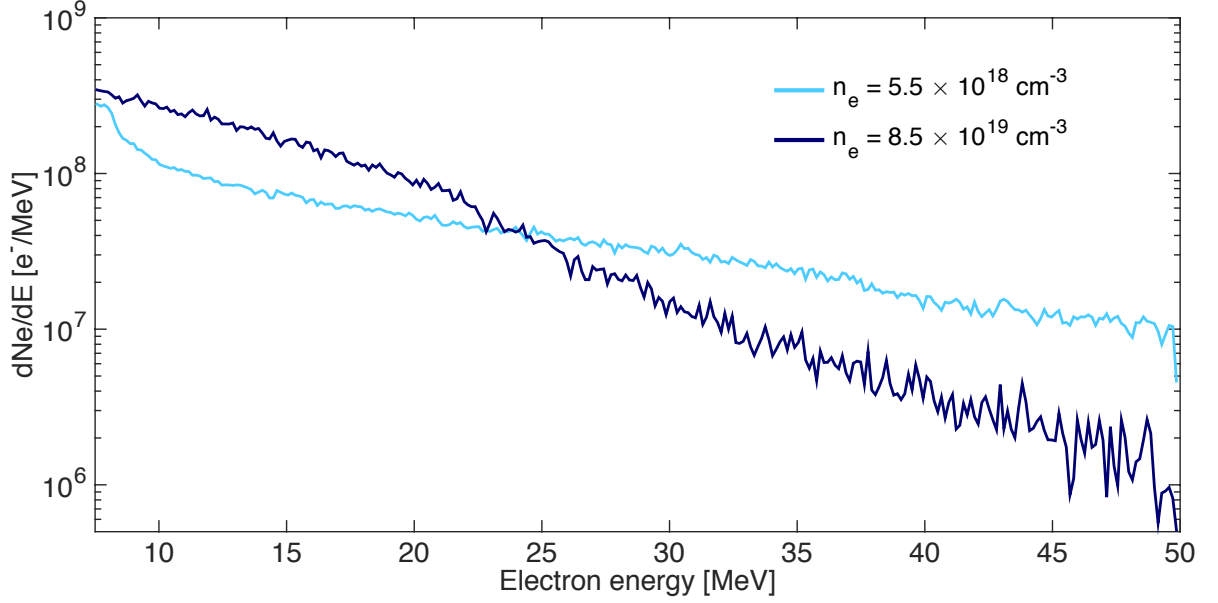
Figure 3.15: Simulated electron spectra for a nitrogen plasma at two electron densities, $n_e = 8.5 \times 10^{19}$ cm^{-3} and $n_e = 5.5 \times 10^{18}$ cm^{-3}.

Again, PIC simulations help us to reproduce the main trends of the spectrum dependency on the plasma density. Simulations are performed using the profile presented in Fig. 3.9, with the peak density varying between $n_e = 8.5 \times 10^{19}$ cm^{-3} and $n_e = 5.5 \times 10^{18}$ cm^{-3}.

Figure 3.15 depicts the simulated electron spectra for the low (light blue) and the high density (dark blue) cases. The main trends of the spectrum dependency on the gas density found in the experiment are retrieved in the simulations. Similarly to the experimental results, at high density the number of electron per MeV drops by a factor ~ 100 between 7 and 50 MeV, whereas at low density the drop is around a factor 10. The second feature retrieved in the simulations is the particular shape of the spectrum at low electron density compare to the high electron case, presenting a fast drop below 10 MeV and a flatter region beyond this value.

Simulations also demonstrate that, as expected, the dynamics of the laser propagation strongly depends on the plasma density. Figure. 3.16 shows the normalized laser amplitude a_0 along the density profile for the two plasma densities. At high density, the relativistic self-focusing of the laser produces a fast increase of the laser intensity around $x \sim 400$ μm. After 300 μm of propagation ($x \sim 700$ μm) the pulse energy is depleted (70% of the laser intensity is lost, either by transfer to the plasma or due to ionization induced defocusing and filamentation) and self-focusing stops. What remains of the laser pulse propagates towards the end of the plasma without exciting strong plasma waves. At low density, self-focusing and pulse depletion are much weaker, therefore the normalized laser amplitude remains lower than 3 over all the plasma length. Electrons coming from ionization of N^{6+} and N^{7+} are injected in several buckets of the wakefield when reaching the density peak. Whatever the density, the laser has thus little effect on electron acceleration in the downramp gradient of the plasma density profile. It is either depleted for high density or weakly focused for low density (with a_0 staying under 2, generating a quite weak wakefield). The strong difference between the two electron spectra must come from another process.

To get insight of the underlying phenomenon which is responsible for the modification of
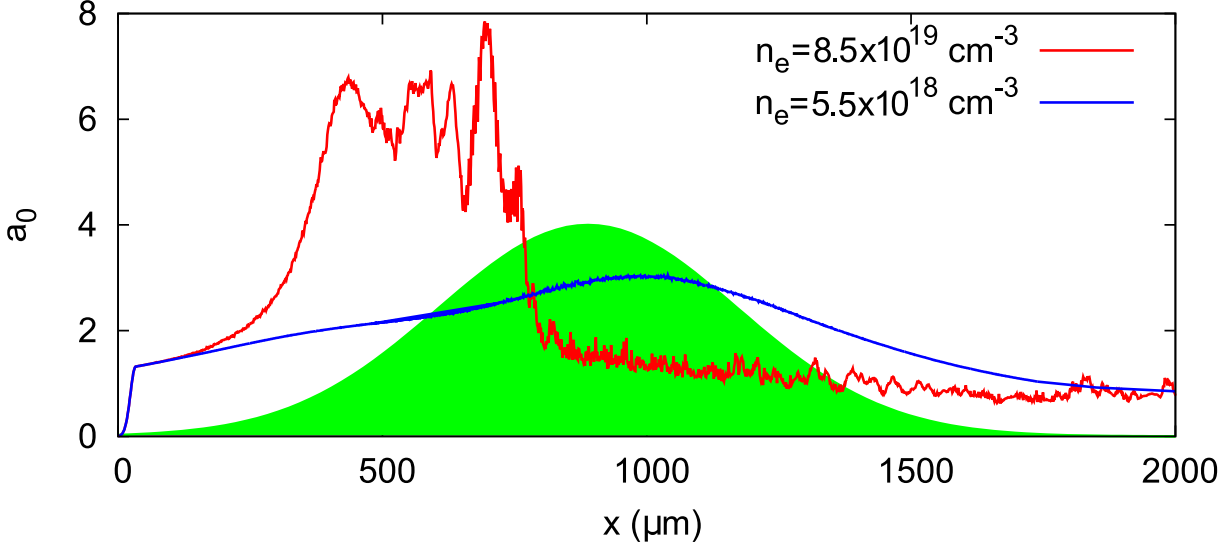
Figure 3.16: Evolution of the normalized laser amplitude a_0 along the propagation in the plasma density profile (in green) coming from simulations, for a high (red) and a low (blue) density nitrogen target.

electron energy distribution during the acceleration process, Fig. 3.17(a) shows the variation of the electron energy distribution for two positions in the gas jet for an electron plasma density of $n_e = 5 \times 10^{18} \mathrm{cm}^{-3}$. Just after the center of the gas jet (around $x = 1200$ μm), the electron spectrum (in red in Fig. 3.17(a)) has a quasi-Maxwellian shape similar to the shape in the high density case. Towards the end of the jet however (around $x = 1700$ μm), the spectrum is flatter, with more high energy electrons and less electrons below 15 MeV. The physical phenomenon flattening the spectrum taking place between $x = 1200$ μm and $x = 1700$ μm (in the downward density gradient) must mainly originate from something else than the laser evolution.

In the low density case, simulations show that electrons are injected around $x = 600$ μm. The ionization injection process leads to the trapping of an electron macro-bunch which is composed of several distinct sub-bunches, where the separation length is approximately the local plasma wavelength λ_p. This multi-bunches structure comes from the beamloading in each bucket, as explained in the previous section. The multi-bunch structure is visible in the spatial distribution of electron density around the middle of the gas jet (as seen in Fig. 3.17(b)). When the multi-bunch propagates through the downward density gradient at the end of the gas jet, its structure starts to blur up. By the middle of the falling gradient of the gas jet ($x = 1200$ μm), the different sub-bunches tend to form a continuous macro electron bunch. Towards the end of the jet (see the electron density spatial distribution in Fig. 3.17(c)), the electron plasma density is much lower. The macro-bunch, with a length close to 60 μm, is able to drive its own wakefield because the bunch length is resonant with the local plasma density (same order of magnitude than the local λ_p). Indeed, the leading part of the accelerated electron bunch can create its own plasma wakefield if the number density of the electron bunch n_{bunch} is larger than the background electron plasma density [Blumenfeld et al., 2007; Pae et al., 2010; Litos et al., 2014]. In our case, one can estimate the mean electron density in the bunch from the simulations as $n_{bunch} \simeq 7 \times 10^{17}$ cm^{-3}. This is larger than the local electron density $n_e = 5.2 \times 10^{17}$ cm^{-3} towards the end of the gas jet around $x = 1700$ μm, allowing for the formation of a very large bubble in the wake of the macro-bunch (with its bunch structure still visible in Fig. 3.17(c)).
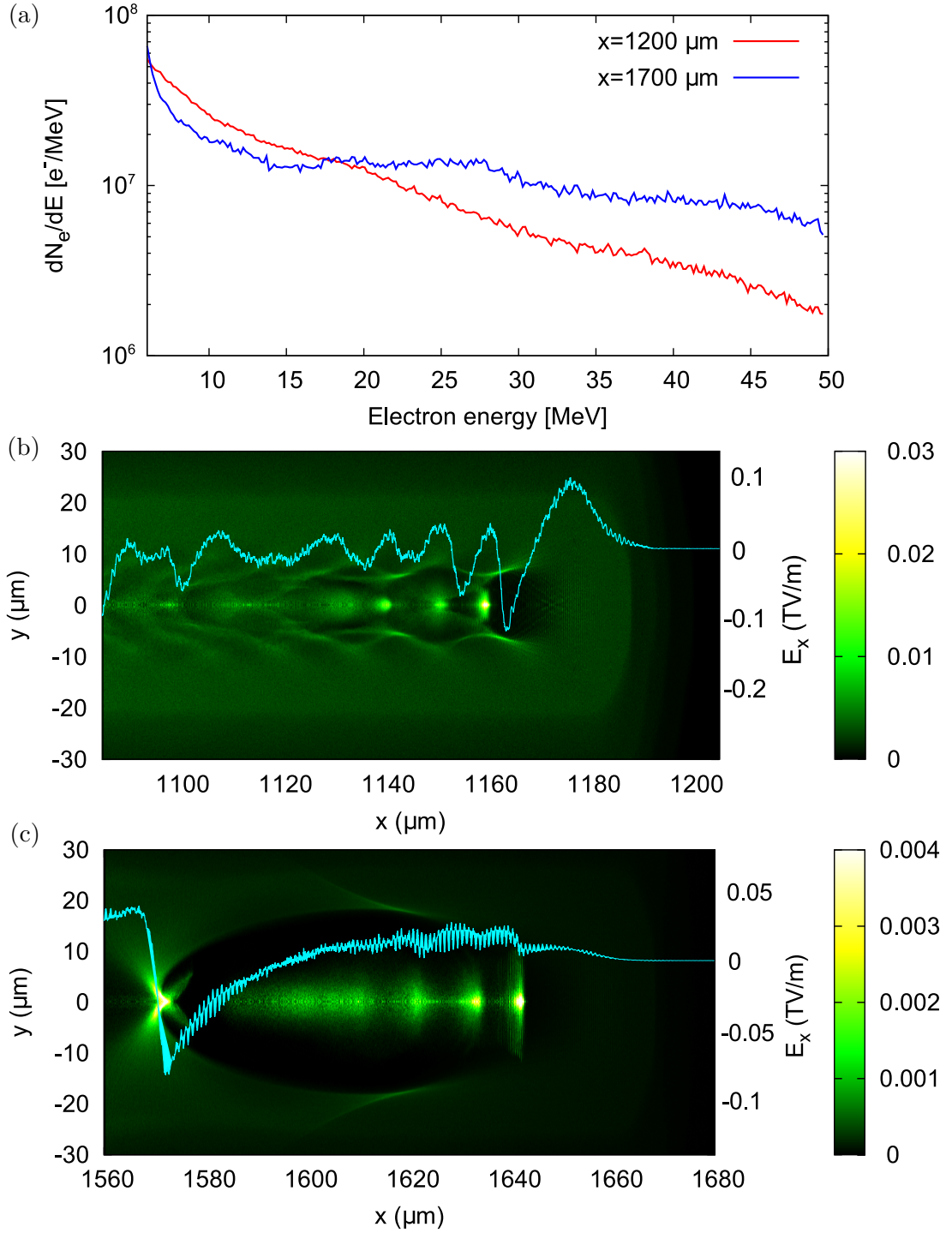
Figure 3.17: (a) Electron spectra around the center (red) and the end (blue) of the gas jet, the center of the gas jet being located at x = 900 μm. (b) Spatial distribution of electron density close to the center (b) and at the end (c) of the gas jet in the low density case. The local electron densities are $n_e = 5.2 \times 10^{17}$ cm^{-3} in (b) and $n_e = 3.5 \times 10^{18}$ cm^{-3} in (c). The superimposed plots in (b) and (c) show the longitudinal electric field on the axis (light blue).
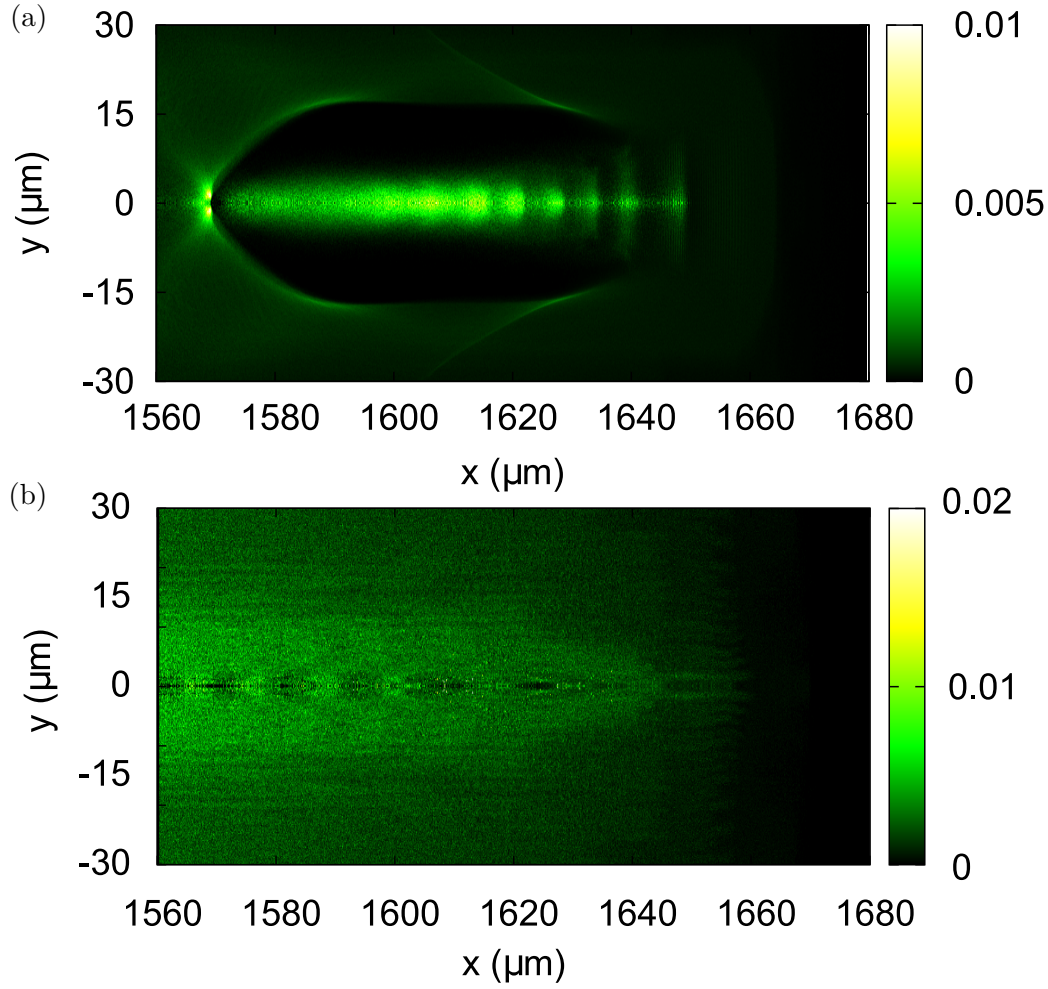
Figure 3.18: Distribution of electron density at the end of the gas jet in the low (a) density case (local electron density $n_e = 5.2 \times 10^{17} \ cm^{-3}$) and high (a) density case (local electron density $n_e = 3 \times 10^{18} \ cm^{-3}$).

The large cavity due to electron wakefield generation at the end of the plasma profile can be seen with more details in Fig. 3.18(a).

Due to the longitudinal field in this bubble, electrons at the tail of the macro-bunch, those injected in the last buckets with the lowest energy, are accelerated. Conversely, those at the head of the bunch are decelerated (the longitudinal electric field is positive, as seen in Fig. 3.17(c)). The acceleration of low energy particles plus the deceleration of high energy ones produces the type of spectrum with a steep slope at low energy and a soft slope at high energy observed in Fig. 3.14. These effects appear in the acceleration of highly charged bunches when the electron density is low enough so that the electron wakefield can be resonantly excited. This is not the case for $n_e = 8.5 \times 10^{19} cm^{-3}$ because the electron beam blows up before reaching the downramp density gradient : no wakefield is observed towards the end of the gas jet (as seen in Fig. 3.18(b)). Indeed, the macro-bunch length in this case is not resonant and is unable to efficiently excite its own wakefield. Once the laser is depleted, electrons do not have any coherent effect on the surrounding plasma and simply propagate towards the end of the gas jet.

To conclude, experiment and simulations underline two important processes occurring when highly charged beams are accelerated. While the laser energy has direct influence on the number of cavities formed and loaded behind the pulse, the accelerating fields in each of these buckets saturate to a critical value independent from the laser energy. In consequence, by simply varying the laser energy it is possible to change the total injected charge in the beam without modifying its energy distribution. At low electron density, the electron wakefield effects are important and strongly affect the spectrum : a quasi-Maxwellian energy distribution turns into a macro-bunch with more energetic electrons. The good shot-to-shot stability and the straightforward tunability of beam charge with the laser energy up to almost 1 nC make laser wakefield acceleration in high-Z gases a promising source for various application experiments.

3.3   Shock assisted ionization injection in a gas mixture
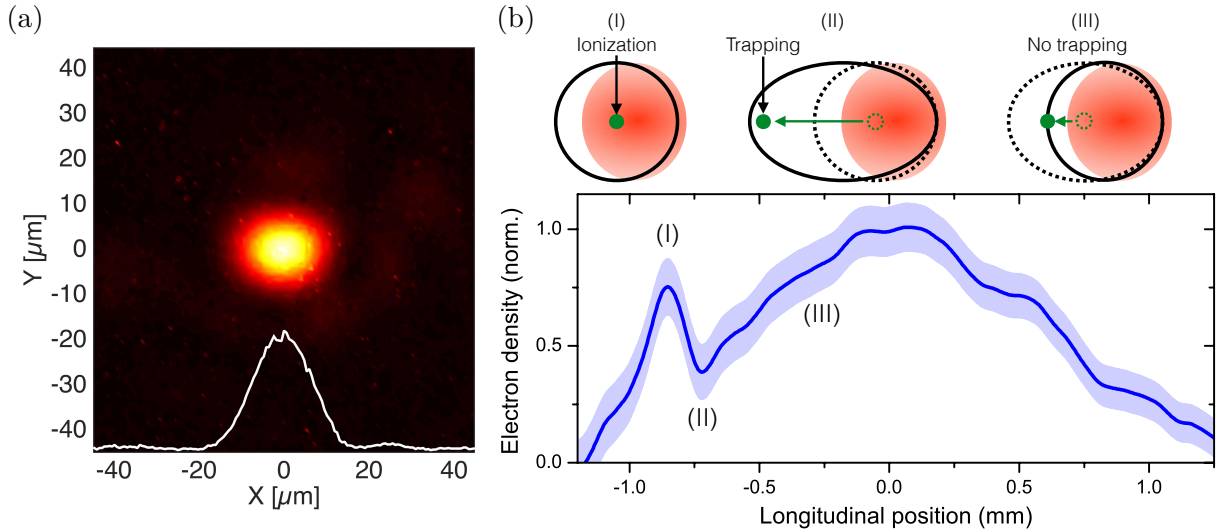
Figure 3.19: (a) Experimental laser focal spot obtained with a 1000 mm focal length off-axis parabola. (b) Typical electron density profile obtained via Abel inversion. The shaded area indicates the standard deviation. Note that the measured shock front is not fully resolved; it may actually be significantly sharper and denser (the resolution is about 40 μm).

As presented in the previous section, ionization injection technique allows to accelerate electron beams with high charge but large energy spread. This poor energy spread comes from the fact that the laser field remains above the threshold for inner shell ionization of the high-Z specie over a significant length leading to continuous electron injection. In chapter 2, we presented the shock injection technique, allowing for the generation of low charge, high quality beams. The idea is to combine the two methods in order to obtain high quality, highly charged electron beams, which would be be ideal candidate for various applications.

The laser propagates in a gas mixture of low and high-Z gases, with a blade inserted at the entrance of the gas jet to form a sharp density transition. When the laser crosses the shock front, the cavity suddenly expands (as explained in chapter 2) and inner-shell electrons ionized there spend more time in the accelerating field. They can thus be injected below the threshold for regular ionization injection, leading to localized trapping and low energy spread (assuming that the laser intensity is below this threshold in the remaining plasma). The principle of shock

assisted ionization injection rests upon the narrow space region where inner shell electrons can be freed and trapped. This principle is illustrated in Fig. 3.19 : electrons ionized close to the center of the plasma cavity when the laser crosses the density transition (region (I) in Fig. 3.19(b)) spend a long time in the accelerating field due to the expansion of the cavity in the shock front (region (II)). Therefore, they are much more likely to be trapped than electrons ionized in the upramp density gradient (region (III)) which have to catch up a shrinking (accelerating) cavity. For low enough laser intensity and plasma density, the injection can thus be restricted to the shock front, potentially allowing for low energy spread electron beams.

3.3.1 Experimental results

The experiment was performed using the same setup as in section 2.3. The laser focal spot (shown in Fig.3.19(a)) is $12.2 \times 15.7 \ \mu m^2$ full width at half maximum (FWHM). The peak laser intensity in vacuum is $I = 5 \pm 0.4 \times 10^{18}$ W.cm^{-2}. It is focused at the entrance of a gas jet using a f/15 off-axis parabola (focal length of 1000 mm). The shock front is formed by putting a 500 μm thick silicon wafer into the gas flow of a 1.5 mm exit diameter supersonic nozzle, with the blade at 3 mm from the nozzle exit (as seen in Fig. 2.20). Its position along the laser propagation axis can be varied in order to tune the electron beam energy. The density profile is characterized at every shot by plasma interferometry. A typical density profile is shown in Fig. 3.19(b). Unless otherwise stated, the gas is a mixture composed of 99% of helium and 1% of nitrogen. Helium is fully ionized in the rising edge of the laser, while nitrogen is ionized to N^{5+}. Electron spectra are measured with a spectrometer described in section 1.4.3. The spectral resolution varies between 2.7% and 3.8% for electron energy between 75 and 200 MeV.

Figure 3.20(a) shows ten consecutive electron spectra obtained with a shock and a gas mixture (99% helium, 1% nitrogen). Electrons are injected at every shot (over hundreds of consecutive shots). The peak energy is 123 MeV and beam charge is about 1 pC. The mean energy spread is 14 ± 2 MeV (11% at 123 MeV), while the energy spread of best shots is about 10 MeV. This is much smaller than typical energy spread obtained with regular ionization injection in a pure high Z gas, as seen in section 3.2. This injection mechanism presents a good stability, as seen on the mean angularly integrated spectrum shown in Fig. 3.20(c), with the standard deviation shown in blue.

The accelerated beam is elliptic, due to the effect of laser polarization on the tunnel-ionization mechanism when inner shell electrons are freed [Chen et al., 2012]. The beam has a divergence of 5 ± 0.6 mrad in the laser polarization direction and 2.6 ± 0.7 mrad in the perpendicular direction. The injection stability is compared with that of shock front injection in pure helium (ten consecutive shots in helium are shown in Fig. 3.20(b), with the corresponding integrated spectrum plotted in (d)). The charge and the energy spread are similar in both cases. In contrast, the stability is much better in the gas mixture; the standard deviation of the electron beam energy and charge are 2.5% and 12% respectively, while in pure helium they are 7% and 24%. The use of gas mixture improves also significantly the rms pointing stability; it is 1.5 mrad in the gas mixture versus 3.2 mrad in pure helium (in other series the rms pointing stability is as low as 0.7 mrad and it is never larger than 1.8 mrad with the gas mixture). Note the poor beam quality in pure helium, compared to results from shock front injection experiments presented in chapter 2. This is likely due to a deficient laser wavefront, to inhomogeneities in the laser spot or to imperfect shock front generation.

In the gas mixture, ionization injection restricts the injection close to the longitudinal axis [Pak et al., 2010; Chen et al., 2012]; therefore it produces an electron beam which is less sensitive to radial inhomogeneities, similar to longitudinal injection [Corde et al., 2013b]. For
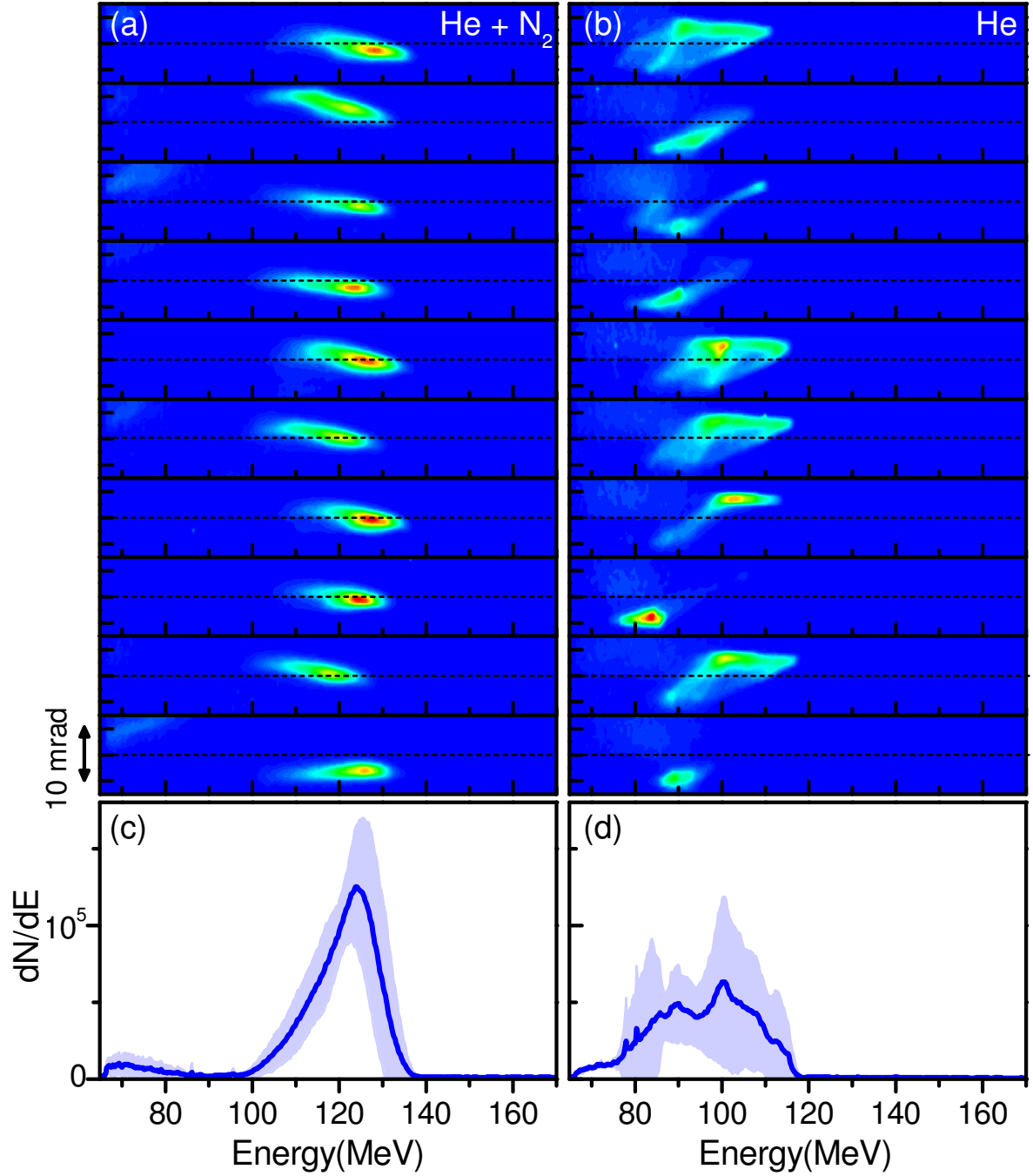
Figure 3.20: Angularly resolved electron spectra of ten consecutive shots, with a shock front and a gas mixture (a) or pure helium (b). The electron density at the center of the density profile is $n_e = 4 \pm 0.1 \times 10^{18}$ cm^{-3} in (a) and $n_e = 3 \pm 0.1 \times 10^{18}$ cm^{-3} in (b). The shock front is located 1.03 ± 0.02 mm from the center of the density profile in (a) and 1.34 ± 0.02 mm in (b). The small differences in density and shock front position explain the difference in the electron beam energy between (a) and (b). The spectra are corrected from the spectrometer dispersion. The color bar goes from 0 (blue) to 83000 electrons per MeV per mrad (red). (c,d) Corresponding mean electron spectra, with standard deviation in colored area.

whatever reasons, Fig. 3.20(b) shows that for given experimental conditions, the use of a gas mixture stabilizes the injection compare to pure helium. Accordingly, shock assisted ionization injection was also observed to depend much less on shock and laser conditions than regular shock injection; for many conditions, there was no injection with pure helium while electrons were injected at every shot with the gas mixture.

3.3.2   Numerical study of the injection mechanism
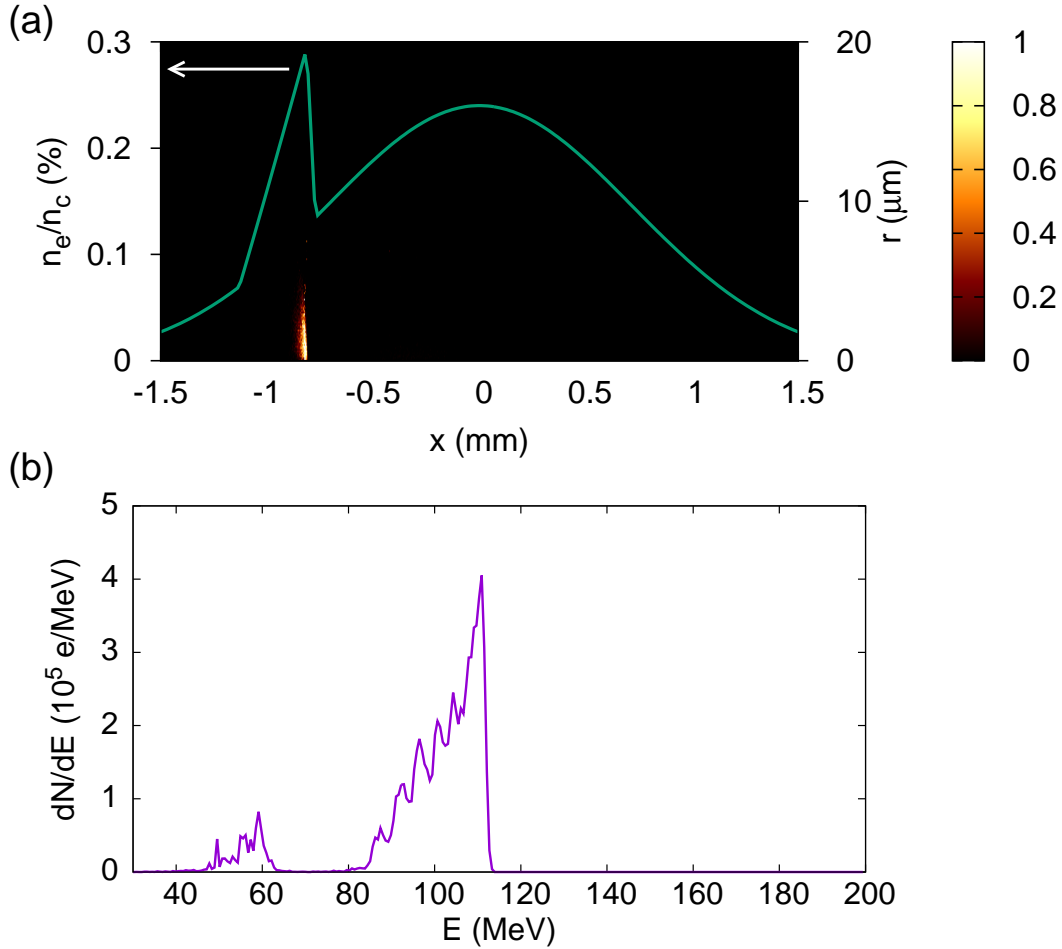
Figure 3.21: Simulation of ionization injection in a shock front. (a) Density profile (left axis) and initial radius of trapped electrons (right axis) close to $x = -0.7$ mm. The color scale indicates the density of trapped electrons in arbitrary unit. (b) Corresponding electron spectrum.

Particle-In-Cell simulations are used to get some insight into the injection mechanism. They are performed using the 3D, fully electromagnetic code CalderCirc [Lifschitz et al., 2009]. Two Fourier modes were used with 70 macro-particles by cell, and mesh sizes $z = 0.2k_0^{-1}$ and $r = 1.5k_0^{-1}$ in the longitudinal and radial directions respectively, with k_0 the laser wavenumber. The laser intensity in vacuum is $I = 3.3 \times 10^{18}$ W.cm^{-2} and the focal spot radius is 16 μm FWHM, close to the experimental parameters. The density profile used in the simulation is shown in Fig. 3.21(a). Because of moderate plasma density and laser intensity used in this simulation, the laser weakly self-focuses and its peak intensity does not exceed $I = 1.5 \times 10^{19}$ W.cm^{-2}.
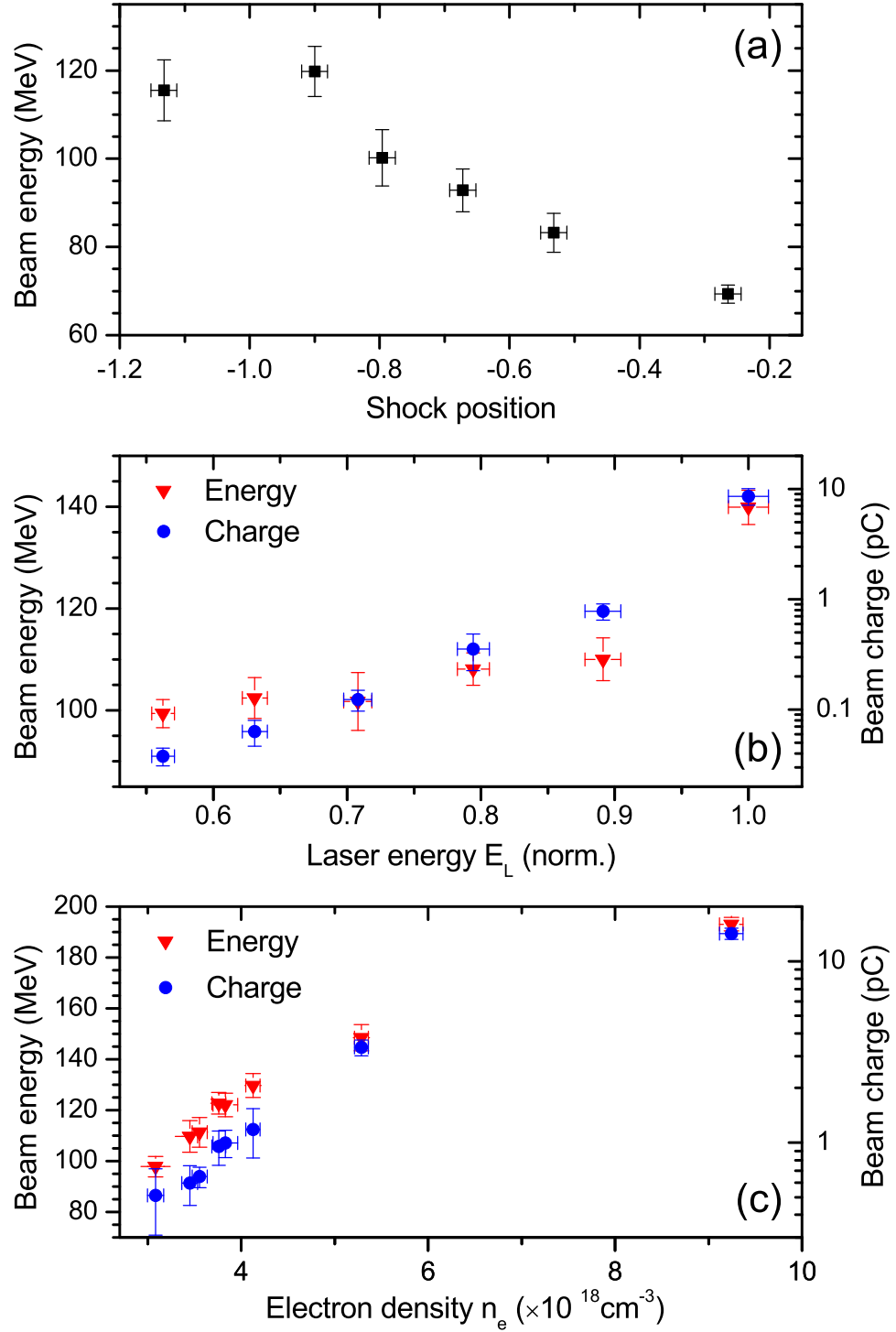
Figure 3.22: Influence of the shock position, laser energy and electron density on the beam properties. (a) Peak energy as a function of the shock position (in mm, with 0 the center of the gas jet), for $n_e = 5.3 \pm 0.4 \times 10^{18}$ cm^{-3}. (b) Electron beam energy and charge as a function of the laser energy (normalized to 1.1 J the maximum laser energy), for $n_e = 5.6 \pm 0.3 \times 10^{18}$ cm^{-3}. (c) Beam charge and energy as a function of the electron density. In (b) and (c), the shock position is $z_s = 1.02 \pm 0.02$ mm. Error bars indicate the standard deviation.

A wakefield is efficiently excited over ~ 1.2 mm only (from $x = -0.5$ mm). Yet, an electron beam with a 1 pC charge is trapped and accelerated up to ~ 110 MeV, as shown on the electron spectrum in Fig. 3.21(b). This peak is due to ionization injection in the shock front, as it appears exactly at the same position as shown in Fig. 3.21(a). Note that the peak around 55 MeV is due to regular ionization injection occurring well after the density transition. Figure 3.21(a) shows the initial position of trapped electrons (colorscale). Most of these electrons originate from a short region preceding the density transition, indicating that injection is actually triggered by the shock.

3.3.3   Tunability of the beam parameters

In addition to improve the stability, shock assisted ionization injection preserves most of the advantages of shock front injection, notably its simplicity (single stage, single laser beam) and the possibility to tune the electron peak energy by varying the position of the silicon wafer. For instance, in Fig. 3.22(a) the energy increases from 70 MeV to 120 MeV when the shock position is moved from 0.26 mm to 0.9 mm from the center of the density profile. From these measurements, the mean longitudinal field and the effective acceleration length are estimated to be about 67.5 ± 8 GeV.m^{-1} and 1.65 ± 0.32 mm respectively. This length is much smaller than the dephasing length, indicating that acceleration is limited by laser diffraction, as observed in the PIC simulation. The longitudinal field is also relatively weak, pointing out that the accelerator is operated in the quasi-linear regime, consistently with the moderate laser intensity and in agreement with the simulations.

Figure 3.22(b) shows that electrons can be injected even with modest laser energy, down to ≈ 670 mJ. While the electron beam energy increases slightly with the laser energy E_L for $E_L \lesssim 1.07$ (with $E_L = 1.1$ J the maximum laser energy), the rise is most significant for larger energies, likely because of better laser self-focusing and hence longer acceleration length. The beam charge (integrated here over two FWHM) increases more steadily with the laser energy, from 38 ± 7 fC up to 8.6 ± 1.5 pC. This increases goes along a growth of the energy spread from 9 ± 1 MeV up to 25 ± 4 MeV. These findings are consistent with ionization injection close to the injection threshold (the injected volume in the phase space increases with the laser intensity).

The charge and the energy of the beam also depend on the electron density n_e, as shown in Fig. 3.22(c). From $n_e = 3.1 \times 10^{18}$ cm^{-3} to $n_e = 9.2 \times 10^{18}$, the charge and energy increase from 0.5 ± 0.2 to 14.2 ± 1 pC and from 98 ± 4 to 193 ± 3 MeV respectively. The charge growth arises likely from the increase of the nitrogen density and of the laser intensity (resulting from enhanced self-focusing). The beam energy increases because of rising accelerating field originating from the increase of the density and better laser self-focusing. It confirms that the acceleration is not limited by dephasing (in the opposite case, the energy would decrease with increasing density).

As the plasma density increases some electrons can be freed after the density transition, leading to injection over a long length and hence to broad energy distributions. This effect is illustrated in Fig. 3.23. Whereas all the charge is concentrated in a single peak at low density (Fig. 3.23(a)), a second peak with a large energy spread is also accelerated when the density is risen above $n_e = 5.3 \times 10^{18}$ cm^{-3} (Fig. 3.23(b-c)). Note that at the threshold density (Fig. 3.23(b)), a second beam is not trapped at each shot. In contrast, for $n_e = 9.2 \times 10^{18}$ cm^{-3} the spectra present always a low energy tail (Fig. 3.23(c)). The energy spread of the tail is very similar to that of electron beams obtained without shock at the same density (Fig. 3.23(d)), confirming that this tail is due to regular ionization injection. The total charge is also similar with or without the shock, about 30 pC, probably because of beam loading. Thus, the drawback of rising the plasma density to increase the beam charge is that it can also increase the charge
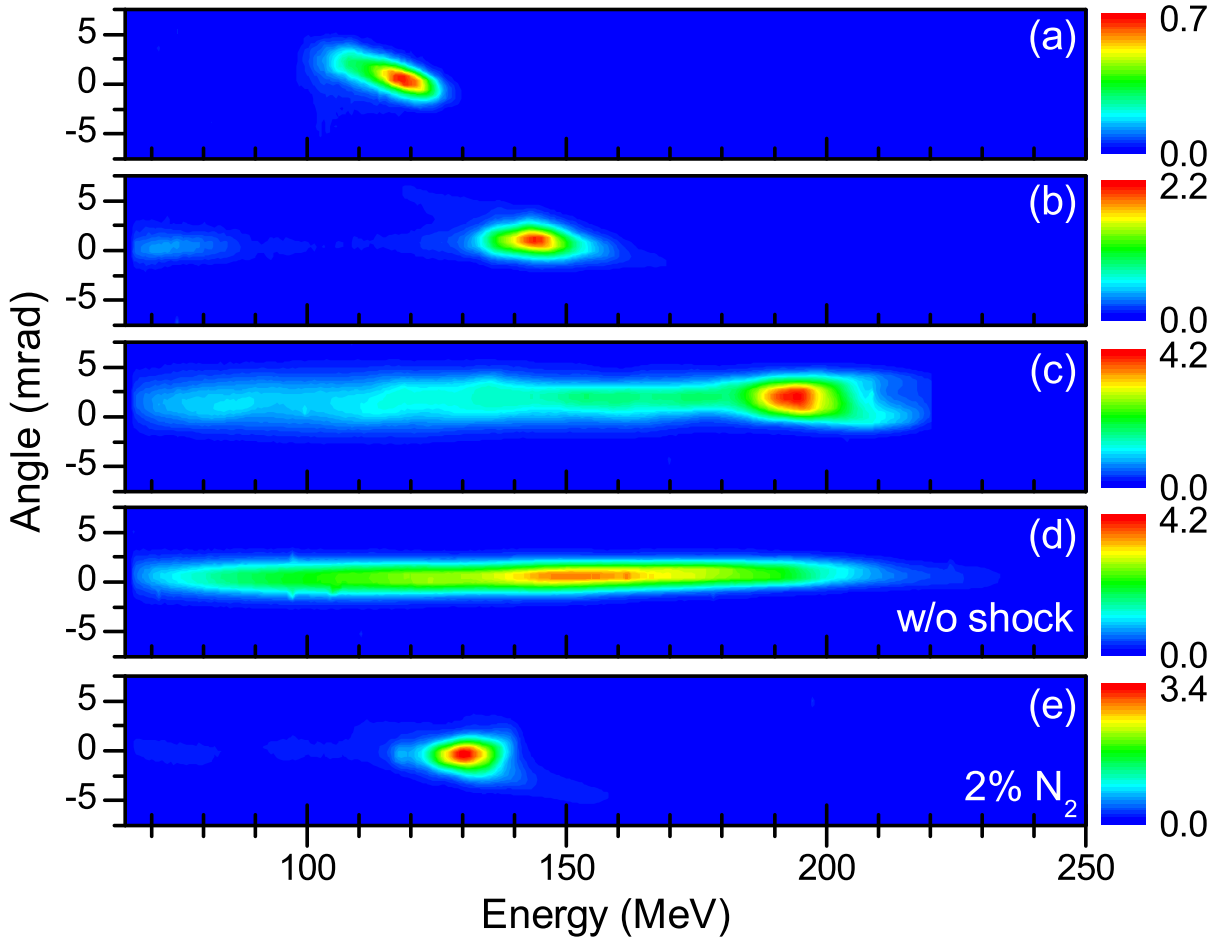
Figure 3.23: Angularly resolved electron spectra for different conditions. (a) Electron density $n_e = 3.7 \times 10^{18}$ cm^{-3}. (b) $n_e = 5.3 \times 10^{18}$ cm^{-3}. (c) $n_e = 9.2 \times 10^{18}$ cm^{-3}. (d) $n_e = 9.2 \times 10^{18}$ cm^{-3}, without shock. (e) $n_e = 5.3 \times 10^{18}$ cm^{-3}, mixture 2% nitrogen, 98% helium. The colorscale is in arbitrary units.

in the low energy tail. A way to increase the beam charge while avoiding this detrimental effect is to rise the fraction of nitrogen in the gas mixture. This is exemplified in Fig. 3.23(b,e) which shows that doubling the proportion of nitrogen (while keeping the same electron density) leads to the injection of more electrons in the electron beam without changing significantly the energy distribution nor the divergence.

We demonstrated a controlled injection technique which gathers most of the advantages of ionization and shock front injections. It is easy to setup and works for a large range of parameters without requiring complex alignment. Compared to ionization injection, electron trapping is confined to a small region, leading to the injection of electron beams with rather low energy spreads (down to 10 MeV). The electron beams were also observed to be much more stable than those obtained by shock front injection in pure helium. In particular the pointing stability was as low as 0.7 mrad. Further optimization of the blade type or the blade mechanical mount may lead to higher charge and to smaller energy spread, down to 5 MeV as obtained with regular shock injection. These results were published in Thaury et al. [2015b].

3.4 Conclusion

In conclusion, we presented in this chapter a comprehensive study of ionization injection mechanism in a pure high Z gas or a mixture of low and high Z gases. The mechanism rests upon the tunnel-ionization of inner shell electrons of the high Z specie where the laser intensity is above the ionization threshold. Electrons freed close to the laser axis can be trapped and accelerated in the wakefield as long as the laser intensity is high enough, leading to highly charged beams (up to 1 nC) but with a very poor energy spread (about 100 %). In a pure high Z gas, such beams undergo two important processes. First, by modifying the laser energy it is possible to change the total injected charge in the beam without changing its energy distribution. Second, self-generated wakefield allows to turn a quasi-Maxwellian energy distribution into a macro-bunch with more energetic electrons for a low enough electron density. By combining this process with the shock injection mechanism, one can gather the advantages of the two techniques, leading to the acceleration of very stable, high quality electron beams with a correct charge (around 10 pC) and a good energy spread (down to 7 %). Accelerated in a gas mixture, such beams are adequate candidates for various application experiments such as LWFA-based FEL [Schlenvoigt et al., 2008].

Chapter 4

Electron phase manipulation by tailoring the plasma density

An important limit for energy gain in laser-plasma wakefield accelerators is the dephasing length, after which the electron beam reaches the decelerating region of the wakefield and starts to decelerate. In this chapter is presented a technique to manipulate the phase of the electron beam in the wakefield, in order to bring the injected electrons back into the accelerating region, hence increasing the final beam energy. This rephasing is operated by placing an upward density step in the beam path. In a first experiment, the principle of this technique is demonstrated using a large energy spread electron beam. Then, the technique is used to increase the energy of mono-energetic electron beams by more than 50%.

Contents

4.1 Overcome a dephasing limited LWFA

4.1.1 Principle of electron rephasing

(a)

(b)
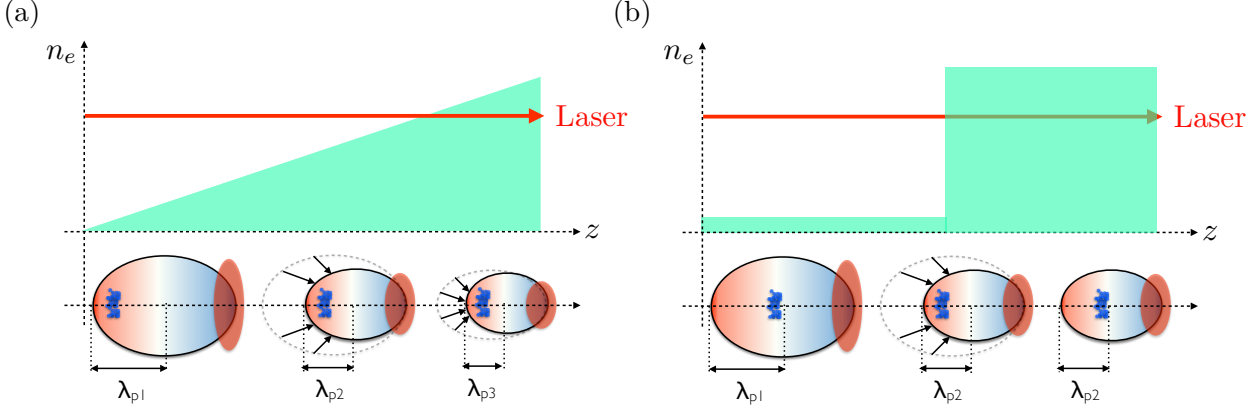
Figure 4.1: Principle of phase matching between the wakefield and electron bunch in an upward density gradient (a) and phase-resetting in a step density gradient (b). In (a), the bubble contracts as it propagates and electrons (blue dots) keep the same phase and remain in the accelerating gradient (in red) instead of dephasing and decelerating in the front half of the cavity (in blue). In (b), electrons are about to dephase in the first density plateau. The bubble abruptly shrinks when crossing the density step and electrons find themselves at the back of the cavity with their phase reset.

The maximum attainable energy for electrons in LWFA is limited by three processes: laser pulse depletion, laser defocusing and dephasing (as seen in section 1.2.7). Each of theses processes occur after a characteristic propagation length and the final electron energy is determined by the process that sets in first. Laser depletion and defocusing determine the distance over which the wakefield structure can be maintained. The effect of the diffraction length ($L_{diff} = 2\pi(\omega_0/\omega_p)\lambda_p$) is usually mitigated by self-focusing or external guiding, while the depletion length ($L_{depl} = (\omega_0/\omega_p)^2 \lambda_p$) can be increased with a larger laser energy. Yet, the excitation of a wakefield is not sufficient to guarantee that the electron beam is accelerated, because of dephasing. Actually, as the laser group velocity and thus the wake velocity are smaller than the electron beam velocity, the electron beam outruns the plasma wave during the acceleration and reaches a phase of the wake where the field is decelerating.

The laser group velocity and hence the dephasing length depend on the plasma density, getting longer for low densities ($L_{deph} = (\omega_0/\omega_p)^2 \lambda_p(4\sqrt{a_0}/3) \propto n_e^{-\frac{3}{2}}$ as shown in eq. (1.66)). It has been proposed years ago to use a spatially tapered plasma density profile to increase this limit and overcome electron dephasing [Katsouleas, 1986; Sprangle et al., 2001]. The idea behind this method is to use an accelerating medium with an upward density ramp along the laser propagation. It is the opposite process of downramp injection (sketched in Fig. 2.1). As discussed in chapter 2, the bubble expands as it propagates in a downward density gradient, allowing for low energy electrons to remain in the accelerating phase long enough to be further accelerated and eventually trapped.

Inversely, as the driving laser pulse encounters higher and higher plasma density, the wakefield period shrinks ($\lambda_{p1} > \lambda_{p2} > \lambda_{p3}$ as seen in Fig. 4.1(a)) and the frontier between the accelerating and decelerating region can move as fast as the electron bunch itself. Electrons

can thus remain in the same phase as the cavity length shortens. The phase matching between wakefield and the electron bunch can be kept much beyond the dephasing length, and therefore leading to higher electron energies. The required density profile to get perfect phase-locking is complex, and its experimental realization is not straightforward. The density tapering effect has been extensively investigated numerically [Suk et al., 2003; Sprangle et al., 2002; Kim et al., 2004b; Rittershofer et al., 2010; Hur and Suk, 2011], however it has been sparsely studied experimentally yet [Kim et al., 2013b].

Another method to overcome the dephasing limitation and reach higher energies is to consider a density step separating two density plateaus. In the first density region, the bunch accelerates up to the local dephasing length L_{deph1} and is about to dephase. When crossing the sharp density transition, the bubble shrinks abruptly ($\lambda_{p2} < \lambda_{p1}$ as seen in Fig. 4.1(b)). The electron bunch, initially close to the center of the ion cavity, shifts to the rear part of the contracted bubble, back into an accelerating region where it gains more energy while accelerating in the second density plateau.

In this section, we present how the phase of electrons in the cavity can be manipulated by tailoring the plasma density. Phase manipulation can allow for maintaining electrons phase in the accelerating gradient and thus increase their energy without being limited by dephasing. It can also be used to improve the beam quality by rotating electrons in their phase-space hence reducing their energy spread.

4.1.2 Phase adjustment of the electron beam

Phase locking

In the case of phase-locking, electrons have to keep exactly the same phase inside the ion cavity while it propagates to experience the same maximum longitudinal field during the whole acceleration. Pukhov and Kostyukov [2008] and Rittershofer et al. [2010] developed the theoretical framework of phase locking in the guided linear regime. Here we evaluate the required density profile for which electron dephasing is mitigated by the wake evolution (see Appendice A for a more detailed calculation). Be sure to note that the very simple model developed here demands quite strong assumptions on the influence of laser intensity evolution during propagation. This simplistic view is useful to understand the physical process of phase-locking and phase-resetting but it cannot be seen as an accurate description of what really happens during electron acceleration in a tapered plasma.

In order to maintain the electron bunch phase Φ_0 constant (Φ_0 the normalized phase of the bunch in the co-moving frame coordinate, with $\Phi_0 = 0$ at the very back of the cavity and $\Phi_0 = 1$ in the cavity center), the phase slippage must be compensated by the cavity wavelength λ modification while propagating at velocity $v_e - v_\varphi$ in an upward density gradient (see Appendice A) :

$$\frac{d\lambda}{dt} = \frac{v_e - v_\varphi}{1 - \Phi_0}. \tag{4.1}$$

The cavity wavelength λ is assumed to depend only on the plasma density $n_e(t)$ as $\lambda(t) = \lambda_p \sqrt{n_0/n_e(t)}$ (with t the time in the co-moving coordinate system), neglecting the influence of the laser intensity and of self-focusing. Deriving eq. (4.1) gives the following equation for the plasma density profile $n_e(z)$ to obtain perfect phase-matching (see Appendice A) :

$$n_e(z) = \frac{n_0}{\left(1 - \frac{z}{L_{inh}}\right)^{\frac{2}{3}}}. \tag{4.2}$$
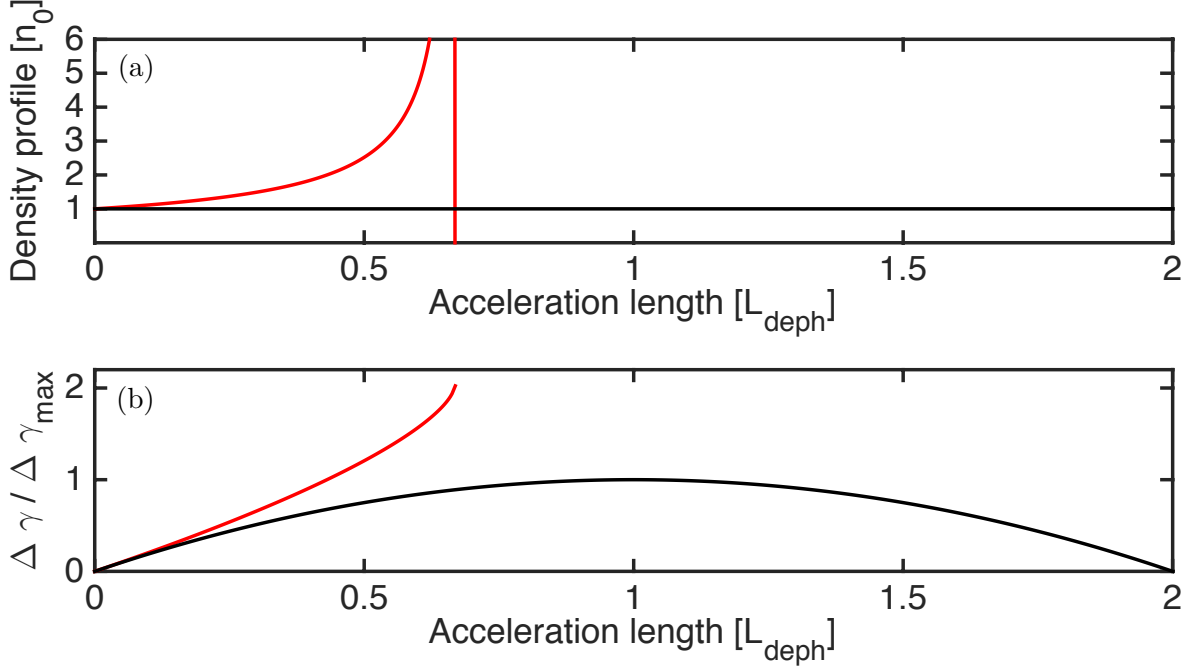
Figure 4.2: (a) Density profile for perfect phase locking between electrons and the wake (in red) and constant density profile (in black). (b) Evolution of energy gain for the corresponding density profiles.

with $L_{inh} = 2(1 - \Phi_0)L_{deph}/3$ the inhibition length after which phase-matching is not possible anymore. The fact that the inhibition length in the upward gradient is shorter than the dephasing length L_{deph} at n_0 is related to the fact that the wake velocity decreases as the density increases [Esarey et al., 2009]. In the upward gradient, the front of the wake slows down while the rear struggles to reach the light velocity c. When n_e approaches the critical density n_c, it is more and more difficult for the wake to accelerate further and catch with the electron bunch. As the laser propagation in the plasma imposes $n_e < n_c$, phase locking of electrons is in fact limited.

The density profile is plotted in red in Fig. 4.2(a), along with a constant density profile (in black) at n_0. Note again that this model allows only for a rough estimation of the perfect matching density profile as the laser evolution is neglected for simplicity. Furthermore, a perfect matching condition of the laser with the plasma and a fully evacuated ion cavity are assumed (which can be far from experimental conditions). We evaluate now the energy gain of an electron in a constant density profile n_0 in the bubble regime. The calculations are detailed in section A.1 :

$$\Delta\gamma(z) = \frac{e}{m_e c^2} E_{z0} \left(z - \frac{1}{2} \frac{z^2}{L_{deph}} \right) \qquad (4.3)$$

with a maximum energy gain obtained when $z = L_{deph}$:

$$\Delta\gamma_{max} = \frac{n_c}{n_0} \sqrt{a_0}. \qquad (4.4)$$

The normalized energy gain $\Delta\gamma/\Delta\gamma_{max}$ in a constant density profile n_0 for $a_0 = 2$ is shown in black in Fig. 4.2(b). Electrons gain energy up to L_{deph}, then dephase and decelerate. In a
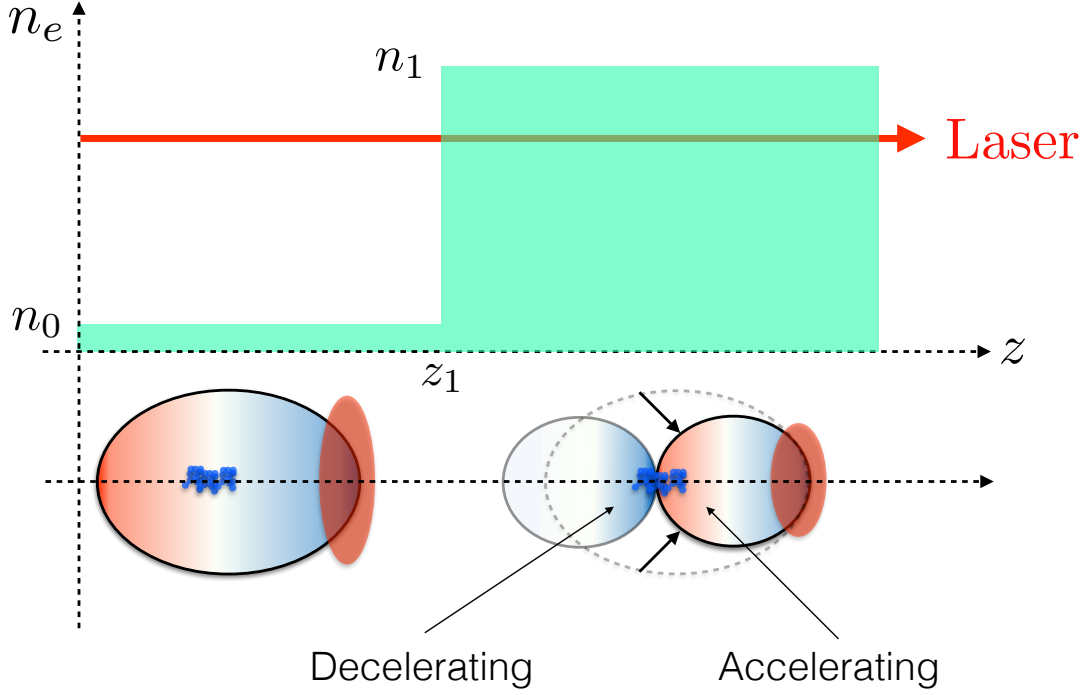
Figure 4.3: Principle of phase-resetting of electrons in a density step. The electron bunch reaches the center of the cavity and is about to dephase before the density transition. After the step, the cavity shrinks and the bunch finds itself located at the rear of the bubble, with some electrons at the head in the accelerating part of the first cavity (those are rephased). The electrons at the rear of the bunch are located in the decelerating part of the second wave period.

perfectly matched density profile however, the normalized energy gain calculated in section A.2 (shown in red in Fig. 4.2(b)) increases further, increasing up to a value almost two times larger when reaching the inhibition length L_{inh}. Such a density profile is however very challenging to realize experimentally.

Phase resetting

A density step is much more easy to set up in an experiment and can also lead to a significant increase of the electron energy, via phase resetting. An example of such phase resetting is shown in Fig. 4.3. An electron is injected at $\Phi_0 = 0$ and accelerates over a distance z_1, then enters a higher density region n_1 where the bubble shrinks abruptly so that the electron goes back to its original phase $\Phi_0 = 0$, at the back of the cavity. For any transition position z_1, there is a unique density n_1 for which the cavity wavelength λ_1 shortens so that the electron phase is reset back to zero. This density is given by (with the calculations detailed in section A.3) :

$$n_1(z_1) = \frac{n_0}{\left(1 - \frac{z_1}{2L_{deph}}\right)^2} \tag{4.5}$$

with $L_{deph} = n_c/n_0\lambda_p$ the dephasing length in the first density region. The perfect phase-reset density profile $n_1(z_1)$ is shown in Fig. 4.4(a) (dashed red line). Note that if the density step is placed at the dephasing length ($z_1 = L_{deph}$), the cavity wavelength has to be reduced by a factor

of two ($\lambda_1 = \lambda_p/2$). The corresponding density for which electrons are perfectly phase-reset after one dephasing length is $n_1 = 4n_0$ (shown in blue in Fig. 4.4(a)).
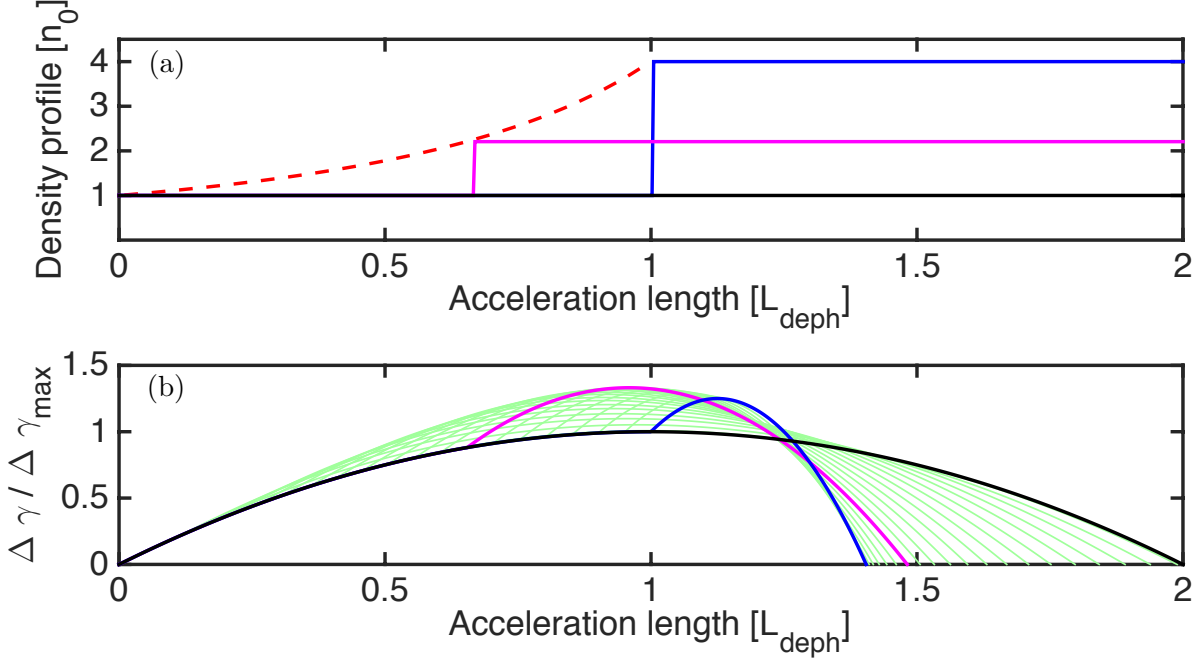
Figure 4.4: (a) Constant density profile (in black) and density profiles required for phase-resetting at two particular positions : $z = L_{deph}$ (in blue) and $z = 2/3L_{deph}$ (in magenta). The dashed red line indicates the evolution of the density n_1 required for perfect phase-resetting function of the transition position z_1. (b) Evolution of energy gain over a cavity length for different phase-reset positions (in green) and for the two previously defined positions (in blue and magenta).

It is possible to estimate the energy gain after phase resetting the electrons (see details in section A.3) :

$$\Delta\gamma(z) = \frac{e}{m_e c^2}\left[\frac{E_{z1}}{2L_{d1}}z^2 + E_{z1}\left(1 - \frac{1}{L_{d1}}\right)z + \left(\frac{E_{z1}}{2L_{d1}} - \frac{E_{z0}}{2L_{deph}}\right)z_1^2 + (E_{z0} - E_{z1})z_1\right]. \quad (4.6)$$

The energy gain for different positions of the density transition z_1 are plotted in green in Fig. 4.4(b). If the density step is placed after one dephasing length ($z_1 = L_{deph}$, in blue in Fig. 4.4(a), the maximum energy gain is :

$$\Delta\gamma_{max} = \Delta\gamma_{max}(n_0) + \Delta\gamma_{max}(4n_0) = \frac{5}{4}\Delta\gamma_{max}(n_0). \quad (4.7)$$

The maximum achievable gain is obtained when the phase-reset happens at $z_1 = 2/3L_{deph}$, with a corresponding optimum density $n_1 = 9/4n_0 = 2.25n_0$ (shown in magenta in Fig. 4.4(a-b)). It leads to a gain of :

$$\Delta\gamma_{max}(2/3L_{deph}) = \frac{4}{3}\Delta\gamma_{max}(n_0). \quad (4.8)$$

By setting a density step around $2/3L_{deph}$ with $n_1 \sim 2n_0$, it is possible to achieve electron rephasing with an energy gain of about 1.33.

Note that in the phase-locking model, laser evolution during propagation is neglected. In an upward density gradient however, laser self-focusing is strongly affected, and thus enhances the relativistic effects causing the cavity expansion. The use of a very sharp density transition can mitigate this effect. Indeed, the cavity expands abruptly at transition whereas laser self-focusing needs some propagation distance to develop and affect the bubble expansion. Phase-reset of electrons in a shock allows for boosting the energy directly after the transition, with a limited laser evolution, by simply moving the bunch back into the accelerating phase. Moreover, the step position and density after the transition can be varied quite easily in order to experimentally optimize electrons rephasing and compensate the effects not taken into account in our simplistic model.

4.2 Experimental demonstration of electron phase manipulation
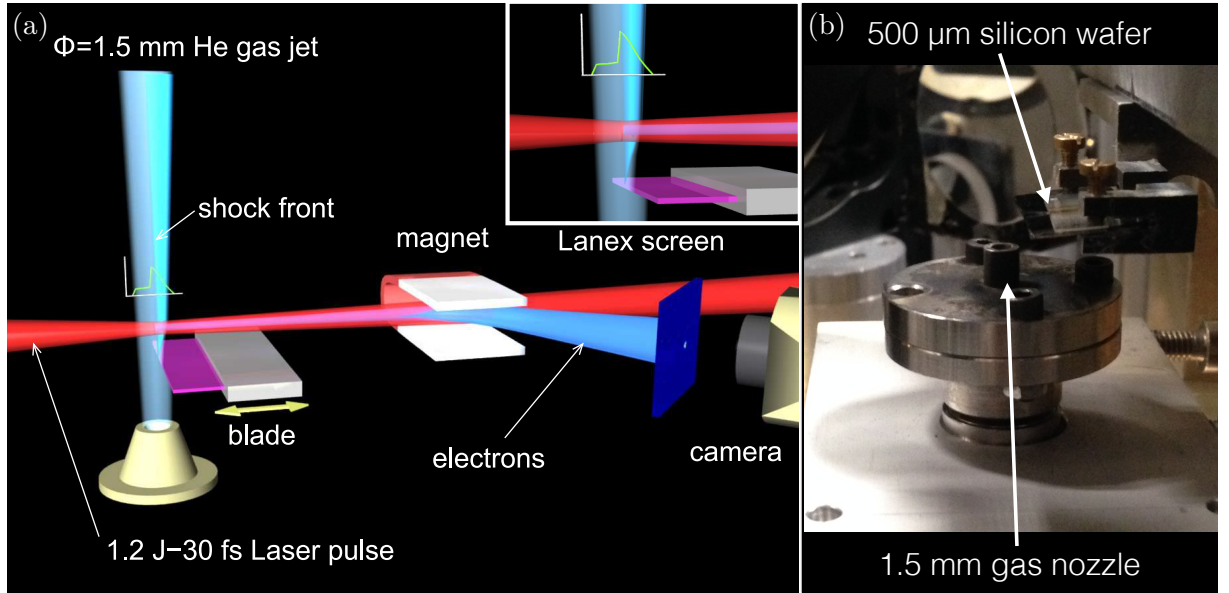
Figure 4.5: (a) Schematic representation of the experimental setup. The blade can move in and out the gas jet. A schematic density profile is shown in green near the gas jet. The inset shows a zoom of the shock formation at the rear of the gas jet. (b) Picture of the nozzle and blade used in the experiment.

In this section, we experimentally demonstrate phase-resetting of electrons with a plasma presenting a low density region followed by a high density one, separated by a sharp density jump (as schemed in Fig. 4.1). In this experiment, a large energy spread electron beam is used to demonstrate the principle of this technique. The density profile is obtained by creating a shock front in a supersonic gas jet.

4.2.1 Experimental setup and diagnostics

The main interaction beam P1 of the "Salle Jaune" laser system (containing 1.2 J) is focused at the entrance of a 1.5 mm diameter supersonic Helium gas jet using a f/10 off-axis parabola (as seen in the experimental setup sketched in Fig. 4.5(a)). The Full Width at Half Maximum (FWHM) focal spot size is 18 ± 0.6 μm (as shown in Fig. 4.6(a)), with a peak intensity on target

of $I = 1 \pm 0.5 \times 10^{19}$ W.cm^{-2}, equivalent to a normalized vector potential $a_0 = 2.2 \pm 0.06$. A 500 μm thick silicon wafer is placed on the leaving side of the gas jet to create a sharp density transition, by using a setup similar to the one in presented in chapter 2 (note that in chapter 2, the shock front is created on the entering side of the gas jet to trigger electron injection in the downward density jump, whereas for now the shock is on the leaving side of the jet and creates a sharp upward density ramp). The longitudinal position of the shock is adjusted by moving the blade in and out. Electron spectra are measured with the spectrometer presented in section 1.4.3.
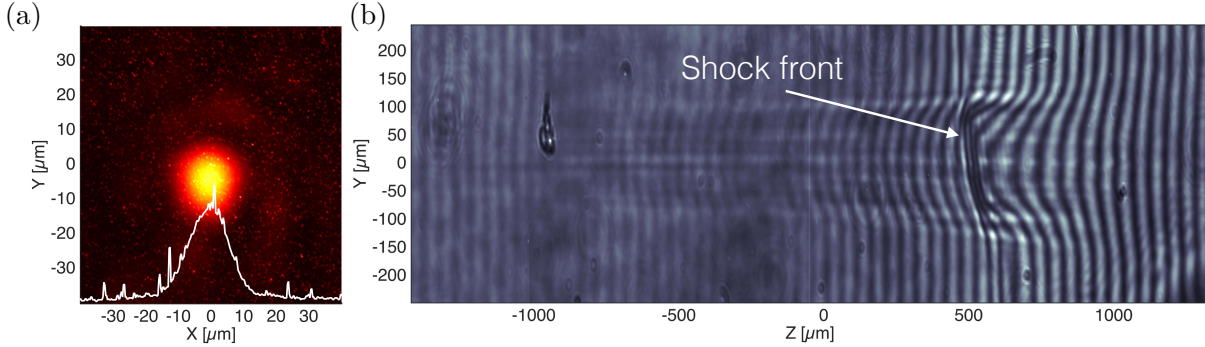
Figure 4.6: (a) Experimental laser focal spot obtained with a 700 mm focal length off-axis parabola. (b) Interferogram of the propagation of the laser in a pure helium gas jet. $Z = 0$ mm corresponds to the center of the nozzle. The shock is visible at $z_s = 500$ μm.

The probe beam P3 combined with a Nomarski interferometer (presented in section 1.4.3) are used to characterize the plasma density spatial distribution. A typical interferogram image with the shock front visible at the rear of the plasma is shown in Fig. 4.6(b). The phase maps for different positions of the blade are recovered from the corresponding interferograms with a Continuous Wavelet Transform algorithm, and are shown in Fig. 4.7(a). Plasma density is then estimated by performing Abel inversion, assuming a cylindrical symmetry around the laser propagation axis before and after the shock. In the vicinity of the shock, the symmetry is not perfect, and thus Abel inversion does not give perfectly exact results. Yet, it allows to get an upper value on the shock front width and position as well as the density before and after the density transition. It is estimated from phase maps to be smaller than 10 μm, the resolution of the imaging system. The retrieved longitudinal plasma density profiles are shown in Fig. 4.7(b) for different positions of the blade. The peak plasma density with the blade out of the jet is $n_0 = 8.5 \times 10^{18}$ cm^{-3} (black curve). The ratio of plasma densities in front of and behind the shock front is about 3, and tends to go down when the blade is shifted out of the gas jet. Beyond the shock, the plasma density gently decreases with a characteristic length of around 1 mm. Note that the position where the laser crosses the shock (referred as the shock position z_s) is different from the blade position, as the laser is fired a few millimeters above the blade. For instance, a blade position of 1.8 mm corresponds to a shock position of roughly $z_s \approx 0$ mm.

4.2.2 Experimental results

Firstly a scan of the gas density n_0 without the blade is performed in order to determine the optimum plasma density for which the electron energy cut-off is the highest. The energy spectrum with a plasma density without transition is shown in the top panel of Fig. 4.8(a) (angle resolved spectrum) and in red in Fig. 4.8(b) (spectrum integrated over the transverse
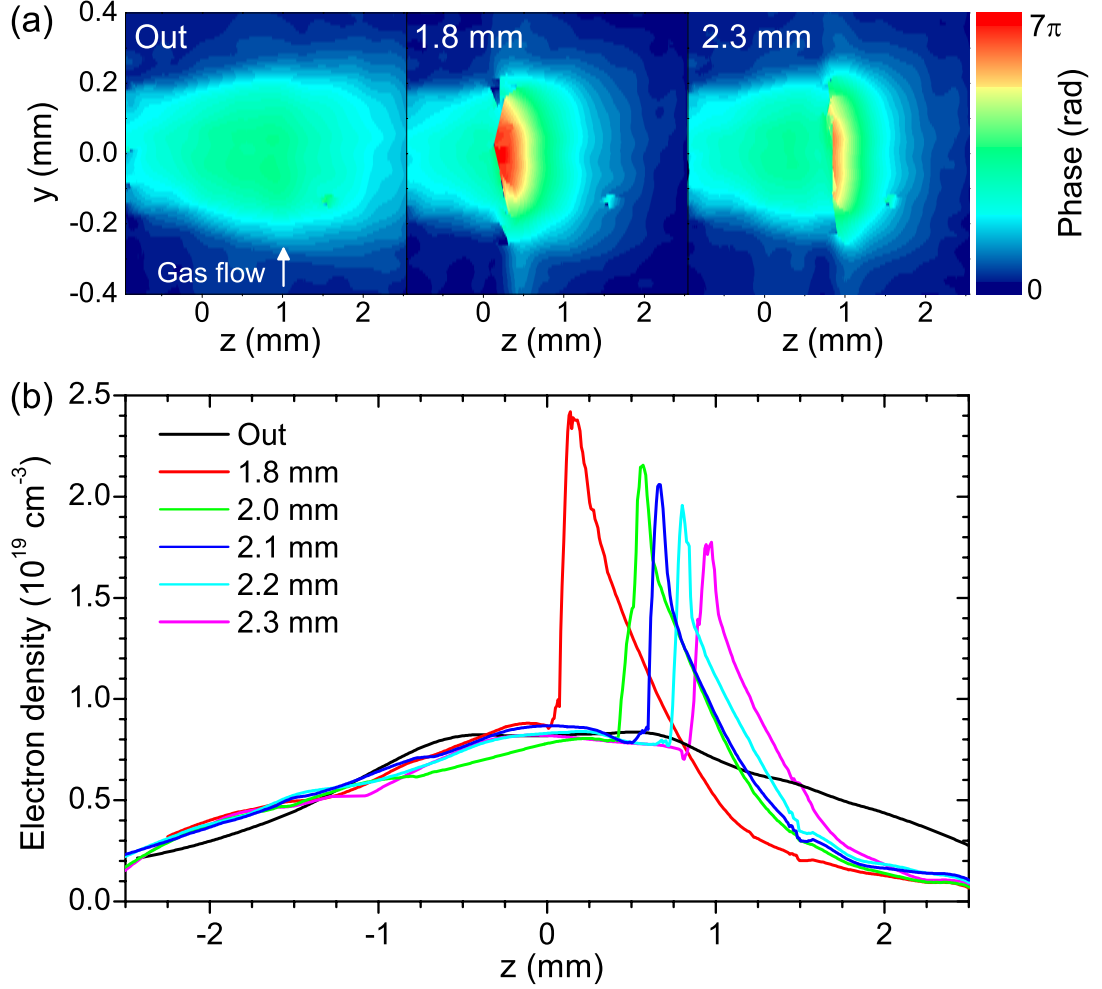
Figure 4.7: (a) Phase maps calculated from the interferometry measurements for different positions of the blade. (b) Longitudinal plasma density profiles for different positions of the blade. The blade position is measured from the center of the gas nozzle at z = 0 mm.

direction). The electron energy distribution corresponds to the Forced Laser Wakefield (FLWF) regime [Malka et al., 2002], with a long plateau feature and a Maxwellian decrease with a cut-off energy around 230 MeV. The cut-off energy is defined as the electron energy where the charge of the beam becomes smaller than 18 femtocoulombs per MeV. Such a spectrum indicates the transverse self-injection of a long bunch [Corde et al., 2013b], which is consistent with an electron plasma peak density $n_0 = 8.5 \times 10^{18}$ cm^{-3} along few millimeters.

When the blade is placed such as the shock is created slightly beyond the center of the gas jet, the spectrum changes drastically, as shown in the bottom panel of Fig. 4.8(a) (corresponding to a shock position of $z_s = 0.7$ mm, measured from the center of the gas nozzle at $z = 0$ mm). Figure 4.8(b) shows the integrated spectrum for this shock position in dark blue. The number of electrons between 100 MeV and 200 MeV substantially drops by a factor 20, and a quasi-monoenergetic peak appears around 300 MeV, with an energy-spread FWHM around 30 %. The cut-off energy at 18 fC/MeV is around 100 MeV higher (up to 360 MeV) than with the flat density profile. The high energy peak containing about 7 pC is well-collimated (divergence lower than 4 mrad FWHM), whereas the low energy branch of the spectrum (between 50 and

107
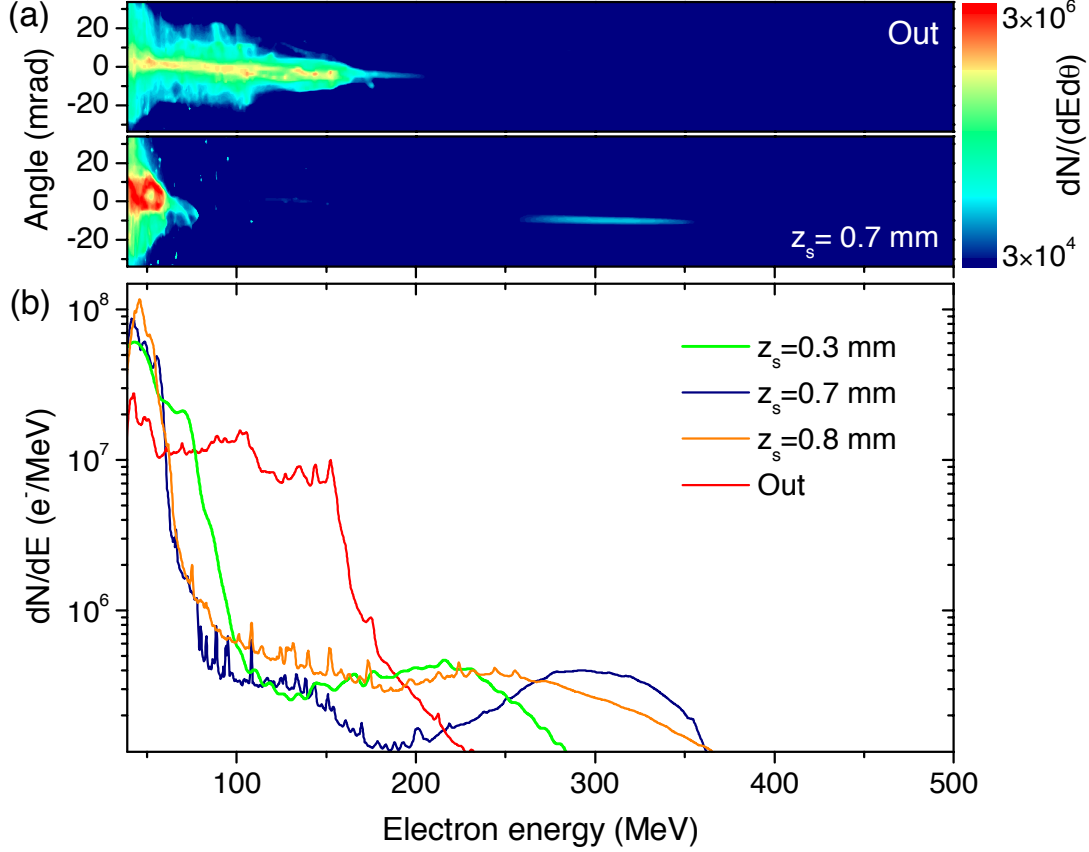
Figure 4.8: (a) Experimental angle resolved electron spectra in logarithmic scale without (top panel) and with the shock at $z_s = 0.7$ mm after the gas jet center (bottom panel). (b) Angle integrated electron spectra in logarithmic scale for four positions of the shock.

100 MeV) presents a larger divergence (about 15 mrad FWHM) than for the case without shock (5 mrad FWHM). Moreover, the number of low energy electrons -with energies lower than 70 MeV- is larger for the density step profile. Note that the total charge without ($Q = 181 \pm 20$ pC) and with ($Q = 211 \pm 12$ pC) the shock are similar. The energy gain of the electron bunch is easily tunable by moving the blade in the gas jet. Yet for different shock positions ($z_s = 0.3$ and 0.8 mm), the high energy peak is not as mono-energetic. The cut-off energy decreases when the blade moves too much into the jet or too far away from the nozzle center. When the shock is placed close to the optimum found in Fig. 4.4(b), electrons can gain maximum energy.

4.2.3   Simulation results

To get more insight on the details of the rephasing process, simulations of the injection and acceleration of electrons along the gas jet are performed using the PIC code CalderCirc [Lifschitz et al., 2009] with a mesh $\Delta x = 0.3\ k_0^{-1}$ and $\Delta r = 1.5 k_0^{-1}$ (with $k_0 = 1/\lambda_0$), and 2 Fourier modes ($m = 0 - 1$). The plasma density profile is defined from the experimentally measured profiles, with a peak density $n_0 = 8.5 \times 10^{18}$ cm^{-3} for the plasma without density transition. The laser intensity is set to $I = 1.0 \times 10^{19}$ W.cm^{-2} and the laser waist to 15 μm.

Figure 4.9 shows the electron density distribution in the longitudinal phase space (z, E) resulting from simulations, for a gas jet without (a) and with the shock (b). The simulated
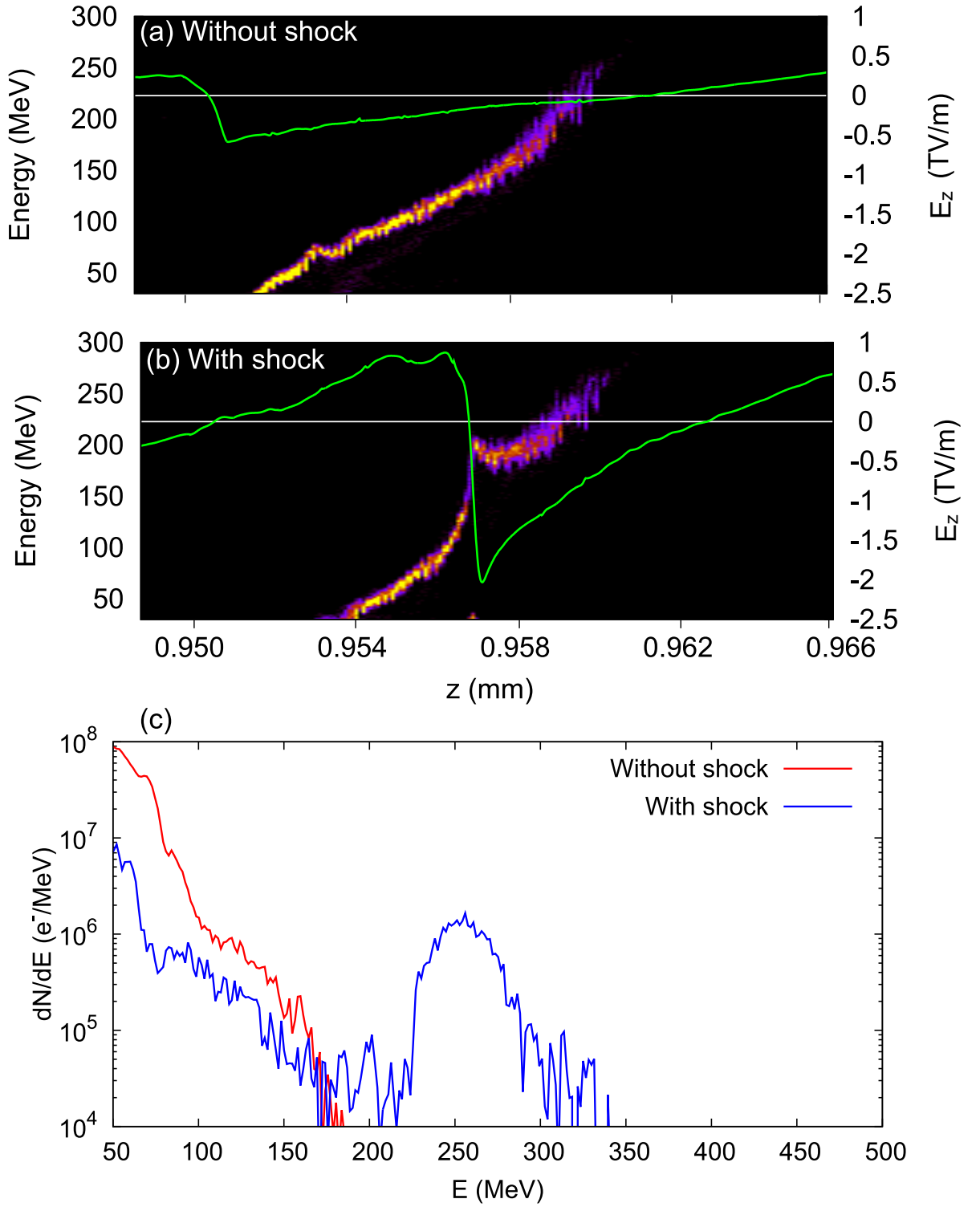
Figure 4.9: Electron density in the phase space (z, E) for a gas jet without (a) and with (b) the shock. Green curve shows the longitudinal electric field on the laser axis. Simulated spectra obtained at the exit are shown in (c). The density transition is at $z_s = 0.900$ mm.
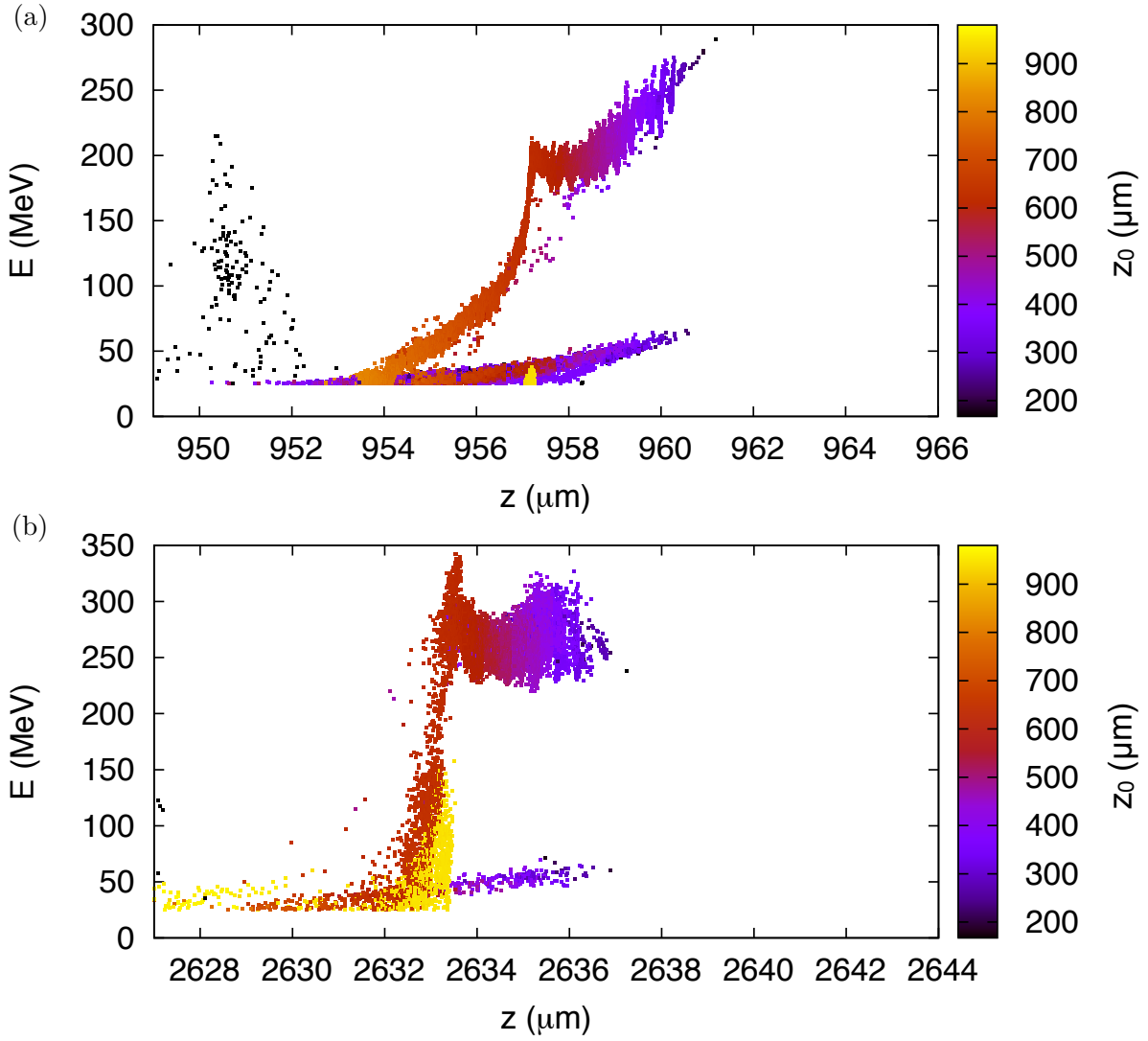
Figure 4.10: Phase-space distribution (z, E) of the electrons just after the density transition (a) and at the end of the gas jet (b). The color scale z_0 represents the position of injection in the wake of each colored simulated macro-particle.

energy spectra of the extracted electrons are shown in Fig. 4.9(c), presenting a distribution similar to those obtained in the experiment. Self-injection of electrons into the bubble begins relatively late during the pulse propagation, around the middle of the gas jet (at $z = 0$ mm). Without shock, self-injection of electrons will continue up to $z \sim 1.3$ mm. Accordingly, this lengthy self-injection process results in a long, large energy spread electron bunch, as shown in Fig. 4.9(a). In the case without shock, the head of the bunch reaches the decelerating region of the bubble after ~ 0.95 mm of acceleration with an energy around 250 MeV (the limit between the accelerating and decelerating regions is the point where the longitudinal field sign switches). As a result, electrons at the head of the bunch dephase and at the end of the gas jet their energy has decreased below 200 MeV, as shown in Fig. 4.9(c).

In the shock case, the phase space drastically changes when the bunch crosses the density step. The left side of the plot shown in Fig. 4.9(b) is about 50 μm far from the shock rising edge

($z_s = 0.9$ mm). Because of the reduction of the bubble size and the resulting positive shift of null field point, when the wakefield crosses the sharp density transition, the head of the bunch shifts back to the accelerating region of the shorten bubble (as pictured in Fig. 4.3). After the density step, it is located at the tail of the contracted bubble, and is efficiently accelerated by the extremely large longitudinal field of $E_x \approx 2$ TV.m^{-1}. The result is a very fast rotation of the head of the bunch in the phase-space (z, E), which produces naturally a quasi-monoenergetic spectrum, as can be seen in Fig. 4.9(c). Beyond the shock, the back half of the bunch is in the region with decelerating field (as pictured in Fig. 4.3). It experiences also a strong defocusing field when crossing the rear of the bubble. The corresponding electrons, in the range between 100 and 200 MeV, are both decelerated and defocused, resulting in a divergence growth at low energy. In a few simulations, it was also observed that some electrons can exit the wakefield if electrons are too strongly defocused.

The electron phase-space with the longitudinal injection position z_0 color-coded is shown in Fig. 4.10 just after the density step (a) and at the end of acceleration (b). Electrons shown in black and purple are self-injected around the middle of the gas jet ($z = 0$ mm) and are rephased after the transition. At the end of acceleration, the quasi mono-energetic peak, which has an energy around 300 MeV, consists of these electrons. The few electrons shown in yellow are injected at the shock position ($z_s = 900$ μm), corresponding to down-ramp injection. In the final energy distribution, they have energies not exceeding 150 MeV (most of them have energies below 100 MeV) and blur with the decelerated part of the main bunch. Simulations show unambiguously that the peak observed experimentally around 300 MeV cannot be attributed to down-ramp injected electrons, and corresponds to the rephased part of the bunch. Note that electrons having very low energy (below 50 MeV in Fig. 4.10(a)) represent electrons which are not trapped in the main bubble and eventually exit the simulation box (in Fig. 4.10(b), most of them have disappeared). These electrons are filtered in Fig. 4.9(a-b).

Energy enhancement from electron rephasing is stronger than expected from the model developed in section 4.1.2 (about 50 % compare to 30 %). Although this difference may originate from the model inaccuracy and strong assumptions, the major reason is the presence of an extremely strong longitudinal electric field at the back of the bubble after the density transition (up to ~ 2 TV.m^{-1}). Indeed, a large number of charge concentrates at the back of the bubble because of the bubble shrinking when crossing the shock, thus largely increasing the electric field locally. A theoretical study is currently undergoing at LOA to get more insight on this effect.

4.2.4   Blade position influence in the jet

The peak energy of the quasi-monoenergetic part of the electron beam can easily be varied by changing the position of the blade in the gas jet. Figure 4.11 shows the influence of the shock position on the cut-off energy and the peak energy. When the blade is moved so far into the gas jet that the shock is almost at the center of the nozzle, the energy cut-off is lower than for a density profile without transition. Indeed, the density transition is far before the position where the dephasing length is reached. As a result, electrons are less accelerated before the density transition, and only the very head of the bunch is re-accelerated in the high density plasma. As the shock is moved towards the end of the gas jet, the cut-off energy increases up to 400 MeV for $z_s \approx 0.65$ mm, corresponding to an energy enhancement of 45 % compared to the transition-free density accelerator. The energy of the quasi-monoenergetic peak is also found to be maximum for $z_s \approx 0.65$ mm, where it reaches 360 MeV.

However, if the shock is placed too far away from the nozzle center, the energy of the quasi-monoenergetic peak decreases. Indeed, the electrons at the head of the bunch (those which
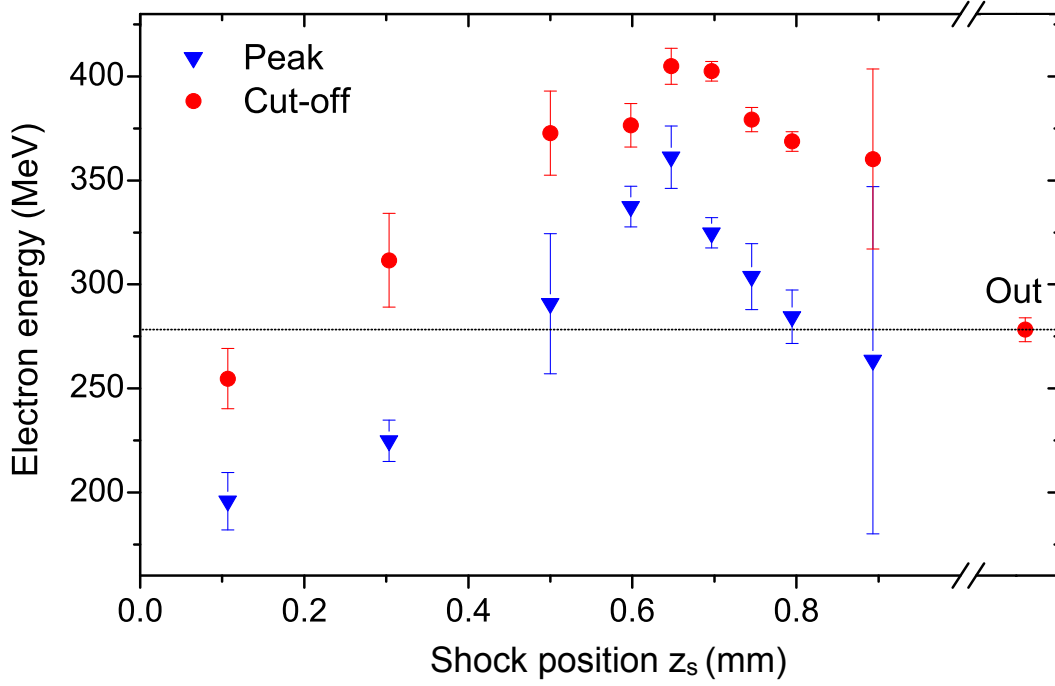
Figure 4.11: Electron cut-off energy at 18 fC/MeV (red dots) and energy of the quasi-monoenergetic peak (blue triangles) as function of the shock position in the gas jet. The error bars show the standard error of the mean over 5 to 39 consecutive shots. While the cut-off energy is measured at every shot, the peak energy cannot be determined on some shots when no peak can be clearly identified. The fraction of shots with a peak depends on the shock position; it is between 100% and 80% for $0.1 < z_s < 0.65$ mm and goes down to 50% for $z_s > 0.75$ mm.

can be accelerated after the density transition) already started to experience the decelerating region of the bubble in the first density plateau, resulting in a lower final energy. The optimal energy boost corresponding to the case where the shock is placed close to $2/3L_{deph}$, the length in this case may be higher than this value. Moreover, the peak energy may decrease when the shock is too close to the jet edge due to the remaining acceleration length after the density jump being too short to reach as large electron energies as before. The plasma density after the shock also diminishes when the blade is placed close to the jet edge (as seen in Fig. 4.7(b)), leading to a lower acceleration field, and then lower electron energies, than when the blade is more inserted. From section 4.1.2, it is clear that optimum rephasing of electrons is obtained when the transition is placed at $2/3L_{deph}$ with a density ratio of 4. In the experiment however, the shock position, density ratio and second density region length are strongly coupled. In Fig. 4.11, the optimal shock position at 0.65 mm (for which the energy is maximum) probably corresponds to a compromise between these three quantities. Ideally, the density ratio, the step position and the second plateau length should be varied independently to obtain the optimum rephasing. The next section presents a method to achieve a better, independent control over these parameters.
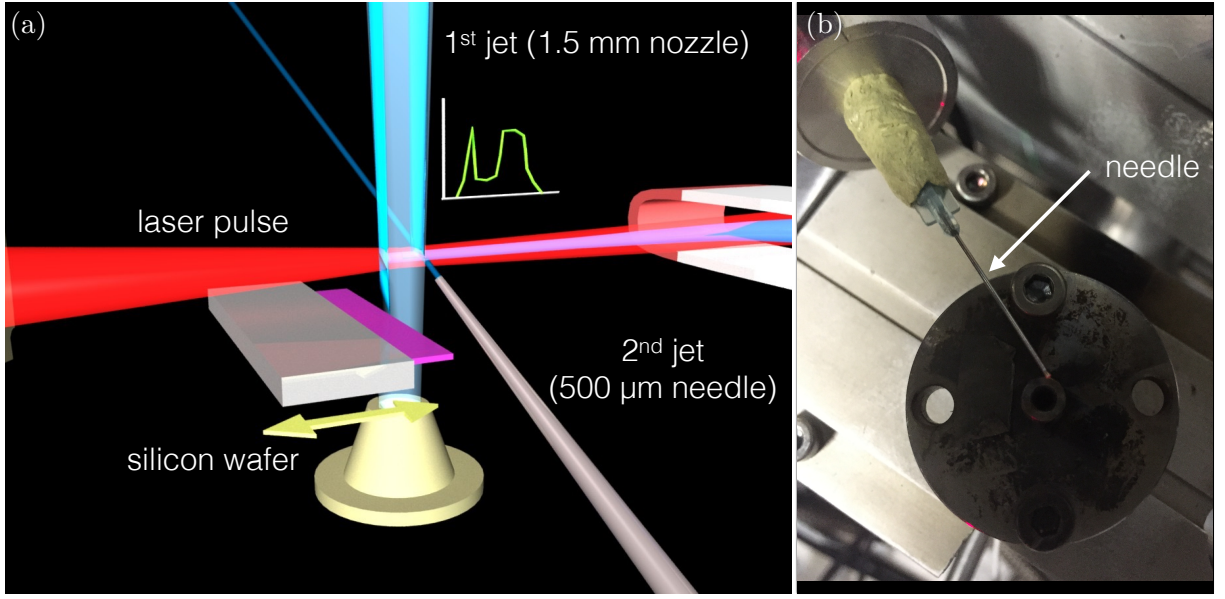
Figure 4.12: (a) Schematic representation of the experimental setup. The blade is used to inject electrons in a sharp transition. The second jet (the needle) is used to form a high density region at the end of the first jet. The resulting density profile is shown in green near the gas jet. (b) Picture of the first nozzle and the needle used in the experiment (the injection blade is out).

4.3 Rephasing of mono-energetic electron beams

4.3.1 Experimental setup

While in section 4.2, only the head of a large energy spread bunch is being rephased and further accelerated, this technique can also be used to rephase and re-accelerate a higher quality, low energy spread electron beam. Such an electron beam can be generated by using shock front injection, as detailed in chapter 2. The experimental setup is modified as sketched in Fig. 4.12(a). The main interaction beam P1 is now focused using a 1 m focal length off-axis parabola, delivering 1.2 J in a focal spot size of 18 μm FWHM (shown in Fig. 4.13(a)). The peak intensity on target is $I = 1 \times 10^{19}$ W.cm^{-2}, equivalent to a normalized vector potential $a_0 = 2.2$. The silicon wafer is placed at the entrance of the jet to generate a sharp downward density gradient allowing for shock front injection of electrons. A second gas jet formed with a 500 μm diameter needle is placed horizontally at the output of the first supersonic jet (as seen in Fig. 4.12(b)), creating a region with a higher tunable density n_{e2}. The needle can be moved relatively to the first jet. Due to the formation of a shock, the sharpness of the transition between these two density regions is similar to that obtained with the previous setup. The resulting plasma density profile (pictured in green near the gas jet in Fig. 4.12(a)) is estimated from the interferometric measurements with the Nomarski interferometer (visible in Fig. 4.13(b)).

4.3.2 Experimental results

The density in the first jet is set so that electrons are injected in the density transition while avoiding continuous self-injection. Such a regime is reached for $n_0 = 1.0 \times 10^{19}$ cm^{-3}. Note that the density seems quite high for self-injection not to trigger. Looking at the plasma in Fig. 4.13(b), the laser pulse does not seem to be efficiently self-focused, thus keeping quite a low
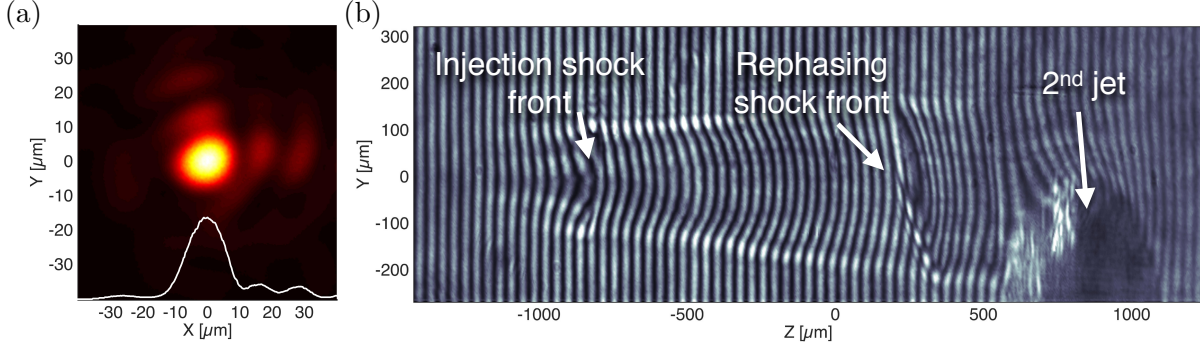
Figure 4.13: (a) Experimental laser focal spot obtained with a 1 m focal length off-axis parabola. (b) Interferogram of the propagation of the laser in a pure helium gas jet. $Z = 0$ mm corresponds to the center of the first nozzle. The shock allowing for injection is visible at $z_1 = -800$ μm, while the density transition created by the second jet used for phase-reset is located around $z_2 = 250$ μm.

energy along the propagation. This may be due to a low quality wavefront of the laser pulse. Shock-injected electrons have a quasi-monoenergetic distribution, as shown in Fig. 4.14(a), with a peak energy of 125 ± 2 MeV and a charge of 10 ± 2 pC (mean values over ten shots). The integrated spectrum over the transverse dimension is shown in light blue in Fig. 4.14(b). The peak energy is quite low for such an experimental setup (electrons were able to reach about 260 MeV in the similar experiment presented in section 2.3). This important discrepancy may come once again from a low quality laser wavefront inducing a weak self-focusing, hence a low intensity. Due to the fact that the cavity is certainly not fully evacuated, the generated accelerating fields may be quite weak in this case.

When the needle is placed so that the transition between the two density regions is close to $z_s = 0.55$ mm, the electron spectrum drastically changes (as shown in Fig. 4.14(a)). The mono-energetic electron beam is rephased in the second jet after crossing the density transition (as explained in section 4.1), it is thus able to be further accelerated up to 220 MeV for an electron density in the second jet of $n_{e,2} = 2.6 \times 10^{19}$ cm^{-3}. Inversely to section 4.2, the bunch is mono-energetic enough so that quite a good chunk of electrons remains in the accelerating part of the first bubble when it shortens. Some electrons at the back of the bunch cross the rear part of the cavity and are decelerated and defocused, forming the continuous, low-energy tail visible in the experimental spectrum presented in Fig. 4.14(b). This low-energy tail may also originate from electron injection in the second gas jet. The mean charge in the rephased quasi mono-energetic peak is 2.8 ± 0.6 pC : about 30 % of shock-injected electrons are rephased while others are decelerated and defocused. Note that the absolute energy spread without (10 ± 2 MeV) and with (12 ± 4 MeV) the second gas jet are very similar. The energy gain in this case is about 75 %, much larger than expected from the simple phase-reset model presented in section 4.1.2. While phase-resetting of electrons certainly happens at the transition between the two density regions, another reason for energy enhancement may be the global increase of the acceleration length. Indeed, when the second gas jet formed by the needle is triggered, the total plasma length increases from 1.6 mm to 2.1 mm. However, the corresponding energy gain would not exceed 30 % (considering a mean density of 2×10^{19} cm^{-3} over 0.5 mm). Thus, the total energy gain is certainly a combination of acceleration length enhancement and phase-resetting at the transition. The energy gain depends strongly on the density in the second gas jet, as
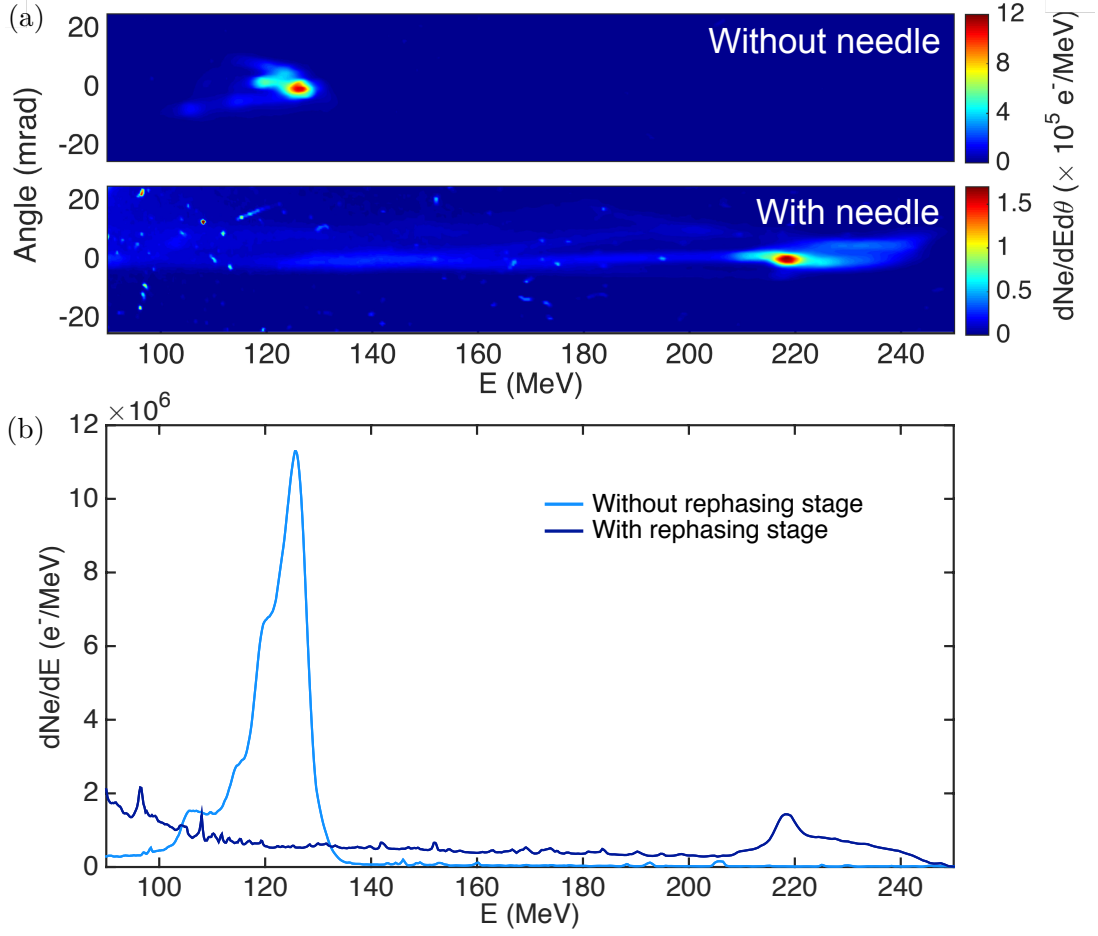
Figure 4.14: (a) Experimental angle resolved electron spectra (corrected from the spectrometer dispersion) of shock-injected electrons with no gas (top panel) and gas at optimal density (bottom panel) flowing from the needle. (b) Corresponding spectra integrated over the transverse dimension.

explained in section 4.1.2. Figure 4.15 shows experimental spectra for different plasma densities n_{e2}, from 0 (top) to 3.1×10^{19} cm^{-3} (bottom). The electron beam starts to rephase in the second jet for an electron density $n_{e,2} = 1.8 \times 10^{19}$ cm^{-3}, with the peak energy increasing up to 154 ± 8 MeV. By further increasing the second jet density, electrons can reach higher and higher energies. Indeed, the density in the first jet is $n_0 = 1.0 \times 10^{19}$ cm^{-3}. From the model presented in section 4.1.2, the energy gain is maximum if $n_{e,2} \sim 2n_0$, as it is observed in this experiment. When the plasma density in the second region is too high however ($n_{e,2} = 3.1 \times 10^{19}$ cm^{-3}, bottom panel of Fig. 4.15), the bubble contracts too strongly at the transition and the electron beam is located behind the cavity, and is thus decelerated and defocused. It may explain that no electrons are observed in the spectrometer range of measurement.

4.4 Conclusion

In conclusion, we presented in this chapter the experimental demonstration of a simple density tailored wakefield accelerator. A sharp upward density gradient was used to rephase the electron
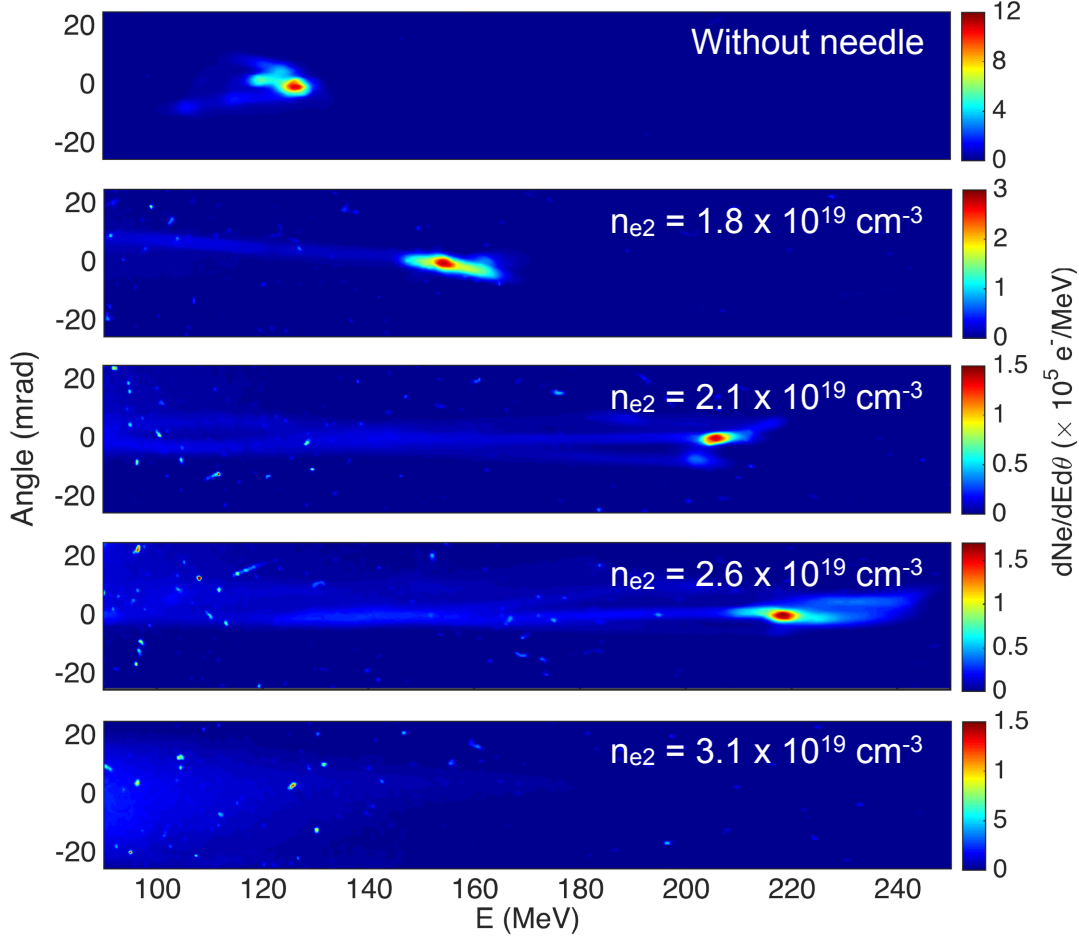
Figure 4.15: Experimental angle resolved electron spectra of shock-injected electrons with no gas flowing from the needle (top panel), and for four different plasma densities in the second jet.

beam with the accelerating field and increase its energy. Note that we demonstrate here a proof-of-concept of phase-resetting, and much remains to be done to achieve quasi phase matching. Our technique can either be used to select a part of a broad energy spread electron beam and increase its energy or to enhance the energy of a mono-energetic electron beam. Experimental results highlight a maximum energy enhancement from phase-resetting of about 50 % compared with a transition-free plasma density. These results were published in Guillaume et al. [2015b]. A way to improve this phase-resetting setup would be to better control the second density region parameters so that the total acceleration length would not change when tuning the second jet density (for instance by using a very supersonic second jet with sharp gradients). Thus, the observed energy gain would originate from phase-resetting of electrons, with an influence of the strongest accelerating fields in the higher density region. A more detailed scan of the second jet position and density would also be necessary in order to study the effects of phase-space rotation that seems to be observed in electron spectra. Moreover, a more detailed numerical study of the electron beam separation (a small part is rephased while most of the electrons are decelerated and defocused) would be quite interesting to perform. It opens a new concept of electron longitudinal phase-space manipulation which is of major importance for several applications.

Chapter 5

Angular momentum evolution of electrons in a laser-plasma accelerator

In this chapter, we show that the evolution of the electrons angular momentum during the acceleration can be induced by an asymmetric plasma cavity, probably originating from a non-perfectly symmetric laser pulse. This explanation for the origin of the angular momentum is supported by experimental results and simulations. Electrons angular momentum is an important process to take into account in betatron based emittance measurement, as it strongly influences the shape and divergence of the x-ray beam angular and spatial properties.

Contents

5.1 Angular momentum of an electron in a LWFA

The angular momentum of an electron in a Laser-Wakefield Accelerator is related to the rotational motion of the electron in the transverse plane (x, y) around its propagation axis z during the acceleration in the ion cavity. It can be described with the vector quantity L_z which is the cross-product of the position vector $\boldsymbol{r}$ of the electron in the plane (x, y) with the linear momentum $\boldsymbol{p}$ of the particle :

$$\boldsymbol{L_z} = \boldsymbol{r} \times \boldsymbol{p} = (xp_y - yp_x)\boldsymbol{e_z}. \tag{5.1}$$

The angular momentum of an electron is schemed in Fig. 5.1. In the next section is presented the impact of the angular momentum of accelerated electrons onto the generation of betatron radiation and its signature in betatron angular profiles.
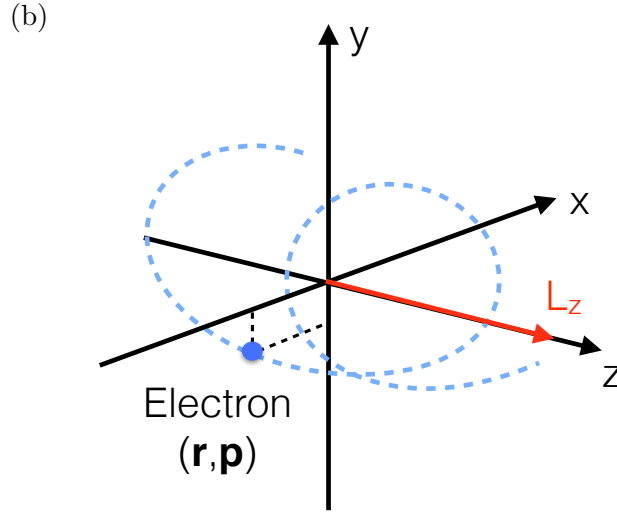
Figure 5.1: Definition of the angular momentum of an electron L_z.

5.2 Correlation between electron bunch and betatron radiation

5.2.1 Betatron oscillation and radiation in the bubble regime

In the bubble regime [Lu et al., 2007], electrons are accelerated and undergo betatron oscillations in the transverse focusing fields of the cavity (as explained in section 1.2.5). The cavity is assumed to be perfectly spherical with cylindrical symmetry along the z-axis. The restoring electrostatic force experienced by a relativistic electron propagating in the cavity is transverse, directed toward the z-axis, and can be written as:

$$\boldsymbol{F_\perp} = -\frac{1}{2}m_e\alpha\omega_p^2 r \; \boldsymbol{e_r} \quad \text{for} \quad r < r_B \tag{5.2}$$

with $\alpha \leq 1$ a coefficient describing a possible deviation from the nominal transverse force of a fully evacuated ion cavity ($\alpha = 1$ for a bubble completely electron-free) and r_B the bubble radius defined in section 1.2.4. For an adiabatic acceleration, the adiabatic invariant J is conserved [Corde, 2012] :

$$J = \frac{p^2}{2m_e\omega_\beta\gamma} + \frac{1}{4\omega_\beta}m_e\alpha\omega_p^2 r^2 \tag{5.3}$$
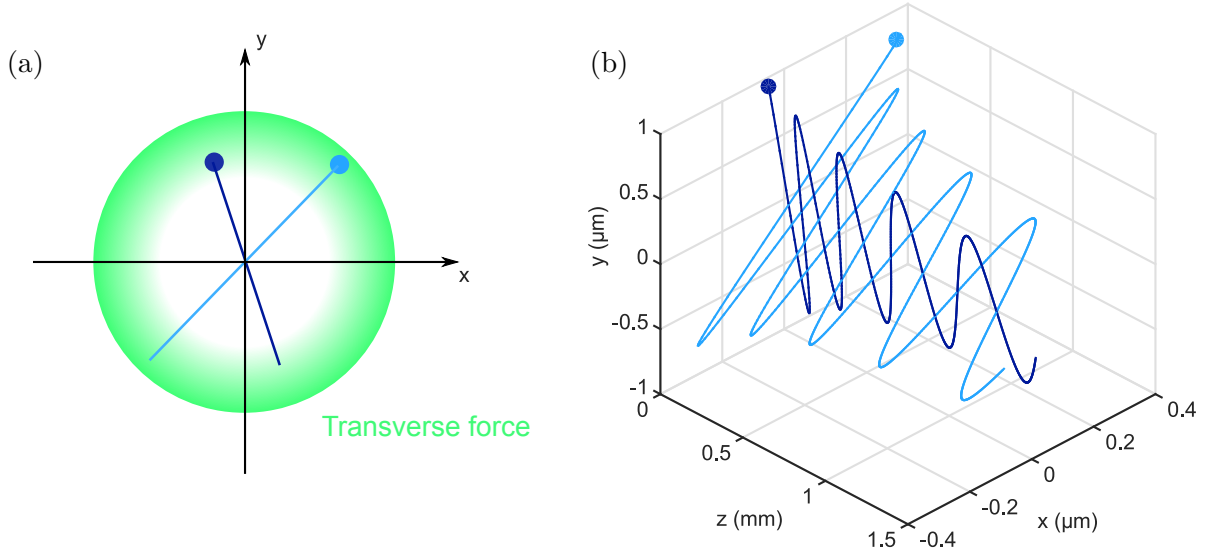
Figure 5.2: (a) Drawing of two electrons experiencing focusing transverse forces in the (x, y) plane of a spherical ion cavity. (b) Corresponding electron orbits during the acceleration along z.

with γ the electron relativistic factor, p its momentum along $\boldsymbol{e_r}$ and $\omega_\beta = \omega_p \sqrt{\frac{\alpha}{2\gamma}}$ the betatron frequency defined in section 1.2.5 (now the α coefficient is taken into account). J represents the normalized modulus of the electron position in the six-dimensional phase space $(\hat{x}, \hat{y}, \hat{z}, \hat{p}_x, \hat{p}_y, \hat{p}_z)$.

In this formalism, the expression of transverse motion is [Corde et al., 2013a] :

$$\hat{r}(t) = \sqrt{\hat{J}} \sin \left[\int_0^t \omega_\beta(t') dt' + \varphi_r \right] \tag{5.4}$$

$$\hat{p}(t) = \sqrt{\hat{J}} \cos \left[\int_0^t \omega_\beta(t') dt' + \varphi_r \right] \quad \text{with} \quad \omega_\beta(t) = \omega_p \sqrt{\frac{\alpha}{2\gamma(t)}} \tag{5.5}$$

where $\hat{r} = (\alpha\gamma/8)^{\frac{1}{4}} k_p r$ and $\hat{p} = p/(2\alpha\gamma)^{\frac{1}{4}} m_e c$ are normalized variables and $\hat{J} = k_p J/m_e c = \hat{r}^2 + \hat{p}^2$ the squared norm in the phase-space (r, p). The transverse motion consists in sinusoidal oscillations along $\boldsymbol{e_r}$ with time-dependent amplitude $\sqrt{\hat{J}(t)}$ and frequency $\omega_\beta(t)$. They depend on time only through γ. The betatron amplitude decreases as $\gamma^{-\frac{1}{4}}$ during acceleration, while the frequency decreases as $\gamma^{-\frac{1}{2}}$. Figure 5.2(a-b) shows the evolution of the trajectories of two electrons with zero initial momentum and different initial positions along the acceleration. Because of a null initial angular momentum, these electrons have planar trajectories. Note that there is a continuous set of initial conditions for electrons injected in the cavity, potentially with a non-null initial momentum. In this case, electron trajectories can be helicoidal (if they have a non-zero momentum perpendicular to $\boldsymbol{e_r}$).

Betatron radiation is emitted during this relativistic motion, with a spectrum defined as [Jackson, 1998] :

$$\frac{dI}{d\omega} = \frac{1}{4\pi\varepsilon_0} \times \sqrt{3} \frac{q_e^2}{c} \gamma \frac{\omega}{\omega_c} \int_{\omega/\omega_c}^\infty K_{\frac{5}{3}} u\, du \tag{5.6}$$

119
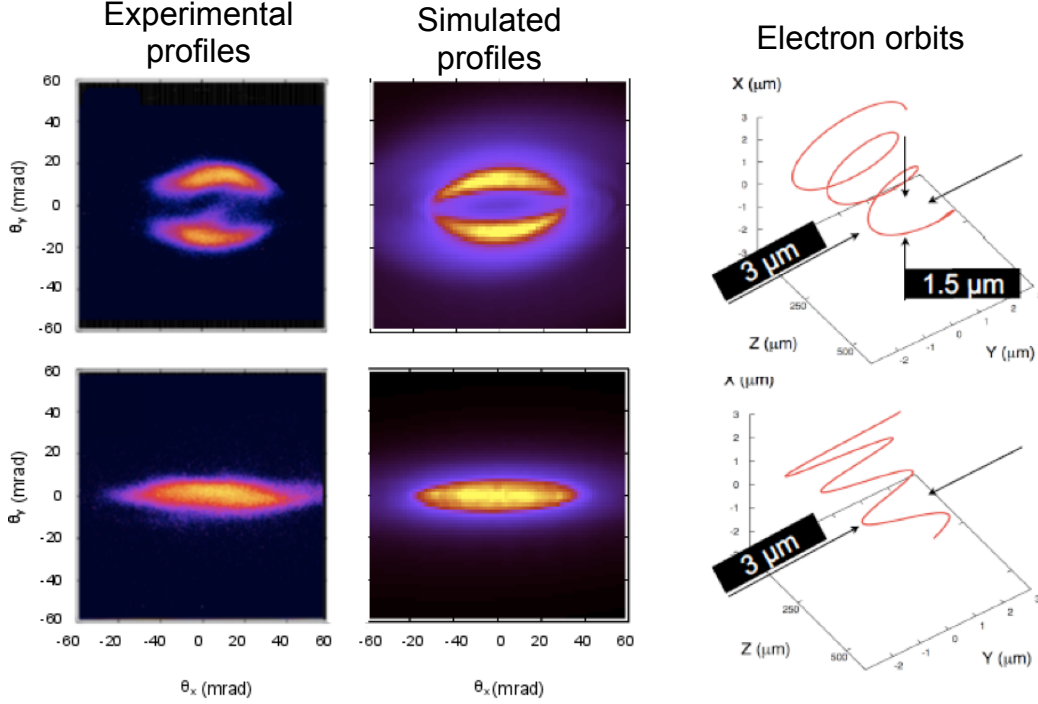
Figure 5.3: Experimental betatron profiles (left), numerical simulation of the beam profiles (middle) and corresponding electron trajectories (right). *Figure from [Phuoc et al., 2006]*

with $\omega_c = 3/2\gamma^3 c/R_c$, R_c the radius of curvature of the electron orbit and $K_{\frac{5}{3}}$ the modified Bessel function. This expression shows that electrons emit more in trajectory sections where the radius of curvature is minimum. The spatial distribution of betatron radiation is obtained by calculating $dI/d\Omega$ (integration over frequencies) as a function of the direction of observation. Radiation for an electron having a planar trajectory consists on an elliptical beam with a divergence $\theta_x \sim p_x/\gamma$ along the oscillating plane and $\theta_y \sim p_y/\gamma$ in the orthogonal direction. Measurement of the betatron spatial profile can thus provide the mean electron momentum during the betatron emission in the wakefield cavity. An experimental study of the correlation between betatron profiles and electron trajectories was performed by Phuoc et al. [2006]. This work reveals that electrons in a ion cavity can carry some angular momentum, as shown in Fig. 5.3. Indeed, betatron profiles observed may be fully elliptical with variable width or doughnut-shaped in some cases (top panels of Fig. 5.3). These profiles correspond to cases where electrons have a helicoidal trajectory, with a non-null angular momentum. However, the origin of electrons angular momentum remains unclear. In this chapter, we propose a possible explanation for the origin of the angular momentum evolution of electrons during acceleration in the case where the laser pulse is asymmetric, inducing an elliptical bubble.

5.2.2 Electron trajectories in an elliptical plasma cavity

Laser wavefront aberrations are recognized to impact the properties of accelerated electron beams [Glinec et al., 2008; Mangles et al., 2009; Popp et al., 2010]. Nevertheless, most numerical simulations of laser-plasma interaction are performed for perfect gaussian laser pulses, so that the scope of the phenomenon remains largely unknown. As electron trajectories and thus the
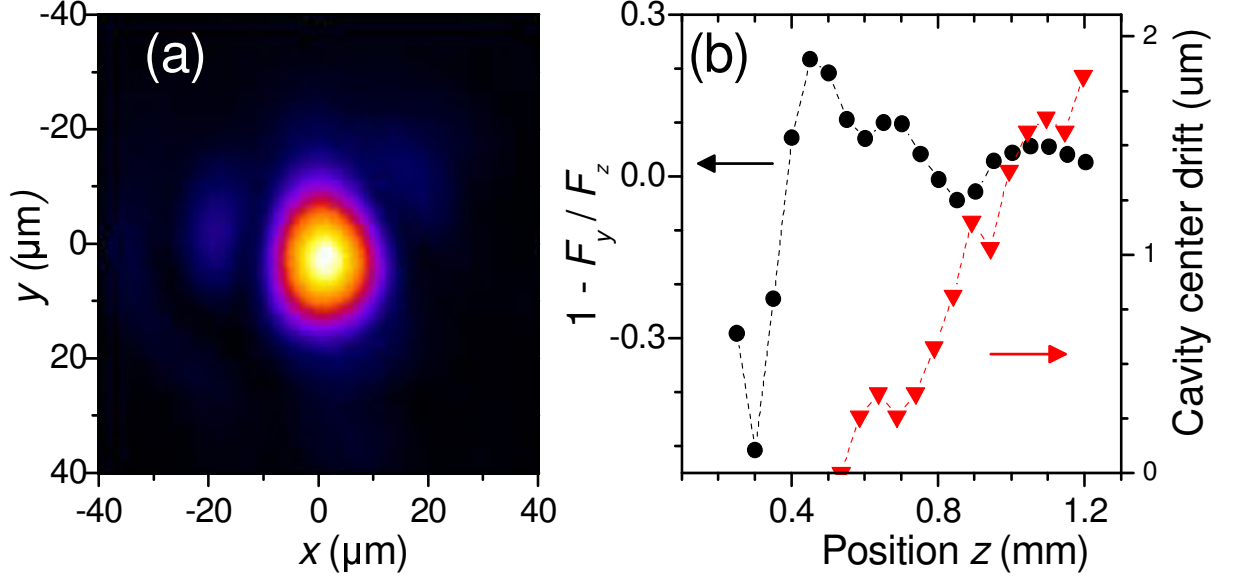
Figure 5.4: Wakefield excitation by a realistic laser pulse. (a) Experimental laser focal spot. (b) Ratio of the transverse forces in two perpendicular directions $1 - F_y/F_z$, and drift of the cavity center in the transverse plane, obtained from a 3D PIC simulation using the focal spot shown in (a).

angular momentum are strongly influenced by the shape of the accelerating cavity, 3D PIC simulations were performed by X. Davoine from CEA/DAM with the code Calder to assess the influence of a distorted laser wavefront on this shape. The normalized laser amplitude was a_0=1.3, with a focal spot width of 22 μm full width at half maximum (FWHM), a pulse duration of 35 fs FWHM and the electron density $n_e = 10^{19}$ cm^{-3}. The simulated focal spot is shown in Fig. 5.4(a); it is elliptical with some energy in the wings. This laser pulse creates a plasma cavity whose center changes in time (mainly on the y axis) and in which the transverse focusing force is anisotropic, as illustrated in Fig. 5.4(b). The force is measured at the center of the plasma cavity at 2 μm from the back of the cavity. The mean absolute ellipticity of the cavity is $\varepsilon = 11\%$. The asymmetry is a function of time because of different self-focusing dynamics in the two transverse directions.

Electrons in such an asymmetric cavity experience a different force in the two transverse directions ($\boldsymbol{x}$ and $\boldsymbol{y}$). For simplicity, the drift of the cavity center is neglected although it may have a similar effect as the force asymmetry, and the cavity is assumed to be elliptical with $\boldsymbol{x}$ the minor axis and $\boldsymbol{y}$ the major axis. The transverse forces are then :

$$\boldsymbol{F_x} = -\frac{1}{2}\alpha m_e \left(1 + \frac{\varepsilon}{2}\right) \omega_p^2 x \ \boldsymbol{e_x} \qquad (5.7)$$

$$\boldsymbol{F_y} = -\frac{1}{2}\alpha m_e \left(1 - \frac{\varepsilon}{2}\right) \omega_p^2 y \ \boldsymbol{e_y} \qquad (5.8)$$

with $\varepsilon \leq 1$ the coefficient that quantifies the asymmetry of the transverse forces, thus the ellipticity of the cavity. In this case, an adiabatic invariant should be defined for each axis : $J_u = \frac{p_u^2}{2m_e\omega_\beta\gamma} + \frac{1}{4\omega_\beta}m_e\alpha\left(1 + \frac{\varepsilon}{2}\right)\omega_p^2 u^2$ with $u = (x, y)$. The normalized adiabatic invariants are $(\hat{J}_x = \hat{x}^2 + \hat{p}_x^2, \hat{J}_y = \hat{y}^2 + \hat{p}_y^2)$ with $\hat{J} = \hat{J}_x + \hat{J}_y = \hat{r}^2 + \hat{p}^2$. The electron orbit in the 4-dimension

121

phase-space (x, y, p_x, p_y) is then given by :

$$\hat{x}(t) = \sqrt{\hat{J}_x} \sin \left[\int_0^t \omega_{\beta x}(t')dt' + \varphi_x \right] \tag{5.9}$$

$$\hat{p_x}(t) = \sqrt{\hat{J}_x} \cos \left[\int_0^t \omega_{\beta x}(t')dt' + \varphi_x \right] \tag{5.10}$$

$$\hat{y}(t) = \sqrt{\hat{J}_y} \sin \left[\int_0^t \omega_{\beta y}(t')dt' + \varphi_y \right] \tag{5.11}$$

$$\hat{p_y}(t) = \sqrt{\hat{J}_y} \cos \left[\int_0^t \omega_{\beta y}(t')dt' + \varphi_y \right]. \tag{5.12}$$

While this formalism is useful to study the electron orbit numerically, the trajectory can also be described in non-normalized units for a better understanding :

$$x(t) = x_0 \left(\frac{\gamma_i}{\gamma(t)} \right)^{\frac{1}{4}} \sin \left[\sqrt{1 + \frac{\varepsilon}{2}} \Phi(t) + \Phi_{x0} \right] \tag{5.13}$$

$$y(t) = y_0 \left(\frac{\gamma_i}{\gamma(t)} \right)^{\frac{1}{4}} \sin \left[\sqrt{1 - \frac{\varepsilon}{2}} \Phi(t) + \Phi_{y0} \right] \tag{5.14}$$

$$p_x(t) = m_e\gamma(t)x_0 \left(\frac{\gamma_i}{\gamma(t)} \right)^{\frac{1}{4}} \left[\omega_p \sqrt{\frac{\alpha}{2\gamma}(1 + \frac{\varepsilon}{2})} \cos \left(\sqrt{1 + \frac{\varepsilon}{2}} \Phi(t) + \Phi_{x0} \right) - \frac{1}{4} \frac{\gamma'(t)}{\gamma(t)} \sin \left(\sqrt{1 + \frac{\varepsilon}{2}} \Phi(t) + \Phi_{x0} \right) \right] \tag{5.15}$$

$$p_y(t) = m_e\gamma(t)y_0 \left(\frac{\gamma_i}{\gamma(t)} \right)^{\frac{1}{4}} \left[\omega_p \sqrt{\frac{\alpha}{2\gamma}(1 - \frac{\varepsilon}{2})} \cos \left(\sqrt{1 - \frac{\varepsilon}{2}} \Phi(t) + \Phi_{y0} \right) - \frac{1}{4} \frac{\gamma'(t)}{\gamma(t)} \sin \left(\sqrt{1 - \frac{\varepsilon}{2}} \Phi(t) + \Phi_{y0} \right) \right] \tag{5.16}$$

with $\Phi(t) = \int_0^t \sqrt{\frac{\alpha}{2\gamma(t')}} \omega_p dt'$ the time-dependent phase of the electron along its elliptical orbit, (x_0, y_0) the initial position, (Φ_{x0}, Φ_{y0}) the initial phases, γ_i the initial relativistic factor of electron when injected in the cavity and γ' the temporal derivative of γ. Note that the second terms in the brackets of p_x and p_y can be neglected in an adiabatic acceleration, as γ evolves quite slowly during the acceleration ($\gamma' \ll \gamma$).

The angular momentum of the electron is defined as $L_z = xp_y - yp_x$, and can be calculated from eqs. (5.13) to (5.16), with the help of trigonometry identities :

$$L_z = xp_y - yp_x = m_e\omega_p x_0 y_0 \sqrt{\frac{\alpha\gamma_i}{2}} \sin \left(\sqrt{1 + \frac{\varepsilon}{2}} \Phi(t) - \sqrt{1 - \frac{\varepsilon}{2}} \Phi(t) - 2\Phi_0 \right). \tag{5.17}$$

For an elliptical bubble ($\varepsilon \neq 0$), electrons oscillate with different time-dependent frequencies along x and y. As a result, their trajectories which are initially planar for electrons with zero angular momentum ($\Phi_{x0} = \Phi_{y0} = \Phi_0$), progressively become helicoidal, before reverting to planar trajectories every time $\Phi(t) = k\pi/(1 - \sqrt{1 - \varepsilon})$ with k an integer (as shown in Fig. 5.5(a-b)). In other words the angular momentum L_z changes in time.

Assuming that the ellipticity of the cavity is small enough ($\varepsilon \ll 1$), eq. (5.17) can be simplified as :

$$\frac{L_z}{m_e\omega_p} = x_0 y_0 \sqrt{\frac{\alpha\gamma_i}{2}} \left(\sin \left(\frac{\varepsilon}{2}\Phi \right) - \frac{\varepsilon}{4} \sin[2(\Phi + \Phi_0)] \right) \tag{5.18}$$

The first term accounts for slow variations of L_z; it is responsible for the transition from planar to helicoidal trajectories. The second term corresponds to high frequency oscillations.
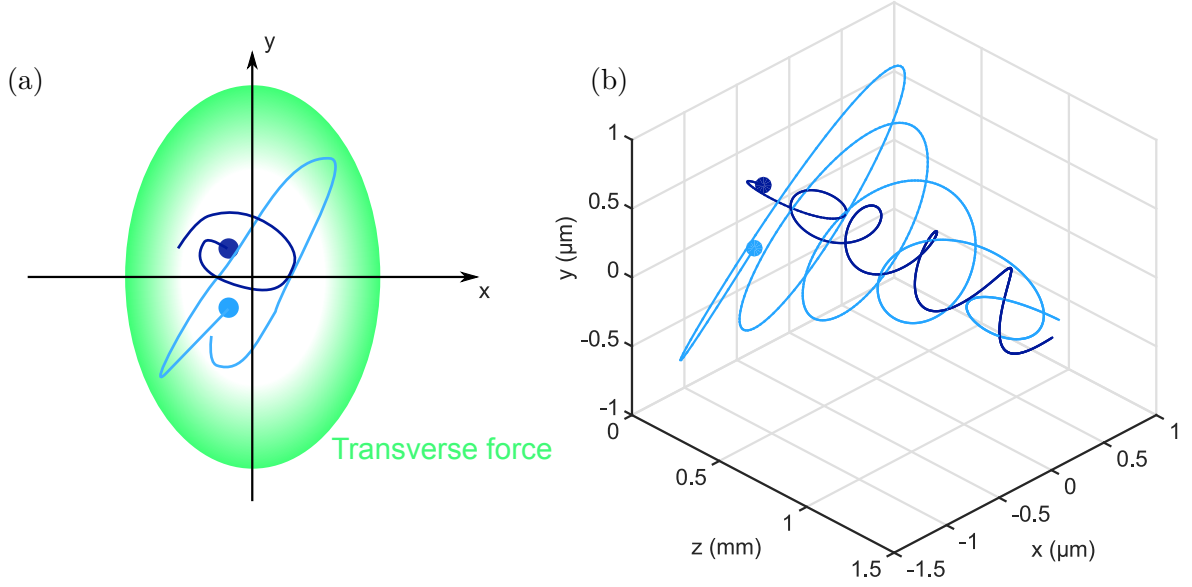
Figure 5.5: (a) Drawing of two electrons experiencing focusing transverse forces in the (x, y) plane of an elliptical ion cavity. (b) Corresponding electron orbits during the acceleration along z.

It is of low amplitude and can be neglected in a first approximation. This equation also shows that, for a given initial radius $r_0 = \sqrt{x_0^2 + y_0^2}$, L_z is maximum when $x_0 = y_0$, that is when electrons are initially in a plane at $45°$ to the ellipse axes, whereas L_z remains 0 at all times for on-axis electrons. Note that the losses of energy and angular momentum by radiation are negligible and were not considered in the derivation of eq. (5.18). The angular momentum conservation is ensured by the fact that electrons and ions from the cavity sheath acquire some angular momentum.

Figure 5.6 shows the trajectory of an electron during its acceleration (a) and the corresponding evolution of its angular momentum (b), with the color varying along z. For a given (x_0, y_0), the angular momentum reaches its peak value when $\Phi(t) = \pi/\varepsilon$. Assuming for simplicity $\gamma = \gamma_i + \kappa t$, we find for $\varepsilon = 0.2$ and typical laser-plasma parameters ($\gamma_i = 25$, $\kappa = 10^{14}$ s^{-1}, $n_e = 8 \times 10^{18}$ cm^{-3} and $\alpha = 0.5$), that L_z is maximum after an acceleration of ≈ 600 μm (as seen in Fig. 5.6(b)). As effective acceleration lengths in experiments are generally about or larger than 1 mm, the slow oscillations of L_z should be observable, assuming that the acceleration length can be precisely controlled.

In summary, from the simple model for transverse forces in the cavity from Lu et al. [2007], we show that the bubble anisotropy (induced by the laser focal spot ellipticity) can change the trajectories of some accelerated electrons, as they gain angular momentum during the acceleration. It hence modifies the properties of the accelerated electrons and the x-rays they emit. Information on the angular momentum content of the electron beam is then obtained from the analysis of betatron X-rays [Rousse et al., 2004; Corde et al., 2013a].
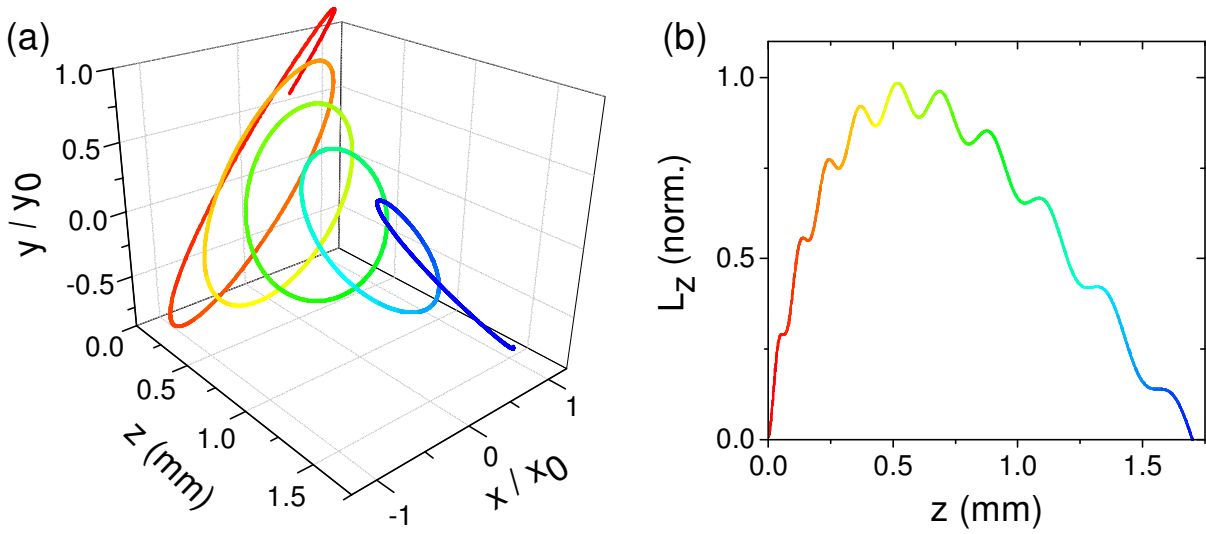
Figure 5.6: Evolution of the angular momentum in an elliptical cavity. (a) Trajectory of an electron. (b) Angular momentum as a function of the longitudinal position z (the color is a function of z). The parameters are $\varepsilon = 0.2$, $\gamma_i = 25$, $\kappa = 10^{14}$ s^{-1}, $n_e = 8 \times 10^{18}$ cm^{-3} and $\alpha = 0.5$).

5.2.3 Principle of optical injection

In order to have sufficient control on the acceleration length so that the angular momentum of electrons can be precisely studied, the colliding pulse injection scheme is chosen. With this technique, exposed briefly in section 1.2.6, the injection is relatively separated from the acceleration. The accelerating wakefield depends only on the propagation of the main driving pulse and the plasma density, remaining the same whatever the properties of the injection beam. The driving pulse generating the wake propagates forward while the injection pulse propagates backward (as seen in Fig. 5.7(a)). When the two pulses collide, a beat wave with half the wavelength of the driving laser is formed and can pre-accelerate electrons directly in the bubble (due to the large ponderomotive force associated with the beat wave), as shown in Fig. 5.7(b). This injection is triggered very locally, as it happens only during the few dozens of femtoseconds when the two pulses collide. Once injected, electrons are accelerated in the remaining acceleration length (Fig. 5.7(c)).

Optical injection is very reproducible, and allows for the generation of high quality, low energy spread electron beams. Beam parameters can be controlled by varying the injection pulse intensity, as well as the collision position z_{col} which is related to the final electron energy (the sooner the two pulses collide, the larger the remaining acceleration length and thus the energy). This fine tunability and stability in electron energy allows for performing a precise experimental study on the betatron profiles dependence as a function of the electron energy.

5.3 Experimental study of the evolution of angular momentum of electrons

The experiment was performed in the frame of Sébastien Corde PhD thesis in 2009 before the beginning of my own thesis. My work consisted in the detailed analysis of experimental results
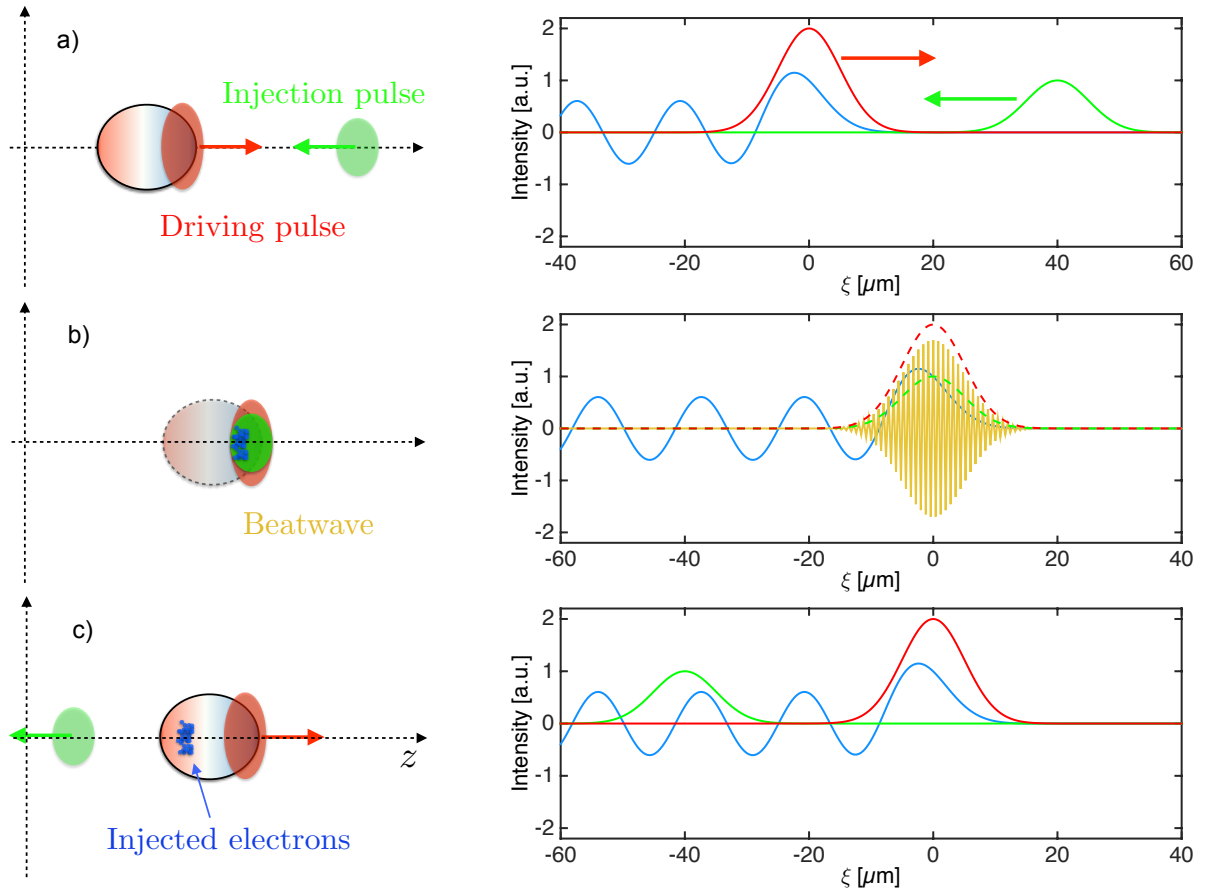
Figure 5.7: Principle of optical injection. (a) The injection pulse (green) propagate in the counter direction of the driving pulse (red) generating a wakefield (blue curve) in the bubble regime. (b) When they collide, the resulting beat wave (orange) triggers a very strong ponderomotive force and pre-accelerate electrons, which are injected in the cavity. (c) After the collision, the driving pulse continues to propagate and trapped electrons (blue dots) can accelerate further.

to highlight the angular momentum evolution of electron during acceleration [Thaury et al., 2013].

5.3.1 Experimental setup and diagnostics

Two synchronized 35 fs FWHM laser pulses of the "Salle Jaune" laser system are used : the pump pulse that drives the accelerating plasma wave contains 1.5 J and the injection pulse that triggers the injection into the main pump pulse wakefield contains 200 mJ. The two pulses have the same linear polarization. They are focused onto a 3 mm supersonic helium gas jet where they collide at a 135 degrees angle (as seen in Fig. 5.8). The pump pulse (respectively the injection pulse) has a mean FWHM focal spot size of 18 μm (respectively 22 μm), and a total energy contained in the focal spot of about 50 % in both cases. The normalized vector potential amplitude is thus $a_0 = 1.3$ (respectively $a_0 = 0.4$). Electron spectra (measured with the spectrometer defined in section 1.4.3) and x-ray angular profiles are recorded simultaneously in a single shot. X-ray profiles are obtained from an x-ray CCD placed on axis at 90 cm from the gas jet, behind a 25 μm Be filter (used to stop the laser from entering the XCCD). In this
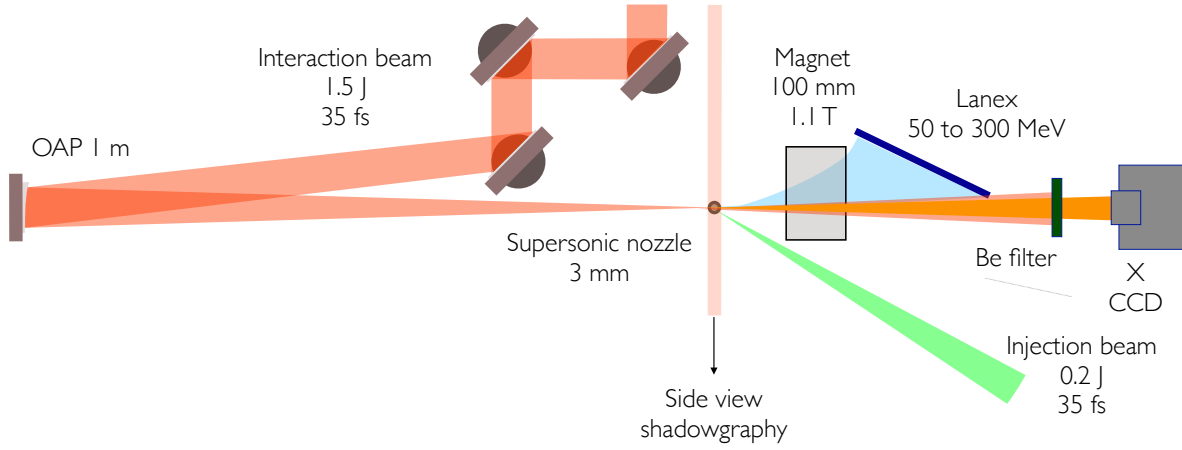
Figure 5.8: Drawing of the experimental setup used in the colliding injection experiment.

experiment, the electron plasma density is $n_e = 8 \times 10^{18}$ cm^{-3}, which corresponds, for these experimental parameters, to an interaction regime where electrons are not self-injected in the wakefield. Consequently, electrons and x-rays are observed only when both laser pulses overlap in time and space.

5.3.2 Optical injection of electrons
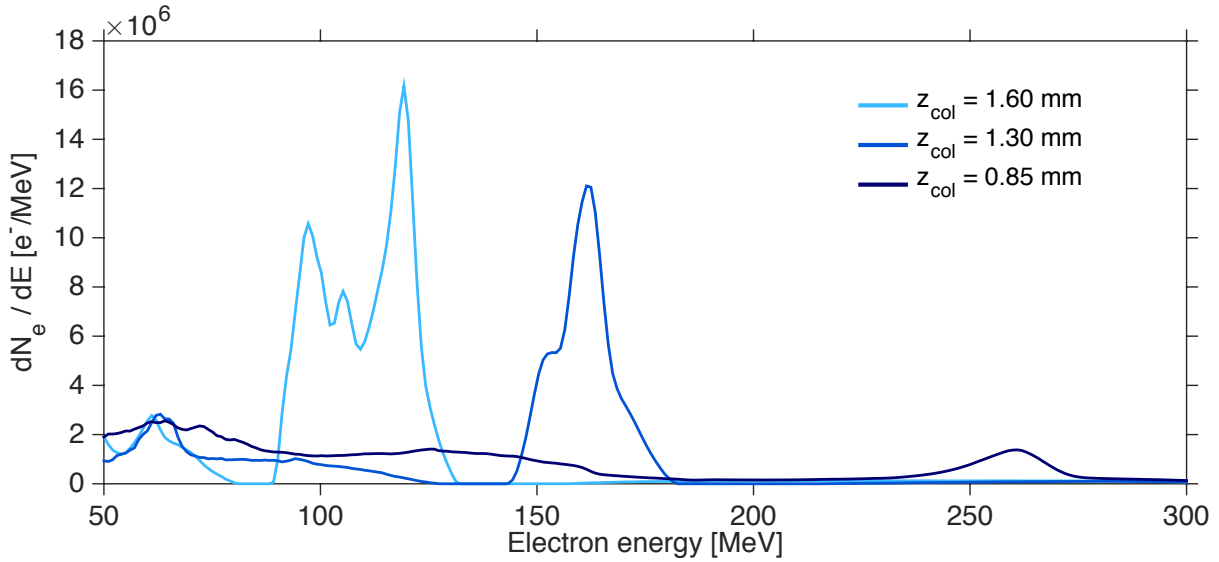
Figure 5.9: Experimental electron spectra for three different collision positions. The position $z_{col} = 1.5$ mm corresponds to a pulse collision occurring at the center of the gas jet.

Typical experimental electron spectra for three different collision positions are shown in Fig. 5.9 (with $z_{col} = 1.5$ mm from the center of the gas jet). Optical injection allows for the generation of quasi mono-energetic beams with a variable energy between 100 and 250 MeV. For a pulse collision close to the center of the gas jet, the energy and charge of the beam are about
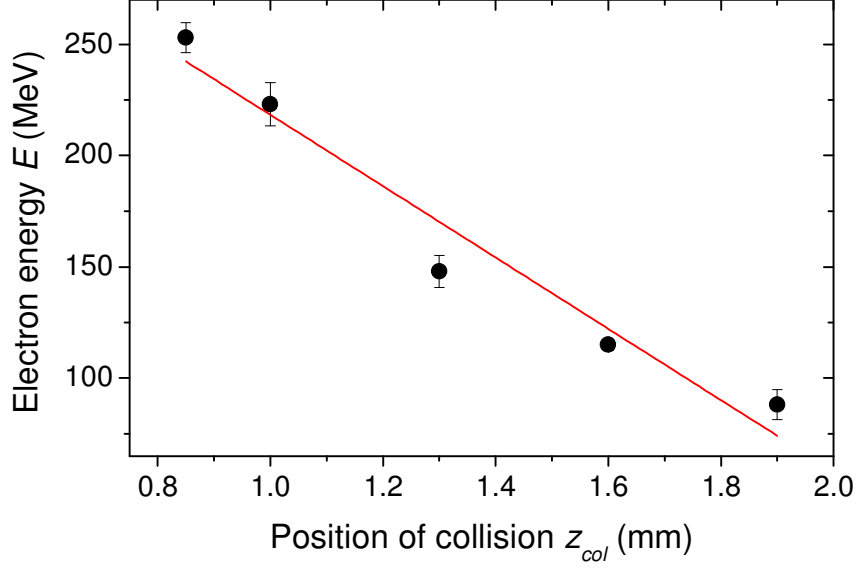
Figure 5.10: Electron beam mean energy as a function of the collision position. The line is a linear fit and the error bar corresponds to the standard error calculated over 1 to 10 shots.

120 MeV and 30 pC, with an energy spread of about 20 %. The divergence of the electron beam is typically around 5 mrad FWHM. For an early collision position, the energy increases up to 260 MeV while the charge decreases down to a few pC (for $z_{col} = 0.85$ mm, as seen in Fig. 5.9). This charge decrease is probably due to the fact that pump pulse self-focusing and self-compression are too weak after such a small propagating length, and thus the wakefield amplitude is weaker during injection (less electrons can be trapped). The remaining acceleration length is however larger, leading to larger electron energy. If the collision happens too late in the jet, the pump pulse is quite depleted and the remaining length is too short to get high energy, thus no electrons can be visible on the spectrometer (which only collects electrons with energies above 50 MeV).

Experimental results in Fig. 5.10 demonstrate that the electron energy E can be tuned from ~ 90 MeV to ~ 250 MeV, by adjusting the collision position z_{col}. The linear fit shows that the relativistic factor γ can be reasonably approximated by a linear function (as shown in section 5.2.2, $\gamma = \gamma_i + \kappa t$). This leads to $E \approx -160 \ z_{col}[\mathrm{mm}] + 481$ MeV, and $\kappa = 160 \times (c/0.511) \approx 10^{14} \ \mathrm{s}^{-1}$.

5.3.3 Betatron profile measurements

In order to study the evolution of the angular momentum of the electron beam, we now focus on X-ray profile measurements. Figure 5.11(a-c) shows single-shot X-ray angular profiles corresponding to electron energies of 120 MeV (a), 160 MeV (b) and 260 MeV (c). The X-ray divergence decreases when E increases, due to a reduction of the electron beam divergence in the acceleration ($\theta_{electrons} \propto \gamma^{-3/4}$). More interestingly, the X-ray profiles also evolve from somewhat rectangular and flat shapes to elliptical shapes.

To quantify this evolution, we define three variables : the flatness f, the curvature c and the ellipticity e. The flatness f of the X-ray profile is given by the ratio of $R_{0.8}$ to $R_{0.5}$, with $R_{0.8}$ and $R_{0.5}$ the mean radii at 80% and 50% of the peak intensity ($f = 1$ for a top-hat beam and $f = 0.57$ for a Gaussian beam). The curvature is defined as $c = R_{0.6}/R_{0.6}^C$ with $R_{0.6}$ the mean radius of the 60% contour line and $R_{60\%}^C$ the mean curvature radius of the 60% contour
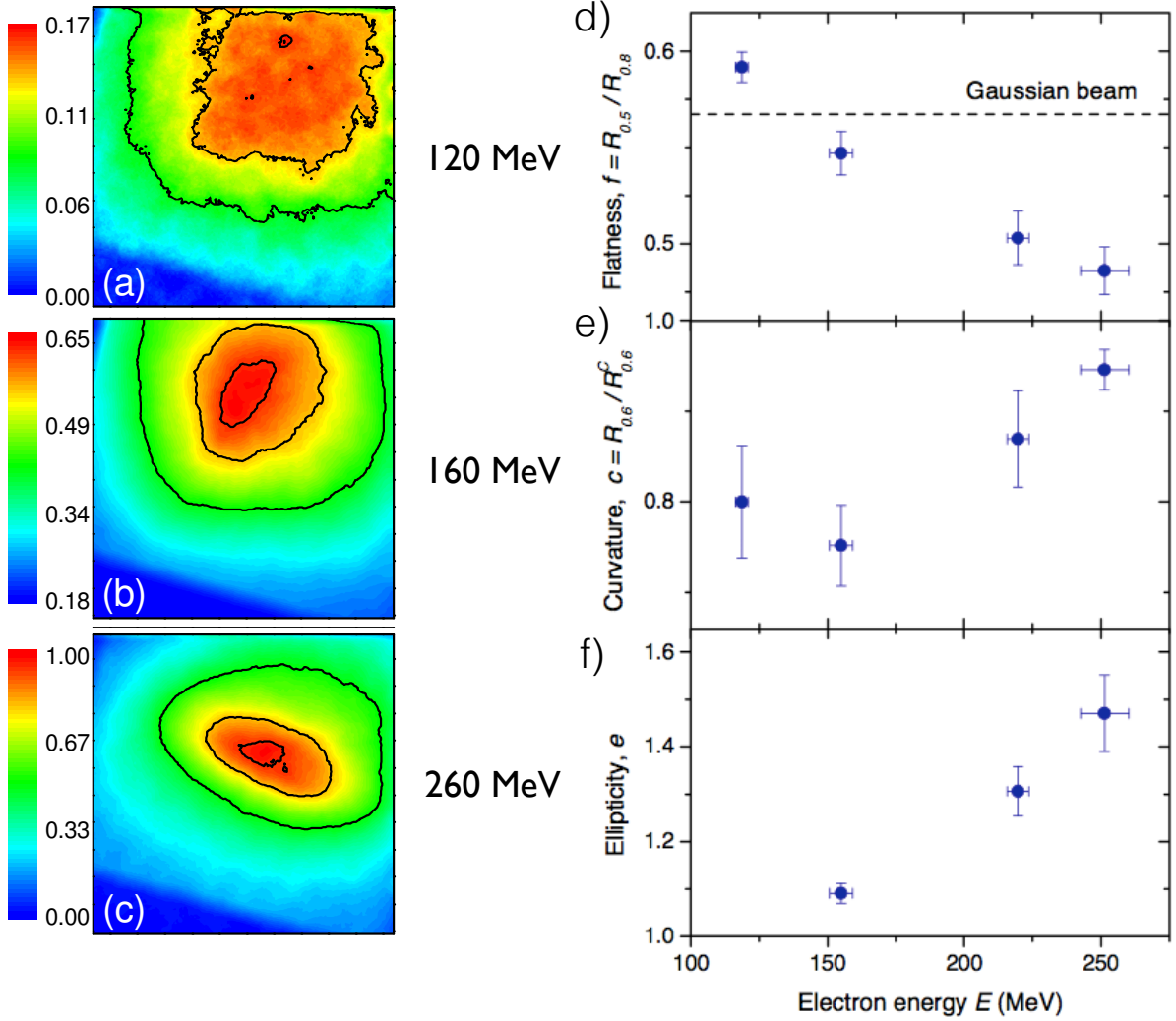
Figure 5.11: (a,b,c) Experimental X-ray angular profiles for different acceleration lengths, corresponding to an electron energy of 120 MeV (a), 160 MeV (b) and 260 MeV (c). A 0.9 mrad mean filter was applied on the experimental images. Contour lines at 50%, 80% and 95% of the peak intensity are superimposed on the angular profiles. (d,e,f) Variation of the flatness (d), the curvature (e) and the ellipticity (f) of the betatron profiles with the electron energy. Each experimental point represents an average over more than 8 shots obtained for the same acceleration length. Error bars indicate the standard error of the mean. For $E = 120$ MeV the ellipticity cannot be computed accurately because X-ray profiles are cut.

line (computed using the algorithm described in [Nguyen and Debled-Rennesson, 2007]). Note that the 60% contour line was chosen as it is always complete for all betatron profiles. It follows that $c = 1$ for a perfect circle, while $c = 0$ for a square. Lastly, the ellipticity is calculated from an ellipse fit of the 50% contour line. It is defined as the ratio of the major to the minor radii of this ellipse. Figure 5.11(d-f) shows that c and e increase with E, while f decreases when E increases. This confirms the trend observed in Fig. 5.11(a-c).

This behavior can be explained by an evolving angular momentum. In the wiggler approximation ($k_p r_0 (\gamma/2)^{1/2} \gg 1$), electrons with $L_z = 0$ radiate an elliptical X-ray beam of divergences $\theta_\parallel = \alpha k_p r_0 / \sqrt{2\gamma}$ along the oscillation direction, and $\theta_\perp = 1/\gamma$ in the direction orthogonal to the oscillations [Corde et al., 2013a]. The measured X-ray profile is an incoherent sum of the contributions of all electrons. For an isotropic electron distribution with $L_z = 0$, all electrons have planar orbits and emit elliptical x-ray beams, the sum results in a circular profile consisting of a central peak with a divergence of $\theta_\perp$ surrounded by a halo with a divergence of $\theta_\parallel$ (as shown in Fig. 5.12(a)). Anisotropic electron distributions with a preferential oscillation direction lead to elliptical profiles with a central peak. These features are consistent with X-ray beams obtained for the longer acceleration length ($E = 260$ MeV, shown in Fig. 5.11(c)).
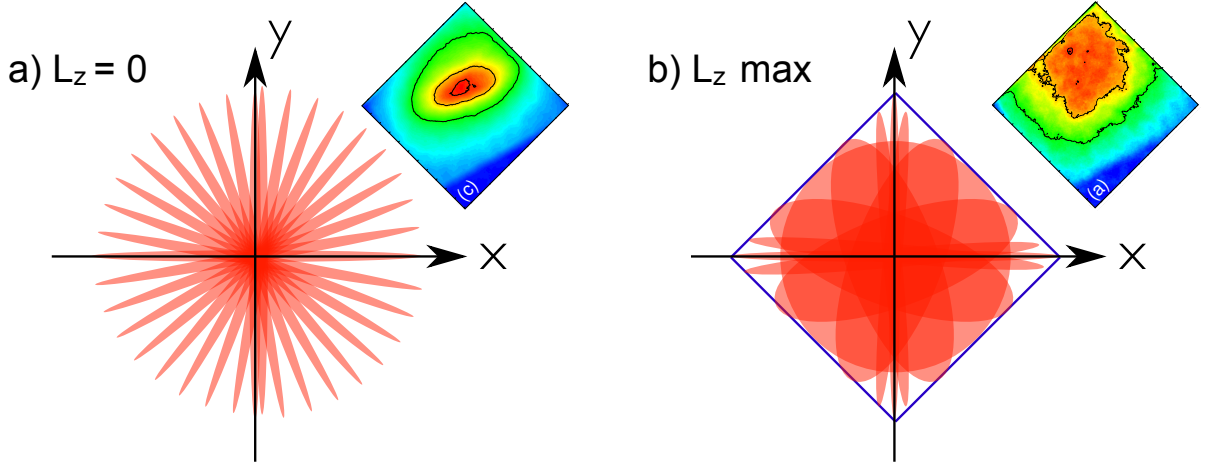
Figure 5.12: Drawing of the resulting X-ray profiles when the angular momentum is zero (a) or maximum (b). Insets show the most similar experimental profiles from Fig. 5.11.

In contrast, electrons with a maximal L_z have circular orbits and emit annular X-ray beams of angular radius $k_p r_0 / \sqrt{2\gamma}$ and thickness $1/\gamma$ [Phuoc et al., 2006]. Summing over electrons of different r_0 results in a flatter beam than for $L_z = 0$ with no central peak. For electrons satisfying eq. (5.18) with $\varepsilon\varphi = k\pi$ (where k is an integer), the orbits are planar with an oscillation amplitude r_0 for electrons initially located on the $\boldsymbol{x}$ and $\boldsymbol{y}$ axes (these electrons do not get any angular momentum), and circular with a radius $r_0/\sqrt{2}$ for electrons such as $x_0 = y_0$ (these electrons gain a maximum angular momentum). More precisely, all trajectories are contained in a square of side length $\sqrt{2}r_0$ with diagonals along the axes of the cavity ellipse, as shown in Fig. 5.12(a). As a result, the X-ray beam obtained by summing over the contribution of electrons of different initial positions and velocities has a square shape and a relatively flat profile, similar to X-ray beams measured for the shorter acceleration length ($E = 120$ MeV, shown in Fig. 5.11(a)). This simple analysis thus suggests that the angular momentum, in our experiment, is maximum for $E \approx 120$ MeV and that it decreases as the electron energy increases further (as shown in Fig. 5.6).
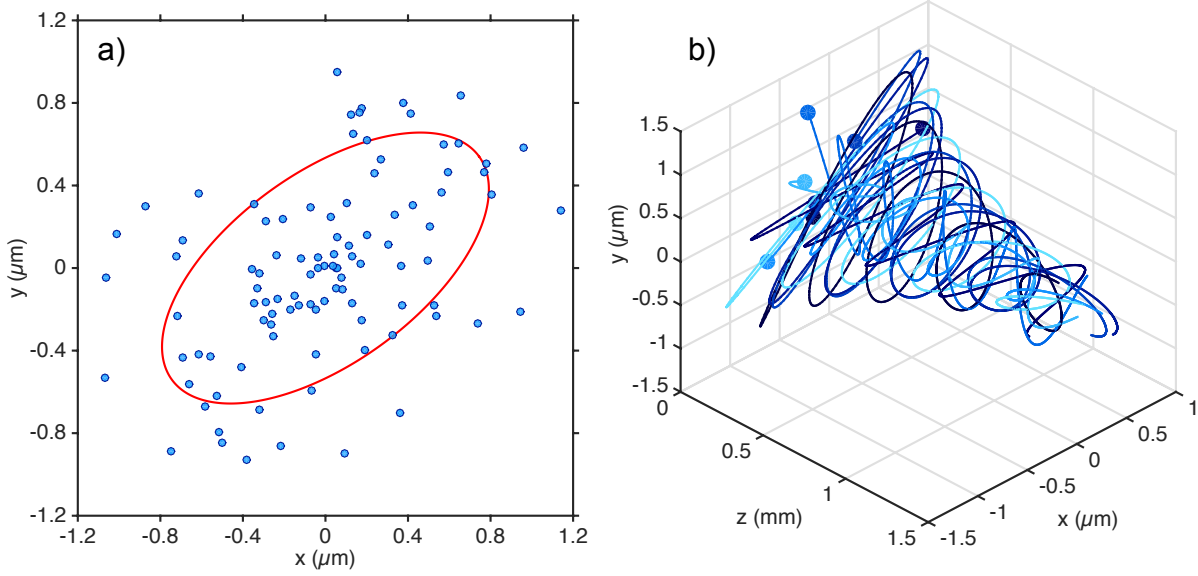
Figure 5.13: (a) Initial transverse distribution of the electron beam for test-particle simulations. (b) Electron orbits for 8 particles along 1.5 mm of acceleration.

Assuming that angular momentum variations are due to the cavity ellipticity and that the electron initial transverse distribution does not depend on the injection position, the results indicate that the phase difference between the oscillations along the x and y axis reaches $\pi/2$ for $E \approx 120$ MeV, that is for an acceleration length of 600 μm. According to eq. (5.18), this implies that the cavity ellipticity is $\varepsilon \approx 0.15\alpha^{-1/2}$. As electrons are further accelerated, the difference of phase keeps increasing, which can explain why the angular momentum decreases in the experiment.

The X-ray beam ellipticity at high energy indicates that the electron distribution is anisotropic (the ellipticity cannot be due to the interaction of the accelerated electrons with the laser, because the ellipse major axis is not parallel to the laser polarization). If electrons were mostly distributed along the x or y axis, they would never develop a significant angular momentum and only elliptical beams would be obtained.

In contrast, the fact that X-ray profiles with a square shape are measured indicates that electrons are preferentially injected with amplitudes $x_0 = y_0$, because only electrons with a maximum L_z can lead to non-elliptical emissions. This implies that the ellipse axes at high electron energy should make a 45° angle with the diagonals of the square profiles observed at low energy (the diagonals should be along the x and y axis).

Accordingly, we experimentally measured, for $E \approx 120$ MeV, a mean angle $\Psi_s = 45(+90)\pm1°$ between the square diagonals and the horizontal axis, and, for $E \approx 260$ MeV a mean angle $\Psi_e = 1(+90) \pm 9°$ between the ellipse axes and the horizontal axis (this indicates that in the experiment the cavity axes are at $\pm45°$ from the horizontal axis). The angle Ψ_s was observed to be very stable shot-to-shot, while Ψ_e drifted from $-13(+90)°$ up to $28(+90)°$. The ellipse axes were also observed to swap in time. The reason is that Ψ_s is determined by the orientation of the elliptical cavity, which should not change significantly shot-to-shot (the focal spot remains roughly the same), while Ψ_e depends on the distribution in the transverse phase space of injected electrons, which is more sensitive to laser propagation and energy fluctuations. Small changes

in the injected distribution can, for instance, originate from ionization induced refraction of the injection pulse [Rae, 1993; Chessa et al., 1999], and from the stochastic nature of the heating process [Sheng et al., 2002].

5.3.4 Simulations
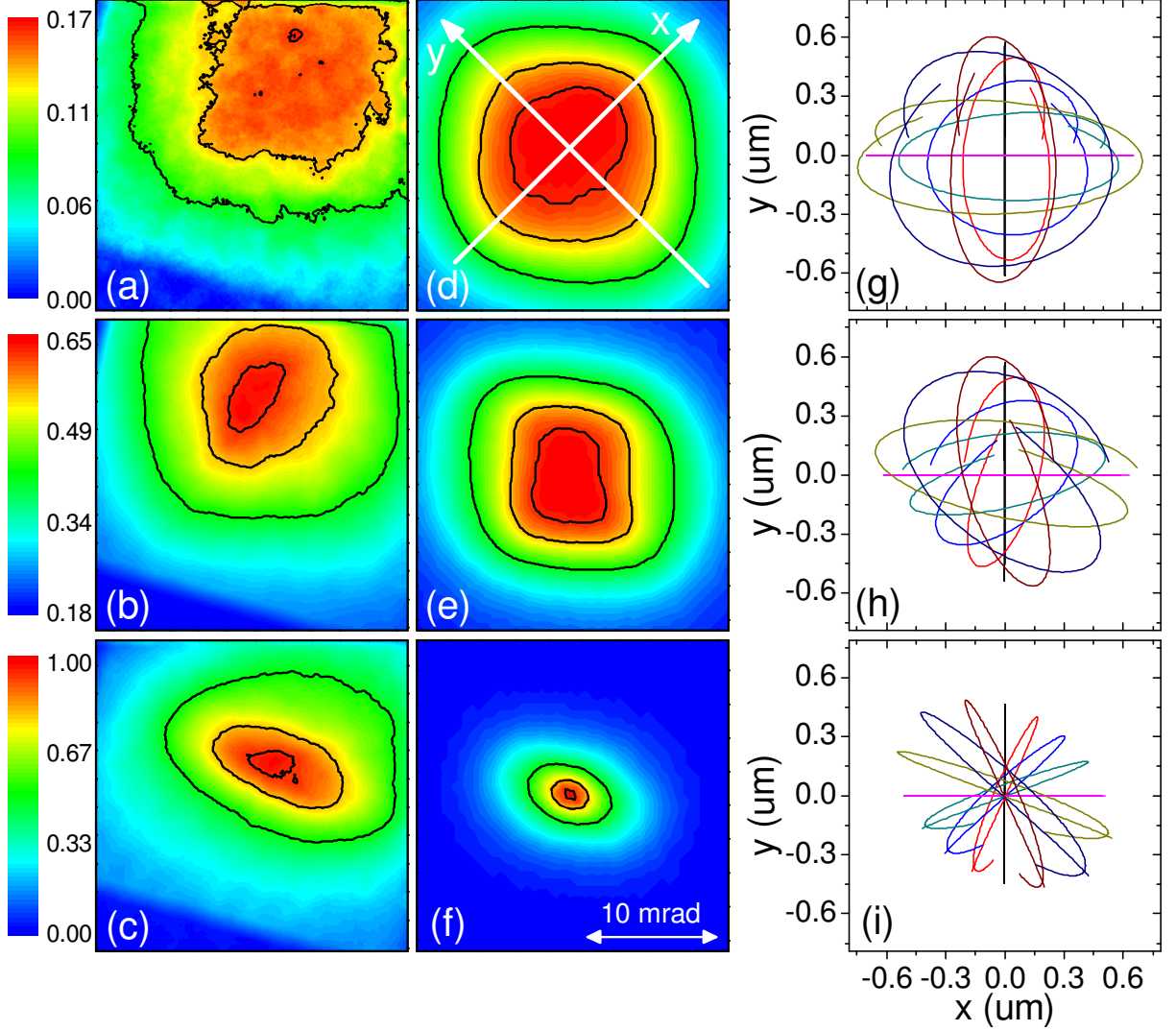
Figure 5.14: Experimental (a,b,c) and simulated (d,e,f) X-ray angular profiles from the experiment (a,b,c) or the simulation (d,e,f) and typical electron trajectories over one betatron period (g,h,i) for three electron energies : 120 MeV (a,d,g), 160 MeV (b,e,h) and 260 MeV (c,f,i).

To confirm this analysis, I performed test-particle simulations, using the experimental energy spread, the longitudinal acceleration force measured in Fig. 5.10, the transverse force from eq. (5.8) and the electron source size $\alpha \times \sigma_x$ calculated from the X-ray spectrum [Corde et al., 2011] (with α the coefficient related to the deviation from a perfectly evacuated bubble : $\alpha = 1$ for an electron-free cavity). I scanned a large range of ε (coefficient related to the ellipticity of the cavity) and of initial electron distributions, and I found that an agreement with experimental data is obtained only for $\varepsilon \approx 0.2$ and $\alpha \approx 0.55$, a matched electron beam (with a phase
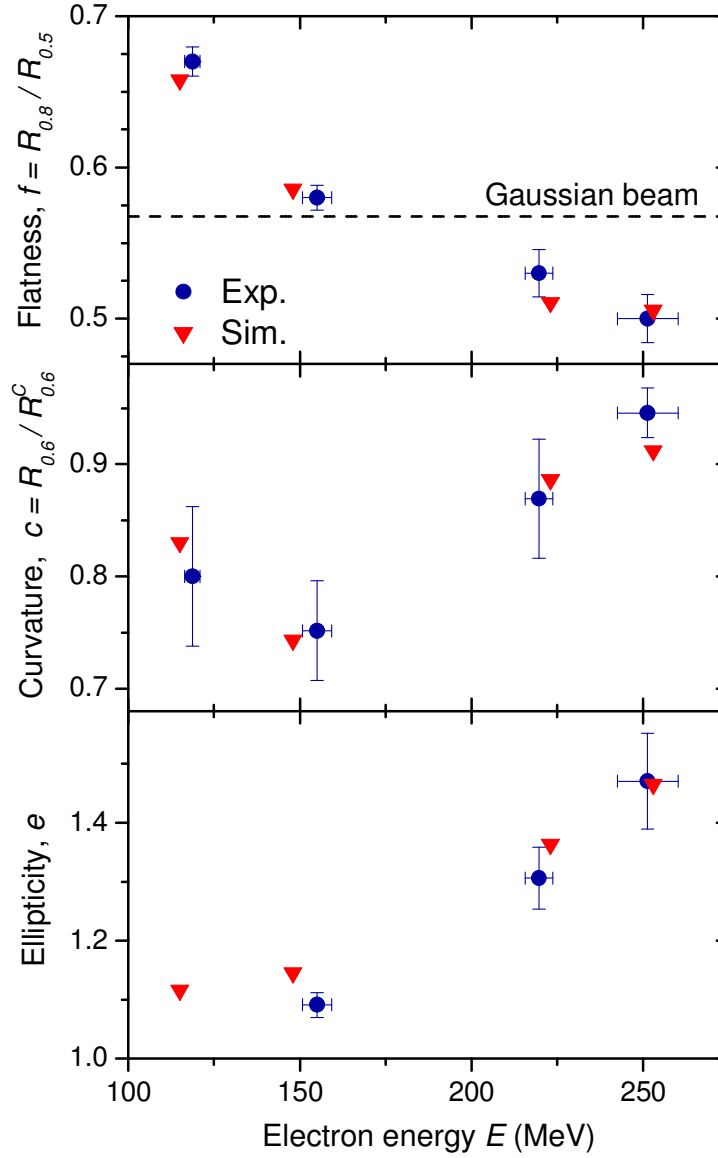
Figure 5.15: Variation of the flatness f, the curvature c and the ellipticity e with the electron energy. The dots corresponds to experimental data (already shown in Fig. 5.11(d,e,f)) and the triangles to simulations. Error bars indicate the standard error of the mean.

φ_0 uniformly distributed between 0 and 2π) and an elliptical initial transverse distribution, oriented at 36° from the x-axis, with an aspect ratio of 0.5 (shown in Fig. 5.13(a)). Typical electron trajectories obtained in this case are plotted in Fig. 5.13(a). As expected, they are linear at the beginning, quickly become helicoidal after 0.5 mm of acceleration and go back to planar after 1.5 mm. The betatron angular profiles are computed using eq. (5.6) for the same electron energies as in the experiment. They are shown in Fig. 5.14(d-f), with the experimental profiles shown in (a-c). Figure 5.14(g-i) shows typical trajectories for 8 electrons for each case (note that only the last betatron period is plotted). They evolve from helicoidal to planar trajectories as the electron energy increases.

The calculated betatron profiles reproduce accurately the experimental divergence as well as

the general shape of the beam and the behavior of f, c and e (as shown in Fig. 5.15), except for the divergence at high electron energy. This discrepancy could be due to the interaction of the electron beam with the laser pulse at the end of the acceleration. Another limitation of the model is the assumption of a steady and perfectly elliptical cavity. In particular, because of different self-focusing dynamics in the two transverse directions, the ellipticity can vary in time. This can modify the extrema of L_z, as well as the electron energy at which these extrema are obtained.

Apart from the difference of divergence, the good overall agreement between the experiment and test-particle simulations indicates that our simple model includes most of the relevant physics. Simulations can therefore be used to estimate the normalized transverse emittance of the bunch in each direction. Indeed, as stated in section 1.3.1 :

$$\varepsilon_x = \sqrt{\langle x^2 \rangle \langle p_x^2 \rangle - \langle x p_x \rangle^2}. \tag{5.19}$$

The same formula can be defined in the y direction. From eqs. (5.13) and (5.15) and neglecting the second term in the bracket of eq. (5.15), it is possible to derive the normalized emittance depending on the simulation parameters :

$$\langle x^2 \rangle = \frac{\sigma_x^2}{2} \sqrt{\frac{\gamma_i}{\gamma}} \tag{5.20}$$

$$\langle p_x^2 \rangle = m_e^2 \omega_p^2 \gamma^2 \frac{\sigma_x^2}{2} \sqrt{\frac{\gamma_i}{\gamma}} \frac{\alpha}{2\gamma} \left(1 + \frac{\varepsilon}{2} \right) \tag{5.21}$$

$$\langle x p_x \rangle^2 = 0 \tag{5.22}$$

with $\sigma_x = \langle x_0^2 \rangle$ the second order momentum of position distribution. We get :

$$\varepsilon_x = \sqrt{\left(1 + \frac{\varepsilon}{2} \right) \sigma_x^4 m_e^2 \omega_p^2 \frac{\alpha \gamma_i}{2}}. \tag{5.23}$$

The initial electron beam is matched, thus the electron have the same norm along the two axes of the phase-space (x, p_x) : $J_x = J_{p_x}$. From section 5.2.2, we can calculate these norms for the initial distribution of electrons :

$$J_x = \frac{m_e \alpha}{4\omega_\beta} \left(1 + \frac{\varepsilon}{2} \right) \omega_p^2 \sigma_x^2 \tag{5.24}$$

$$J_{p_x} = \frac{1}{2m_e \gamma_i \omega_\beta} \sigma_p^2 \tag{5.25}$$

with σ_p the initial distribution of momentum. By calculating $J_x = J_{p_x}$, we get $\sigma_p^2 = m_e^2 \omega_p^2 \frac{\alpha \gamma_i}{2} \left(1 + \frac{\varepsilon}{2} \right) \sigma_x^2$. Thus, the normalized emittance is :

$$\varepsilon_x = \sigma_x \sigma_{p_x} \tag{5.26}$$

$$\varepsilon_y = \sigma_y \sigma_{p_y} \tag{5.27}$$

with the same derivation done for ε_y.

From the simulation parameters ($\varepsilon = 0.22$, $\alpha = 0.55$, $\sigma_x = \sigma_y = 0.46$ μm), we obtain $\varepsilon_x \sim 1.5\pi$ mm.mrad. Note that the quantity measured in Corde et al. [2011] is $\alpha \sigma_x$, thus $\varepsilon_x \propto \alpha^{\frac{3}{2}}$. Since the simulation fits both the measured X-ray spectra and the angular profiles, they provide both α and the emittance. Estimating these two quantities is essential in betatron based emittance measurements because the inferred emittance varies as $\alpha^{3/2}$. Assuming that the cavity is fully evacuated ($\alpha = 1$), as done for instance in Plateau et al. [2012], may thus lead to underestimate the emittance.

5.4 Conclusion

In conclusion, we demonstrated that the angular momentum content of an electron beam, accelerated in an anisotropic cavity, is time varying, and we provided experimental evidence of such variations. Such an asymmetric cavity can be formed because of the elliptic shape of the laser focal spot due to optical aberrations such as astigmatism. These results have important consequences for several emittance measurement techniques. Neglecting the angular momentum can in particular result in unreliable estimates of the emittance in X-ray based measurements, because the spatial properties of X-rays strongly depend on the angular momentum content. Indeed, neglecting the angular momentum may lead to underestimate the emittance (the transverse size of the beam being distributed over two directions when modified by the angular momentum). In addition, the angular momentum growth is a source of fluctuations, which can, for instance, induce large shot-to-shot changes in betatron profiles. To avoid such effects, the laser pulse should be free of aberration in order to produce an axisymmetric cavity. Conversely, it could be beneficial to take advantage of an asymmetric cavity to manipulate the shape of X-ray beams and produce a radiation with a net angular momentum. This would require a precise control of the transverse distribution of injected electrons.

Chapter 6

The laser-plasma lens

LWFA electron beams have typical divergence of a few milliradians with a few femtoseconds duration. Yet, a suitable magnetic lens to transport and collimate such a beam is difficult to realize. In this chapter, we propose to use a laser-plasma lens in which the field gradients are five order of magnitude larger than in conventional magnet optics. This collimating scheme is first studied analytically, allowing to find the best suitable set of parameters for the focusing stage to efficiently collimate the beam. Then, we experimentally demonstrate a reduction of the beam divergence by nearly a factor of three, which should allow for an efficient coupling of the beam with a conventional beam transport line.

Contents

6.1 Physics of the laser-plasma lens

6.1.1 Motivations

A major potential application of LWFA electron bunches is to inject them into a magnetic undulator in which they wiggle and produce high-frequency radiation. Indeed, due to their very large charge density (due to their small duration and normalized transverse emittance ε_n), the brightness of this radiation could be extremely high. For high enough charge density, free-electron laser (FEL) effect can happen, leading to even brighter radiation [Nakajima, 2008]. Furthermore, in the context of multi-stage LWFA [Schroeder et al., 2010], as the beam diverges at the end of each acceleration stage, it must be refocused into the next stage. The feasibility of such applications relies upon the ability to transport and focus the electron beam at the entrance of each acceleration stage.

Particularly, the transverse emittance of the beam ε_n (as defined in section 1.3.1) increases during drift in free space because of the beam energy spread : electrons having different energies rotate with different speeds in the transverse trace-space ((x, θ_x) as defined in section 1.3.1), thus increasing the transverse spread of the beam. Indeed, the beam emittance is not constant due to the correlation increase of the transverse positions of electrons and their longitudinal momentum. While the drift length satisfies $L_d \lesssim \varepsilon_n / (\gamma_0 \sigma_E \sigma_\theta^2)$, the emittance increase remains tolerable [Floettmann, 2003] (with γ_0 the mean Lorentz factor, σ_E the RMS relative energy spread and σ_θ the RMS divergence). For "Salle-Jaune" like electron bunches, this imposes the drift length to be smaller than about $1 \sim 2$ cm (for $\varepsilon_n = \pi$ mm.mrad, a mean energy of 250 MeV, a relative energy spread of 5 % and a divergence of 5 mrad). Consequently, it is essential to reduce the divergence of the electron beam within a few centimeters after the accelerator exit for efficient transport.

A common way to focus electron beams is to use quadrupole magnets. Because of the relatively low field gradients (from 50 to 500 T.m^{-1}), such devices have to be placed several decimeters behind the accelerator exit [Fuchs et al., 2009] (mainly because of the large focal length), thus the electrons propagate freely over this large distance. Moreover, electrons are focused differently in the two transverse directions in quadrupole lenses. A beam transport line based on quadrupole devices will therefore degrade the quality of a LWFA electron beam [Migliorati et al., 2013]. Ideally, the beam must be focused much closer, before its emittance increases too much.

Plasmas sustain enormous field gradients, they are thus ideal candidates to radically reduce the size of the focusing device, avoiding any significant emittance growth. A plasma lens placed a few millimeters behind the accelerator exit could be the alternative [Chen, 1987]. In a plasma lens, the electron beam enters a gas jet and forms its own focusing ion cavity by expelling the gas electrons. This effect was studied extensively for conventional accelerators [Chen et al., 1990; Su et al., 1990; Rosenzweig et al., 1991; Nakanishi et al., 1991; Hairapetian et al., 1994; Govil et al., 1999; Ng et al., 2001; Thompson et al., 2010], but is not applicable to focus LWFA electron beams due to their short duration. Indeed, the head of the bunch creating the wake erodes quickly and the focusing fields are very weak and non-uniform over a finite length at the head [Barov et al., 1998; Thompson et al., 2010]. This is an important drawback since for ultrashort LWFA bunches, this length is similar to the bunch length [Lehe et al., 2014b], which would therefore not be focused properly.

In this chapter, we propose a new focusing scheme, referred to as the laser-plasma lens. It has a very short focal length (because of the strong field gradients in the plasma) without the drawbacks of the regular plasma lens.

6.1.2 Principle of the laser-plasma lens

The main idea behind the laser plasma lens is to take advantage of betatron oscillations of electrons in the transverse focusing fields of a laser wakefield to focus the electron beam. A second, low-density gas jet is placed after a millimeter-scale drift space following the first gas jet, as shown in Fig. 6.1(a). The first jet is used as the acceleration stage, where electrons are self-injected and accelerated. They drift freely and diverge over a millimeter distance along with the laser pulse and enter the second gas jet where the laser drives a wakefield. The focusing fields of this wakefield focus the electron bunch.

Acceleration stage and betatron oscillations: In the acceleration stage, the electron density n_1 and the laser intensity are high enough for the laser pulse to drive a wakefield in the bubble regime and inject electrons. Electrons experience betatron oscillations during the acceleration because of the focusing fields in the ion cavity. As seen in section 1.3.1, electrons in the transverse trace space (x, x') are represented with an ellipse whose area denotes the beam normalized emittance ε_n ($x' = dx/dz$ define in section 1.3.1 is denoted θ_x in this chapter, as it directly measures the divergence of electrons). When oscillating in the bubble, the bunch rotates in the trace space along a given ellipse (blue dotted ellipse in Fig. 6.1(b)). The divergence of the beam is typically a few milliradians at the accelerator end (plain blue ellipse in Fig. 6.1(b)).

Free drift: When exiting the first gas jet, the laser pulse is not self-focused anymore and diverges freely. The high divergence electron bunch is also not focused anymore by the wakefield and expands radially while propagating in the drift space of length L_d. This corresponds to an horizontal extension (in the x direction) of the bunch ellipse in its trace space while keeping constant divergence θ_x and emittance (the ellipse area is conserved), as shown in Fig. 6.1(c). For a given x, the area in the transverse direction becomes thinner and thinner during the free drift.

Focusing stage and collimation: In the second, low-density gas jet, the laser drives a wakefield in the linear regime (the laser pulse intensity quickly decreases as it diffracts in the free space before reaching the second jet). The focusing fields in this regimes are much weaker than those in the bubble regime. The electron bunch undergoes weaker betatron oscillations, and rotates slower and along a larger ellipse in the trace space (as seen in Fig. 6.1(d)). After a fraction of betatron oscillation, the bunch ellipse major axis is aligned with the x axis and the divergence is minimized. If the collimation stage length L_l is chosen so that focusing stops at this point (along with the drift length L_d and the second jet density n_2), the electron beam reaches its minimal divergence. By choosing carefully these three parameters (L_d, L_l, n_2), the final divergence of the beam can be greatly reduced compare to the divergence at the end of the accelerating stage.

6.1.3 Analytical model

In order to determine the best set of parameters (L_d, L_l, n_2) to be used experimentally to get the smallest beam divergence, an analytical model was developed in the frame of Rémi Lehe PhD thesis [Lehe et al., 2014a; Lehe, 2014]. This simplified model does not take into account space-charge effects (considering low charge bunches) and considers the wakefield in the focusing stage to be in the linear regime. The laser pulse is gaussian and the expression of the gas density
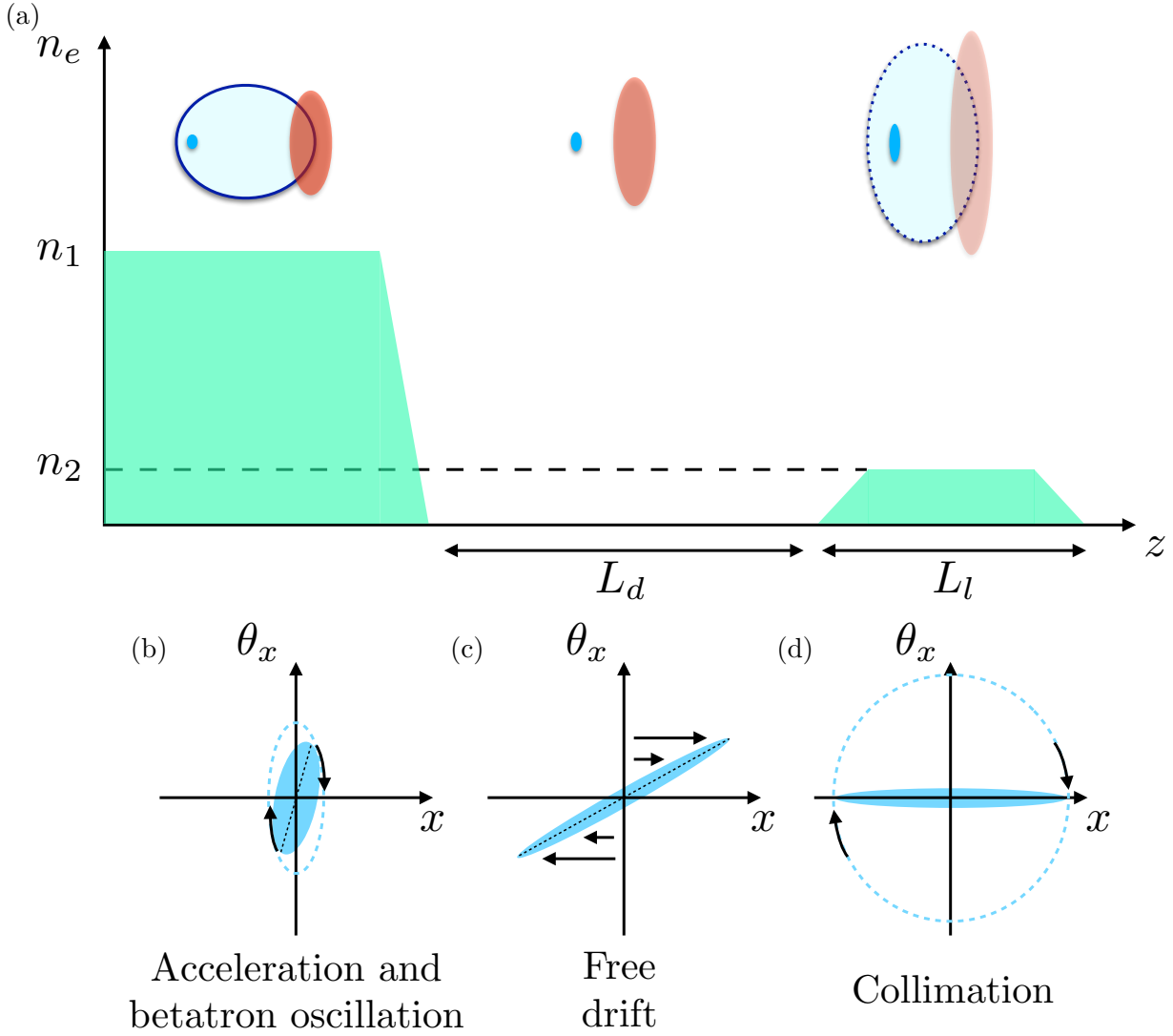
Figure 6.1: Schematic representation of the laser-plasma lens. The density profiles of the two jets are represented in green. The driving laser pulse (red) generates a bubble in the first jet and accelerates an electron bunch (blue). The laser and electron bunch enter the second jet (length L_l, density n_2) after propagating in the drift space (length L_d). Note that the wakefield in the second jet is in the linear regime although it is represented by a bubble for a clearer understanding. The evolution of the electron bunch in its transverse trace space is represented in the lower panel.
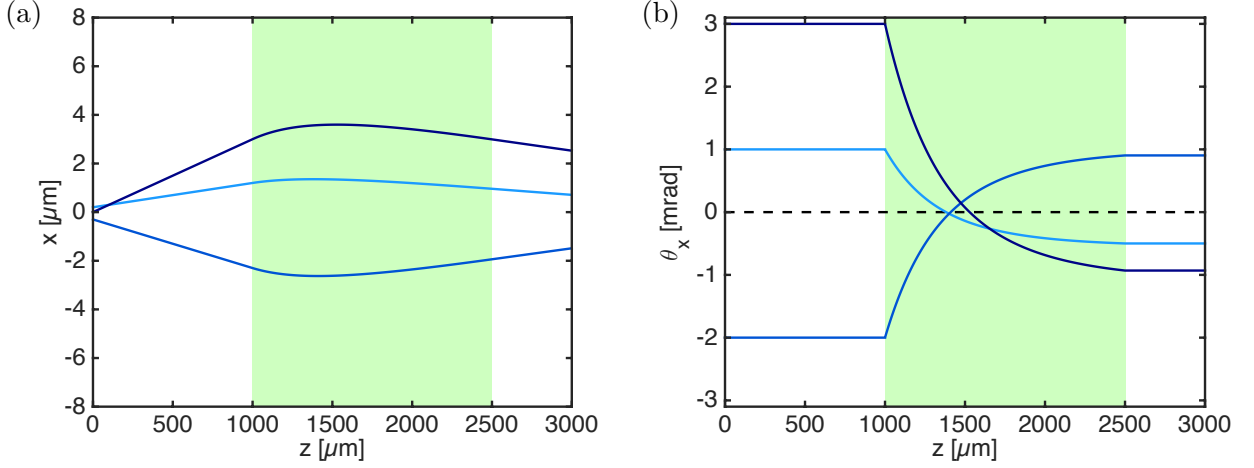
Figure 6.2: Evolution of the transverse position x (a) and propagation angle θ_x (b) of three individual electrons with the same energy (250 MeV) with different initial conditions (x_0, θ_0) : (0.2 μm ,1 mrad) in lighter blue, (-0.3 μm , -2 mrad) in blue and (0 μm , 3 mrad) in darker blue. The green area represents the focusing stage (length $L_l = 1.5$ mm) while the white area before represents the drift space (length $L_d = 1$ mm). The laser amplitude is $a_0 = 4$.

depending on the propagation direction z is assumed to be step-like:

$$n(z) = \begin{cases} n_1 & \text{for } z < 0 \text{ (Acceleration)} \\ 0 & \text{for } 0 < z < L_d \text{ (Drift)} \\ n_2 & \text{for } L_d < z < L_d + L_l \text{ (Focusing)}. \end{cases}$$

After exiting the acceleration stage, an individual electron has an initial transverse position and transverse angle (x_0, θ_0). While propagating in the drift space, the electron does not experience any force and its transverse position x and angle θ_x evolve as :

$$\begin{cases} x(z) = x_0 + \theta_0 z \\ \theta_x(z) = \theta_0 \end{cases} \qquad \text{for } 0 < z < L_d. \tag{6.1}$$

When reaching the second jet (at $z = L_d$), the electron experiences the focusing forces of the wakefield. In the linear regime, the gradient of the focusing fields evolves as z^{-4} [Lehe et al., 2014a]. However, electrons must be in a focusing phase of the wakefield in order to be collimated : $k_p d < \pi$ with k_p the plasma wavenumber and d the distance between the electron and the center of the laser pulse. This imposes an upper limit for the focusing stage density : $n_2 < \pi/4r_e d^2$ (r_e the classical radius of the electron). Assuming that the drift length L_d is much larger than the laser Rayleigh length Z_R and that the electron is not accelerated further in the second jet (the accelerating field is relatively weak in the linear regime), one can derive the expressions of the evolution of x and θ_x in the focusing stage ($L_d < z < L_d + L_l$, see Lehe et al. [2014a] and Lehe [2014] for detailed calculation) :

$$\begin{cases} x(z) = \chi \theta_0 z \cos\left(\frac{k_{foc} Z_R^2}{L_d} - \frac{k_{foc} Z_R^2}{z} + \varphi\right) \\ \theta_x(z) = \chi \theta_0 \left[\cos\left(\frac{k_{foc} Z_R^2}{L_d} - \frac{k_{foc} Z_R^2}{z} + \varphi\right) - \frac{k_{foc} Z_R^2}{z} \sin\left(\frac{k_{foc} Z_R^2}{L_d} - \frac{k_{foc} Z_R^2}{z} + \varphi\right)\right] \end{cases} \tag{6.2}$$

139
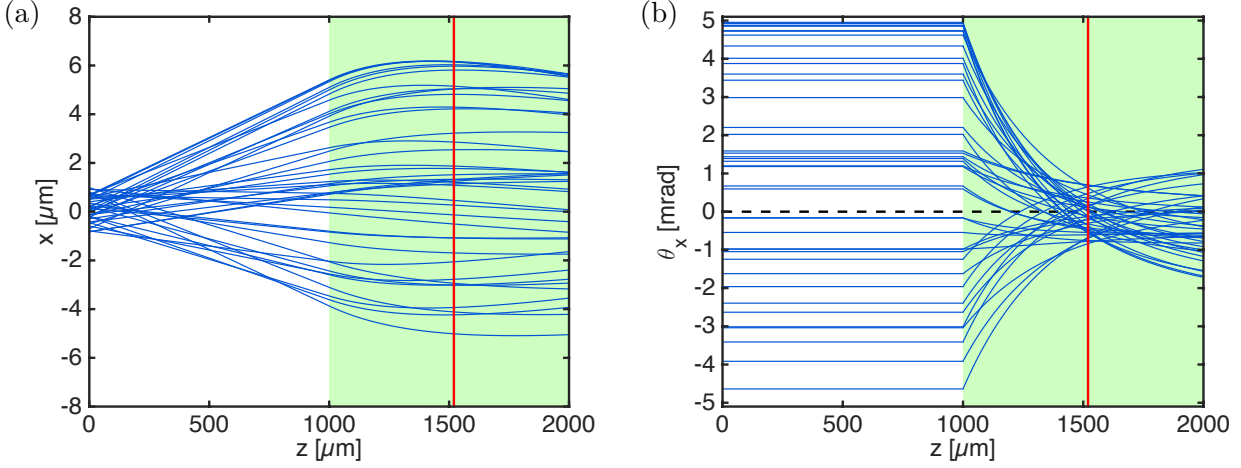
Figure 6.3: Evolution of the transverse position x (a) and propagation angle θ_x (b) for several electrons of the bunch with the same energy (250 MeV) and with random initial conditions (x_0, θ_0). The green area represents the focusing stage (length L_l) while the white area before represents the drift space (length $L_d = 1$ mm). The red line represents the optimal length L_l which minimizes the bunch rms divergence. The other parameters are the same than before.

where $\chi > 0$ and $\varphi \in [0, 2\pi[$ are the modulus and the phase of the complex number

$$\chi e^{i\varphi} \equiv \left(1 + \frac{x_0}{\theta_0 L_d}\right) + i\frac{x_0}{k_{foc} Z_R^2 \theta_0} \tag{6.3}$$

and k_{foc} is defined as:

$$k_{foc}^2 = \sqrt{\frac{\pi}{4 \ln(2)}} (ck_p \tau) \exp\left(-\frac{(ck_p \tau)^2}{16 \ln(2)}\right) \frac{a_0(0)^2}{\gamma \, w(0)^2} \sin(k_p d), \tag{6.4}$$

where $w(0)$ and $a_0(0)$ are the waist and peak amplitude of the laser pulse at the exit of the first jet, τ the FWHM duration and γ the electron Lorentz factor. Considering typical "Salle Jaune" values for electron and laser parameters ($w(0) = 7$ μm, $a_0(0) = 4$, $\tau = 28$ fs, $\gamma = 128$ and $d = 10$ μm) and realistic values for the laser-plasma lens ($L_d = 1$ mm, $L_l = 1.5$ mm and $n_2 = 1.5 \times 10^{18}$ cm^{-3}), the evolution of x and θ_x for different initial conditions (x_0, θ_0) are represented in Fig. 6.2. The absolute value of the propagation angle decreases in the focusing stage as the electron propagates in the second jet. Indeed, the laser keeps diverging in the second jet (the density is too low for self-focusing to happen) thus the focusing forces become weaker. For a given set of initial conditions (x_0, θ_0), the divergence eventually becomes zero : the second stage should stop at this point for ideal collimation ($\theta_x(L_d + L_l) = 0$). This happens when the length L_l satisfies :

$$\frac{k_{foc} Z_R^2}{L_d + L_l} \tan\left(\frac{k_{foc} Z_R^2}{L_d} - \frac{k_{foc} Z_R^2}{L_d + L_l} + \varphi\right) = 1. \tag{6.5}$$

Nevertheless, this condition cannot be fulfilled for all electrons of the bunch simultaneously (as seen in Fig. 6.2(b), electrons with different initial conditions do not have zero divergence at the same point). Indeed, φ depends on (x_0, θ_0) and k_{foc} depends on γ. Physically, this can be understood because the normalized emittance of the bunch is non-zero, forbidding the bunch to
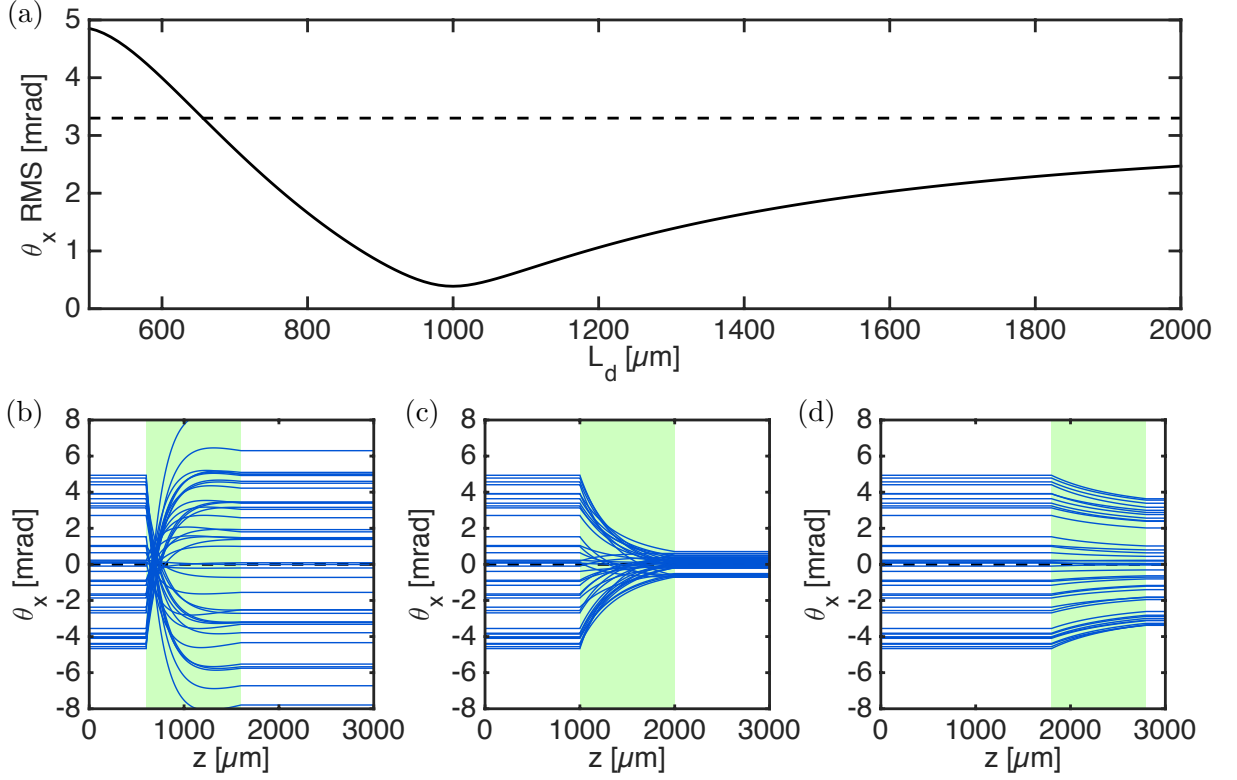
Figure 6.4: (a) Evolution of the final RMS divergence of the bunch as a function of the drift length L_d, with all other parameters fixed ($a_0 = 4$, $d = 10$ μm, $w(0) = 7$ μm, $\gamma = 128$). The dashed line represents the initial RMS divergence of the bunch (3.3 mrad). The evolution of the divergence θ_x of some electrons of the bunch are represented as a function of z for three different values of the drift length : $L_d = 600$ μm (b), $L_d = 1000$ μm (c) and $L_d = 1800$ μm (d).

have a zero divergence. Considering that $\varphi \ll 1$ for LWFA electrons, a good choice for the lens parameters is that they satisfy the condition :

$$\frac{k_{foc}Z_R^2}{L_d + L_l} \tan\left(\frac{k_{foc}Z_R^2}{L_d} - \frac{k_{foc}Z_R^2}{L_d + L_l}\right) = 1. \tag{6.6}$$

The focusing stage density n_2 (controlling the value of k_{foc}) and length L_l must be tuned in relation with the drift length L_d for optimal collimation. The evolution of x and θ_x are represented for a given n_2 and L_d in Fig. 6.3 for several electrons of the bunch with random initial conditions. The condition presented in eq. (6.6) is used to find the optimal L_l to have a minimum final bunch divergence; the result is plotted as a red line in Fig. 6.3. Even if this condition is satisfied, the bunch still has a non-zero RMS divergence due to its finite normalized emittance ε_n. Assuming that ε_n is conserved during the focusing process, this imposes a lower bound on the final RMS divergence of the bunch:

$$\sigma_\theta > \sigma_{\theta,min} = \frac{\varepsilon_n}{\gamma L_d \sigma_{\theta,0}}. \tag{6.7}$$

The drift length L_d is thus a major parameter to improve the beam collimation. Increasing L_d allows for reducing the achievable divergence; L_d should not be too long however, since the laser
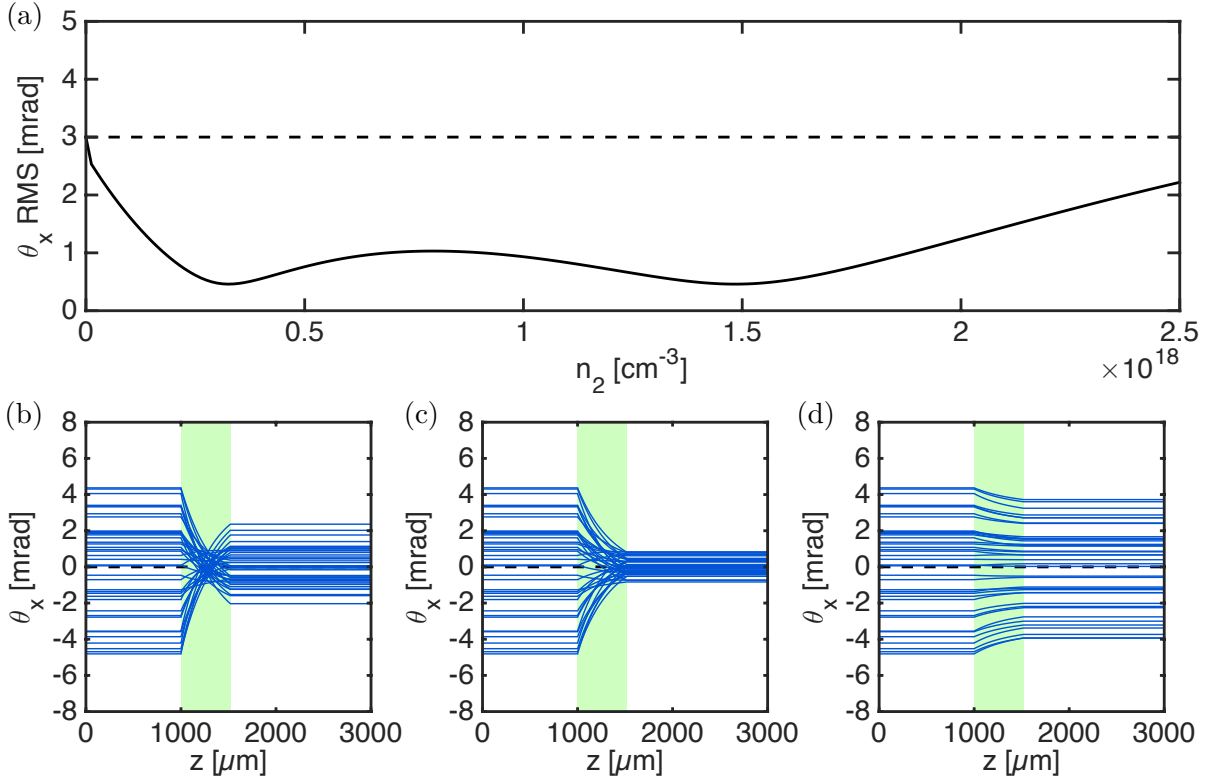
Figure 6.5: (a) Evolution of the final RMS divergence of the bunch as a function of the electron density in the focusing stage n_2, with all other parameters fixed. The dashed line represents the initial RMS divergence of the bunch (3 mrad). The evolution of the divergence θ_x of some electrons of the bunch are represented as a function of z for three different values of the density : $n_2 = 0.75 \times 10^{18}$ cm^{-3} (b), $n_2 = 1.5 \times 10^{18}$ cm^{-3} (c) and $n_2 = 2.5 \times 10^{18}$ cm^{-3} (d).

intensity (and thus the focusing fields strength) quickly decreases as it diffracts in the free space. As a result, there is always a trade-off between low minimal divergence and efficient wakefield generation in the focusing stage.

It is difficult experimentally to know precisely some of the important quantities as the laser waist $w(0)$ and the intensity at the entrance of the lens $a_0(0)$, as well as the distance between the laser and the electron bunch d. It is thus mandatory to scan one of the plasma lens parameters (L_d, L_l, n_2) while keeping the others constant in order to reach optimal collimation. The length L_l is difficult to vary since it is determined by the diameter of the nozzle producing the second gas jet. The drift length L_d and density n_2 are far more easy to change. It is thus interesting to predict analytically the evolution of the bunch divergence by changing these two parameters.

Drift length scan : L_l is chosen to be 1 mm, and the density $n_2 = 1.75 \times 10^{18}$ cm^{-3} so that electrons are in a focusing phase of the wakefield. The drift length is varied between 500 μm et 2000 μm. The final RMS divergence σ_θ depending on L_d is plotted in Fig. 6.4(a), with the evolution of θ_x for several electrons of the bunch for three values of L_d shown in Fig. 6.4(b-d). If L_d is too large ($L_d = 1800$ μm, Fig. 6.4(d)), the laser diffracts too much and is not intense enough when reaching the second jet to efficiently drive a wakefield : the focusing forces are weak and the bunch cannot be focused enough. For a low value of L_d ($L_d = 600$ μm, Fig. 6.4(b)), the

bunch is overfocused because the wakefield is too strong (due to a large laser intensity). There is an optimal value for L_d (close to $L_d = 1000$ μm, Fig. 6.4(c)) for which σ_θ is minimal.

Second jet density scan : L_d is chosen to be 1 mm and L_l is 520 μm. The final RMS divergence as a function of the second jet density n_2 is plotted in Fig. 6.5(a) while n_2 is kept low enough so that electrons are in a focusing phase of the wakefield ($n_2 < \pi/4r_e d^2$ so that k_{foc} is real). Indeed, for high values of n_2, the plasma wavelength is very short and the electron bunch can find itself in the defocusing part of the linear wakefield. For densities higher than this limit, k_{foc} has an imaginary part and the lens is defocusing, which would increase the final RMS divergence compare to the initial one. This case is not considered here, and should be avoided experimentally by keeping n_2 sufficiently low. The divergence is minimum for two values of n_2, as the condition of eq. (6.6) is not a bijective function of n_2. For a density between these two minimum values, the electron bunch is overfocused : electrons with a positive (respectively negative) initial θ_x have a negative (respectively positive) θ_x at the end of the second jet and the final RMS divergence is quite high (for $n_2 = 0.75 \times 10^{18}$ cm^{-3}, Fig. 6.5(b)). For the second optimal value of n_2, the divergence is optimal. For $n_2 = 1.5 \times 10^{18}$ cm^{-3}, electrons have their propagation angle reduced at the utmost while keeping the same sign (as seen in Fig. 6.5(c)). For n_2 larger than 1.5×10^{18} cm^{-3} , the bunch is not focused enough and σ_θ is still high (around 2.1 mrad for $n_2 = 2.5 \times 10^{18}$ cm^{-3}, Fig. 6.5(d)).

Thanks to this simple model, one can predict the range of values for (L_d, L_l, n_2) that need to be scanned in an experiment to obtain good divergence reduction. Furthermore, the evolution of the divergence with L_d and n_2 is quite smooth, so that these parameters have not to be tuned with an extremely high precision to reach the optimum divergence value. The model predicts a divergence reduction up to a factor 3 - 4 with typical parameters for the plasma-lens. Several PIC simulations were run in order to confirm the model validity, showing good agreement with the analytical estimations [Lehe et al., 2014a; Lehe, 2014].

6.2 Experimental demonstration of electrons focusing with a laser-plasma lens

6.2.1 Experimental setup

The laser-plasma lens was experimentally demonstrated with the "Salle Jaune" laser system at LOA. The interaction beam P_1 delivers a linearly polarized, 28 fs FWHM laser pulse containing 1.8 J. It is focused at the entrance of a first gas jet using a f/15 off-axis parabola (focal length of 1000 mm). The FWHM focal spot size is 12 ± 0.6 μm, containing 50 ± 2 % of the total energy. An image of the focal spot and its transverse profile can be seen in Fig. 6.7(a). The peak laser intensity and the corresponding normalized vector potential a_0 are $1.8 \pm 0.6 \times 10^{19}$ W.cm^{-2} and 3.0 ± 0.05, respectively. The Rayleigh length in vacuum is ~ 400 μm. It is likely significantly shorter at the accelerator exit because of self-focusing.

The experimental setup is pictured in Fig. 6.6(a). Helium gas jets were used for both the acceleration and the focusing stages. The two gas jets were produced by supersonic nozzles. The first nozzle has an exit diameter of 3 mm and a Mach number of 3, and the second has a diameter of 0.8 mm and a Mach number of 1.6. The laser was fired at 1.6 mm above the nozzle exits. The electron density profiles of both gas jets were characterized by interferometry (as shown in Fig. 6.7(b)). The density profile in the acceleration stage had a plateau of 2.4 ± 0.1
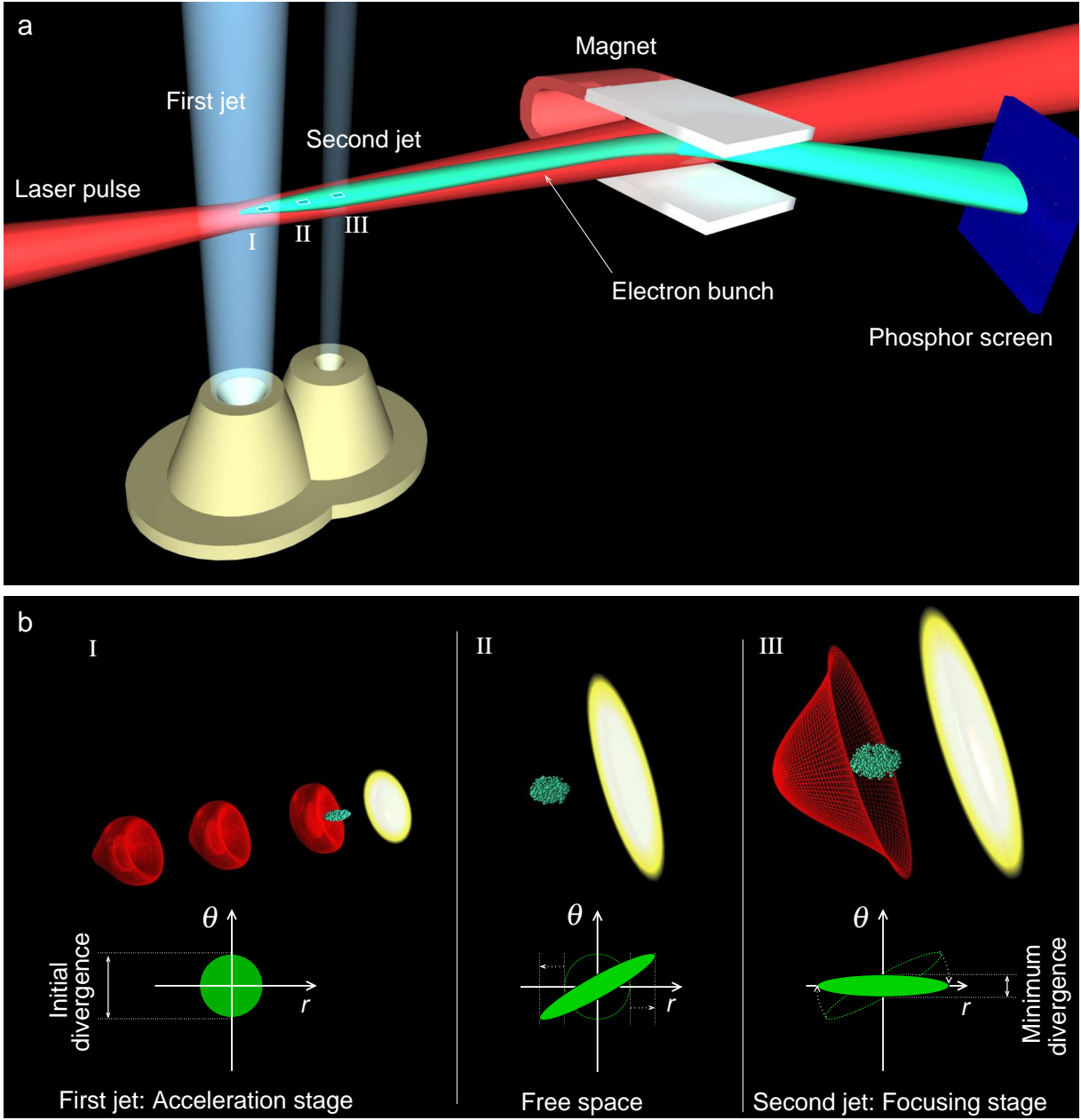
Figure 6.6: (a) Experimental setup of the laser-plasma lens. (b) Trace spaces at the end of the acceleration (I), drift (II) and focusing (III) stages. The laser pulse (in yellow) generates a wakefield (in red) in which electrons (in green) are accelerated (I) and focused (III) after propagating in free space (II).

mm surrounded by 600 ± 100 μm gradients. The peak electron density was $n_1 = 9.2 \pm 0.5 \times 10^{18}$ cm^{-3}. In the second gas jet, the density profile was triangular with 1 ± 0.1 mm gradients. The measured density profile can be seen in Fig. 6.7(c). The distance between the two gas jets L_d was measured at half-maximum. Note that the nozzles have tilted (and not horizontal so that they can be set close enough without their mount interfering with each other).

The electron divergence was measured, in the vertical direction, from electron spectra mea-
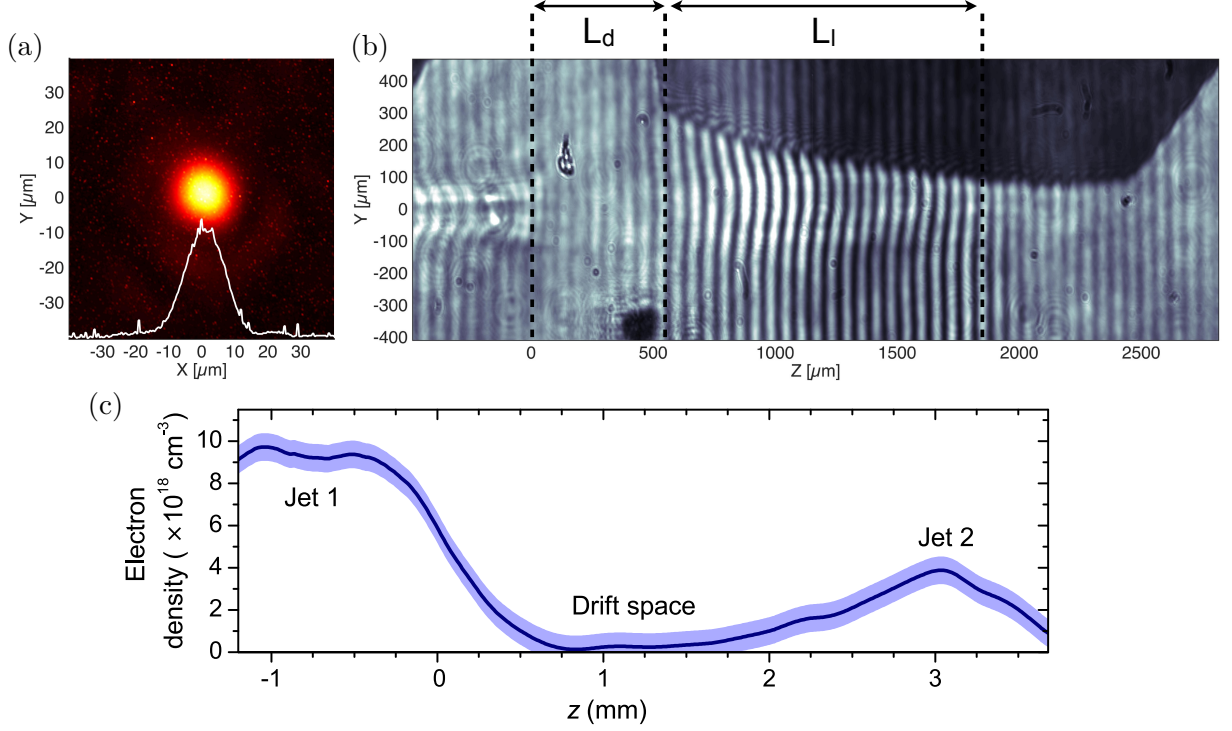
Figure 6.7: (a) Experimental laser focal spot obtained with a 1 m focal length off-axis parabola. (b) Interferogram image of the propagation of the laser in the two gas jets. $Z = 0$ mm corresponds to the middle of the downward gradient of the first gas jet. The laser forms a plasma of length L_l in the second gas jet. The distance between the two gas jets (drift length L_d) is measured at half-maximum. (c) Measured density profile from interferometry and Abel inversion for $L_d \sim 2.3$ mm (measured at half maximum). In the experiment the density of the first jet was constant, while the density of the second jet was tuned. The filled area indicates the uncertainty on the measurement.

sured with the spectrometer presented in section 1.4.3. The energy resolution varies between 1% (for 140 MeV electrons with a beam divergence of 1.5 mrad) and 10% (for 300 MeV electrons with a beam divergence of 4 mrad). The angular resolution is ~ 0.3 mrad. Two-dimensional footprints of the electron beam showed that the divergence is very similar in the horizontal and vertical directions. These footprints cannot be used to estimate the divergence reduction because of chromatic effects. The principle of the laser-plasma lens explained in the previous section is illustrated by the trace-space traces in Fig. 6.6(b).

6.2.2 Experimental results

Firstly, electron beam parameters are optimized with only the first gas jet triggered (the second jet is turned off). Due to the low density in the first gas jet ($n_1 = 9.2 \pm 0.5 \times 10^{18}$ cm^{-3}), electrons are likely to be injected in the longitudinal self-injection regime [Corde et al., 2013b]. Figure 6.8(a) shows ten consecutive experimental angular resolved spectra obtained in this regime. The mean integrated electron spectrum for these ten shots is shown in Fig. 6.8(b), with the colored area representing the standard deviation. This spectrum shows a very good stability. Longitudinal self-injection regime was chosen here because of the very good stability
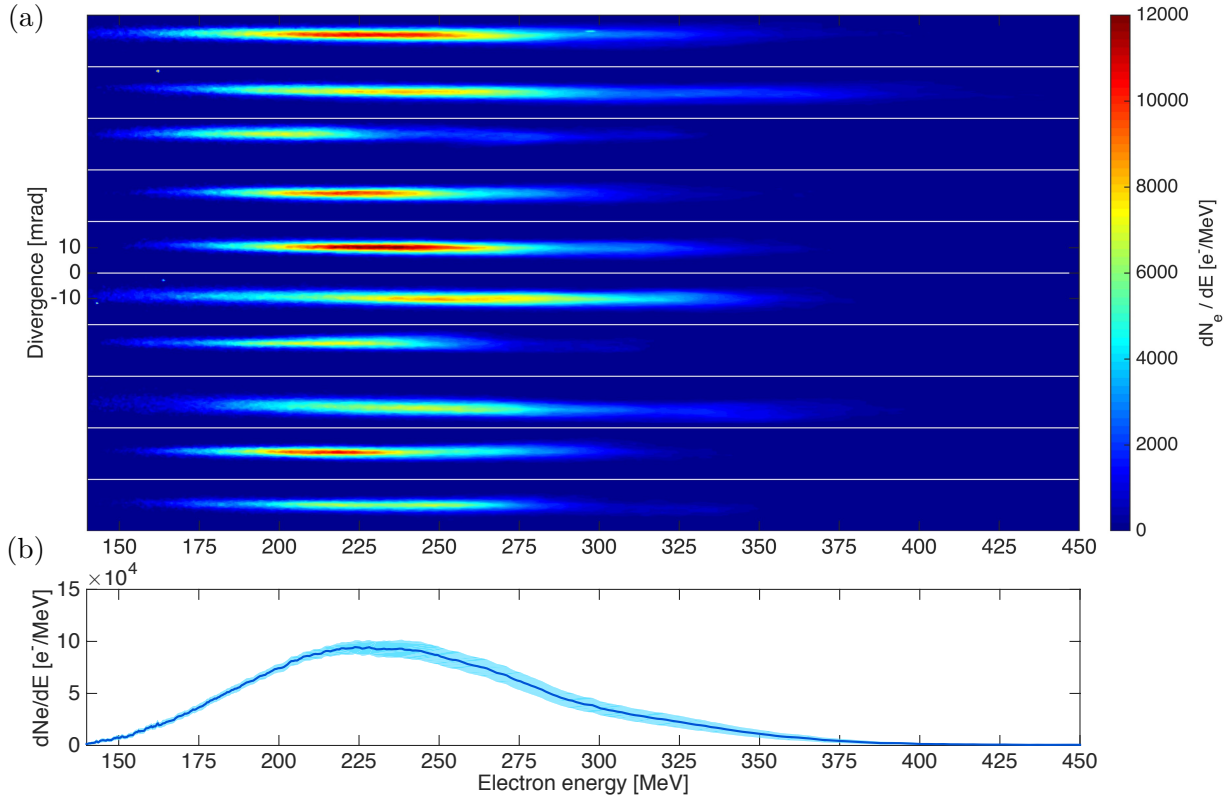
Figure 6.8: (a) Experimental angular resolved spectra of longitudinal injected electrons for ten consecutive shots. (b) Mean electron spectrum over ten shots, with the width of the curve corresponding to the RMS of the signal. The parameters are $a_0 = 3.0$ and $n_1 = 9.2 \pm 0.5 \times 10^{18}$ cm^{-3}.

and quite large energy spread. Indeed, in order to potentially observe beam focusing with the laser-plasma lens, it is mandatory to have stable beams (especially a stable divergence) and large energy spread (to be sure electrons can be collimated with the laser-plasma lens over a wide energy range). The standard error of the mean is calculated over ten shots for each beam parameters (with the FWHM divergence calculated at 270 MeV):

$$E_{peak} = 234 \pm 5 \text{ MeV}$$
$$\Delta E = 92 \pm 10 \text{ MeV}$$
$$\Delta E / E = 39 \pm 4\%$$
$$Q_{peak} = 5.9 \pm 0.6 \text{ pC}$$
$$\sigma_{\theta,270MeV} = 4.1 \pm 0.6 \text{ mrad}$$

The second gas jet (focusing stage) is now turned on, with a drift length $L_d = 1.8$ mm and a electron density $n_2 = 3.9 \times 10^{18}$ cm^{-3}. The resulting angular resolved spectrum is shown in Fig. 6.9(b), while the spectrum without the laser-plasma lens can be seen in (a). The beam
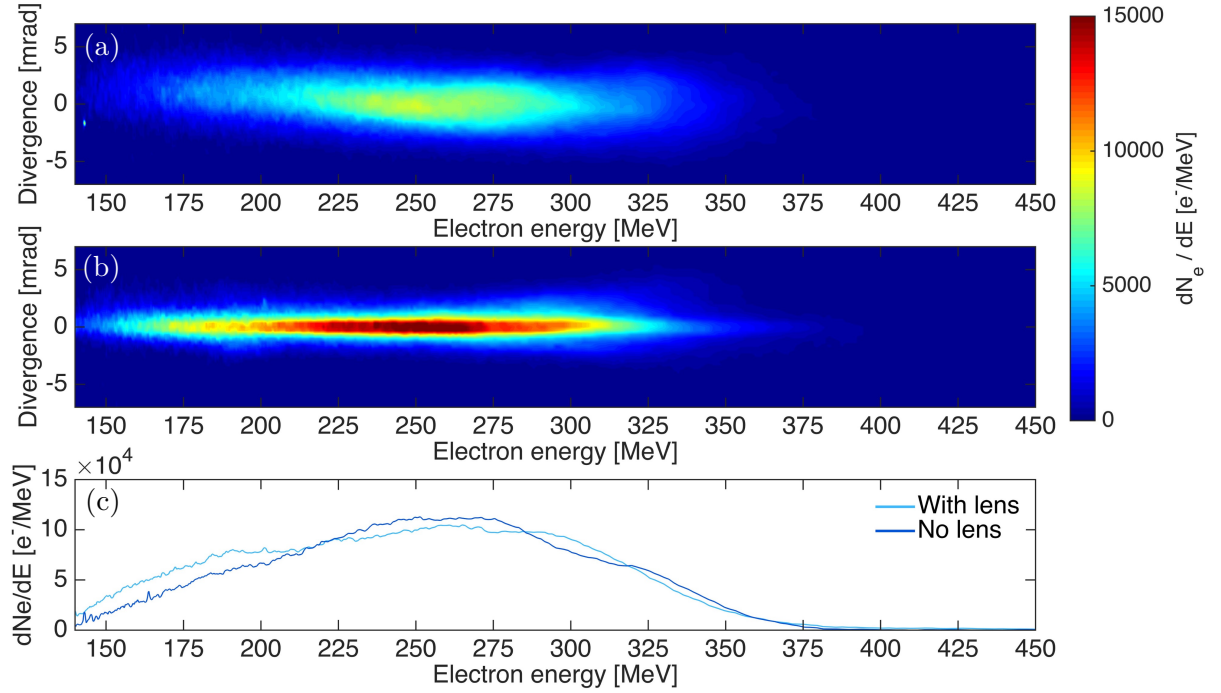
Figure 6.9: (a) Typical angularly resolved spectrum without laser-plasma lens. (b) Typical spectrum obtained for $L_d = 1.8$ mm and $n_2 = 3.9 \times 10^{18}$ cm^{-3}. The color scale indicates the number of electrons per MeV and mrad. (c) Corresponding integrated electron spectra with and without the focusing stage.

parameters at the output of the focusing stage are :

$$E_{peak} = 232 \pm 6 \text{ MeV}$$
$$\Delta E = 92 \pm 10 \text{ MeV}$$
$$\Delta E/E = 40 \pm 4\%$$
$$Q_{peak} = 6.6 \pm 0.6 \text{ pC}$$
$$\sigma_{\theta,270MeV} = 1.6 \pm 0.2 \text{ mrad}$$

The beam divergence is strongly decreased by the laser-plasma lens, down to 1.6 mrad (divergence reduction by a factor of 2.6), while all the other parameters hardly vary. As seen in Fig. 6.9(c), the integrated electron spectrum does not vary much with the lens. That is an important advantage of the laser-plasma lens : it modifies the beam divergence without having a significant effect on the energy distribution of electrons or the charge. The divergence reduction factor is almost 3, close to the one predicted by the model presented in the previous section.

The divergence reduction factor is not the same for different electron energies (as seen in Fig. 6.10). Without the second jet, the divergence increases with the electron energy. When the lens in on, the divergence FWHM of the beam does not vary much with the energy, thus implying that the divergence reduction factor is larger for higher energies. This effect is explained in more details in a following subsection.
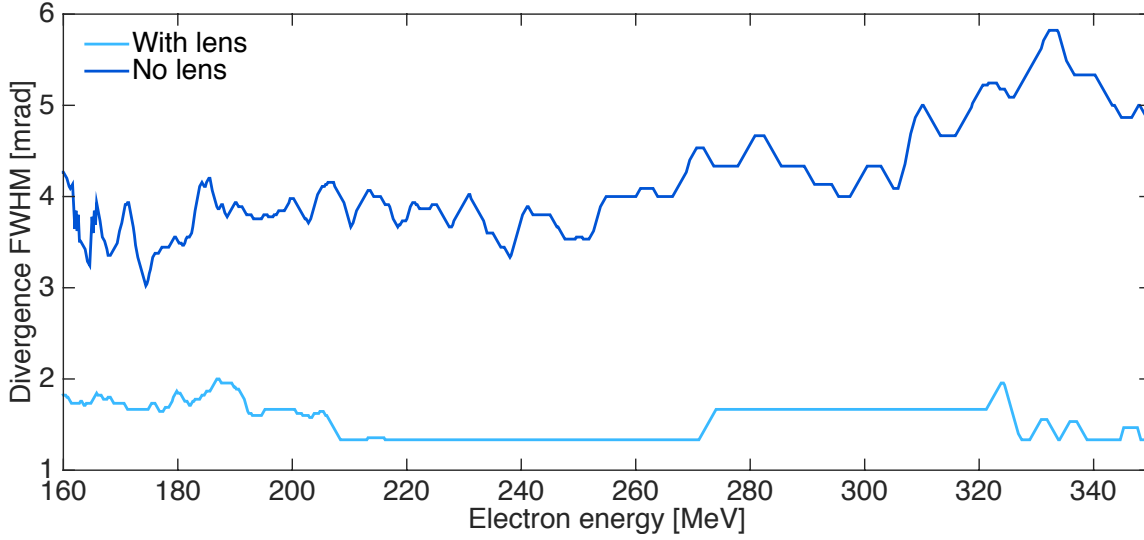
Figure 6.10: FWHM divergence of the beam as a function of electron energy with and without the focusing stage.

6.2.3 Influence of the drift length

As shown in section 6.1.3, the final divergence of the beam depends on the distance L_d between the end of the accelerator and the lens. This distance is varied experimentally by moving the second jet away or closer from the first one. The divergence decreases as L_d increases for $L_d < 1.8$ mm and increases with L_d for $L_d > 1.8$ mm, as shown in Fig. 6.11. This evolution of the divergence with the drift length is governed by two effects. Firstly, the minimum achievable divergence described in eq. (6.7) depends on L_d. As previously explained, if L_d increases, $\sigma_{\theta,min}$ decreases, thus decreasing the minimum divergence. However, by doing so, the laser intensity decreases as well and the focusing fields are weaker for longer L_d.

Indeed, the Rayleigh length Z_R at the accelerator exit is lower than 400 μm. After $L_d = 1.8$ mm of propagation (corresponding to the local minimum of the beam divergence), the laser beam diameter and intensity are thus $\Phi > 54$ μm FWHM and $I < 8.3 \times 10^{17}$ W.cm^{-2}. The wakefield in the lens is in the linear regime and thus, the strength of the focusing fields strongly depends on the laser beam size and intensity. As explained in section 6.1.3, these fields can be too strong for short L_d, leading to excessive focusing, and too low for long L_d, leading to insufficient focusing (as shown in Fig 6.4). In Fig. 6.11, the transverse force seems to vanish for $L_d \geq 4 \sim 5$ mm, while the lowest divergence is obtained for $L_d = 1.8$ mm. The experimental dependence with the drift length is in good accordance with the model described in section 6.1.3, as well for the divergence reduction factor as for the curve shape. The only discrepancy concerns the value of L_d for which the minimum divergence is reached. This may come from the difference of other parameters in the model (d the distance between the laser pulse and the electron bunch or a_0 the normalized laser amplitude for instance), from the difference between the perfect density plateau considered in the model and the experimental density profiles, or with the measurement method of the drift length. In the model, L_d is considered from the very end of the accelerator to the beginning of the upward gradient of the lens. In the experiment however, L_d is measured from the middle of the accelerator downward density gradient to the middle of the lens upward density gradient (as any other measure would be far less accurate).
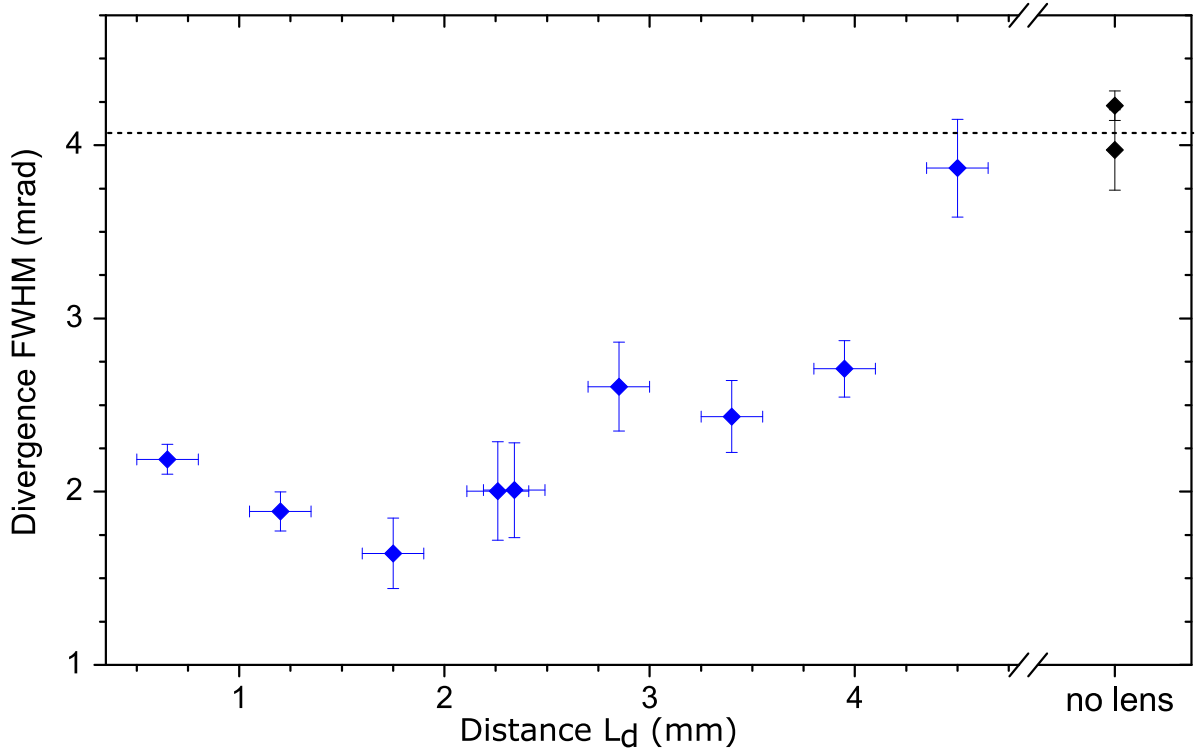
Figure 6.11: FWHM divergence of the beam, at 270 MeV, as a function of L_d (blue diamonds). The divergence measured without the laser- plasma lens is indicated by the black diamonds on the right and the dashed line. The peak electron density in the focusing stage is $n_2 = 3.9 \times 10^{18}$ cm^{-3}. Data points were averaged over 10 shots; the vertical error bars correspond to the standard error of the mean and the horizontal bars correspond to the precision on the measurement of L_d. Two series of 10 shots were fired for $L_d = 2.3$ mm and for the case without lens.

6.2.4 Influence of the plasma lens density

As predicted by the model, both the electron density n_2 and the length of the second jet L_l can impact the lens properties. It is difficult to experimentally vary L_l as it would require to change the gas nozzle during a scan. The lens electron density n_2 is much more easily tunable. Its influence is illustrated in Fig. 6.12. The divergence of the beam decreases as n_2 varies from 0.75×10^{18} cm^{-3} to 6.1×10^{18} cm^{-3}. As described in the model in section 6.1.3, the focusing force varies as $[k_p c \tau \exp\left(-(ck_p\tau)^2/16\ln(2)\right)] \sin(k_p d)$ (see eq. (6.4)). The term in brackets corresponds to the amplitude of the transverse wakefield. It is maximum when the laser pulse is resonant with the plasma wave, for $k_p c\tau = 1$. The strength of the lens depends also on the position of the electron beam in the wakefield, described by the sine term. Electrons experience the largest focusing force when $k_p d = \pi/2$ and are defocused for $k_p d > \pi$. The combination of both terms leads to a complex influence of the electron density on the focusing strength.

For low electron densities ($n_2 \lesssim 1 \times 10^{18}$ cm^{-3} in Fig. 6.12), the focusing fields are very weak and the divergence is hardly reduced. As the density increases, the transverse focusing fields arise, which leads to the desired beam collimation. In Fig. 6.12, the lowest divergence is obtained for $n_2 = 4.3 \times 10^{18}$ cm^{-3}. The fact that the divergence remains almost constant for higher densities suggests that the focusing force has a local maximum around $n_2 = 4.3 \times 10^{18}$ cm^{-3}. For even higher densities (not investigated in the experiment), the divergence should

149
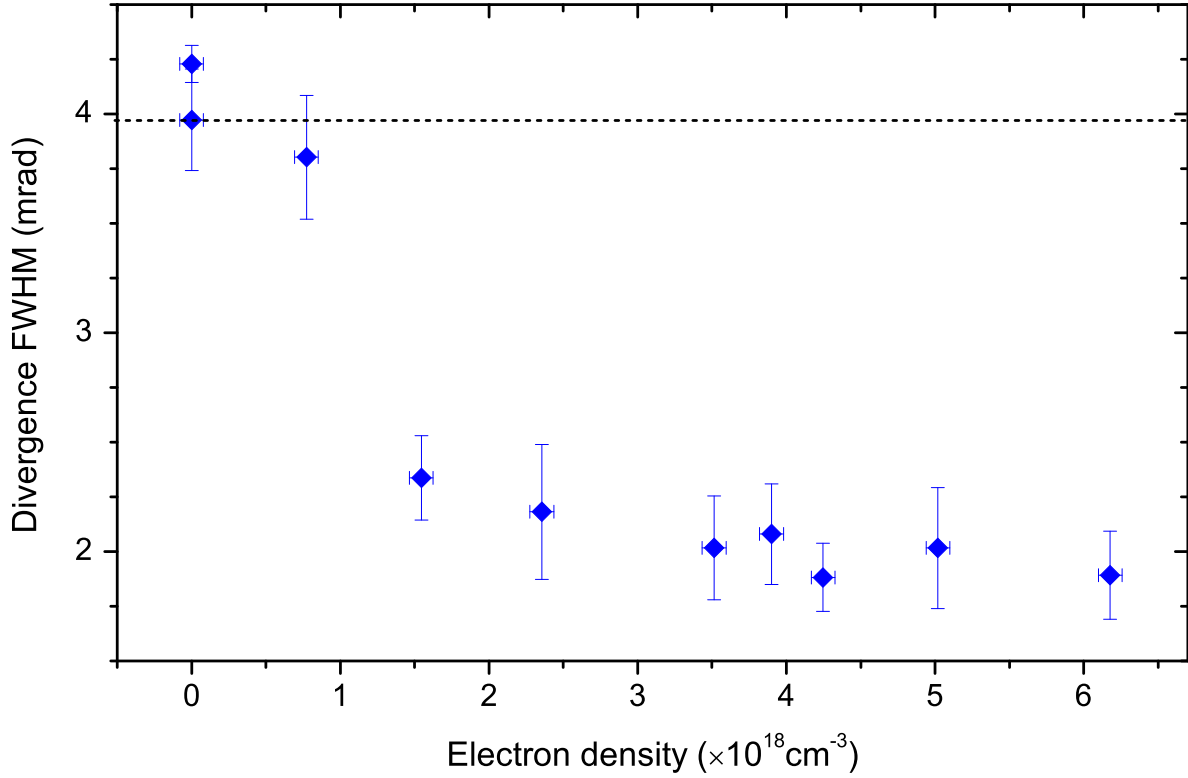
Figure 6.12: FWHM divergence of the beam, at 270 MeV, as a function of n_2 (blue diamonds). The drift length is $L_d = 2.3$ mm. The divergence measured without the laser-plasma lens is indicated by the black dashed line. Data points were averaged over at least 11 shots; the vertical error bars correspond to the standard error of the mean and the horizontal bars correspond to the precision on the backing pressure. The analysis of the interferograms leads to an additional systematic error on the density of ± 5 %.

increase and eventually exceed the initial divergence when the fields become defocusing (for $k_p d > \pi$). Note that, for long L_d, the mean density, which is effectively experienced by the electron beam during the focusing process, may be significantly smaller than the peak density n_2, because the focusing process is likely to occur only in the rising edge of the second gas jet.

6.2.5 Chromaticity of the laser-plasma lens

Up to now, the electron beam was implicitly assumed to be monoenergetic, and in Figs. 6.11 and 6.12, only the divergence at 270 MeV was considered. Yet, Fig. 6.10 reveals that electrons of different energies are not focused to the same extend. This is also shown in Fig. 6.13, which displays the reduction factor of the beam divergence as a function of both the electron energy and the distance between the two stages L_d. The reduction factor can be varied from 1 (no collimation) up to 2.6 for a given electron energy simply by varying L_d.

A couple of observations can be made from this plot. Firstly, the divergence reduction factor is larger towards higher energies. This is likely due to the decrease of the minimum achievable divergence $\sigma_{\theta,min}$ (defined in section 6.1.3) at higher energies, both because $\sigma_{\theta,min}$ varies as $\gamma \sigma_\theta^{-1}$, and because in this particular experiment, the divergence σ_θ at the end of the accelerator increases with γ (as seen in Fig. 6.10). Secondly, the optimal drift length L_d decreases as the
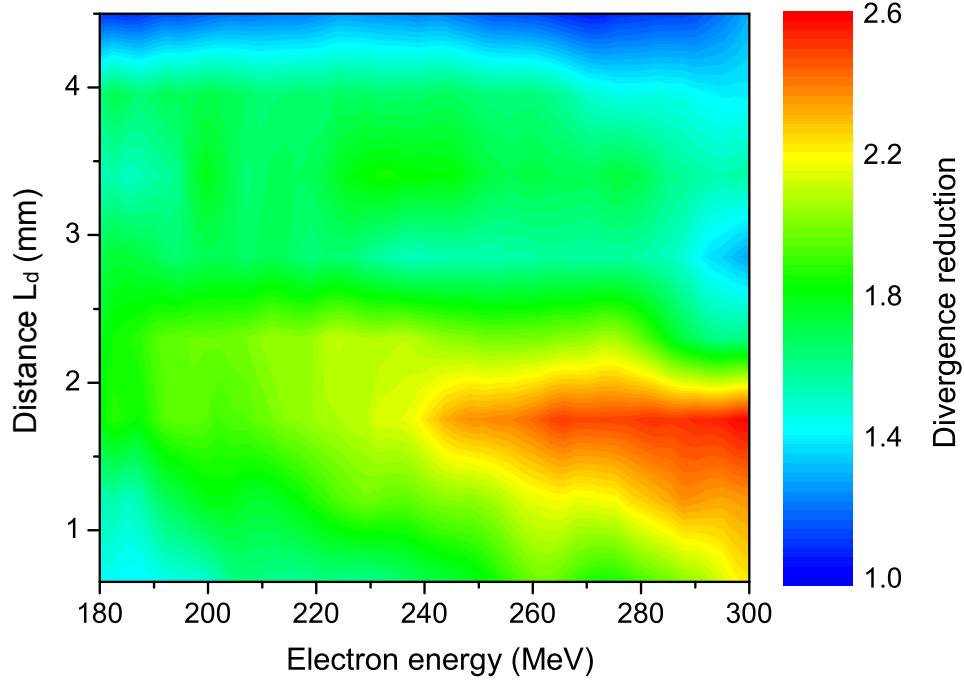
Figure 6.13: Chromaticity of the laser-plasma lens. The colour map shows the factor of reduction of the divergence, as a function of the electron energy and of the distance L_d between the accelerator and the lens (for height different values of L_d). The peak electron density in the focusing stage is $n_2 = 3.9 \times 10^{18}$ cm^{-3}.

electron energy increases. This is because the amplitude of the transverse fields required to focus the beam increases with the electron energy. Lengthening L_d tends to lessen the focusing fields and hence enhances the focusing of low-energy electrons (similar results can be obtained by decreasing the electron density). Nonetheless, an electron beam with an energy spread exceeding 100 MeV can be strongly focused, as a whole, using a laser-plasma lens, thanks to the quite good achromaticity of the laser-plasma lens.

6.3 Conclusion

In this chapter, we demonstrated the collimation of a laser-wakefield electron beam with a laser-plasma lens. The model developed by Lehe [2014] allowed to choose a good range of parameters for the drift length L_d and the second jet density n_2 so that experimental demonstration of electron beam focusing was possible [Thaury et al., 2015a]. The laser-plasma lens is a new concept allowing to control and manipulate the transverse momentum quantity of the electron beam.

An electron beam was accelerated in a laser-plasma accelerator up to 300 MeV before going through a laser-plasma lens. At the lens exit, the beam divergence was reduced by a factor of 2 for the whole beam and a factor of 2.6 for its high-energy part. This factor was limited by the fast decrease of the laser intensity in the lens. Stronger collimation could be obtained by using a shorter gas jet for the acceleration stage (allowing for a larger laser intensity when the pulse reaches the second stage), a gas jet with sharper gradients for the lens, or a more energetic laser pulse. Nevertheless, the demonstrated divergence reduction should already be

sufficient to transport the electron beam with a quadrupole lens set after the laser-plasma lens. For state of the art laser-plasma accelerators, the emittance growth should remain negligible over a propagation distance of ~ 30 cm, which should be enough to transport the beam with compact quadrupoles. Alternatively, the collimated electron beam could be sent directly into an optical [Andriyash et al., 2012] or a plasma undulator [Andriyash et al., 2014] to form a millimeter scale, possibly coherent, synchrotron source.

Conclusion

Summary of the results

This section summarizes the main results presented in this thesis.

Firstly, I presented in chapter 2 a comprehensive study of shock front formation in supersonic gas jets when encountering a sharp obstacle, supported by several fluid simulations. This process was used experimentally to create a sharp downward density gradient in order to locally control injection of electrons into the wakefield. We obtained high-quality electron beams (~ 5 % energy spread, 2 mrad divergence) with low charge ($\sim 1 - 10$ pC) and tunable final energy (up to 250 MeV). The parameters of these stable electron beams can be easily modified by changing the properties of the shock (notably its position in the gas jet).

In chapter 3, I showed that accelerating electrons in a pure high Z gas can lead to very stable, heavily-charged (up to 1 nC) electron beams (however with large energy spread). This method is based on ionization injection, allowing to trap a lot of electrons ionized directly into the accelerating cavity. The physics of acceleration of these highly-charged beams is extensively studied, underlining two important effects. First, tuning the laser energy allows for modifying the total charge without affecting the energy distribution. Second, self-generated wakefield allows to turn a quasi-Maxwellian energy distribution into a macro-bunch with more energetic electrons, for a low enough electron density. Furthermore, I showed that combining the ionization injection technique in a gas mixture with the shock front method presented in chapter 2 can lead to very stable, high quality (7 % energy spread, 3 mrad, 10 pC) electron beams.

Using a sharp density transition similar to that presented in chapter 2, but now reversed at the end of a gas jet, I showed in chapter 4 the possibility to manipulate the electron bunch phase in the cavity. This new technique allows for overcoming the dephasing limit which restricts the maximum achievable energy in several LWFA experiments. I first presented experimental evidence of this effect by increasing the energy of a small fraction of a broad spectrum electron beam (obtained via transverse self-injection). I then used this method to enhance the energy of a monoenergetic electron beam (produced in a sharp density transition) while preserving its good energy spread and divergence.

In chapter 5, I provided a presumable origin for the angular momentum of an electron beam. Optical aberrations in the laser pulse can lead to the formation of an anisotropic cavity in which transverse focusing forces are different depending on the electron position, resulting in the evolution of the beam angular momentum during the acceleration. The signature of this effect is visible into the betatron x-ray profiles emitted by the bunch, whose shape and flatness significantly depend on the angular momentum. Betatron based emittance measurements should take

angular momentum into account to avoid underestimating the bunch emittance.

Finally, I demonstrate in chapter 6 a new method to collimate laser-wakefield electron beams with a laser-plasma lens. This setup consists of a second gas jet placed at the exit of the accelerator. The laser pulse drives a wakefield in this second jet whose focusing forces are taken advantage of to reduce the divergence of the trailing electron bunch. A simple analytical model describing the principle is presented, underlining the major importance of the second jet length, density and distance from the first jet. Experimental demonstration of the laser-plasma lens shows a divergence reduction by a factor of 2.6 for electrons up to 300 MeV, in accordance with the model predictions.

A major axis of this thesis was to study the pros and cons of different injection techniques in order to produce high-quality electron beams with interesting parameters (charge, maximum energy, energy spread and divergence) for numerous applications while achieving a good stability and reproducibility. While sharp density transition injection, ionization injection and shock-assisted ionization injection were extensively studied in this work, others injection methods were used to study other physical effects of the beam (such as colliding injection, transverse and longitudinal self-injection). A summary of these different techniques, with the beam parameters and stability characteristics associated to each one of them, is given in Table 1. Note that this comparison between these injection techniques is valid for a "Salle Jaune"-like laser system (1 J, 30 fs), and that the characteristics of each one of them would be quite different for a Petawatt class system for instance.

	Charge	Energy spread	Typical energy range	Divergence	Controlability	Stability	Setup simplicity
Transverse self-injection	50 - 100 pC	10 - 100 %	80 - 400 MeV	5 - 10 mrad	– –	– –	+ +
Longitudinal self-injection	5 -10 pC	40 %	100 - 400 MeV	4 mrad	+	+ +	+ +
Optical injection	20 - 30 pC	5 - 10 %	50 - 300 MeV	6 mrad	+ +	+	–
High Z gas ionization injection	1 nC	Maxwellian	5 - 30 MeV	10 mrad	+	+ +	+ +
Shock front injection	1 - 10 pC	5 - 10 %	80 - 250 MeV	2 mrad	+ +	+	+
Shock-assisted ionization injection	1 - 10 pC	7 - 10 %	80 - 150 MeV	3 mrad	+ +	+ +	+

Table 1: Summary of different injection techniques studied in the frame of my thesis. Longitudinal injection (respectiveley optical injection) beam parameters come from the experiment presented in chapter 5 (respectively in chapter 6).

Each method has its perks and drawbacks depending on which beam characteristic is the most important for the considered usage of the electron beam. Several applications are presented in the following section, with the most appropriate injection process to make use of.

Perspectives

These results open up several prospects for applications based on laser-wakefield accelerated electron beams.

Radiography : A first application taking advantage of the micrometer source size and milliradians divergence of laser-wakefield electron beams is non-destructive testing of dense matter. The simplest way to produce high energy X and gamma radiation is to convert the beam into bremsstrahlung into a high Z material [Glinec et al., 2005; Ben-Ismail et al., 2011]. The basic experimental setup is presented in Fig. 1. A tantalum converter is placed at the output of the accelerator : gamma-rays are produced when electrons are slowed down in this dense material. The image of a dense object placed in the beam path is then obtained onto an image plate. The signal must be accumulated over several shots to have a correct signal-to-noise ratio, thus requiring very stable electron beams with high charge. Electron acceleration in pure high Z gases produced via ionization injection (presented in chapter 3) meet these charge and stability criteria, and were used in a recent radiography experiment performed at LOA. Furthermore, the low energy of these electrons (between 10 and 50 MeV) are interesting to produce X-rays in the range of 10-50 keV.

We measured the gamma-ray source size using a knife-edge for different distances between the gas jet exit and the tantalum converter. At 0.5 mm from the exit, the source size is estimated to be about 65 μm, while it remains below 100 μm at 1.5 mm distance and goes up to 350 μm at 3.5 mm from the gas jet. Figure 1 shows a radiography of industry standard image quality indicators (DIN EN 462), with the smallest features resolved having a size of about 200 μm. Such a micrometrical, femtosecond gamma source is of interest to probe dense structures (in military or aeronautic industry for instance) or material response to very fast constraints.
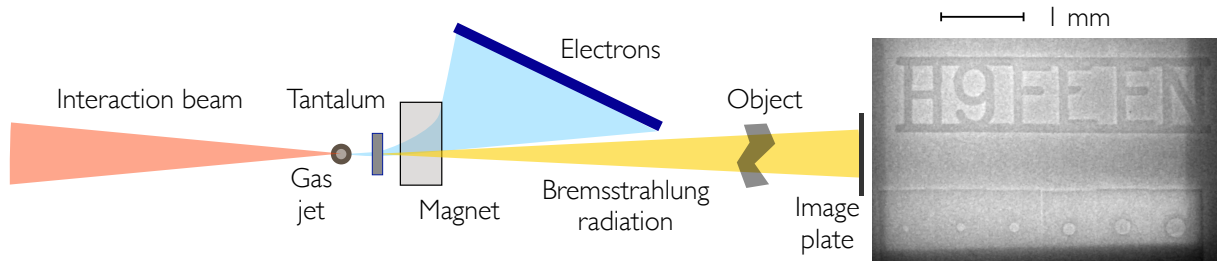
Figure 1: Drawing of the experimental setup of gamma ray generation via bremsstrahlung of electrons in a tantalum converter. The tantalum is placed between 0.5 mm and 3.5 mm after the gas jet, with the object placed at 2 m from the jet and the detector at 2.5 m.

Radiotherapy : High energy electrons (> 200 MeV) are interesting candidates to treat tumors thanks to the larger penetration depth than low energy electrons from conventional table-top accelerators [Glinec et al., 2006b; Lundh et al., 2012]. In order to achieve a good dose deposition with a penetration depth larger than 10 cm, the electron beam needs to be focused. The laser-plasma lens could be used, taking good advantage of the easy focal plane tunability by varying the drift length and plasma density in the second jet to reach different depths in tissues. Furthermore, a medical device based on laser-wakefield accelerated electrons would require a very good stability and reliability. While there is a long way to go before meeting the same criteria as conventional medical accelerators (much more stable with a higher repetition rate

and a charge of hundreds of pC), an interesting step would be to use a controllable and stable injection technique such as shock-assisted ionization injection (as shown in Table 1).

Multi-stage acceleration : In the context of potential future LWFA-based colliders, the electron beam is accelerated up to TeV energies in a series of stacked accelerating media [Schroeder et al., 2010]. Before each stage, a new laser pulse is injected into the corresponding gas target and drives a quasi-linear wakefield in which the incoming electron bunch is further accelerated. Such a multi-stage accelerator requires a very high-quality injector stage before the first acceleration stage in order to control the beam parameters carefully. Shock-assisted ionization injection or colliding pulse injection would be interesting candidates thanks to their very good stability and low energy spread (as seen in Table 1). Moreover, it is mandatory to transport the bunch from one stage to another. Indeed, the beam diverges in the free drift between two stages and must be focused quickly to avoid emittance growth [Mehrling et al., 2012]. The laser-plasma lens would be very useful in this case as the outgoing laser of a given acceleration stage could also serve to form the lens and focus the electrons onto the entrance of the following stage. Furthermore, achieving such high energies would require a very large number of consecutive stages, and thus of laser pulses. This number could be reduced by using longer gas targets with a tailored plasma density to overcome dephasing and accelerate the beam further in a single stage. A quasi-phase matching regime may be achievable by considering a multi-step increasing density profile. The electron bunch would reach dephasing in the first density region, then be phase-resetted by crossing a first step and accelerate further in the second plateau, and so on. By combining the laser-plasma lens and a density tailored plasma for quasi-phase matching, it would be possible to greatly reduce the size (hence the cost) of LWFA-based linear colliders.
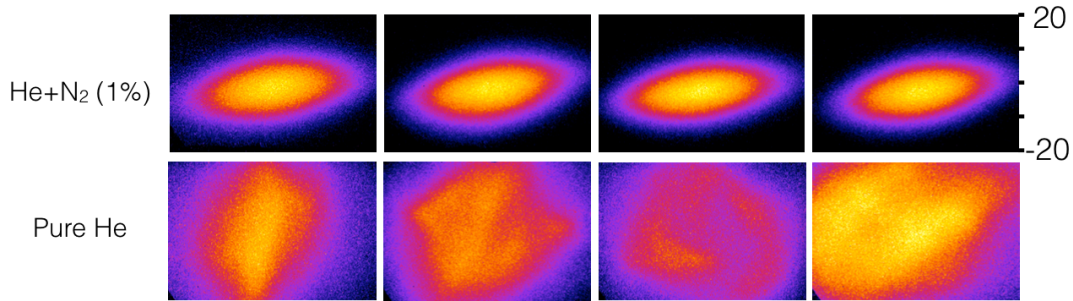
Figure 2: Betatron x-ray profiles from ionization injection in a gas mixture of helium with 1% of nitrogen (top panel, four consecutive shots) and from transverse self-injection in pure helium (bottom panel, four consecutive shots). The colorscale is the same for the eight images.

Betatron radiation generation : Another major application of electron beams is the generation of x-ray betatron radiation during the acceleration. While large efforts have been made in the last few years to enhance betatron radiation brightness, these x-ray beams are intrinsically not very stable shot-to-shot as their properties rely largely on electron trajectories during the acceleration, and thus on the initial transverse distribution of the bunch set during injection. We demonstrated recently at LOA a simple method that allows to produce stable and bright Betatron beams by taking advantage of ionization injection in a gas mixture (helium with a few percent of nitrogen). This injection method is less sensitive to the transverse inhomogeneities of the laser spot and to laser propagation than transverse injection, and leads to the production

of more stable electrons beams than with transverse self-injection (as seen in Fig. 2). In addition, electrons gain a net transverse momentum from the laser field along its polarization direction when ionized close to the peak of the pulse, therefore producing polarized x-ray beams. By varying the polarization direction of the laser, it is easy to tune the polarization of the radiation as well. Experimental results show that the pointing stability of the x-ray beam is better than 10% of the beam divergence, with flux fluctuation of the order of 20% and a polarization degree reaching up to 80%.

LWFA Free Electron Lasers :   One of the most ambitious application of electron beams is the LWFA-based Free Electron Laser (FEL) [Maier et al., 2012; Couprie et al., 2014], combining an LWFA with a magnetic short-period undulator. The required energy (about 300-500 MeV for typical undulators) is well within the range of state-of-the-art laser-plasma accelerators. The great challenges lie in the charge, energy spread and divergence of the bunch. In LWFA, energy spread and charge are strongly coupled and depend mainly on the injection method and beamloading dynamics during acceleration. With shock-front assisted injection or optical injection, relatively low energy-spread, stable beams are generated, yet with low charge (see Fig. 1). Moreover, the laser-plasma lens could be used as a first element to transport the beam from the accelerator exit to the entrance of a conventional magnetic transport line to help keeping the emittance of the bunch unspoiled. A first experiment is planned at LOA in the frame of the *LUNEX5* project in 2016 to demonstrate the feasibility of such a FEL design.

Plasma based undulator :   A new type of plasma-based undulator was proposed at LOA in 2014 [Andriyash et al., 2014] to produce a bright and compact incoherent X-ray source. The main idea is to insert a periodic array of metallic nanowires directly after the laser-wakefield accelerator, as schemed in Fig. 3. After exiting the gas jet, the laser pulse hits the wires and ionize them, creating positively charged columns with very strong space-charge fields (up to 1 TV.m^{-1} according to PIC simulations). The trailing electron bunch enters this plasma undulator and starts to wiggle in the periodic field, producing synchrotron emission. In this context, the experiment is planned to be performed within the next few months at LOA. The laser-plasma lens may be useful to reduce the divergence of the electron beam and thus the width of the emitted spectrum, and increase the brightness of the radiation [Andriyash et al., 2014].
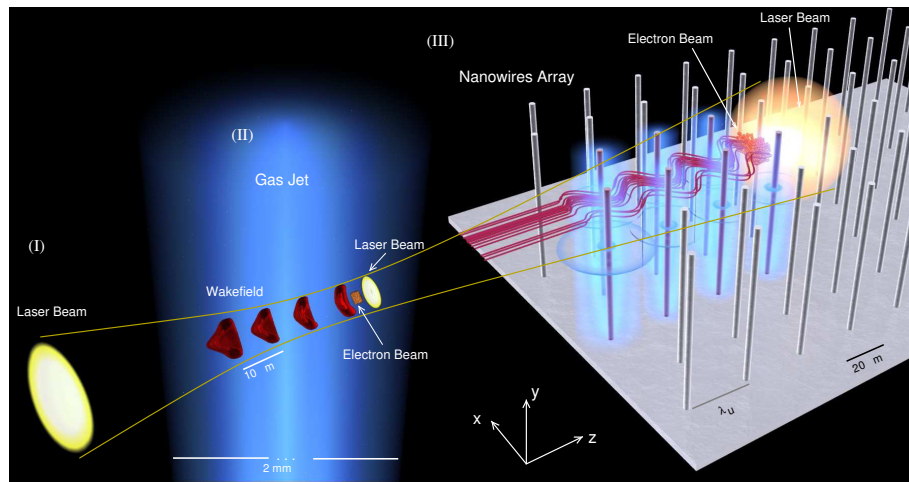
Figure 3: Drawing of the nanowire undulator. *(Courtesy of A. Lifschitz)*

Appendix A

Phase locking and phase resetting of electrons

This section develops the calculations demonstrating the expressions of the energy gain in a constant density profile (in section A.1), the optimum density profile and energy gain for phase-locking (in section A.2) and for phase resetting (in section A.3).

A.1 Energy gain in a constant density profile

The energy gain of an electron accelerated in a constant density profile n_0 between z_0 and z in the bubble regime can be estimated by [Lu et al., 2007]:

$$\Delta\gamma(z) = \frac{e}{m_e c^2} \int_{z_0}^{z} E_z(z')dz'. \tag{A.1}$$

where E_z is the longitudinal electric field in the cavity. Assuming the complete blow-out regime ($L_{deph} = n_c/n_0\lambda_p$ with λ_p the cavity length and n_c the critical density as defined in section 1.1.4) and the longitudinal electric field to be sawtooth like : $E_z(0 < z < 2L_{deph}) = E_{z0} \times (1 - z/L_{deph})$, where $E_{z0} = (m_e\omega_p c/e)\sqrt{a_0}$ is the maximum longitudinal field in the blow-out regime (with a_0 the normalized amplitude of the laser). The expression of the energy gain becomes :

$$\Delta\gamma(z) = \frac{e}{m_e c^2} E_{z0} \int_{z_0}^{z} (1 - \frac{z'}{L_{deph}})dz'. \tag{A.2}$$

Considering $z_0 = 0$, the energy gain is :

$$\Delta\gamma(z) = \frac{e}{m_e c^2} E_{z0} \left(z - \frac{1}{2}\frac{z^2}{L_{deph}} \right). \tag{A.3}$$

The maximum energy gain is reached when $z = L_{deph}$, which is therefore

$$\Delta\gamma_{max} = \frac{n_c}{n_0}\sqrt{a_0} = \left(\frac{\omega_0}{\omega_p}\right)^2 \sqrt{a_0}. \tag{A.4}$$

A.2 Phase-locking of electrons

The initial normalized phase of an electron is $\Phi_0 = 1 - \xi_0/\lambda_p$ with ξ_0 the position of the particle with respect to the front of the wake in the co-moving coordinate and λ_p the cavity wavelength.

In order to keep the same phase Φ_0 all along the acceleration in an upward density gradient $n_e(z)$, the phase slippage of the accelerating electron has to be compensated by varying the cavity wavelength. Assuming that the electron is initially at the very back of the cavity ($\xi_0 = -\lambda_p$), the position of the electron at velocity $v_e - v_\varphi$ in the co-moving coordinate, after an infinitesimal time dt is :

$$\xi(dt) = \xi_0 + (v_e - v_\Phi)dt. \tag{A.5}$$

In the same time dt, the cavity must shortens by $d\lambda$ to compensate electron movement, with the cavity wavelength after dt :

$$\lambda(dt) = \lambda_p - d\lambda. \tag{A.6}$$

The phase-matching condition $\Phi(dt) = 1 - \xi(dt)/\lambda(dt) = \Phi_0$ gives the relation :

$$-(1 - \Phi_0)d\lambda = (v_\Phi - v_e)dt. \tag{A.7}$$

The mandatory change for the cavity wavelength λ to achieve perfect phase-locking is thus given by :

$$\frac{d\lambda}{dt} = \frac{v_e - v_\Phi}{1 - \Phi_0}. \tag{A.8}$$

We assume a highly relativistic electron ($v_e \sim c$) and a laser propagating at the group velocity in an underdense plasma ($v_g(t) = c\sqrt{1 - n_e(t)/n_c} \sim c(1 - n_e(t)/2n_c)$ with $n_0 \ll n_c$) with a constant amplitude a_0 (self-focusing is neglected). We assume also that the phase velocity of the wake is equal to the group velocity of the pulse $v_\Phi \sim v_g$ and that the cavity wavelength λ depends only on the plasma density as $\lambda(t) = \lambda_p \sqrt{n_0/n_e}$, then :

$$\frac{d\lambda}{dt} = -\frac{\lambda_p}{2}\frac{n_0^{\frac{1}{2}}}{n_e(t)^{\frac{3}{2}}}\frac{dn_e(t)}{dt}. \tag{A.9}$$

Combining eq. (A.8) and eq. (A.9), we get :

$$\frac{dn_e}{dt} - \alpha n_e^{\frac{5}{2}} = 0 \text{ with } \alpha = \frac{c}{\lambda_p\sqrt{n_0}n_c(1 - \Phi_0)}. \tag{A.10}$$

This equation can be solved considering the initial condition $n_e(t = 0) = n_0$:

$$n_e(t) = \frac{n_0}{\left(1 - \frac{3}{2}n_0^{\frac{3}{2}}\alpha t\right)^{\frac{2}{3}}}. \tag{A.11}$$

For $z = ct$ and $L_{deph} = \lambda_p n_c/n_0$ (first approximation neglecting the laser pulse intensity influence on the cavity wavelength, which is a rather strong assumption), the perfectly matching density profile writes as :

$$n_e(z) = \frac{n_0}{\left(1 - \frac{3}{2(1-\Phi_0)}\frac{z}{L_{deph}}\right)^{\frac{2}{3}}}. \tag{A.12}$$

We define the inhibition length $L_{inh} = 2(1 - \Phi_0)L_{deph}/3$ after which the plasma density goes to infinity. Note that this singularity in the phase-matching profile happens at $2/3L_{deph}$ for $\Phi_0 = 0$. The plasma density profile is then :

$$n_e(z) = \frac{n_0}{\left(1 - \frac{z}{L_{inh}}\right)^{\frac{2}{3}}}. \tag{A.13}$$

Assuming the phase-locking density profile (with $\Phi_0 = 0$) and that the electrons remain at the same phase during the whole acceleration, the electric field is considered to depend only on the density as :

$$E_z(z) = E_{z0}\sqrt{\frac{n_e(z)}{n_0}} = E_{z0}\frac{1}{\left(1 - \frac{z}{L_{inh}}\right)^{\frac{1}{3}}}. \tag{A.14}$$

The energy gain of an electron in the phase-locking density profile calculated in eq. (A.13) is then :

$$\Delta\gamma(z) = \frac{e}{m_e c^2}E_{z0}\int_0^z (1 - \frac{z'}{L_{inh}})^{\frac{-1}{3}}dz' \tag{A.15}$$

thus giving :

$$\Delta\gamma(z) = \frac{e}{m_e c^2}E_{z0}\frac{3L_{inh}}{2}\left(1 - \frac{z}{L_{inh}}\right)^{\frac{2}{3}}. \tag{A.16}$$

A.3   Phase-resetting of electrons

An electron is assumed to be injected at phase $\Phi_0 = 0$ in a step density profile (low density region n_0 followed by a higher density region n_1, separated by a density step at $z = z_1$). When crossing the density transition, the cavity has to shrink down so that the phase Φ_1 just after the transition goes back to zero. The position of the electron at velocity $v_e - v_\varphi$ (with $v_e \sim c$) in the co-moving coordinate after the step (at time t_1) is :

$$\xi_1 = (v_e - v_\Phi)t_1 = \frac{(v_e - v_\Phi)}{c}z_1. \tag{A.17}$$

Considering the same strong assumptions that in section A.2 (notably $v_\Phi \sim v_g \sim c(1 - n_e(t)/2n_c)$ with $n_0 \ll n_c$), we get :

$$\xi_1 = \frac{1}{2}\frac{n_0}{n_c}z_1. \tag{A.18}$$

In order to compensate this phase slippage at z_1, the cavity wavelength λ_p must shortens by ξ_1 exactly in the n_1 density region :

$$\lambda_1 = \lambda_p - \xi_1 = \lambda_p\sqrt{\frac{n_0}{n_1}}. \tag{A.19}$$

Combining eqs. (A.18) and (A.19), we obtain :

$$n_1(z_1) = \frac{n_0}{\left(1 - \frac{z_1}{2L_{deph}}\right)^2} \tag{A.20}$$

with $L_{deph} = n_c/n_0\lambda_p$ the dephasing length in the first density region.

The longitudinal electric field in the cavity after the density transition is sawtooth-like as $E_z(z > z_1) = E_{z1} \times (1 - (z - z_1)/L_{d1})$ with $E_{z1} = (m_e\omega_{p1}c/e)\sqrt{a_0}$ and $L_{d1} = \lambda_1 n_c/n_1$ respectively the maximum longitudinal field and the dephasing length in the density region n_1. The total energy gain of an electron accelerated in the density plateau n_0 up to z_1, perfectly rephased and accelerated up to z in the n_1 density region is :

$$\Delta\gamma(z) = \Delta\gamma_0(z_1) + \Delta\gamma_1(z). \tag{A.21}$$

Since the energy gain in a constant density profile has already been calculated in section A.1, we directly get from eq. (A.3) :

$$\Delta\gamma_0(z_1) = \frac{e}{m_e c^2} E_{z0} \left(z_1 - \frac{1}{2}\frac{z_1^2}{L_{deph}} \right) \tag{A.22}$$

and

$$\Delta\gamma_1(z) = \frac{e}{m_e c^2} E_{z1} \left((z - z_1) - \frac{1}{2}\frac{(z - z_1)^2}{L_{d1}} \right) \tag{A.23}$$

thus :

$$\Delta\gamma(z) = \frac{e}{m_e c^2} \left[\frac{E_{z1}}{2L_{d1}}z^2 + E_{z1}\left(1 - \frac{1}{L_{d1}}\right)z + \left(\frac{E_{z1}}{2L_{d1}} - \frac{E_{z0}}{2L_{deph}}\right)z_1^2 + (E_{z0} - E_{z1})z_1 \right]. \tag{A.24}$$

Appendix B

List of publications

Electron rephasing in a Laser-Wakefield Accelerator
E. Guillaume, A. Döpp, C. Thaury, K. Ta Phuoc, A. Lifschitz, J-P. Goddet, A. Tafzi, D. Douillet,
G. Rey, S.W. Chou, L. Veisz, and V. Malka
Phys. Rev. Lett. 115 (2015) 155002

Physics of fully-loaded laser-plasma accelerators
E. Guillaume, A. Döpp, C. Thaury, A. Lifschitz, J-P. Goddet, A. Tafzi, F. Sylla, G. Iaquanello,
T. Lefrou, P. Rousseau, K. Ta Phuoc, and V. Malka
Phys. Rev. ST Accel. Beams 18 (2015) 061301

Demonstration of relativistic electron beam focusing by a laser-plasma lens
C. Thaury, E. Guillaume, A.Döpp, R. Lehe, A. Lifschitz, K. Ta Phuoc, J. Gautier, J-P Goddet,
A. Tafzi, A. Flacco, F. Tissandier, S. Sebban, A. Rousse and V. Malka
Nature Communications 6 (2015) 6860

Shock assisted ionization injection in laser-plasma accelerators
C. Thaury, E. Guillaume, K. Ta Phuoc, M. Hansson, G. Grittani, A. Lifschitz, J. Gautier, J.-P.
Goddet, A. Tafzi, O. Lundh, and V. Malka
Scientific Reports 5, Article number: 16310 (2015)

Laser-plasma lens for laser-wakefield accelerators
R. Lehe, C. Thaury, E. Guillaume, A.F. Lifschitz and V. Malka
Phys. Rev. ST Accel. Beams 17 (2014) 121301

Angular-Momentum Evolution in Laser-Plasma Accelerators
C. Thaury, E. Guillaume, S. Corde, R. Lehe, M. Le Bouteiller, K. Ta Phuoc, X. Davoine, J. M.
Rax, A. Rousse, and V. Malka
Phys. Rev. Lett. 111 (2013) 135002

Single Shot Radiography Using an All-optical Compton Backscattering Source
A. Döpp, E. Guillaume, C. Thaury, J. Gautier, A. Lifschitz, E. Conejeroc, C. Ruiz, V. Malka,
A. Rousse and K. Ta Phuoc
Physics Procedia 77 (2015) 9-14

A bremsstrahlung gamma-ray source based on laser wakefield acceleration in high Z gases
A. Döpp, E. Guillaume, C. Thaury, A. Lifschitz, F. Sylla, J-P. Goddet, A. Tafzi, G. Iaquanello, T. Lefrou, P. Rousseau, C. Ruiz, K. Ta Phuoc and V. Malka
Submitted to Plasma Phys. Control. Fusion (2015)

Stable and polarized Betatron x-ray radiation from a laser plasma accelerator in ionization injection regime
A. Döpp, B. Mahieu, A. Doche, C. Thaury, E. Guillaume, A. Lifschitz, G. Grittani, O. Lund, M. Hansson, J. Gautier, M. Kozlova, J-P. Goddet, P. Rousseau, A. Tafzi, V. Malka, A. Rousse, S. Corde and K. Ta Phuoc
Submitted to Nature Communications (2015)

Effect of the Third Order Dispersion on laser pulse propagation in an underdense plasma
E. Guillaume, C. Thaury, A. Lifschitz, A. Döpp, K. Ta Phuoc, H.T. Kim, K.H. Pae, C.H. Nam, and V. Malka
Submitted to Opt. Lett. (2015)

Coherent control of laser-wakefield electron acceleration driven by PW laser pulses
H. T. Kim, K. H. Pae, V. B. Pathak, A. Lifschitz, F. Sylla, I. J. Kim, S. K. Lee, J. H. Sung, H. W. Lee, E. Guillaume, C. Thaury, K. Nakajima, L. O. Silva, J. Vieira, V. Malka, and C. H. Nam
Submitted to Phys. Rev. Lett. (2015)

Bibliography

Amiranoff, F., Baton, S., Bernard, D., Cros, B., Descamps, D., Dorchies, F., Jacquet, F., Malka, V., Marquès, J. R., Matthieussent, G., Miné, P., Modena, A., Mora, P., Morillo, J., and Najmudin, Z. (1998). Observation of laser wakefield acceleration of electrons. *Phys. Rev. Lett.*, 81:995–998. Available from: http://link.aps.org/doi/10.1103/PhysRevLett.81.995. 22

Ammosov, M. V., Delone, N. B., and Krainov, V. P. (1986). Tunnel ionization of complex atoms and of atomic ions in an alternating electromagnetic field. *Sov. Phys. JETP*, 64(1191):2008–2013. Available from: http://www.jetp.ac.ru/cgi-bin/e/index/e/64/6/p1191?a=list. 70

Andriyash, I., d'Humières, E., Tikhonchuk, V., and Balcou, P. (2012). X-ray amplification from a raman free-electron laser. *Physical review letters*, 109(24):244802. Available from: http://journals.aps.org/prl/abstract/10.1103/PhysRevLett.109.244802. 152

Andriyash, I., Lehe, R., Lifschitz, A., Thaury, C., Rax, J.-M., Krushelnick, K., and Malka, V. (2014). An ultracompact x-ray source based on a laser-plasma undulator. *Nature communications*, 5. Available from: http://www.nature.com/ncomms/2014/140822/ncomms5736/abs/ncomms5736.html. 152, 157

Augst, S., Strickland, D., Meyerhofer, D. D., Chin, S. L., and Eberly, J. H. (1989). Tunneling ionization of noble gases in a high-intensity laser field. *Phys. Rev. Lett.*, 63:2212–2215. Available from: http://link.aps.org/doi/10.1103/PhysRevLett.63.2212. 77

Bajlekov, S. I., Heigoldt, M., Popp, A., Wenz, J., Khrennikov, K., Karsch, S., and Hooker, S. M. (2013). Longitudinal electron bunch profile reconstruction by performing phase retrieval on coherent transition radiation spectra. *Phys. Rev. ST Accel. Beams*, 16:040701. Available from: http://link.aps.org/doi/10.1103/PhysRevSTAB.16.040701. 31

Barov, N., Conde, M. E., Gai, W., and Rosenzweig, J. B. (1998). Propagation of short electron pulses in a plasma channel. *Phys. Rev. Lett.*, 80:81–84. Available from: http://link.aps.org/doi/10.1103/PhysRevLett.80.81. 136

Ben-Ismaïl, A., Lundh, O., Rechatin, C., Lim, J. K., Faure, J., Corde, S., and Malka, V. (2011). Compact and high-quality gamma-ray source applied to 10 micrometer-range resolution radiography. *Appl. Phys. Lett.*, 98(26):264101. Available from: http://link.aip.org/link/?APL/98/264101/1. 75

Ben-Ismail, A., Lundh, O., Rechatin, C., Lim, J. K., Faure, J., Corde, S., and Malka, V. (2011). Compact and high-quality gamma-ray source applied to 10 μm-range resolution radiography. *Applied Physics Letters*, 98(26):264101. Available from: http://scitation.aip.org/content/aip/journal/apl/98/26/10.1063/1.3604013. 155

Blumenfeld, I., Clayton, C. E., Decker, F.-J., Hogan, M. J., Huang, C., Ischebeck, R., Iverson, R., Joshi, C., Katsouleas, T., Kirby, N., Lu, W., Marsh, K. A., Mori, W. B., Muggli, P., Oz, E., Siemann, R. H., Walz, D., and Zhou, M. (2007). Energy doubling of 42[thinsp]gev electrons in a metre-scale plasma wakefield accelerator. *Nature*, 445(7129):741–744. Available from: http://dx.doi.org/10.1038/nature05538. 88

Bourgeois, N., Cowley, J., and Hooker, S. M. (2013). Two-pulse ionization injection into quasi-linear laser wakefields. *Phys. Rev. Lett.*, 111:155004. Available from: http://link.aps.org/doi/10.1103/PhysRevLett.111.155004. 26

Brantov, A. V., Esirkepov, T. Z., Kando, M., Kotaki, H., Bychenkov, V. Y., and Bulanov, S. V. (2008). Controlled electron injection into the wake wave using plasma density inhomogeneity. *Physics of Plasmas (1994-present)*, 15(7):–. Available from: http://scitation.aip.org/content/aip/journal/pop/15/7/10.1063/1.2956989. 25

Brijesh, P., Thaury, C., Phuoc, K. T., Corde, S., Lambert, G., Malka, V., Mangles, S., Bloom, M., and Kneip, S. (2012). Tuning the electron energy by controlling the density perturbation position in laser plasma accelerators. *Physics of Plasmas (1994-present)*, 19(6):063104. Available from: http://scitation.aip.org/content/aip/journal/pop/19/6/10.1063/1.4725421. 25

Bruhwiler, D. L., Dimitrov, D. A., Cary, J. R., Esarey, E., Leemans, W., and Giacone, R. E. (2003). Particle-in-cell simulations of tunneling ionization effects in plasma-based accelerators. *Physics of Plasmas (1994-present)*, 10(5):2022–2030. Available from: http://scitation.aip.org/content/aip/journal/pop/10/5/10.1063/1.1566027. 70

Buck, A., Wenz, J., Xu, J., Khrennikov, K., Schmid, K., Heigoldt, M., Mikhailova, J. M., Geissler, M., Shen, B., Krausz, F., Karsch, S., and Veisz, L. (2013). Shock-front injector for high-quality laser-plasma acceleration. *Phys. Rev. Lett.*, 110:185006. Available from: http://link.aps.org/doi/10.1103/PhysRevLett.110.185006. 1, 25, 42, 53

Bulanov, S., Naumova, N., Pegoraro, F., and Sakai, J. (1998). Particle injection into the wave acceleration phase due to nonlinear wake wave breaking. *Phys. Rev. E*, 58:R5257–R5260. Available from: http://link.aps.org/doi/10.1103/PhysRevE.58.R5257. 25

Bulanov, S. V., Inovenkov, I. N., Kirsanov, V. I., Naumova, N. M., and Sakharov, A. S. (1992a). Nonlinear depletion of ultrashort and relativistically strong laser pulses in an underdense plasma. *Physics of Fluids B: Plasma Physics (1989-1993)*, 4(7):1935–1942. Available from: http://scitation.aip.org/content/aip/journal/pofb/4/7/10.1063/1.860046. 11

Bulanov, S. V., Inovenkov, I. N., Kirsanov, V. I., Naumova, N. M., and Sakharov, A. S. (1992b). Nonlinear depletion of ultrashort and relativistically strong laser pulses in an underdense plasma. *Physics of Fluids B: Plasma Physics (1989-1993)*, 4(7):1935–1942. Available from: http://scitation.aip.org/content/aip/journal/pofb/4/7/10.1063/1.860046. 27

Bulanov, S. V., Pegoraro, F., Pukhov, A. M., and Sakharov, A. S. (1997). Transverse-wake wave breaking. *Phys. Rev. Lett.*, 78:4205–4208. Available from: http://link.aps.org/doi/10.1103/PhysRevLett.78.4205. 22

Burza, M., Gonoskov, A., Svensson, K., Wojda, F., Persson, A., Hansson, M., Genoud, G., Marklund, M., Wahlström, C.-G., and Lundh, O. (2013). Laser wakefield acceleration using

wire produced double density ramps. *Phys. Rev. ST Accel. Beams*, 16:011301. Available from: http://link.aps.org/doi/10.1103/PhysRevSTAB.16.011301. 25, 42

Chen, M., Esarey, E., Schroeder, C. B., Geddes, C. G. R., and Leemans, W. P. (2012). Theory of ionization-induced trapping in laser-plasma accelerators. *Physics of Plasmas*, 19(3):–. Available from: http://scitation.aip.org/content/aip/journal/pop/19/3/10.1063/1.3689922. 92

Chen, P. (1987). A possible final focusing mechanism for linear colliders. *Particle Accelerators*, 20:171–182. Available from: http://www.slac.stanford.edu/cgi-wrap/getdoc/slac-pub-3823.pdf. 136

Chen, P., Oide, K., Sessler, A. M., and Yu, S. S. (1990). Plasma-based adiabatic focuser. *Phys. Rev. Lett.*, 64:1231–1234. Available from: http://link.aps.org/doi/10.1103/PhysRevLett.64.1231. 136

Chessa, P., De Wispelaere, E., Dorchies, F., Malka, V., Marquès, J. R., Hamoniaux, G., Mora, P., and Amiranoff, F. (1999). Temporal and angular resolution of the ionization-induced refraction of a shgongort laser pulse in helium gas. *Phys. Rev. Lett.*, 82:552–555. Available from: http://link.aps.org/doi/10.1103/PhysRevLett.82.552. 131

Chien, T.-Y., Chang, C.-L., Lee, C.-H., Lin, J.-Y., Wang, J., and Chen, S.-Y. (2005). Spatially localized self-injection of electrons in a self-modulated laser-wakefield accelerator by using a laser-induced transient density ramp. *Phys. Rev. Lett.*, 94:115003. Available from: http://link.aps.org/doi/10.1103/PhysRevLett.94.115003. 25

Clayton, C. E., Marsh, K. A., Dyson, A., Everett, M., Lal, A., Leemans, W. P., Williams, R., and Joshi, C. (1993). Ultrahigh-gradient acceleration of injected electrons by laser-excited relativistic electron plasma waves. *Phys. Rev. Lett.*, 70:37–40. Available from: http://link.aps.org/doi/10.1103/PhysRevLett.70.37. 22

Corde, S. (2012). *From laser-plasma accelerators to femtosecond X-ray sources: study, development and applications.* Theses, Ecole Polytechnique X. Available from: https://pastel.archives-ouvertes.fr/pastel-00680257. 118

Corde, S., Phuoc, K. T., Fitour, R., Faure, J., Tafzi, A., Goddet, J. P., Malka, V., and Rousse, A. (2011). Controlled betatron x-ray radiation from tunable optically injected electrons. *Phys. Rev. Lett.*, 107:255003. Available from: http://link.aps.org/doi/10.1103/PhysRevLett.107.255003. 131, 133

Corde, S., Ta Phuoc, K., Lambert, G., Fitour, R., Malka, V., Rousse, A., Beck, A., and Lefebvre, E. (2013a). Femtosecond x rays from laser-plasma accelerators. *Rev. Mod. Phys.*, 85:1–48. Available from: http://link.aps.org/doi/10.1103/RevModPhys.85.1. 20, 119, 123, 129

Corde, S., Thaury, C., Lifschitz, A., Lambert, G., Ta Phuoc, K., Davoine, X., Lehe, R., Douillet, D., Rousse, A., and Malka, V. (2013b). Observation of longitudinal and transverse self-injections in laser-plasma accelerators. *Nat Commun*, 4. Available from: http://dx.doi.org/10.1038/ncomms2528. 24, 92, 107, 145

Couprie, M., Benabderrahmane, C., Betinelli, P., Bouvet, F., Buteau, A., Cassinari, L., Daillant, J., Denard, J., Eymard, P., Gagey, B., et al. (2014). The lunex5 project in france. In *X-Ray Lasers 2012*, pages 55–62. Springer. 2, 157

Davoine, X., Beck, A., Lifschitz, A., Malka, V., and Lefebvre, E. (2010). Cold injection for electron wakefield acceleration. *New Journal of Physics*, 12(9):095010. Available from: http://stacks.iop.org/1367-2630/12/i=9/a=095010. 26

Davoine, X., Lefebvre, E., Rechatin, C., Faure, J., and Malka, V. (2009). Cold optical injection producing monoenergetic, multi-gev electron bunches. *Phys. Rev. Lett.*, 102:065001. Available from: http://link.aps.org/doi/10.1103/PhysRevLett.102.065001. 1, 26

Decker, C. D. and Mori, W. B. (1994). Group velocity of large amplitude electromagnetic waves in a plasma. *Phys. Rev. Lett.*, 72:490–493. Available from: http://link.aps.org/doi/10.1103/PhysRevLett.72.490. 11

Decker, C. D., Mori, W. B., Katsouleas, T., and Hinkel, D. E. (1996a). Spatial temporal theory of raman forward scattering. *Physics of Plasmas (1994-present)*, 3(4):1360–1372. Available from: http://scitation.aip.org/content/aip/journal/pop/3/4/10.1063/1.871728. 11

Decker, C. D., Mori, W. B., Tzeng, K., and Katsouleas, T. (1996b). The evolution of ultra?intense, short?pulse lasers in underdense plasmas. *Physics of Plasmas (1994-present)*, 3(5):2047–2056. Available from: http://scitation.aip.org/content/aip/journal/pop/3/5/10.1063/1.872001. 11

Esarey, E., Hubbard, R. F., Leemans, W. P., Ting, A., and Sprangle, P. (1997). Electron injection into plasma wakefields by colliding laser pulses. *Phys. Rev. Lett.*, 79:2682–2685. Available from: http://link.aps.org/doi/10.1103/PhysRevLett.79.2682. 1, 26

Esarey, E. and Pilloff, M. (1995). Trapping and acceleration in nonlinear plasma waves. *Physics of Plasmas (1994-present)*, 2(5):1432–1436. Available from: http://scitation.aip.org/content/aip/journal/pop/2/5/10.1063/1.871358. 16, 85

Esarey, E., Schroeder, C. B., Cormier-Michel, E., Shadwick, B. A., Geddes, C. G. R., and Leemans, W. P. (2007). Thermal effects in plasma-based acceleratorsa). *Physics of Plasmas (1994-present)*, 14(5):–. Available from: http://scitation.aip.org/content/aip/journal/pop/14/5/10.1063/1.2714022. 16

Esarey, E., Schroeder, C. B., and Leemans, W. P. (2009). Physics of laser-driven plasma-based electron accelerators. *Rev. Mod. Phys.*, 81:1229–1285. Available from: http://link.aps.org/doi/10.1103/RevModPhys.81.1229. 11, 25, 102

Esarey, E., Shadwick, B., Schroeder, C., and Leemans, W. (2004a). Nonlinear pump depletion and electron dephasing in laser wakefield accelerators. *Advanced Accelerator Concepts*, 737:578–584. 27

Esarey, E., Shadwick, B. A., Catravas, P., and Leemans, W. P. (2002). Synchrotron radiation from electron beams in plasma-focusing channels. *Phys. Rev. E*, 65:056505. Available from: http://link.aps.org/doi/10.1103/PhysRevE.65.056505. 20

Esarey, E., Shadwick, B. A., Schroeder, C. B., and Leemans, W. P. (2004b). Nonlinear pump depletion and electron dephasing in laser wakefield accelerators. *AIP Conference Proceedings*, 737(1):578–584. Available from: https://extras.springer.com/2004/978-0-7354-0220-1/cdr_pdfs/indexed/stage4_copyr/578_1.pdf. 27

Esarey, E., Sprangle, P., Krall, J., and Ting, A. (1996). Overview of plasma-based accelerator concepts. *IEEE Transactions on Plasma Science*, 24(2):252?288. Available from: `http://ieeexplore.ieee.org/xpl/articleDetails.jsp?arnumber=509991`. 11

Esirkepov, T., Bulanov, S. V., Yamagiwa, M., and Tajima, T. (2006). Electron, positron, and photon wakefield acceleration: Trapping, wake overtaking, and ponderomotive acceleration. *Phys. Rev. Lett.*, 96:014803. Available from: `http://link.aps.org/doi/10.1103/PhysRevLett.96.014803`. 16

Faure, J., Glinec, Y., Pukhov, A., Kiselev, S., Gordienko, S., Lefebvre, E., Rousseau, J.-P., Burgy, F., and Malka, V. (2004). A laser-plasma accelerator producing monoenergetic electron beams. *Nature*, 431(7008):541–544. Available from: `http://dx.doi.org/10.1038/nature02963`. 1, 22

Faure, J., Glinec, Y., Santos, J. J., Ewald, F., Rousseau, J.-P., Kiselev, S., Pukhov, A., Hosokai, T., and Malka, V. (2005). Observation of laser-pulse shortening in nonlinear plasma waves. *Phys. Rev. Lett.*, 95:205003. Available from: `http://link.aps.org/doi/10.1103/PhysRevLett.95.205003`. 12

Faure, J., Rechatin, C., Lundh, O., Ammoura, L., and Malka, V. (2010a). Injection and acceleration of quasimonoenergetic relativistic electron beams using density gradients at the edges of a plasma channel. *Physics of Plasmas (1994-present)*, 17(8):083107. Available from: `http://scitation.aip.org/content/aip/journal/pop/17/8/10.1063/1.3469581`. 1, 25

Faure, J., Rechatin, C., Lundh, O., Ammoura, L., and Malka, V. (2010b). Injection and acceleration of quasimonoenergetic relativistic electron beams using density gradients at the edges of a plasma channel. *Physics of Plasmas (1994-present)*, 17(8):083107. Available from: `http://scitation.aip.org/content/aip/journal/pop/17/8/10.1063/1.3469581`. 25

Faure, J., Rechatin, C., Norlin, A., Lifschitz, A., Glinec, Y., and Malka, V. (2006a). Controlled injection and acceleration of electrons in plasma wakefields by colliding laser pulses. *Nature (London)*, 444:737–739. Available from: `http://dx.doi.org/10.1038/nature05393`. 1

Faure, J., Rechatin, C., Norlin, A., Lifschitz, A., Glinec, Y., and Malka, V. (2006b). Controlled injection and acceleration of electrons in plasma wakefields by colliding laser pulses. *Nature*, 444(7120):737–739. 26

Fedosejevs, R., Wang, X. F., and Tsakiris, G. D. (1997). Onset of relativistic self-focusing in high density gas jet targets. *Phys. Rev. E*, 56:4615–4639. Available from: `http://link.aps.org/doi/10.1103/PhysRevE.56.4615`. 75

Floettmann, K. (2003). Some basic features of the beam emittance. *Phys. Rev. ST Accel. Beams*, 6:034202. Available from: `http://link.aps.org/doi/10.1103/PhysRevSTAB.6.034202`. 136

Fubiani, G., Esarey, E., Schroeder, C. B., and Leemans, W. P. (2004). Beat wave injection of electrons into plasma waves using two interfering laser pulses. *Phys. Rev. E*, 70:016402. Available from: `http://link.aps.org/doi/10.1103/PhysRevE.70.016402`. 26

Fuchs, M., Weingartner, R., Popp, A., Major, Z., Becker, S., Osterhoff, J., Cortrie, I., Zeitler, B., Horlein, R., Tsakiris, G. D., Schramm, U., Rowlands-Rees, T. P., Hooker, S. M., Habs, D., Krausz, F., Karsch, S., and Gruner, F. (2009). Laser-driven soft-x-ray undulator source. *Nat Phys*, 5(11):826–829. Available from: `http://dx.doi.org/10.1038/nphys1404`. 136

Geddes, C. G. R., Nakamura, K., Plateau, G. R., Toth, C., Cormier-Michel, E., Esarey, E., Schroeder, C. B., Cary, J. R., and Leemans, W. P. (2008). Plasma-density-gradient injection of low absolute-momentum-spread electron bunches. *Phys. Rev. Lett.*, 100:215004. Available from: http://link.aps.org/doi/10.1103/PhysRevLett.100.215004. 1, 25

Geddes, C. G. R., Toth, C., van Tilborg, J., Esarey, E., Schroeder, C. B., Bruhwiler, D., Nieter, C., Cary, J., and Leemans, W. P. (2004). High-quality electron beams from a laser wakefield accelerator using plasma-channel guiding. *Nature*, 431(7008):538–541. Available from: http://dx.doi.org/10.1038/nature02900. 1, 22

Gibbon, P. (2005). *Short pulse laser interactions with matter.* Imperial College Press. 9, 12

Glinec, Y., Faure, J., Guemnie-Tafo, A., Malka, V., Monard, H., Larbre, J. P., De Waele, V., Marignier, J. L., and Mostafavi, M. (2006a). Absolute calibration for a broad range single shot electron spectrometer. *Review of Scientific Instruments*, 77(10):–. Available from: http://scitation.aip.org/content/aip/journal/rsi/77/10/10.1063/1.2360988. 38

Glinec, Y., Faure, J., Le Dain, L., Darbon, S., Hosokai, T., Santos, J., Lefebvre, E., Rousseau, J., Burgy, F., Mercier, B., et al. (2005). High-resolution γ-ray radiography produced by a laser-plasma driven electron source. *Physical review letters*, 94(2):025003. 2, 155

Glinec, Y., Faure, J., Lifschitz, A., Vieira, J. M., Fonseca, R. A., Silva, L. O., and Malka, V. (2008). Direct observation of betatron oscillations in a laser-plasma electron accelerator. *EPL (Europhysics Letters)*, 81(6):64001. Available from: http://stacks.iop.org/0295-5075/81/i=6/a=64001. 120

Glinec, Y., Faure, J., Malka, V., Fuchs, T., Szymanowski, H., and Oelfke, U. (2006b). Radiotherapy with laser-plasma accelerators: Monte carlo simulation of dose deposited by an experimental quasimonoenergetic electron beam. *Medical physics*, 33(1):155–162. Available from: http://scitation.aip.org/content/aapm/journal/medphys/33/1/10.1118/1.2140115. 155

Goldstein, H. (1980). *Classical Mechanics.* Addison-Wesley Pub. Co. Available from: http://www.amazon.com/gp/product/0201029189. 28

Gonsalves, A. J., Nakamura, K., Lin, C., Panasenko, D., Shiraishi, S., Sokollik, T., Benedetti, C., Schroeder, C. B., Geddes, C. G. R., van Tilborg, J., Osterhoff, J., Esarey, E., Toth, C., and Leemans, W. P. (2011). Tunable laser plasma accelerator based on longitudinal density tailoring. *Nat. Phys.*, 7:862–866. Available from: http://dx.doi.org/10.1038/nphys2071. 25, 28

Gordon, D., Tzeng, K. C., Clayton, C. E., Dangor, A. E., Malka, V., Marsh, K. A., Modena, A., Mori, W. B., Muggli, P., Najmudin, Z., Neely, D., Danson, C., and Joshi, C. (1998). Observation of electron energies beyond the linear dephasing limit from a laser-excited relativistic plasma wave. *Phys. Rev. Lett.*, 80:2133–2136. Available from: http://link.aps.org/doi/10.1103/PhysRevLett.80.2133. 22

Gordon, D. F., Hafizi, B., Hubbard, R. F., Peñano, J. R., Sprangle, P., and Ting, A. (2003). Asymmetric self-phase modulation and compression of short laser pulses in plasma channels. *Phys. Rev. Lett.*, 90:215001. Available from: http://link.aps.org/doi/10.1103/PhysRevLett.90.215001. 12

Govil, R., Leemans, W. P., Backhaus, E. Y., and Wurtele, J. S. (1999). Observation of return current effects in a passive plasma lens. *Phys. Rev. Lett.*, 83:3202–3205. Available from: http://link.aps.org/doi/10.1103/PhysRevLett.83.3202. 136

Guillaume, E., Döpp, A., Thaury, C., Lifschitz, A., Goddet, J., Tafzi, A., Sylla, F., Iaquanello, G., Lefrou, T., Rousseau, P., et al. (2015a). Physics of fully-loaded laser-plasma accelerators. *Physical Review Special Topics-Accelerators and Beams*, 18(6):061301. Available from: http://journals.aps.org/prstab/abstract/10.1103/PhysRevSTAB.18.061301. 26, 75

Guillaume, E., Döpp, A., Thaury, C., Ta Phuoc, K., Lifschitz, A., Grittani, G., Goddet, J.-P., Tafzi, A., Chou, S. W., Veisz, L., and Malka, V. (2015b). Electron rephasing in a laser-wakefield accelerator. *Phys. Rev. Lett.*, 115:155002. Available from: http://link.aps.org/doi/10.1103/PhysRevLett.115.155002. 116

Hafizi, B., Ting, A., Sprangle, P., and Hubbard, R. F. (2000). Relativistic focusing and ponderomotive channeling of intense laser beams. *Phys. Rev. E*, 62:4120–4125. Available from: http://link.aps.org/doi/10.1103/PhysRevE.62.4120. 11

Hairapetian, G., Davis, P., Clayton, C. E., Joshi, C., Hartman, S. C., Pellegrini, C., and Katsouleas, T. (1994). Experimental demonstration of dynamic focusing of a relativistic electron bunch by an overdense plasma lens. *Phys. Rev. Lett.*, 72:2403–2406. Available from: http://link.aps.org/doi/10.1103/PhysRevLett.72.2403. 136

Hur, M. S. and Suk, H. (2011). Numerical study of 1.1 gev electron acceleration over a-few-millimeter-long plasma with a tapered density. *Physics of Plasmas (1994-present)*, 18(3):–. Available from: http://scitation.aip.org/content/aip/journal/pop/18/3/10.1063/1.3561781. 101

Jackson, J. D. (1998). *Classical Electrodynamics Third Edition*. Wiley, third edition. Available from: http://www.amazon.com/exec/obidos/redirect?tag=citeulike07-20&path=ASIN/047130932X. 119

Kalal, M. and Nugent, K. (1988). Abel inversion using fast fourier transforms. *Applied optics*, 27(10):1956–1959. 39

Kalmykov, S., Yi, S. A., Khudik, V., and Shvets, G. (2009a). Electron self-injection and trapping into an evolving plasma bubble. *Phys. Rev. Lett.*, 103:135004. Available from: http://journals.aps.org/prl/abstract/10.1103/PhysRevLett.103.135004. 19

Kalmykov, S., Yi, S. A., Khudik, V., and Shvets, G. (2009b). Electron self-injection and trapping into an evolving plasma bubble. *Phys. Rev. Lett.*, 103:135004. 23

Karsch, S., Osterhoff, J., Popp, A., Rowlands-Rees, T. P., Major, Z., Fuchs, M., Marx, B., Horlein, R., Schmid, K., Veisz, L., Becker, S., Schramm, U., Hidding, B., Pretzler, G., Habs, D., Gruner, F., Krausz, F., and Hooker, S. M. (2007a). Gev-scale electron acceleration in a gas-filled capillary discharge waveguide. *New Journal of Physics*, 9(11):415. Available from: http://stacks.iop.org/1367-2630/9/i=11/a=415. 12

Karsch, S., Osterhoff, J., Popp, A., Rowlands-Rees, T. P., Major, Z., Fuchs, M., Marx, B., Hörlein, R., Schmid, K., Veisz, L., Becker, S., Schramm, U., Hidding, B., Pretzler, G., Habs, D., Grüner, F., Krausz, F., and Hooker, S. M. (2007b). Gev-scale electron acceleration in a gas-filled capillary discharge waveguide. *New Journal of Physics*, 9(11):415. Available from: http://stacks.iop.org/1367-2630/9/i=11/a=415. 27

Katsouleas, T. (1986). Physical mechanisms in the plasma wake-field accelerator. *Phys. Rev. A*, 33:2056–2064. Available from: http://link.aps.org/doi/10.1103/PhysRevA.33.2056. 100

Katsouleas, T. and Mori, W. B. (1988). Wave-breaking amplitude of relativistic oscillations in a thermal plasma. *Phys. Rev. Lett.*, 61:90–93. Available from: http://link.aps.org/doi/10.1103/PhysRevLett.61.90. 22

Keldysh, L. (1965). Ionization in the field of a strong electromagnetic wave. *JETP*, 20:1307. Available from: http://www.jetp.ac.ru/cgi-bin/dn/e_020_05_1307.pdf. 8

Khachatryan, A. G. (2002). Trapping, compression, and acceleration of an electron bunch in the nonlinear laser wakefield. *Phys. Rev. E*, 65:046504. Available from: http://link.aps.org/doi/10.1103/PhysRevE.65.046504. 22

Kim, H. T., Pae, K. H., Cha, H. J., Kim, I. J., Yu, T. J., Sung, J. H., Lee, S. K., Jeong, T. M., and Lee, J. (2013a). Enhancement of electron energy to the multi-gev regime by a dual-stage laser-wakefield accelerator pumped by petawatt laser pulses. *Phys. Rev. Lett.*, 111:165002. Available from: http://link.aps.org/doi/10.1103/PhysRevLett.111.165002. 1, 67

Kim, J. U., Hafz, N., and Suk, H. (2004a). Electron trapping and acceleration across a parabolic plasma density profile. *Phys. Rev. E*, 69:026409. Available from: http://link.aps.org/doi/10.1103/PhysRevE.69.026409. 25

Kim, J. U., Hafz, N., and Suk, H. (2004b). Electron trapping and acceleration across a parabolic plasma density profile. *Phys. Rev. E*, 69:026409. Available from: http://link.aps.org/doi/10.1103/PhysRevE.69.026409. 101

Kim, M. S., Jang, D. G., Lee, T. H., Nam, I. H., Lee, I. W., and Suk, H. (2013b). Characteristics of a tapered capillary plasma waveguide for laser wakefield acceleration. *Applied Physics Letters*, 102(20):–. Available from: http://scitation.aip.org/content/aip/journal/apl/102/20/10.1063/1.4807440. 101

Kostyukov, I., Nerush, E., Pukhov, A., and Seredov, V. (2010a). A multidimensional theory for electron trapping by a plasma wake generated in the bubble regime. *New Journal of Physics*, 12(4):045009. Available from: http://iopscience.iop.org/article/10.1088/1367-2630/12/4/045009/meta;jsessionid=5703DECA3A95433E2BE41B54F219EB45.c1. 19, 23

Kostyukov, I., Nerush, E., Pukhov, A., and Seredov, V. (2010b). A multidimensional theory for electron trapping by a plasma wake generated in the bubble regime. *New Jour. Phys.*, 12:045009. 23

Kotaki, H., Hayashi, Y., Kawase, K., Mori, M., Kando, M., Homma, T., Koga, J. K., Daido, H., and Bulanov, S. V. (2011). Manipulation and electron-oscillation-measurement of laser accelerated electron beams. *Plasma Physics and Controlled Fusion*, 53(1):014009. Available from: http://stacks.iop.org/0741-3335/53/i=1/a=014009. 26, 75

Kotaki, H., Masuda, S., Kando, M., Koga, J. K., and Nakajima, K. (2004). Head-on injection of a high quality electron beam by the interaction of two laser pulses. *Physics of Plasmas (1994-present)*, 11(6):3296–3302. Available from: http://scitation.aip.org/content/aip/journal/pop/11/6/10.1063/1.1751171. 26

Kruer, W. (2003). *The Physics of Laser Plasma Interactions*. Frontiers in physics. Westview Press. Available from: http://books.google.fr/books?id=uAF_HWb8FAQC. 12

Leemans, W., Gonsalves, A., Mao, H.-S., Nakamura, K., Benedetti, C., Schroeder, C., Tóth, C., Daniels, J., Mittelberger, D., Bulanov, S., Vay, J.-L., Geddes, C., and Esarey, E. (2014). Multi-gev electron beams from capillary-discharge-guided subpetawatt laser pulses in the self-trapping regime. *Phys. Rev. Lett.*, 113:245002. Available from: http://link.aps.org/doi/10.1103/PhysRevLett.113.245002. 1, 12, 27, 28

Leemans, W. P., Nagler, B., Gonsalves, A. J., Toth, C., Nakamura, K., Geddes, C. G. R., Esarey, E., Schroeder, C. B., and Hooker, S. M. (2006). Gev electron beams from a centimetre-scale accelerator. *Nat. Phys.*, 2:696. Available from: http://dx.doi.org/10.1038/nphys418. 1, 12, 27

Lehe, R. (2014). *Improvement of laser-wakefield accelerators: towards a compact free electron laser*. Theses, Ecole Polytechnique. Available from: https://pastel.archives-ouvertes.fr/tel-01088398. 137, 139, 143, 151

Lehe, R., Lifschitz, A., Davoine, X., Thaury, C., and Malka, V. (2013). Optical transverse injection in laser-plasma acceleration. *Phys. Rev. Lett.*, 111(8):085005. Available from: http://journals.aps.org/prl/abstract/10.1103/PhysRevLett.111.085005. 1, 26

Lehe, R., Thaury, C., Guillaume, E., Lifschitz, A., and Malka, V. (2014a). Laser-plasma lens for laser-wakefield accelerators. *Phys. Rev. ST Accel. Beams*, 17:121301. Available from: http://link.aps.org/doi/10.1103/PhysRevSTAB.17.121301. 137, 139, 143

Lehe, R., Thaury, C., Lifschitz, A., Rax, J.-M., and Malka, V. (2014b). Transverse dynamics of an intense electron bunch traveling through a pre-ionized plasma. *Physics of Plasmas (1994-present)*, 21(4):043104. Available from: http://scitation.aip.org/content/aip/journal/pop/21/4/10.1063/1.4870336. 136

Lifschitz, A. F., Davoine, X., Lefebvre, E., Faure, J., Rechatin, C., and Malka, V. (2009). Particle-in-Cell modelling of laser-plasma interaction using Fourier decomposition. *J. Comput. Phys.*, 228:1803. Available from: http://www.sciencedirect.com/science/article/pii/S0021999108005950. 40, 77, 94, 108

Lifschitz, A. F., Faure, J., Malka, V., and Mora, P. (2005). Gev wakefield acceleration of low energy electron bunches using petawatt lasers. *Physics of Plasmas (1994-present)*, 12(9):–. Available from: http://scitation.aip.org/content/aip/journal/pop/12/9/10.1063/1.2010347. 22

Litos, M., Adli, E., An, W., Clarke, C. I., Clayton, C. E., Corde, S., Delahaye, J. P., England, R. J., Fisher, A. S., Frederico, J., Gessner, S., Green, S. Z., Hogan, M. J., Joshi, C., Lu, W., Marsh, K. A., Mori, W. B., Muggli, P., Vafaei-Najafabadi, N., Walz, D., White, G., Wu, Z., Yakimenko, V., and Yocky, G. (2014). High-efficiency acceleration of an electron beam in a plasma wakefield accelerator. *Nature*, 515(7525):92–95. Available from: http://dx.doi.org/10.1038/nature13882. 88

Lu, W., Huang, C., Zhou, M., Mori, W. B., and Katsouleas, T. (2006). Nonlinear theory for relativistic plasma wakefields in the blowout regime. *Phys. Rev. Lett.*, 96:165002. Available from: http://link.aps.org/doi/10.1103/PhysRevLett.96.165002. 18

Lu, W., Tzoufras, M., Joshi, C., Tsung, F. S., Mori, W. B., Vieira, J., Fonseca, R. A., and Silva, L. O. (2007). Generating multi-gev electron bunches using single stage laser wakefield acceleration in a 3d nonlinear regime. *Phys. Rev. ST Accel. Beams*, 10:061301. Available from: http://link.aps.org/doi/10.1103/PhysRevSTAB.10.061301. 18, 19, 23, 83, 118, 123, 159

Lundh, O., Lim, J., Rechatin, C., Ammoura, L., Ben-Ismail, A., Davoine, X., Gallot, G., Goddet, J.-P., Lefebvre, E., Malka, V., and Faure, J. (2011). Few femtosecond, few kiloampere electron bunch produced by a laser-plasma accelerator. *Nat Phys*, 7(3):219–222. Available from: http://www.nature.com/nphys/journal/v7/n3/abs/nphys1872.html. 31

Lundh, O., Rechatin, C., Faure, J., Ben-Ismael, A., Lim, J., De Wagter, C., De Neve, W., and Malka, V. (2012). Comparison of measured with calculated dose distribution from a 120-mev electron beam from a laser-plasma accelerator. *Medical Physics*, 39(6):3501–3508. Available from: http://scitation.aip.org/content/aapm/journal/medphys/39/6/10.1118/1.4719962. 2, 155

Lundh, O., Rechatin, C., Lim, J., Malka, V., and Faure, J. (2013). Experimental measurements of electron-bunch trains in a laser-plasma accelerator. *Phys. Rev. Lett.*, 110:065005. Available from: http://link.aps.org/doi/10.1103/PhysRevLett.110.065005. 31

Maier, A. R., Meseck, A., Reiche, S., Schroeder, C. B., Seggebrock, T., and Grüner, F. (2012). Demonstration scheme for a laser-plasma-driven free-electron laser. *Phys. Rev. X*, 2:031019. Available from: http://link.aps.org/doi/10.1103/PhysRevX.2.031019. 2, 157

Mainfray, G. and Manus, G. (1991). Multiphoton ionization of atoms. *Reports on Progress in Physics*, 54(10):1333. Available from: http://stacks.iop.org/0034-4885/54/i=10/a=002. 8

Malka, V., Faure, J., and Gauduel, Y. A. (2010). Ultra-short electron beams based spatio-temporal radiation biology and radiotherapy. *Mutation Research/Reviews in Mutation Research*, 704(1?3):142 – 151. Available from: http://www.sciencedirect.com/science/article/pii/S1383574210000104. 2, 75

Malka, V., Fritzler, S., Lefebvre, E., Aleonard, M.-M., Burgy, F., Chambaret, J.-P., Chemin, J.-F., Krushelnick, K., Malka, G., Mangles, S. P. D., Najmudin, Z., Pittman, M., Rousseau, J.-P., Scheurer, J.-N., Walton, B., and Dangor, A. E. (2002). Electron acceleration by a wake field forced by an intense ultrashort laser pulse. *Science*, 298(5598):1596–1600. Available from: http://www.sciencemag.org/content/298/5598/1596.abstract. 12, 22, 107

Mangles, S. P. D., Genoud, G., Kneip, S., Burza, M., Cassou, K., Cros, B., Dover, N. P., Kamperidis, C., Najmudin, Z., Persson, A., Schreiber, J., Wojda, F., and Wahlström, C.-G. (2009). Controlling the spectrum of x-rays generated in a laser-plasma accelerator by tailoring the laser wavefront. *Applied Physics Letters*, 95(18):181106. Available from: http://scitation.aip.org/content/aip/journal/apl/95/18/10.1063/1.3258022. 120

Mangles, S. P. D., Murphy, C. D., Najmudin, Z., Thomas, A. G. R., Collier, J. L., Dangor, A. E., Divall, E. J., Foster, P. S., Gallacher, J. G., Hooker, C. J., Jaroszynski, D. A., Langley, A. J., Mori, W. B., Norreys, P. A., Tsung, F. S., Viskup, R., Walton, B. R., and Krushelnick, K. (2004). Monoenergetic beams of relativistic electrons from intense laser-plasma interactions. *Nature*, 431(7008):535–538. Available from: http://dx.doi.org/10.1038/nature02939. 1, 22

McGuffey, C., Thomas, A. G. R., Schumaker, W., Matsuoka, T., Chvykov, V., Dollar, F. J., Kalintchenko, G., Yanovsky, V., Maksimchuk, A., Krushelnick, K., Bychenkov, V. Y., Glazyrin, I. V., and Karpeev, A. V. (2010). Ionization induced trapping in a laser wakefield accelerator. *Phys. Rev. Lett.*, 104:025004. Available from: http://link.aps.org/doi/10.1103/PhysRevLett.104.025004. 1, 26, 74

Mehrling, T., Grebenyuk, J., Tsung, F. S., Floettmann, K., and Osterhoff, J. (2012). Transverse emittance growth in staged laser-wakefield acceleration. *Phys. Rev. ST Accel. Beams*, 15:111303. Available from: http://link.aps.org/doi/10.1103/PhysRevSTAB.15.111303. 156

Migliorati, M., Bacci, A., Benedetti, C., Chiadroni, E., Ferrario, M., Mostacci, A., Palumbo, L., Rossi, A. R., Serafini, L., and Antici, P. (2013). Intrinsic normalized emittance growth in laser-driven electron accelerators. *Phys. Rev. ST Accel. Beams*, 16:011302. Available from: http://link.aps.org/doi/10.1103/PhysRevSTAB.16.011302. 136

Mo, M. Z., Ali, A., Fourmaux, S., Lassonde, P., Kieffer, J. C., and Fedosejevs, R. (2012). Quasimonoenergetic electron beams from laser wakefield acceleration in pure nitrogen. *Applied Physics Letters*, 100(7):074101. Available from: http://adsabs.harvard.edu/abs/2012ApPhL.100g4101M. 26, 75

Modena, A., Najmudin, Z., Dangor, A. E., Clayton, C. E., Marsh, K. A., Joshi, C., Malka, V., Darrow, C. B., Danson, C., Neely, D., and Walsh, F. N. (1995). Electron acceleration from the breaking of relativistic plasma waves. *Nature*, 377(6550):606–608. Available from: http://dx.doi.org/10.1038/377606a0. 22

Mora, P. and Antonsen, T. M. (1997). Kinetic modeling of intense, short laser pulses propagating in tenuous plasmas. *Physics of Plasmas*, 4(1):217–229. Available from: http://scitation.aip.org/content/aip/journal/pop/4/1/10.1063/1.872134. 8, 72

Mori, M., Kondo, K., Mizuta, Y., Kando, M., Kotaki, H., Nishiuchi, M., Kado, M., Pirozhkov, A. S., Ogura, K., Sugiyama, H., Bulanov, S. V., Tanaka, K. A., Nishimura, H., and Daido, H. (2009). Generation of stable and low-divergence 10-mev quasimonoenergetic electron bunch using argon gas jet. *Phys. Rev. ST Accel. Beams*, 12:082801. Available from: http://link.aps.org/doi/10.1103/PhysRevSTAB.12.082801. 26, 75

Nakajima, K. (2008). Compact x-ray sources: Towards a table-top free-electron laser. *Nat. Phys.*, 4:92 – 93. 28, 68, 136

Nakajima, K., Fisher, D., Kawakubo, T., Nakanishi, H., Ogata, A., Kato, Y., Kitagawa, Y., Kodama, R., Mima, K., Shiraga, H., Suzuki, K., Yamakawa, K., Zhang, T., Sakawa, Y., Shoji, T., Nishida, Y., Yugami, N., Downer, M., and Tajima, T. (1995). Observation of ultrahigh gradient electron acceleration by a self-modulated intense short laser pulse. *Phys. Rev. Lett.*, 74:4428–4431. Available from: http://link.aps.org/doi/10.1103/PhysRevLett.74.4428. 22

Nakanishi, H., Yoshida, Y., Ueda, T., Kozawa, T., Shibata, H., Nakajima, K., Kurihara, T., Yugami, N., Nishida, Y., Kobayashi, T., Enomoto, A., Oogoe, T., Kobayashi, H., Newberger, B. S., Tagawa, S., Miya, K., and Ogata, A. (1991). Direct observation of plasma-lens effect. *Phys. Rev. Lett.*, 66:1870–1873. Available from: http://link.aps.org/doi/10.1103/PhysRevLett.66.1870. 136

Ng, J. S. T., Chen, P., Baldis, H., Bolton, P., Cline, D., Craddock, W., Crawford, C., Decker, F. J., Field, C., Fukui, Y., Kumar, V., Iverson, R., King, F., Kirby, R. E., Nakajima, K., Noble, R., Ogata, A., Raimondi, P., Walz, D., and Weidemann, A. W. (2001). Observation of plasma focusing of a 28.5 gev positron beam. *Phys. Rev. Lett.*, 87:244801. Available from: http://link.aps.org/doi/10.1103/PhysRevLett.87.244801. 136

Nguyen, T. and Debled-Rennesson, I. (2007). Curvature estimation in noisy curves. In Kropatsch, W., Kampel, M., and Hanbury, A., editors, *Computer Analysis of Images and Patterns*, volume 4673 of *Lecture Notes in Computer Science*, pages 474–481. Springer Berlin Heidelberg. Available from: http://link.springer.com/chapter/10.1007/978-3-540-74272-2_59. 129

Osterhoff, J. (2009). *Stable, ultra-relativistic electron beams by laser-wakefield acceleration*. PhD thesis, lmu. 13

Pae, K. H., Choi, I. W., and Lee, J. (2010). Self-mode-transition from laser wakefield accelerator to plasma wakefield accelerator of laser-driven plasma-based electron acceleration. *Physics of Plasmas*, 17(12):–. Available from: http://scitation.aip.org/content/aip/journal/pop/17/12/10.1063/1.3522757. 88

Pak, A., Marsh, K. A., Martins, S. F., Lu, W., Mori, W. B., and Joshi, C. (2010). Injection and trapping of tunnel-ionized electrons into laser-produced wakes. *Phys. Rev. Lett.*, 104:025003. Available from: http://link.aps.org/doi/10.1103/PhysRevLett.104.025003. 1, 26, 75, 83, 92

Phuoc, K. T., Corde, S., Shah, R., Albert, F., Fitour, R., Rousseau, J.-P., Burgy, F., Mercier, B., and Rousse, A. (2006). Imaging electron trajectories in a laser-wakefield cavity using betatron x-ray radiation. *Physical review letters*, 97(22):225002. Available from: http://journals.aps.org/prl/abstract/10.1103/PhysRevLett.97.225002. 120, 129

Plateau, G. R., Geddes, C. G. R., Thorn, D. B., Chen, M., Benedetti, C., Esarey, E., Gonsalves, A. J., Matlis, N. H., Nakamura, K., Schroeder, C. B., Shiraishi, S., Sokollik, T., van Tilborg, J., Toth, C., Trotsenko, S., Kim, T. S., Battaglia, M., Stöhlker, T., and Leemans, W. P. (2012). Low-emittance electron bunches from a laser-plasma accelerator measured using single-shot x-ray spectroscopy. *Phys. Rev. Lett.*, 109:064802. Available from: http://link.aps.org/doi/10.1103/PhysRevLett.109.064802. 28, 133

Pollock, B. B., Clayton, C. E., Ralph, J. E., Albert, F., Davidson, A., Divol, L., Filip, C., Glenzer, S. H., Herpoldt, K., Lu, W., Marsh, K. A., Meinecke, J., Mori, W. B., Pak, A., Rensink, T. C., Ross, J. S., Shaw, J., Tynan, G. R., Joshi, C., and Froula, D. H. (2011a). Demonstration of a narrow energy spread, 0.5 gev electron beam from a two-stage laser wakefield accelerator. *Phys. Rev. Lett.*, 107:045001. Available from: http://link.aps.org/doi/10.1103/PhysRevLett.107.045001. 1, 26, 75

Pollock, B. B., Clayton, C. E., Ralph, J. E., Albert, F., Davidson, A., Divol, L., Filip, C., Glenzer, S. H., Herpoldt, K., Lu, W., Marsh, K. A., Meinecke, J., Mori, W. B., Pak, A., Rensink, T. C., Ross, J. S., Shaw, J., Tynan, G. R., Joshi, C., and Froula, D. H. (2011b). Demonstration of a narrow energy spread, $\sim$ 0.5 gev electron beam from a two-stage laser wakefield accelerator. *Phys. Rev. Lett.*, 107:045001. Available from: http://link.aps.org/doi/10.1103/PhysRevLett.107.045001. 28

Popp, A., Vieira, J., Osterhoff, J., Major, Z., Hörlein, R., Fuchs, M., Weingartner, R., Rowlands-Rees, T. P., Marti, M., Fonseca, R. A., Martins, S. F., Silva, L. O., Hooker, S. M., Krausz, F., Grüner, F., and Karsch, S. (2010). All-optical steering of laser-wakefield-accelerated electron beams. *Phys. Rev. Lett.*, 105:215001. Available from: http://link.aps.org/doi/10.1103/PhysRevLett.105.215001. 120

Pukhov, A. and Kostyukov, I. (2008). Control of laser-wakefield acceleration by the plasma-density profile. *Phys. Rev. E*, 77:025401. Available from: http://link.aps.org/doi/10.1103/PhysRevE.77.025401. 101

Pukhov, A. and Meyer-ter Vehn, J. (2002). Laser wake field acceleration: the highly non-linear broken-wave regime. *Applied Physics B*, 74(4-5):355–361. Available from: http://dx.doi.org/10.1007/s003400200795. 18

Rae, S. C. (1993). Ionization-induced defocusing of intense laser pulses in high-pressure gases. *Optics Communications*, 97:25–28. Available from: http://www.sciencedirect.com/science/article/pii/0030401893906118. 131

Rechatin, C., Faure, J., Ben-Ismail, A., Lim, J., Fitour, R., Specka, A., Videau, H., Tafzi, A., Burgy, F., and Malka, V. (2009). Controlling the phase-space volume of injected electrons in a laser-plasma accelerator. *Phys. Rev. Lett.*, 102(16):164801. 26

Ren, C., Duda, B. J., Hemker, R. G., Mori, W. B., Katsouleas, T., Antonsen, T. M., and Mora, P. (2001). Compressing and focusing a short laser pulse by a thin plasma lens. *Phys. Rev. E*, 63:026411. Available from: http://link.aps.org/doi/10.1103/PhysRevE.63.026411. 12

Rigaud, O., Fortunel, N. O., Vaigot, P., Cadio, E., Martin, M. T., Lundh, O., Faure, J., Rechatin, C., Malka, V., and Gauduel, Y. A. (2010). Exploring ultrashort high-energy electron-induced damage in human carcinoma cells. *Cell Death and Disease*, 1:e73. Available from: http://www.ncbi.nlm.nih.gov/pmc/articles/PMC3032345/. 75

Rittershofer, W., Schroeder, C. B., Esarey, E., Grüner, F. J., and Leemans, W. P. (2010). Tapered plasma channels to phase-lock accelerating and focusing forces in laser-plasma accelerators. *Physics of Plasmas (1994-present)*, 17(6):063104. Available from: http://scitation.aip.org/content/aip/journal/pop/17/6/10.1063/1.3430638. 101

Rosenzweig, J. B., Breizman, B., Katsouleas, T., and Su, J. J. (1991). Acceleration and focusing of electrons in two-dimensional nonlinear plasma wake fields. *Phys. Rev. A*, 44:R6189–R6192. Available from: http://link.aps.org/doi/10.1103/PhysRevA.44.R6189. 136

Rousse, A., Ta Phuoc, K., Shah, R., Pukhov, A., Lefebvre, E., Malka, V., Kiselev, S., Burgy, F., Rousseau, J. P., Umstadter, D., and Hulin, D. (2004). Production of a kev x-ray beam from synchrotron radiation in relativistic laser-plasma interaction. *Phys. Rev. Lett.*, 93(13):135005. Available from: http://journals.aps.org/prl/abstract/10.1103/PhysRevLett.93.135005. 123

Rowlands-Rees, T. P., Kamperidis, C., Kneip, S., Gonsalves, A. J., Mangles, S. P. D., Gallacher, J. G., Brunetti, E., Ibbotson, T., Murphy, C. D., Foster, P. S., Streeter, M. J. V., Budde, F., Norreys, P. A., Jaroszynski, D. A., Krushelnick, K., Najmudin, Z., and Hooker, S. M. (2008). Laser-driven acceleration of electrons in a partially ionized plasma channel. *Phys. Rev. Lett.*, 100:105005. Available from: http://link.aps.org/doi/10.1103/PhysRevLett.100.105005. 12

Schlenvoigt, H.-P., Haupt, K., Debus, A., Budde, F., Jackel, O., Pfotenhauer, S., Schwoerer, H., Rohwer, E., Gallacher, J. G., Brunetti, E., Shanks, R. P., Wiggins, S. M., and Jaroszynski, D. A. (2008). A compact synchrotron radiation source driven by a laser-plasma wakefield accelerator. *Nat Phys*, 4:130–133. Available from: http://www.nature.com/nphys/journal/v4/n2/abs/nphys811.html. 28, 98

Schmid, K., Buck, A., Sears, C. M. S., Mikhailova, J. M., Tautz, R., Herrmann, D., Geissler, M., Krausz, F., and Veisz, L. (2010). Density-transition based electron injector for laser driven wakefield accelerators. *Phys. Rev. ST Accel. Beams*, 13:091301. Available from: http://link.aps.org/doi/10.1103/PhysRevSTAB.13.091301. 1, 25, 42, 53, 54

Schreiber, J., Bellei, C., Mangles, S. P. D., Kamperidis, C., Kneip, S., Nagel, S. R., Palmer, C. A. J., Rajeev, P. P., Streeter, M. J. V., and Najmudin, Z. (2010). Complete temporal characterization of asymmetric pulse compression in a laser wakefield. *Phys. Rev. Lett.*, 105:235003. Available from: http://link.aps.org/doi/10.1103/PhysRevLett.105.235003. 12

Schroeder, C. B., Esarey, E., Geddes, C. G. R., Benedetti, C., and Leemans, W. P. (2010). Physics considerations for laser-plasma linear colliders. *Phys. Rev. ST Accel. Beams*, 13:101301. Available from: http://link.aps.org/doi/10.1103/PhysRevSTAB.13.101301. 28, 67, 136, 156

Schroeder, C. B., Esarey, E., and Shadwick, B. A. (2005). Warm wave breaking of nonlinear plasma waves with arbitrary phase velocities. *Phys. Rev. E*, 72:055401. Available from: http://link.aps.org/doi/10.1103/PhysRevE.72.055401. 16

Shadwick, B. A., Schroeder, C. B., and Esarey, E. (2009). Nonlinear laser energy depletion in laser-plasma acceleratorsa). *Physics of Plasmas (1994-present)*, 16(5):–. Available from: http://scitation.aip.org/content/aip/journal/pop/16/5/10.1063/1.3124185. 27

Sheng, Z.-M., Mima, K., Sentoku, Y., Jovanović, M. S., Taguchi, T., Zhang, J., and Meyer-ter Vehn, J. (2002). Stochastic heating and acceleration of electrons in colliding laser fields in plasma. *Phys. Rev. Lett.*, 88:055004. Available from: http://link.aps.org/doi/10.1103/PhysRevLett.88.055004. 131

Singh, K. P. and Sajal, V. (2009). Quasimonoenergic collimated electrons from the ionization of nitrogen by a chirped intense laser pulse. *Physics of Plasmas (1994-present)*, 16(4):–. Available from: http://scitation.aip.org/content/aip/journal/pop/16/4/10.1063/1.3116646. 26

Sprangle, P., Esarey, E., and Ting, A. (1990). Nonlinear theory of intense laser-plasma interactions. *Phys. Rev. Lett.*, 64:2011–2014. Available from: http://link.aps.org/doi/10.1103/PhysRevLett.64.2011. 11

Sprangle, P., Hafizi, B., Peñano, J., Hubbard, R., Ting, A., Moore, C., Gordon, D., Zigler, A., Kaganovich, D., and Antonsen, T. (2001). Wakefield generation and gev acceleration in tapered plasma channels. *Phys. Rev. E*, 63:056405. Available from: http://link.aps.org/doi/10.1103/PhysRevE.63.056405. 100

Sprangle, P., Peñano, J. R., Hafizi, B., Hubbard, R. F., Ting, A., Gordon, D. F., Zigler, A., and Antonsen, T. M. (2002). Gev acceleration in tapered plasma channels. *Physics of Plasmas (1994-present)*, 9(5):2364–2370. Available from: http://scitation.aip.org/content/aip/journal/pop/9/5/10.1063/1.1446039. 101

Strickland, D. and Mourou, G. (1985). Compression of amplified chirped optical pulses. *Optics Communications*, 55(6):447 – 449. Available from: http://www.sciencedirect.com/science/article/pii/0030401885901518. 32

Su, J. J., Katsouleas, T., Dawson, J. M., and Fedele, R. (1990). Plasma lenses for focusing particle beams. *Phys. Rev. A*, 41:3321–3331. Available from: http://link.aps.org/doi/10.1103/PhysRevA.41.3321. 136

Suk, H., Barov, N., Rosenzweig, J. B., and Esarey, E. (2001). Plasma electron trapping and acceleration in a plasma wake field using a density transition. *Phys. Rev. Lett.*, 86:1011–1014. Available from: http://link.aps.org/doi/10.1103/PhysRevLett.86.1011. 25

Suk, H., Kim, C., Kim, G., Kim, J., Ko, I., and Lee, H. (2003). Energy enhancement in the self-injected laser wakefield acceleration using tapered plasma densities. *Physics Letters A*, 316(3–4):233 – 237. Available from: http://www.sciencedirect.com/science/article/pii/S0375960103011344. 101

Sun, G., Ott, E., Lee, Y. C., and Guzdar, P. (1987). Self?focusing of short intense pulses in plasmas. *Physics of Fluids (1958-1988)*, 30(2):526–532. Available from: http://scitation.aip.org/content/aip/journal/pof1/30/2/10.1063/1.866349. 11

Tajima, T. and Dawson, J. M. (1979). Laser electron accelerator. *Phys. Rev. Lett.*, 43:267–270. Available from: http://link.aps.org/doi/10.1103/PhysRevLett.43.267. 1

Teychenné, D., Bonnaud, G., and Bobin, J.-L. (1993). Wave-breaking limit to the wake-field effect in an underdense plasma. *Phys. Rev. E*, 48:R3248–R3251. Available from: http://link.aps.org/doi/10.1103/PhysRevE.48.R3248. 16

Teychenné, D., Bonnaud, G., and Bobin, J.-L. (1994). Oscillatory relativistic motion of a particle in a power-law or sinusoidal-shaped potential well. *Physical Review E*, 49(4):3253. 16

Thaury, C., Guillaume, E., Corde, S., Lehe, R., Le Bouteiller, M., Ta Phuoc, K., Davoine, X., Rax, J. M., Rousse, A., and Malka, V. (2013). Angular-momentum evolution in laser-plasma accelerators. *Phys. Rev. Lett.*, 111:135002. Available from: http://link.aps.org/doi/10.1103/PhysRevLett.111.135002. 125

Thaury, C., Guillaume, E., Döpp, A., Lehe, R., Lifschitz, A., Phuoc, K. T., Gautier, J., Goddet, J.-P., Tafzi, A., Flacco, A., Tissandier, F., Sebban, S., Rousse, A., and Malka, V. (2015a). Demonstration of relativistic electron beam focusing by a laser-plasma lens. *Nature communications*, 6. 151

Thaury, C., Guillaume, E., Lifschitz, A., Ta Phuoc, K., Hansson, M., Grittani, G., Gautier, J., Goddet, J. P., Tafzi, A., Lundh, O., and Malka, V. (2015b). Shock assisted ionization injection in laser-plasma accelerators. *Scientific Reports*, 5:16310 EP –. Available from: http://dx.doi.org/10.1038/srep16310. 97

Thomas, A., Mangles, S., Najmudin, Z., Kaluza, M., Murphy, C., and Krushelnick, K. (2007). Measurements of wave-breaking radiation from a laser-wakefield accelerator. *Physical review letters*, 98(5):054802. Available from: http://journals.aps.org/prl/abstract/10.1103/PhysRevLett.98.054802. 60

BIBLIOGRAPHY

Thompson, M. C., Badakov, H., Rosenzweig, J. B., Travish, G., Barov, N., Piot, P., Fliller, R., Kazakevich, G. M., Santucci, J., Li, J., and Tikhoplav, R. (2010). Observations of low-aberration plasma lens focusing of relativistic electron beams at the underdense threshold. *Physics of Plasmas (1994-present)*, 17(7):073105. Available from: `http://scitation.aip.org/content/aip/journal/pop/17/7/10.1063/1.3457924`. 136

Ting, A., Esarey, E., and Sprangle, P. (1990). Nonlinear wake?field generation and relativistic focusing of intense laser pulses in plasmas. *Physics of Fluids B: Plasma Physics (1989-1993)*, 2(6):1390–1394. Available from: `http://scitation.aip.org/content/aip/journal/pofb/2/6/10.1063/1.859561`. 11

Umstadter, D., Kim, J. K., and Dodd, E. (1996). Laser injection of ultrashort electron pulses into wakefield plasma waves. *Phys. Rev. Lett.*, 76:2073–2076. Available from: `http://link.aps.org/doi/10.1103/PhysRevLett.76.2073`. 1, 26

Verluise, F., Laude, V., Cheng, Z., Spielmann, C., and Tournois, P. (2000). Amplitude and phase control of ultrashort pulses by use of an acousto-optic programmable dispersive filter: pulse compression and shaping. *Optics letters*, 25(8):575–577. Available from: `http://proxy.osapublishing.org/ol/abstract.cfm?uri=ol-25-8-575`. 32

Von Mises, R., Geiringer, H., and Ludford, G. S. S. (2004). *Mathematical theory of compressible fluid flow*. Courier Corporation. 45

Wang, X., Zgadzaj, R., Fazel, N., Li, Z., Yi, S. A., Zhang, X., Henderson, W., Chang, Y.-Y., Korzekwa, R., Tsai, H.-E., Pai, C.-H., Quevedo, H., Dyer, G., Gaul, E., Martinez, M., Bernstein, A. C., Borger, T., Spinks, M., Donovan, M., Khudik, V., Shvets, G., Ditmire, T., and Downer, M. C. (2013). Quasi-monoenergetic laser-plasma acceleration of electrons to 2 gev. *Nat Commun*, 4. 1988. Available from: `http://dx.doi.org/10.1038/ncomms2988`. 1

Weingartner, R., Raith, S., Popp, A., Chou, S., Wenz, J., Khrennikov, K., Heigoldt, M., Maier, A. R., Kajumba, N., Fuchs, M., Zeitler, B., Krausz, F., Karsch, S., and Grüner, F. (2012). Ultralow emittance electron beams from a laser-wakefield accelerator. *Phys. Rev. ST Accel. Beams*, 15:111302. Available from: `http://link.aps.org/doi/10.1103/PhysRevSTAB.15.111302`. 30

Wiggins, S. M., Issac, R. C., Welsh, G. H., Brunetti, E., Shanks, R. P., Anania, M. P., Cipiccia, S., Manahan, G. G., Aniculaesei, C., Ersfeld, B., Islam, M. R., Burgess, R. T. L., Vieux, G., Gillespie, W. A., MacLeod, A. M., van der Geer, S. B., de Loos, M. J., and Jaroszynski, D. A. (2010). High quality electron beams from a laser wakefield accelerator. *Plasma Physics and Controlled Fusion*, 52(12):124032. Available from: `http://stacks.iop.org/0741-3335/52/i=12/a=124032`. 28

Xie, B.-S., Wu, H.-C., Wang, H., Wang, N.-Y., and Yu, M. Y. (2007). Analysis of the electromagnetic fields and electron acceleration in the bubble regime of the laser-plasma interaction. *Physics of Plasmas (1994-present)*, 14(7). Available from: `http://scitation.aip.org/content/aip/journal/pop/14/7/10.1063/1.2750648`. 18

Zhang, P., Saleh, N., Chen, S., Sheng, Z. M., and Umstadter, D. (2003). Laser-energy transfer and enhancement of plasma waves and electron beams by interfering high-intensity laser pulses. *Phys. Rev. Lett.*, 91:225001. Available from: `http://link.aps.org/doi/10.1103/PhysRevLett.91.225001`. 26

« La esperienza non falla mai, ma sol fallano i nostri giudizi, promettendosi di lei cose che non sono in sua potestà. A torto si lamentan li omini della isperienza, la quale con somme rampogne quella accusano esser fallace. Ma lascino stare essa esperienza, e voltate tale lamentazione contro alla vostra ignoranzia, la quale vi fa transcorrere, co' vostri vani e instolti desideri, a impromettervi di quelle cose che non sono in sua potenzia, dicendo quella esser fallace. A torto si lamentano li omini della innocente esperienzia, quella accusando di fallacie e di bugiarde dimonstrazioni. »

Leonardo Da Vinci, *Codice Atlantico*, 154, 1478-1519

« Experience does not err; only your judgments err by expecting from her what is not in her power. Men wrongly complain of Experience; with great abuse they accuse her of leading them astray but they set Experience aside, turning from it with complaints as to our ignorance causing us to be carried away by vain and foolish desires to promise ourselves, in her name, things that are not in her power; saying that she is fallacious. Men are unjust in complaining of innocent Experience, constantly accusing her of error and of false evidence. »

Leonardo Da Vinci, *Codex Atlanticus*, 154, 1478-1519

« L'expérience n'est jamais en défaut. Seul l'est notre jugement, qui attend d'elle des choses étrangères à son pouvoir. Les hommes se plaignent injustement de l'expérience et lui reprochent amèrement d'être trompeuse. Laissez l'expérience tranquille et tournez plutôt vos reproches contre votre propre ignorance qui fait que vos désirs vains et insensés vous égarent au point d'attendre d'elle des choses qui ne sont pas en son pouvoir. Les hommes se plaignent à tort de l'innocente expérience et l'accusent de mensonge et de démonstrations fallacieuses. »

Léonard De Vinci, *Codex Atlanticus*, 154, 1478-1519

Abstract

Laser-plasma accelerators provide a promising compact alternative to conventional accelerators. Plasma waves with extremely strong electric fields are generated when a high intensity laser is focused into an underdense gas target. Electrons that are trapped in these laser-driven plasma waves can be accelerated up to energies of a few GeVs. Despite their great potential, laser-wakefield accelerators face some issues, regarding notably the stability and reproducibility of the beam when electrons are injected in the accelerating structure.

In this manuscript, different techniques of electron injection are presented and compared, notably injection in a sharp density gradient and ionization injection. It is shown that combining these two methods allows for the generation of stable and tunable electron beams.

We also studied a way to manipulate the electron bunch in the phase-space in order to accelerate the bunch beyond the dephasing limit. Such a technique was used with quasi-monoenergetic electron beams to enhance their energy. Moreover, the origin of the evolution of the angular momentum of electrons observed experimentally was investigated. Finally, we demonstrated experimentally a new method – the laser-plasma lens – to strongly reduce the divergence of the electron beam.

Résumé

Les accélérateurs laser-plasma, plus compacts, constituent une alternative prometteuse aux accélérateurs conventionnels. Quand un laser ultra-intense est focalisé dans une cible de gaz sousdense, des ondes plasma présentant des champs électriques de grande amplitude sont générées. Les électrons qui sont piégés dans ces ondes plasmas peuvent être accélérés jusqu'à des énergies de plusieurs GeV. Malgré leur fort potentiel, les accélérateurs laser-plasma font face à plusieurs difficultés, notamment en ce qui concerne la stabilité et la reproductibilité du faisceau au moment de l'injection dans la structure accélératrice.

Dans ce manuscript, plusieurs techniques d'injection d'électrons sont présentées et comparées, notamment les méthodes d'injection dans un gradient raide de densité et d'injection par ionisation. Nous montrons qu'il est possible d'obtenir des faisceaux d'électrons stables et contrôlables en combinant ces deux techniques.

Nous étudions également un moyen de manipuler le paquet d'électrons dans l'espace des phases afin de s'affranchir de la limite de déphasage et d'accélérer un peu plus les électrons. Cette technique est utilisée pour augmenter l'énergie de faisceaux d'électrons quasi-monoénergétiques. Par ailleurs, nous analysons l'origine de l'évolution du moment angulaire des électrons, précédemment observé expérimentalement. Enfin, nous présentons la démonstration expérimentale d'une nouvelle méthode permettant de réduire fortement la divergence du faisceau d'électron, la lentille laser-plasma.